SENSORDEVICES 2013

The Fourth International Conference on Sensor Device Technologies and Applications

WISH 2013

The Third International Workshop on Intelligent Sensor Hub

ISBN: 978-1-61208-297-4

August 25-31, 2013

Barcelona, Spain

SENSORDEVICES 2013 Editors

Sergey Yurish, IFSA - Barcelona, Spain

Francois Pacull, CEA-Leti Minatec, France

SENSORDEVICES 2013

Foreword

The Fourth International Conference on Sensor Device Technologies and Applications [SENSORDEVICES 2013], held between August 25-31, 2013 in Barcelona, Spain, continued a series of events focusing on sensor devices themselves, the technology-capturing style of sensors, special technologies, signal control and interfaces, and particularly sensors-oriented applications. The evolution of the nano-and microtechnologies, nanomaterials, and the new business services make the sensor device industry and research on sensor-themselves very challenging.

SENSORDEVICES 2013 also featured the following workshop:
- WISH 2013, The Third International Workshop on Intelligent Sensor Hub

We take here the opportunity to warmly thank all the members of the SENSORDEVICES 2013 Technical Program Committee, as well as the numerous reviewers. The creation of such a high quality conference program would not have been possible without their involvement. We also kindly thank all the authors who dedicated much of their time and efforts to contribute to SENSORDEVICES 2013. We truly believe that, thanks to all these efforts, the final conference program consisted of top quality contributions.

Also, this event could not have been a reality without the support of many individuals, organizations, and sponsors. We are grateful to the members of the SENSORDEVICES 2013 organizing committee for their help in handling the logistics and for their work to make this professional meeting a success. We hope that SENSORDEVICES 2013 was a successful international forum for the exchange of ideas and results between academia and industry and for the promotion of progress in the area of sensor device technologies and applications.

We are convinced that the participants found the event useful and communications very open. We hope Barcelona provided a pleasant environment during the conference and everyone saved some time for exploring this beautiful city.

SENSORDEVICES 2013 Chairs:

SENSORDEVICES Advisory Chairs
Sergey Yurish, IFSA - Barcelona, Spain
Petre Dini, Concordia University, Canada / China Space Agency Center, China
Elena Gaura, Coventry University, UK
Vittorio Ferrari, Università di Brescia, Italy

SENSORDEVICES 2013 Research/Industry Chairs
Raluca - Ioana Stefan-van Staden, National Institute of Research for Electrochemistry and Condensed Matter, Bucharest, Romania
Alberto Yúfera, Centro Nacional de Microelectronica (CNM-CSIC) - Sevilla, Spain

SENSORDEVICES Special Area Chairs

Ultrasonic and piezoelectric sensors

Thomas Herzog, Fraunhofer Institute for Non-Destructive Testing IZFP - Dresden, Germany

Henning Heuer, Fraunhofer Institute for Non-Destructive Testing IZFP - Dresden, Germany

Optical sensors

Vítor Carvalho, Minho University, Portugal

Irinela Chilibon, National Institute of Research and Development for Optoelectronics - Bucharest, Romania

Gas sensors

Dongfang Yang, National Research Council Canada - London, Canada

Nanosensors

Marco Tartagni, University of Bologna - Cesena, Italy

Testing and validation

Ksenia V. Sapozshnikova D.I. Mendeleyev Institute for Metrology - St. Petersburg, Russia

Vibration sensors

Subodh Kumar Singhal, National Physical Laboratory, New Delhi, India

SENSORDEVICES 2013

Committee

SENSORDEVICES Advisory Chairs

Sergey Yurish, IFSA - Barcelona, Spain
Petre Dini, Concordia University, Canada / China Space Agency Center, China
Elena Gaura, Coventry University, UK
Vittorio Ferrari, Università di Brescia, Italy

SENSORDEVICES 2013 Research/Industry Chairs

Raluca - Ioana Stefan-van Staden, National Institute of Research for Electrochemistry and Condensed Matter, Bucharest, Romania
Alberto Yúfera, Centro Nacional de Microelectronica (CNM-CSIC) - Sevilla, Spain

SENSORDEVICES Special Area Chairs

Ultrasonic and piezoelectric sensors
Thomas Herzog, Fraunhofer Institute for Non-Destructive Testing IZFP - Dresden, Germany
Henning Heuer, Fraunhofer Institute for Non-Destructive Testing IZFP - Dresden, Germany

Optical sensors
Vítor Carvalho, Minho University, Portugal
Irinela Chilibon, National Institute of Research and Development for Optoelectronics - Bucharest, Romania

Gas sensors
Dongfang Yang, National Research Council Canada - London, Canada

Nanosensors
Marco Tartagni, University of Bologna - Cesena, Italy

Testing and validation
Ksenia V. Sapozshnikova D.I. Mendeleyev Institute for Metrology - St. Petersburg, Russia

Vibration sensors
Subodh Kumar Singhal, National Physical Laboratory, New Delhi, India

SENSORDEVICES 2013 Technical Program Committee

Ammar Aryan, Université de Caen Basse-Normandie, France
Selcuk Atalay, Inonu University - Malatya, Turkey
Francisco Javier Arcega Solsona, University of Zaragoza, Spain

Marek Miskowicz, AGH University of Science and Technology - Cracow, Poland
Tarek Mohammad, University of Western Ontario - London, Canada
Gaidi Mounir, Centre de Recherches et des Technologies de l'Energie (CRTEn), Tunisie
Eros Pasero, Politecnico di Torino, Italy
Vittorio M.N. Passaro, Politecnico di Bari, Italy
Radislav A. Potyrailo, GE Global Research Center, U.S.A.
Konandur Rajanna, Indian Institute of Science - Bangalore, India
Càndid Reig, University of Valencia, Spain
Teresa Restivo, University of Porto, Portugal
Aldo Romani, University of Bologna, Italy
Mounir Bousbia Salah, University of Annaba, Algeria
Ksenia V. Sapozshnikova D.I. Mendeleyev Institute for Metrology - St. Petersburg, Russia
Majid Sarrafzadeh, University of California Los Angeles, U.S.A.
Subodh Kumar Singhal, National Physical Laboratory - New Delhi, India
Junho Song, Sunnybrooke Research Institutes/University of Toronto, Canada
Nickolaj Starodub, National University of Life and Environmental Sciences of Ukraine, / T. Shevchenko Kiev State University of Ukraine, Ukraine
Arndt Steinke, CiS Forschungsinstitut für Mikrosensorik und Photovoltaik GmbH - Erfurt, Germany
Raluca - Ioana Stefan-van Staden, National Institute of Research for Electrochemistry and Condensed Matter, Bucharest, Romania
Chelakara S. Subramanian, Florida Institute of Technology - Melbourne, USA
Roman Szewczyk, Warsaw University of Technology, Poland
Marco Tartagni, University of Bologna - Cesena, Italy
Roald Taymanov, D.I.Mendeleyev Institute for Metrology, Russia
Reshef Tenne, Weizmann Institute, Israel
Pankaj Vadgama, Queen Mary University of London, U.K.
Antonio Valente, University of Trás-os-Montes and Alto Douro (UTAD) - Vila Real, Portugal
Manuela Vieira, UNINOVA/ISEL, Portugal
Dongfang Yang, National Research Council Canada - London, Canada
Dan Yaping, Harvard University, USA
Alberto Yúfera, Seville Microelectronics Institute (IMSE-CNM), Spain
Sergey Y. Yurish, IFSA, Spain
Cyrus Zamani, University of Barcelona, Spain
Dan Zhang, University of Ontario Institute of Technology, Canada
Weiping Zhang, Shanghai Jiao Tong University, P. R. China
Ya-Pu Zhao, Chinese Academy of Sciences - Beijing, China

WISH 2013 Workshop Chair

Stephane Gervais-Ducouret, Freescale Semiconductor, Inc., France
Francois Pacull, CEA-Leti Minatec, France

WISH 2013 Technical Program Committee

Stephane Gervais-Ducouret, Freescale Semiconductor, Inc., France
Suzanne Lesecq, CEA, France
Francois Pacull, CEA-Leti Minatec, France

Laurent Perroton, ESIEE - Cite Descartes, France
Jasvinder Singh, Cork Institute of Technology, Ireland

Copyright Information

For your reference, this is the text governing the copyright release for material published by IARIA.

The copyright release is a transfer of publication rights, which allows IARIA and its partners to drive the dissemination of the published material. This allows IARIA to give articles increased visibility via distribution, inclusion in libraries, and arrangements for submission to indexes.

I, the undersigned, declare that the article is original, and that I represent the authors of this article in the copyright release matters. If this work has been done as work-for-hire, I have obtained all necessary clearances to execute a copyright release. I hereby irrevocably transfer exclusive copyright for this material to IARIA. I give IARIA permission or reproduce the work in any media format such as, but not limited to, print, digital, or electronic. I give IARIA permission to distribute the materials without restriction to any institutions or individuals. I give IARIA permission to submit the work for inclusion in article repositories as IARIA sees fit.

I, the undersigned, declare that to the best of my knowledge, the article is does not contain libelous or otherwise unlawful contents or invading the right of privacy or infringing on a proprietary right.

Following the copyright release, any circulated version of the article must bear the copyright notice and any header and footer information that IARIA applies to the published article.

IARIA grants royalty-free permission to the authors to disseminate the work, under the above provisions, for any academic, commercial, or industrial use. IARIA grants royalty-free permission to any individuals or institutions to make the article available electronically, online, or in print.

IARIA acknowledges that rights to any algorithm, process, procedure, apparatus, or articles of manufacture remain with the authors and their employers.

I, the undersigned, understand that IARIA will not be liable, in contract, tort (including, without limitation, negligence), pre-contract or other representations (other than fraudulent misrepresentations) or otherwise in connection with the publication of my work.

Exception to the above is made for work-for-hire performed while employed by the government. In that case, copyright to the material remains with the said government. The rightful owners (authors and government entity) grant unlimited and unrestricted permission to IARIA, IARIA's contractors, and IARIA's partners to further distribute the work.

Table of Contents

Dynamic Characterization of Bi-material Cantilevers

R Bijster, J de Vreugd, H Sadeghian
Department of optomechatronics
TNO
The Netherlands
Email: Hamed.SadeghianMarnani@tno.nl

***Abstract*—In this paper, an experimental-theoretical method is proposed to accurately determine the thermal diffusivity, characteristic time constant and layer thicknesses of a bi-material cantilever using a transient, non-destructive and non-contact measurement. The technique is based on the well-known optical beam deflection method. A time dependent, sinusoidal heat load is locally applied to induce a time varying thermal profile over the length of the beam, resulting in a mismatch-strain between the two layers that bends the cantilever. A measurement of the phase difference between the thermo-mechanical response and the input signal can be used to extract the thermal diffusivity, characteristic time constant and the location of the heat source. For this reason a closed-form analytical solution for the thermo-mechanical response is presented. The dynamic response of the system is characterized using the transfer function in the Laplace domain. The analytical solution includes a Gaussian distributed, time-dependent heat source of known width at a location along the beam. A constant convective heat transfer coefficient can be included to allow measurement in ambient conditions. A combination of a measurement of the thermal diffusivity and the effective conductance are used to calculate the mutual layer thicknesses of the two layers.**

Keywords-bilayer cantilevers; characterization; diffusivity.

I. INTRODUCTION

Bi-material cantilevers are widely used in nano-instrumentation as actuators and sensors. The material properties and geometry of these cantilevers vary largely between batches and are not well controlled. In this paper, a method is proposed to accurately determine the thermal diffusivity, effective conductance and layer thicknesses by means of a transient, non-destructive, non-contact measurement. This allows quick characterization of bi-material cantilevers, e.g., after production or for acceptance testing.

II. THEORY

The thermal diffusivity is a measure for the velocity at which heat spreads throughout a medium, e.g., a micro-cantilever. It cannot be measured directly and needs to be determined through a proxy. In this derivation, it is assumed that a cantilever beam is concerned, although the derivation could equally well be performed for other boundary conditions. The cantilever is assumed to be heated locally with a Gaussian power distribution (e.g. by using a laser). This is typical for the optical beam deflection method, popular in Scanning Probe Microscopy setups. The heating results in a temperature distribution over the length of the beam. It is assumed, that the temperature distribution over the thickness of the cantilever is negligible. The temperature distribution over the length of the cantilever causes a mismatch strain on the interface between the two layers of the cantilever due to the unequal expansion coefficients of the materials. The mismatch strain results in a bending of the cantilever. If the input signal is varied sinusoidally, the cantilever will oscillate at the same frequency. The rotation at a specific location, however, will lag behind with respect to the input signal. This phase shift is caused by the thermal diffusivity and is dependent on spot position and input frequency. The relation between these variables will be derived in the following sections.

A. Temperature distribution

The temperature distribution along the length of the beam is dominated by the heat equation. This heat equation can be formulated in its most general form as

$$\frac{\partial T(x,t)}{\partial t} = D\frac{\partial^2 T(x,t)}{\partial x^2} - B\left(T(x,t) - T_{env}\right) + f(x,t) \tag{1}$$

where $T(x,t)$ is the temperature along the beam in Kelvin, x is the running coordinate along the length ($x = 0$ at the base, $x = L$ at the tip), D is the thermal diffusivity in $\mathrm{m}^2\,\mathrm{s}^{-1}$, B is the characteristic time constant for convective heat transfer in s^{-1} and $f(x,t)$ is a heat source function. The environment is defined by means of two non-zero boundary conditions(e.g. a Dirichlet boundary condition at the base and a Neumann boundary conditions at the tip) including a non-zero initial condition. To simplify the solution of (1) a change of variables is used. When it is assumed that the base temperature is constant and equal to the environmental temperature T_{env}, one can define

$$u(x,t) = T(x,t) - T_{env} \tag{2}$$

With this change in variables both boundary conditions and the initial condition can be set to zero when required and the equation reduces to

$$u_t = Du_{xx} - Bu + f(x,t) \tag{3}$$

 ISBN: 978-1-61208-297-4

This is a realistic assumption for most microcantilevers, because these are often mounted on a base that is far greater in dimensions and heat capacity. The transformed equation has to meet the following boundary and initial conditions:

$$u(0,t) = u_x(L,t) = u(x,0) = 0 \tag{4}$$

It is assumed, that the source function can be described with

$$f(x,t) = a(t) \exp\left(-\frac{(x-b)^2}{2c^2}\right) \tag{5}$$

where a is a term in $\mathrm{W\,m^{-1}}$ that determines the amplitude of the distribution, b is the coordinate of the center position of the spot and c is a constant that determines the width of the spot. The constant c is related to the Full-Width Half Maximum of the beam as follows from (6)

$$c = \frac{FWHM}{2\sqrt{2\ln 2}} \tag{6}$$

Using a Gaussian distribution gives a good representation of the physical laser spot. The problem can be solved using the Method of Laplace. Taking the Laplace transform of (3) results in the following ODE

$$\frac{\partial^2 \tilde{u}}{\partial x^2} - \frac{s+B}{D}\tilde{u} = -\frac{\tilde{f}}{D} \tag{7}$$

where $\tilde{u}$ and $\tilde{f}$ are the Laplace transformed function of $u(x,t)$ and source function $f(x,t)$ respectively. The amplitude of the signal can be a function of time, while the position of the source is assumed constant. This implies that the source function can be written as

$$\tilde{f} = \tilde{F}(s) \cdot \exp\left(-\frac{(x-b)^2}{2c^2}\right) \tag{8}$$

The homogeneous solution for the ODE of (7) can be verified to be

$$\tilde{u}_c = c_1 \exp\left(\sqrt{\frac{s+B}{D}}\right) + c_2 \exp\left(-\sqrt{\frac{s+B}{D}}\right) = c_1\tilde{u}_1 + c_2\tilde{u}_2 \tag{9}$$

The particular solution can be found using the Method of Variation of Parameters in which the solution is expressed as a function of the fundamental solutions $\tilde{u}_1$ and $\tilde{u}_2$.

$$\tilde{u}_p = -\tilde{u}_1 \int \frac{\tilde{u}_2 \tilde{g}}{W(\tilde{u}_1, \tilde{u}_2)} dx + \tilde{u}_2 \int \frac{\tilde{u}_1 \tilde{g}}{W(\tilde{u}_1, \tilde{u}_2)} dx \tag{10}$$

where W is the Wronskian of the fundamental solutions

$$W(\tilde{u}_1, \tilde{u}_2) = \tilde{u}_1\tilde{u}_2' - \tilde{u}_2\tilde{u}_1' \tag{11}$$

and $g(x) = -\tilde{f}/D$. The general solution then becomes

$$\tilde{u} = c_1\tilde{u}_1 + c_2\tilde{u}_2 + \tilde{u}_p \tag{12}$$

where the constants can be solved for using the conditions of (4). Due to the complexity and length of the intermediate results, these equations have been solved using Maple algebraic software.

B. Rotation of the cantilever

The curvature of the beam can be given as a function of the geometry and the mismatch strain by

$$\kappa = \frac{\partial^2 z}{\partial x^2} = \beta\epsilon_m \tag{13}$$

with ϵ_m the mismatch strain, κ the beam curvature in m and z the out of plane displacement of the cantilever in m. The mismatch strain itself can be easily calculated as

$$\epsilon_m = \Delta\alpha\,(T(x) - T_{SFT}) \tag{14}$$

where $\Delta\alpha$ is the difference in thermal expansion coefficient of the used materials, $T(x)$ is the temperature along the beam and T_{SFT} is the Stress-Free Temperature. The constant β is a function of the geometry and material properties of the individial layers. It is defined using the following equations [1]:

$$\beta = \frac{6hm}{t_2}\left(\frac{1+h}{1+2hm\,(2+3h+2h^2)+h^4m^2}\right) \tag{15}$$

In this relation the following auxiliary parameters are defined:

$$h = \frac{t_1}{t_2} \tag{16}$$

$$m = \frac{M_1}{M_2} \tag{17}$$

$$M_i = \frac{E_i}{1-\nu_i} \tag{18}$$

where E is the Young's modulus of the material, t is the layer thickness, ν the Poisson ratio and the subscript i refers to the respective layer (1, top; 2, bottom). Integration with respect to x results in an expression for the rotation:

$$\tilde{\theta} = \beta\Delta\alpha \int \tilde{u}dx + \beta\Delta\alpha\,(T_{env} - T_{SFT})\,x + \theta_0 \tag{19}$$

The second term on the right hand side of this equation gives the static cantilever rotation due to the environmental conditions. In measurements this can easily be aligned for such that this term effectively becomes zero. In this case only the dynamic effects that influence the period and phase are considered, which reduces this equation to:

$$\tilde{\theta}_{dyn} = \int \tilde{u}dx + \theta_{0,dyn} \tag{20}$$

The term $\theta_{0,dyn}$ can be solved for using the boundary condition that the rotation at the base of the cantilever always has to be zero. The transfer function for the rotation of the cantilever due to a local heat input is given by (21).

 ISBN: 978-1-61208-297-4

$$G(s) = \frac{\sqrt{2\pi}c}{8(s+B)\cosh(k_3)}\{ - 2\exp(k_1)[\mathrm{erf}(\mathrm{m}_1) + \mathrm{erf}(\mathrm{m}_2)] + 2\exp(k_2)[\mathrm{erf}(\mathrm{m}_4) - \mathrm{erf}(\mathrm{m}_3)] + 4\cosh(k_3)\mathrm{erf}(\mathrm{m}_5) + \exp(k_4)[\mathrm{erf}(\mathrm{m}_3) - \mathrm{erf}(\mathrm{m}_4)] + \exp(k_5)[\mathrm{erf}(\mathrm{m}_2) + \mathrm{erf}(\mathrm{m}_4)] + \exp(k_6)[\mathrm{erf}(\mathrm{m}_3) - \mathrm{erf}(\mathrm{m}_1)] + \exp(k_7)[\mathrm{erf}(\mathrm{m}_1) + \mathrm{erf}(\mathrm{m}_2)]\} \quad (21)$$

The auxiliary terms in this equation are omitted here for brevity and can be found in the Appendix. The phase lag of

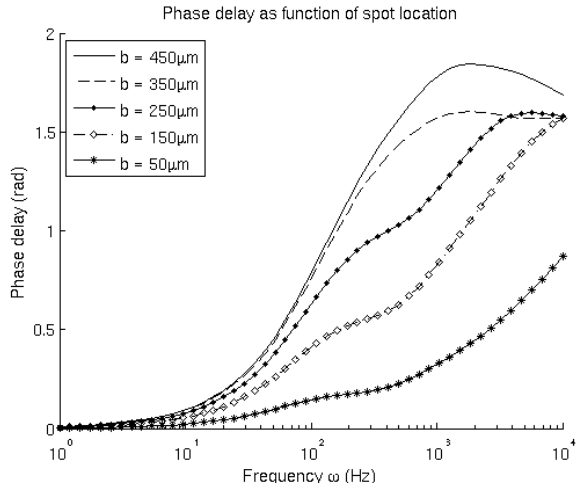

Figure 1. Phase shift as function of position. $L = 500$ µm, $D = 7 \cdot 10^{-5}$ m^2 s^{-1}, Full-Width Half Minimum of spot = 30 µm, spot location indicated in legend in µm.

the response with respect to the input is easily found from the transfer function by substituting $s = j\omega$. The argument of the complex output gives the phase angle. The phase lag for the rotation of the cantilever for a known location is depicted in Figure 1. Similarly the delay as a function of thermal diffusivity is plotted in Figure 2. Dependent on position and thermal diffusivity clearly distinct phase delays are found. With a proper initial guess of the parameters, for example based on manufacturer specifications, this allows for recovery of the thermal diffusivity by fitting the theoretical model to the measurement data.

C. Calculation of layer thicknesses

With traditional techniques, e.g., optical microscopy or Scanning Electron Microscopy (SEM), the thickness of a micro-cantilever cannot be measured with sufficient accuracy. The accuracy of these measurements is at approximately 1 µm in the same order of magnitude of the actual thickness. If the material properties are known (e.g. from

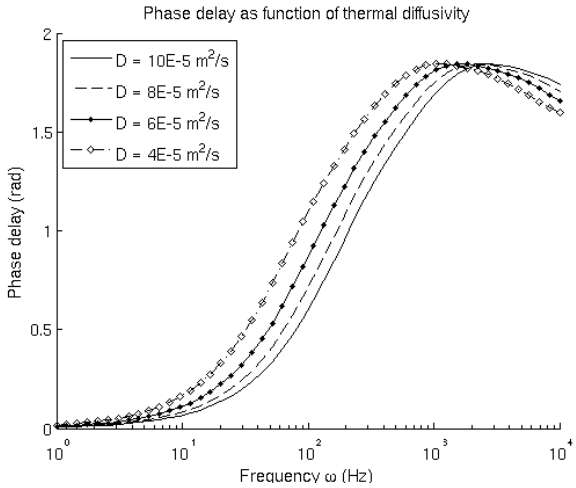

Figure 2. Phase shift as function of thermal diffusivity. $L = 500$ µm, Full-Width Half Minimum of spot = 30 µm, $b = 450$ µm. Thermal diffusivity is indicated in legend in m^2 s^{-1}.

measurement), equations can be derived with only the layer thicknesses as unknowns. One set of equations is given by the expressions for the thermal diffusivity D and the effective conductance G of a one-dimensional cantilever. The one dimensional heat equation can be written as

$$kAu_{xx} = c_p \rho A u_t \quad (22)$$

in which k is the thermal conductance in W m^{-1} K^{-1}, A is the cross-sectional area in m^2 and c_p is the specific heat capacity under constant pressure in J kg^{-1} K^{-1}. Assuming heat transfer mainly occurs in the longitudinal direction and is negligible in the other directions, the thermal conductance can be written in terms of the two layers as

$$kA = (k_1 t_1 + k_2 t_2)\, w \quad (23)$$

where w represents the width of the beam. The total heat capacity can then also be rewritten as a function of the two layers by

$$c_p \rho A = (c_{p,1}\rho_1 t_1 + c_{p,2}\rho_2 t_2)\, w \quad (24)$$

With the thermal diffusivity D defined by

$$D = \frac{k}{\rho c_p} \quad (25)$$

this results in the final expression for the thermal diffusivity

$$D = \frac{k_1 t_1 + k_2 t_2}{c_{p,1}\rho_1 t_1 + c_{p,2}\rho_2 t_2} \quad (26)$$

The effective conductance can also be expressed as a function of the two layer thicknesses using

$$G = (k_1 t_1 + k_2 t_2)\frac{w}{L} \quad (27)$$

Equations (26) and (27) form the required set that allows solving for the thicknesses, given that the thermal properties

of the layers are known. Solving the given system for the two mutual thicknesses results in the following expressions:

$$t_2 = \frac{GL\left(\frac{1}{D} - \frac{\rho_1 c_{p,1}}{k_1}\right)}{w\left(\rho_2 c_{p,2} - \frac{\rho_1 c_{p,1} k_2}{k_1}\right)} \tag{28}$$

$$t_1 = \frac{GL}{wk_1} - \frac{k_2}{k_1} t_2 \tag{29}$$

Assuming that the thermal diffusivity and effective conductance have been measured exactly and the material properties are known, the quality of the estimation of thicknesses via this method can be assessed. Here, cantilevers with a mono-crystalline silicon substrate and a gold reflective coating have been used. For these materials the material properties are known from literature within an accuracy of a few percent [2][3][4][5][6][7][8].

For this method, both the thermal diffusivity and the effective conductance need to be known. The thermal diffusivity is determined as explained earlier. The effective conductance can be determined as described below.
For a cantilever with the temperature distribution known when power is applied at the tip, the effective conductance can be expressed as

$$G = \frac{P}{\Delta T} \tag{30}$$

where G is the effective conductance in $\mathrm{W\,K^{-1}}$, P is the applied power in W and ΔT is the temperature difference between tip and base in K. Generally it is not possible to measure the tip temperature in an AFM setup and other means need to be used to find the effective conductance. One such method is described by Sheng, Narayanaswamy, Goh, and Chen[9], which use the changes in beam rotation caused by changes in the applied power and changes in the base temperature. In that scenario however, it is still assumed that the heat is applied at the tip of the cantilever. A similar analysis has been done for the general case in which the beam is heated locally at an arbitrary position along its length.

In the following derivation, it is assumed that the beam is locally heated by a laser with a Gaussian distributed spot as introduced earlier. Only the steady state solution will be considered. If vacuum conditions are assumed, the problem can be stated as

$$Du_{xx} + \frac{D}{\frac{k_1 t_1 + k_2 t_2}{t_1 + t_2}} \frac{P(x,t)}{(t_1 + t_2)\, w} = u_t \tag{31}$$

with $P(x,t)$ in $\mathrm{W\,m^{-1}}$. If one uses P_0 to represent the total power impinging on the cantilever, the term a can be derived from the forcing function using the following relation:

$$P_0 = \int_0^L a \exp\left(-\frac{(x-b)^2}{2c^2}\right) dx \tag{32}$$

Solving this equation for the term a results in

$$a = P_0 \left(1/2c\sqrt{2\pi}\left(\mathrm{erf}\left(\frac{\mathrm{b}}{\mathrm{c}}\frac{\sqrt{2}}{2}\right) + \mathrm{erf}\left(\frac{\mathrm{L\text{-}b}}{\mathrm{c}}\frac{\sqrt{2}}{2}\right)\right)\right)^{-1} \tag{33}$$

Because only steady state is considered the partial derivative with respect to time t equals zero. The problem then becomes a simple ODE that after repeated integration gives the temperature distribution over the beam. The ODE is reduced to

$$u_{xx} = -\frac{a}{\bar{k}} \exp\left(\frac{-(x-b)^2}{2c^2}\right) \tag{34}$$

with $\bar{k}$ defined as

$$\bar{k} = (k_1 t_1 + k_2 t_2)\, w \tag{35}$$

The two integration constants can be solved for by considering the boundary conditions of (4). The temperature distribution with respect to the base temperature is given by

$$\begin{aligned} u(x) = {} & \\ & - P_0 \left(\sqrt{2}c\left\{\exp\left(-\frac{(b-x)^2}{2c^2}\right) - \exp\left(-\frac{b^2}{2c^2}\right)\right\}\right. \\ & + \sqrt{\pi}\left\{(b-x)\,\mathrm{erf}\left(\frac{\sqrt{2}}{2}\frac{\mathrm{b\text{-}x}}{\mathrm{c}}\right) - x\,\mathrm{erf}\left(\frac{\sqrt{2}}{2}\frac{\mathrm{L\text{-}b}}{\mathrm{c}}\right)\right. \\ & \left.\left. - b\,\mathrm{erf}\left(\frac{\sqrt{2}}{2}\frac{\mathrm{b}}{\mathrm{c}}\right)\right\}\right) \\ & \Big/ \left\{\bar{k}\sqrt{\pi}\left(\mathrm{erf}\left(\frac{\sqrt{2}}{2}\frac{\mathrm{b}}{\mathrm{c}}\right) + \mathrm{erf}\left(\frac{\sqrt{2}}{2}\frac{\mathrm{L\text{-}b}}{\mathrm{c}}\right)\right)\right\} \end{aligned} \tag{36}$$

By defining $H \equiv \beta\Delta\alpha$ and using the earlier developed relations for the rotation of the cantilever, one can deduce that

$$\theta_r(x) = H \int u(x)\, dx + H\,(T_{env} - T_{SFT})\, x + c_3 \tag{37}$$

where the integration constant can be solved for by considering that the rotation at the base shall be zero and constant. Substituting $x = b$, for the rotation is measured at the location of actuation, results in the total mechanical response to be equal to (38).

 ISBN: 978-1-61208-297-4

$$\theta_r\left(x=b\right)=$$
$$H\left(P_0 b^2\sqrt{\pi}\left\{\operatorname{erf}\left(\frac{\sqrt{2}}{2}\frac{\text{L-b}}{\text{c}}\right)+\operatorname{erf}\left(\frac{\sqrt{2}}{2}\frac{\text{b}}{\text{c}}\right)\right\}\right.$$
$$2b\sqrt{\pi}\bar{k}\left(T_{env}-T_{SFT}\right)\left\{\operatorname{erf}\left(\frac{\sqrt{2}}{2}\frac{\text{b}}{\text{c}}\right)-\operatorname{erf}\left(\frac{\sqrt{2}}{2}\frac{\text{L-b}}{\text{c}}\right)\right\}$$
$$\left.-P_0\sqrt{\pi}c2\operatorname{erf}\left(\frac{\sqrt{2}}{2}\frac{\text{b}}{\text{c}}\right)-P_0 bc\sqrt{2}\exp\left(-\frac{b^2}{2c^2}\right)\right)$$
$$\Big/\left\{2\bar{k}\sqrt{\pi}\left(\operatorname{erf}\left(\frac{\sqrt{2}}{2}\frac{\text{b}}{\text{c}}\right)+\operatorname{erf}\left(\frac{\sqrt{2}}{2}\frac{\text{L-b}}{\text{c}}\right)\right)\right\} \quad (38)$$

By studying the change in beam rotation caused by a change in incident power and a change in base temperature two expressions can be derived to solve for the unknown constants H and $\bar{k}$. Expressions for these changes can be found using partial differentiation of (38) with respect to P_0 and T_{env} respectively. This results in the following set of relations.

$$\frac{\partial\theta_r\left(x=b\right)}{\partial P_0}=$$
$$H\left(b^2\sqrt{\pi}\left\{\operatorname{erf}\left(\frac{\sqrt{2}}{2}\frac{\text{L-b}}{\text{c}}\right)+\operatorname{erf}\left(\frac{\sqrt{2}}{2}\frac{\text{b}}{\text{c}}\right)\right\}\right.$$
$$+\left(b^2-c^2\right)\sqrt{\pi}\operatorname{erf}\left(\frac{\sqrt{2}}{2}\frac{\text{b}}{\text{c}}\right)+bc\sqrt{2}\exp\left(-\frac{b^2}{c^2}\right)\Big)$$
$$\Big/\left\{2\bar{k}\sqrt{\pi}\left(\operatorname{erf}\left(\frac{\sqrt{2}}{2}\frac{\text{b}}{\text{c}}\right)+\operatorname{erf}\left(\frac{\sqrt{2}}{2}\frac{\text{L-b}}{\text{c}}\right)\right)\right\} \quad (39)$$

$$\frac{\partial\theta_r\left(x=b\right)}{\partial T_{env}}=Hb \quad (40)$$

The position of the spot can be found in multiple ways and the thermal diffusivity can be derived from experiments as explained earlier. Combined with the found value for $\bar{k}$ one now has two functions of t_1 and t_2 that can be solved for: (26) and (35).

III. Experiments

The developed relations have been compared to experimentation. In this section the used setup and obtained results will be discussed.

A. Experimental setup

The setup implements the optical lever technique to actuate and measure the rotation of the beam. A sketch of the setup is given in Figure 3. A 633 nm (red) fiber laser is used. The beam passes through a collimator to obtain a collimated beam of 1.5 mm wide. The light then passes through a $\lambda/2$ waveplate to shift the polarization. In the polarizing beam splitter the light is partially reflected to the beam dump, the remaining light passes straight through. The amount that passes through is regulated using the waveplates. The light continues by passes through another $\lambda/2$ waveplate to change the polarization again. In the second polarizing beam splitter the light is reflected to a power meter and the rest passes on through a $\lambda/4$ waveplate that changes the polarization from linear to circular. The light is then focused on the cantilever using a $f = 20$ mm, $10\times$ microscope objective. Part of the power of the light is absorbed, changing the rotation of the beam. The light is reflected under a slight angle back into the microscope objective. On the way back, the light passes through the $\lambda/4$ waveplate again. Because the light has been reflected in the meantime, the polarization is now shifted by $90°$. The light is reflected by the polarizing beam splitter onto the OPS detector. The remaining light passes straight through and eventually ends up at the detector of the camera. The Maypa OPS is a linear Position Sensitive

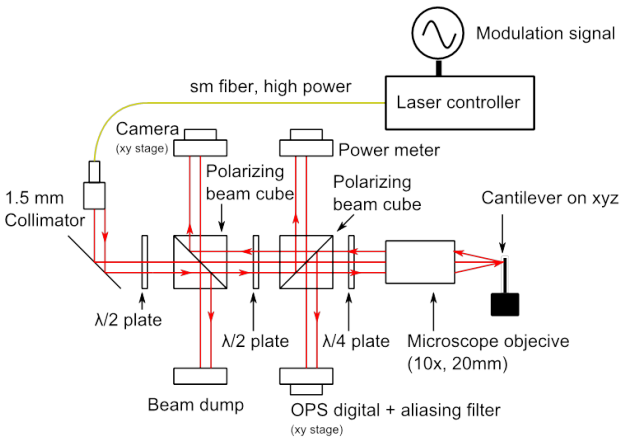

Figure 3. Schematic drawing of tabletop AFM setup[10].

Detector (PSD) that registers the position of the spot in a plane perpendicular to the incoming beam and its intensity. The OPS is mounted on an XY-stage that allows alignment of the sensor. The OPS is aligned such that at a given reference power level, the resulting rotation of the cantilever is set as datum. The camera present in the setup is used for optical alignment of the laser spot on the cantilever. The cantilever is mounted on an XYZ translational stage for this purpose. It can be used to move the laser spot along the cantilever and to get it into focus of the laser beam. More details regarding the tabletop AFM setup are given by Sadeghian et al. [10].

For the performed experiments the Nanoworld ARROW-TL8Au cantilevers have been used. These have a rectangular plan form with a triangular shaped end. The cross-section is rectangular and consists of a approximately 1 µm thick Silicon substrate and an approximately 30 nm Gold reflective

 ISBN: 978-1-61208-297-4

coating. The absence of a tip and the relatively high beam ratio of 5 make it a proper candidate for the validation of the theory. From discussions with the manufacturer it became clear that between the substrate and the reflective coating a third layer is added to prevent diffusion of the gold atoms into the silicon substrate. This intermediate layer has a thickness of approximately 4 nm and can be composed of either titanium or chromium. The actual used material is unknown. In the analysis, it is assumed that the effect of this layer is negligble compared to the thicker reflective coating and much thicker substrate. The dimensions of the cantilever plan form can be found in Figure 4. The accuracy of this measurement is 1 µm. Using SEM the thickness can therefore not be measured. The predicted thicknesses from theory can therefore not be validated against an absolute reference. Using the described setup, cantilevers can be

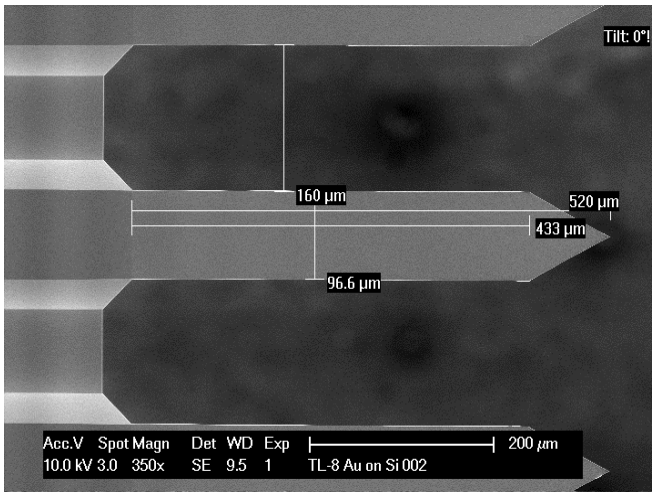

Figure 4. SEM of Nanoworld ARROW-TL8Au cantilevers used in measurements including dimensions.

actuated upto approximately 10 kHz. After that the signal to noise ratio (SNR) will become too low for registration of the movement of the cantilever.

B. Experimental procedure

The laser spot is placed in a required reference position by correlation of photographs taken using the microscope objective and CCD camera present in the setup with the SEM of the cantilever as depicted in Figure 5. After alignment the required laser power is set manually and the laser is focused. The OPS is aligned such that the returning laser beam hits it as close to its center as possible to reduce the effects of any sensor non-linearity. Any remaining sensor signal caused by the initial rotation of the cantilever is nulled in postprocessing. The setup is mounted on a pneumatically stabilized table and stored in a light tight container to reduce the effects of environmental vibration and stray light.

To determine the thermal diffusivity of the cantilever, the phase delay of the rotation with respect to the input signal is

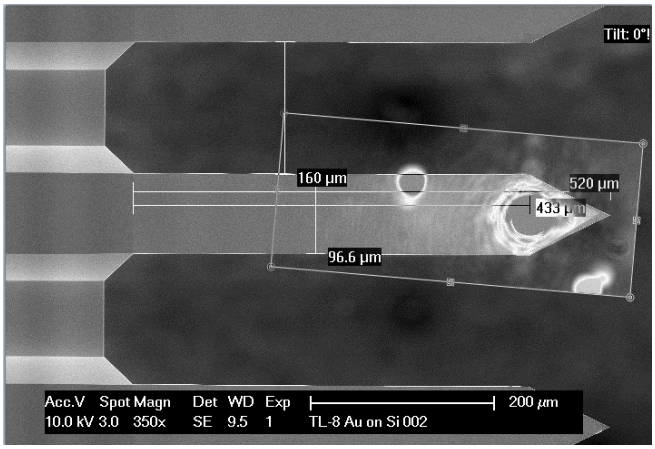

Figure 5. Alignment of the laser spot on the cantilever by correlation of CCD images with SEM of the cantilever.

measured. This is done by modulating the laser diode current sinusoidially. The mean current (I_{DC}) is set to the level that was also set after the detector alignment. The amplitude of the wave (I_{AC}) can be chosen freely, as long as the minimum and maximum currents as specified for the laser diode are not exceeded. The diode current is then modulated as

$$I_{LD} = I_{DC} + I_{AC} \sin(\omega_i t) \tag{41}$$

The frequency ω is set to several values on a logarithmic interval between 1 and $10,000$ Hz for the ARROW-TL8Au cantilevers. The acquisition time is dependent on the actuation frequency and is taken to cover at least ten full cycles with a minimum of 0.1 s. For the used cantilevers this is sufficient to reach a steady mean cantilever temperature. As the initial temperature is not known exactly, using temperature fluctuations around a steady mean negates the need for inclusion of the transient. A generic sine function is later fitted to the steady state cycles of the measured rotation and the phase shift is extracted.

C. Results

The phase angle is used to fit (21) to the processed delay measurements. It is assumed in this fit that the experiment was performed in vacuum and B is thus equal to zero. The found diffusivity is therefore an overestimate. However, as the error is systematic, the results can be used to judge the validity of the derived equations. This decision is justified by the large uncertainty in convective heat transfer coefficient. The convective time constant B can be related to the convective heat transfer coefficient via

$$B = \frac{hA}{mc_p} \tag{42}$$

where h is the heat transfer coefficient in $\mathrm{W\,m^{-2}\,K^{-1}}$, A is the area involved in convective heat transfer in $\mathrm{m^2}$ and the product $m \cdot c_p$ is the total heat capacity of the

cantilever in $\mathrm{J\,K^{-1}}$. The total heat capacity is unknown, as well as the exact area exposed to convective heat transfer. The convective heat transfer coefficient is unknown and values reported in literature vary largely. For example, Sheng, Narayanaswamy, Goh, and Chen[9] report values of $h = 500 - 5000\ \mathrm{W\,m^{-2}\,K^{-1}}$. The physics behind this large convective heat transfer coeffient is currently poorly understood [11][12]. For this reason it was decided to assume no convective heat transfer and accept the systematic error. Future experiments in vacuum are required for full validation of the theory.

In estimating the thermal diffusivity all frequencies between 1 and 2000 Hz were used. Higher frequencies were discarded because the mechanical resonance frequency of the cantilever dominated here. This effect was not covered in the developed theoretical model. The non-linear fitting procedure requires an initial guess for the thermal diffusivity. Based on manufacturer specifications the thermal diffusivity is assumed $D = 7 \cdot 10^{-5}\ \mathrm{m^2\,s^{-1}}$. The spot positions are obtained from correlation of the CCD camera images with the SEM of the cantilever. The found diffusivities are plotted as a function of the laser spot center position in Figure 6. As can be seen in the diagram,

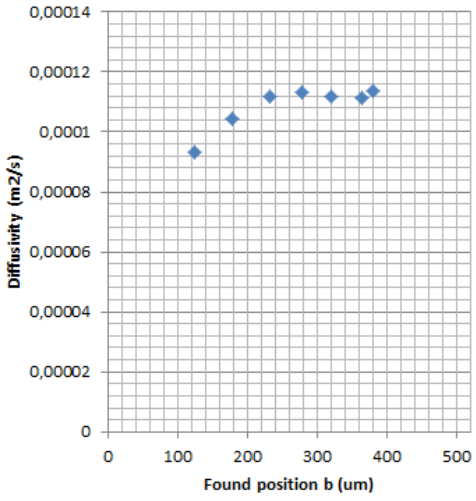

Figure 6. Found diffusivity as function of spot center position.

the variation of the estimation of the thermal diffusivity is small for a large range of spot center positions. However, when the spot gets closer to the base of the cantilever, the estimation of thermal diffusivity drops considerably. It is currently speculated that this is caused by a significant heat leak into the base causing the temperature of the base to change. This will have to be verified in future experiments. During measurements it was noticed that the extracted thermal diffusivity was dependent on the incident laser power. The incident mean laser power was set to $1.33, 2.00, 2.69$ and 3.26 mW. Per mean power setting, wave magnitudes of $0.3802, 0.7604$ and 1.1407 mW were superimposed. The found thermal diffusivities are plotted in Figure 7. As can be seen in Figure 7 the derived diffusivity

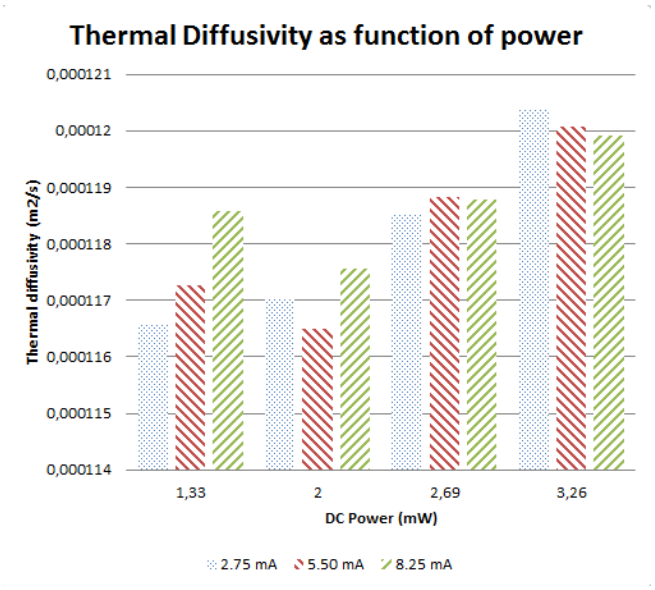

Figure 7. Found thermal diffusivity as a function of power, assuming vacuum conditions. Spot located at $b = 433$ µm.

varies with both AC power and DC power. No clear trend is evident from the results. Although at DC power settings of $1.33, 2.69$ and 3.26 mW a higher AC power seems to increase the estimate, although this is not true for 2.00 mW. Also the change in diffusivity does not seem to adhere any evident relation. The reasons for this dependency are currently not well understood.

IV. Conclusion and Future Work

A theoretical model is derived that allows the determination of the thermal diffusivity of a cantilever microbeam using the optical beam deflection method. Via this non-contact, non-destructive method also the effective conductance and the layer thicknesses can be determined if the material properties are known. Initial experimental results show that proposed method is capable of resolving the thermal diffusivity of microcantilevers. Experiments conducted in vacuum conditions are required for full validation of the theoretical model.

Acknowledgment

This research was financially supported by enabling technology program Materials. Special gratitude goes to dr. Rodolf Herfst for his help on the experimental table-top AFM setup used in this research.

 ISBN: 978-1-61208-297-4

APPENDIX

The transfer function for the rotation of the cantilever due to a local heat input is given by

$$\begin{aligned} G(s) = \frac{\sqrt{2\pi}c}{8(s+B)\cosh(k_3)}\{ & \\ & -2\exp(k_1)[\operatorname{erf}(\mathrm{m}_1)+\operatorname{erf}(\mathrm{m}_2)] \\ & +2\exp(k_2)[\operatorname{erf}(\mathrm{m}_4)-\operatorname{erf}(\mathrm{m}_3)] \\ & \quad +4\cosh(k_3)\operatorname{erf}(\mathrm{m}_5) \\ & +\exp(k_4)[\operatorname{erf}(\mathrm{m}_3)-\operatorname{erf}(\mathrm{m}_4)] \\ & +\exp(k_5)[\operatorname{erf}(\mathrm{m}_2)+\operatorname{erf}(\mathrm{m}_4)] \\ & +\exp(k_6)[\operatorname{erf}(\mathrm{m}_3)-\operatorname{erf}(\mathrm{m}_1)] \\ & \quad +\exp(k_7)[\operatorname{erf}(\mathrm{m}_1)+\operatorname{erf}(\mathrm{m}_2)]\} \end{aligned}$$

where the auxiliary parameters are given by:

$$k_1 = \frac{2D(b-L)\sqrt{\frac{s+B}{D}}+(s+B)c^2}{2D}$$

$$k_2 = \frac{2D(b-L)\sqrt{\frac{s+B}{D}}+(s+B)c^2}{2D}$$

$$k_3 = \sqrt{\frac{s+B}{D}}L$$

$$k_4 = \frac{2D(L-2b)\sqrt{\frac{s+B}{D}}+(s+B)c^2}{2D}$$

$$k_5 = \frac{-2DL\sqrt{\frac{s+B}{D}}+(s+B)c^2}{2D}$$

$$k_6 = \frac{2DL\sqrt{\frac{s+B}{D}}+(s+B)c^2}{2D}$$

$$k_7 = \frac{2D(2b-L)\sqrt{\frac{s+B}{D}}+(s+B)c^2}{2D}$$

$$m_1 = \frac{\sqrt{2}\left(b+c^2\sqrt{\frac{s+B}{D}}\right)}{2c}$$

$$m_2 = \frac{\sqrt{2}\left(L-b-c^2\sqrt{\frac{s+B}{D}}\right)}{2c}$$

$$m_3 = \frac{\sqrt{2}\left(L-b+c^2\sqrt{\frac{s+B}{D}}\right)}{2c}$$

$$m_4 = \frac{\sqrt{2}\left(-b+c^2\sqrt{\frac{s+B}{D}}\right)}{2c}$$

$$m_5 = \frac{\sqrt{2}}{2}\frac{b}{c}$$

REFERENCES

[1] W. Young and R. G. Budynas, *Roark's Formulas for Stress and Strain*, 7th ed. New York: McGraw-Hill, 2002.

[2] B. Bardes, H. Baker, W. Cubberly, and A. I. Committee, *Metals Handbook*, 9th ed., B. Bardes, P. Baker, Hugh, Cubberly, and William, Eds. American Society for Metals, 1978.

[3] C. Gibson, D. Smith, and C. Roberts, "Calibration of silicon atomic force microscope cantilevers," *Nanotechnology*, vol. 16, pp. 234–238, 2005.

[4] J. Jou, C. Liao, and K. Jou, "A method for the determination of gold thin film's mechanical properties," *Thin Solid Films*, vol. 238, pp. 70–72, 1994.

[5] Y. Ju, "Phonon heat transport in silicon nanostructures," *Applied Physics Letters*, vol. 87, p. 153106, 2005.

[6] W. Liu and M. Asheghi, "Phonon-boundary scattering in ultrathin single-crystal silicon layers," *Applied Physics Letters*, vol. 84, p. 3819, 2004.

[7] S. Okuda, M. Kobiyama, and T. Inami, "Mechanical Properties and Thermal Stability of Nanocrystalline Gold Prepared by Gas Deposition Method," *Materials Transactions, JIM*, vol. 40, no. 5, pp. 412–415, 1999.

[8] D. Son, J. Jeong, and D. Kwon, "Film-thickness considerations in microcantilever-beam test in measuring mechanical properties of metal thin films," *Thin Solid Films*, vol. 437, pp. 182–187, 2003.

[9] S. Sheng, A. Narayanaswamy, S. Goh, and G. Chen, "Thermal conductance of bimaterial microcantilevers," *Applied Physics Letters*, vol. 92, no. 063509, 2008.

[10] H. Sadeghian and R. Herfst, "Systematic characterization of optical beam deflection measurement for micromechanical systems," *unpublished*.

[11] M. Kasper, V. Natrajan, N. Privorotskaya, K. Christensen, and W. King, "Natural advection from a microcantilever heat source," *Applied Physics Letters*, vol. 96, p. 063113, 2010.

[12] K. Kim and W. King, "Thermal conduction between heated microcantilever and a surrounding air environment," *Applied Thermal Engineering*, vol. 29, pp. 1631–1641, 2009.

 ISBN: 978-1-61208-297-4

Monitoring of Hazardous Scenarios using Multi-Sensor Devices

M. Bartholmai, E. Koeppe, P. P. Neumann
Sensors, Measurement and Testing Methods
BAM Federal Institute for Materials Research and Testing
Berlin, Germany
matthias.bartholmai@bam.de

***Abstract*— The combination of different types of sensors to multi-sensor devices offers excellent potential for monitoring applications. This should be demonstrated by means of four different examples of actual developments carried out by Federal Institute for Materials Research and Testing (BAM): monitoring and indoor localization of relief forces, a micro-drone for gas measurement in hazardous scenarios, sensor-enabled radio-frequency identification (RFID) tags for safeguard of dangerous goods, and a multifunctional sensor for spatially resolved under-surface monitoring of gas storage areas. Objective of the presented projects is to increase the personal and technical safety in hazardous scenarios. These examples should point to application specific challenges for the applied components and infrastructure, and it should emphasize the potential of multi-sensor systems.**

Keywords-monitoring; multi-sensor device; hazardous scenarios; data-fusion

I. INTRODUCTION

The safe operation in hazardous scenarios (conflagrations, chemical incidents, etc.) and handling of dangerous substances (toxic, explosive, harmful for human and/or the environment) often requires the usage of sensor systems, e.g., to measure the status of a process, to enable early warning in case of an accident, or to evaluate the situation after an accident happened. In many cases not only one measuring variable is sufficient for a comprehensive evaluation of such scenarios, demanding for technical solutions with integration of multiple types of sensors. Technical enhancements like miniaturization, data processing, and wireless communication are the basis for application specific multi-sensor solutions. Data-fusion offers sophisticated possibilities to analyze and clarify the hazard potential of relevant situations – in many cases quasi in real-time.

The following examples present multi-sensor concepts applied to different scenarios of condition monitoring and safety management. Often similar issues and requirements must be taken into account, regardless of whether the monitoring object is a firefighter, a cask for radioactive material or a subsurface storage area.

The paper is structured in 6 sections. The sections II till V describe the above mentioned examples on basis of the physical principle, functionality and application. Section VI gives a short summary and the most relevant conclusions.

II. MONITORING AND INDOOR LOCALIZATION OF RELIEF FORCES

Rescue forces often operate in dangerous scenarios and situations in which their localization can be crucial for safe operation and return. Fire, landslip-, or flood scenarios pose hazards like suffocation, burn, or undercooling. The localization and quick recovery raise the survival chance clearly. The use of Global Positioning system (GPS) technology allows the exact localization of persons or objects everywhere a sufficient satellite reception is possible. However, in many hazardous scenarios no or only insufficient GPS reception is available. This may be the case in underground, indoor, or fire scenarios, making GPS localization complicated or impossible.

Objectives of the ongoing project "Localization and monitoring of relief forces in hazardous scenarios" with acronym OMEGa are the development and validation of a monitoring system, which complements GPS localization with indoor navigation [1] and in addition measures the most important vital functions. The overall system consists of two units, which operate spatially separated and communicate via radio with each other. The first unit are portable multi-sensor devices, which serve as personal protective equipment (PPE-Device) of the rescue force and should be implemented, e.g., by integration in the clothes. The second unit consists of the components of the control station for data processing and display (Figure 1).

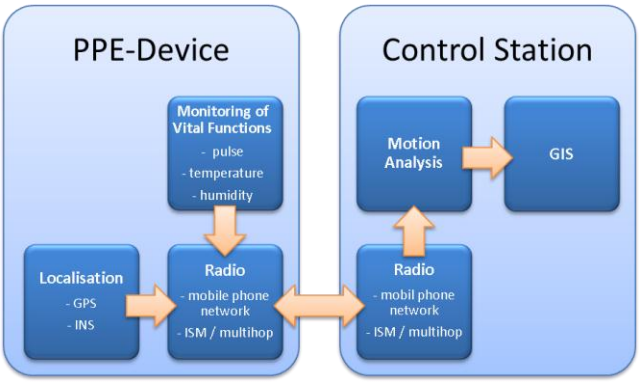

Figure 1: Scheme of the OMEGa units.

The multi-sensor device (Figure 2) should consist of an outdoor localization system (GPS), an inertial navigation

system (INS) for indoor localization, and sensors for monitoring of vital functions like pulse, temperature and humidity at the body surface. The communication between both units should be implemented through a redundant solution of two radio modes, based on mobile phone network and ISM band, the latter with multihop routing. Principal elements of the control station are analysis tools for calculating motion sequences from the sensor data and a geographical information system (GIS) to track and monitor the equipped persons in map-based software.

Figure 2: Prototype of the OMEGa multi-sensor device.

Indoor localization on basis of an INS is the most sophisticated challenge in the OMEGa project. The INS itself is a multi-sensor microelectromechanical systems (MEMS) device consisting of 3-axes accelerometers, gyroscopes, magnetic field, and barometric pressure sensors, partly redundant. The calculation of motion sequences from the combined sensor data is performed by data-fusion algorithms, which are currently under development [1, 2].

III. MICRO-DRONE FOR GAS MEASUREMENT IN HAZARDOUS SCENARIOS

A research project was carried out at BAM with the objective to develop a flying remote-controlled measuring system. The system is capable of operating in a variety of scenarios of gas emission, e.g., exhaust gas from a chimney, flue gas in case of a fire, gas emission in case of an accident of chemical or hazardous goods [3]. Another addressed field of application is spatially resolved emission control of geodynamic active regions, waste disposals, stockpiles, landfills, CO_2 storage areas (carbon capture and storage, CCS), industrial sites and pollution critical areas. Due to its mobility the system can measure the gas concentration in the immediate vicinity of the object, which causes the emission. A further stage of extension is the enhancement of the system for identification of gas source locations, and gas distribution modeling/mapping (GDM). The latter applications are implemented based on the combined analysis of position dependent gas concentrations and wind vector data.

Figure 3: Micro-drone with multi-sensor equippment in flight.

Gas concentration measurement from an air-borne platform (AR 100-B, Airrobot, Germany, Figure 3) is demanding in terms of weight, dimensions, energy consumption, influence of the rotors, and speed of the sensing device. A gas-sensing payload was developed on basis of a commercially available gas detector (X-am 5600, Draeger, Germany), which was originally designed as personal safety equipment. The device features low weight and compact design. The modular concept allows the ad hoc exchange of four sensors in the gas detector, which enables users to customize it for their specific application.

Due to the weight restrictions imposed by the platform (max. payload 200 g), the micro-drone does not carry any wind sensing modalities. Instead, wind measurements are estimated by fusing the different on-board sensors of its inertial measurement unit to compute the parameters of the wind triangle [4].

The wind triangle is commonly used in navigation and describes the relationships between the flight vector, the ground vector, and the wind vector. The micro-drone can be operated manually or in GPS mode, e.g., by autonomous waypoint following.

Both, gas distribution modeling and plume-tracking were enabled using data-fusion algorithms. For plume tracking three promising algorithms were implemented and adapted accordingly to meet the system characteristics of the micro-drone: the surge-cast algorithm (a variant of the silkworm moth algorithm), the zigzag/dung beetle algorithm, and a newly developed algorithm called “pseudo gradient-based algorithm”. First successful tests were performed in real-world experiments [5].

To build a predictive gas distribution model, the Kernel DM+V/W algorithm introduced by Reggente and Lilienthal [6] was used. The input to this algorithm is a set $D = \{(x_i,r_i,v_i)\}1\leq i\leq n$ of gas sensor measurements r_i and wind measurements v_i collected at locations x_i. The output is a grid model that computes a confidence estimate, as well as the distribution mean and variance for each cell k of the gridmap (Figure 4).

Additional sensors for temperature and humidity are integrated into the gas-sensing payload but so far not taken into account. It is conceivable to use these data for sensor compensation algorithms or to correlate the environmental conditions, e.g., in the case of fire. Integration of optical or IR data is another viable aspect.

 ISBN: 978-1-61208-297-4

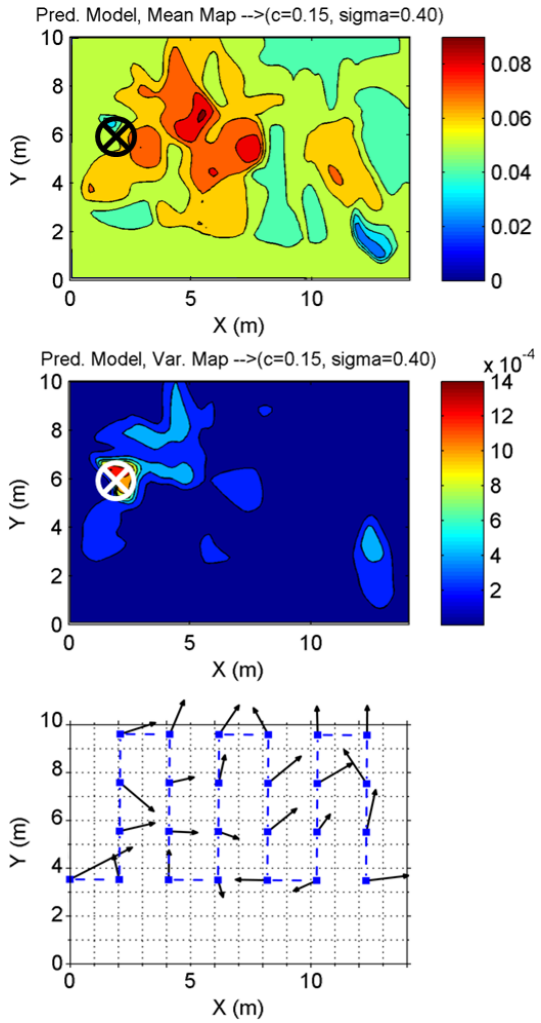

Figure 4: GDM Experiment: Predictive mean (top) and variance map (middle) of the gas distribution and the corresponding mean airflow map (bottom) and the path of the micro-drone created using Kernel DM+V/W. The gas source was located approx. at position (2, 6) m and is denoted by the cross. The concentration value of CO2 is given in % by volume.

IV. SENSOR-ENABLED RFID TAGS FOR SAFEGUARD OF DANGEROUS GOODS

The project "Sensor-enabled RFID tags for safeguard of dangerous goods" with acronym SIGRID investigates and assesses possibilities to improve safety and security of dangerous goods transports through the use of the latest RFID technology [7]. This technology can be used to greatly enhance the transparency of the supply chain and aid logistics companies in complying with regulations. In the context of SIGRID custom RFID sensor tags (Figure 5) were developed to monitor dangerous goods during transport and help to prevent hazards by allowing timely countermeasures. This requires the combination of communication technology and sensor functionality with low power consumption and small design.

To achieve long battery-life, the use of very energy efficient sensors is mandatory. Other desirable properties of the sensors include high accuracy, long lifetime, and short response time. For gas sensors a high selectivity is also very important. Currently four types of sensors are integrated in the RFID tag, which are a combined humidity and temperature sensor, gas sensors for carbon monoxide (CO) and oxygen (O_2), and a tilt sensor. Other interesting sensor options that might be tested in future include sensors for detecting the filling level and sensors for monitoring the operation of equipment that is built into the container like a stirring unit.

Figure 5: Prototype of the sensor enabled RFID tag

The integrated sensors enable the system for recognizing and evaluating of different scenarios. Adequate gas sensors indicate an emission from the containments via measured concentrations. If a possible gas release from the transported substance cannot be detected because of lacking the proper sensor, the O_2-sensor can indicate a leakage through decreasing oxygen values. For numerous dangerous goods a maximal transport temperature is defined to prevent any chemical reaction. Temperatures can be measured and compared periodically to substance specific values. If that value or a tolerance is exceeded an alarm or countermeasure can be activated. The tilt sensor can be triggered on heavy vibrations or tilting of the containment. In case of a dangerous good accident the available information about the type, amount, and condition of the dangerous goods can be used to accurately inform the relief forces. Unavailable or inaccurate information represents a significant problem. This often leads to a delay of the rescue operation, because relief forces must be aware of the involved substances and their condition to effectively protect themselves against them.

Sensor-Tags, data communication, and software are combined to an interactive solution, which can tackle various scenarios during dangerous goods transports. The underlying information is provided by a data base with expert knowledge, in this case the BAM dangerous goods database "GEFAHRGUT" [8]. Possible extensions of the system take into account vehicle data or GPS information in terms of route planning and geo-fencing.

V. MULTIFUNCTIONAL SENSOR FOR SPATIALLY RESOLVED UNDER-SURFACE MONITORING OF GAS STORAGE AREAS

One of the main unsolved issues of under-ground storages for, e.g., carbon dioxide, hydrogen, and natural gas (primarily methane) is the comprehensive surveillance of

these areas with reasonable effort and costs. Conventional sensors, such as soil air probes or borehole probes, can only be used for punctual or locally limited measurements. Further they require invasive application, which causes structural influences.

Figure 6: Prototype of the sensor enabled RFID tag.

BAM in cooperation with the company MeGaSen UG carries out a research project to enhance and validate an innovative approach for distributed subsurface monitoring of gas storage areas. The concept combines different measurement technologies to one multifunctional sensor: membrane-based gas measurement technology for in-situ monitoring of gases in soil [9] and fiber optical sensing of temperature and strain as a measure for structural change [10].

The gas sensor (Figure 6) is based on the principle of selective permeation of gases through a membrane. The measuring method combines the gas specific diffusion rates through a membrane with Dalton's law of partial pressures. It enables the calculation of gas concentrations with the ideal gas law using measurements of pressure, time, and temperature. The sensor is implemented in form of a flexible tube. The synthetic material allows a variable subsurface installation, e.g., in meander or network form (Figure 7). So far the gas concentration measurement is implemented for carbon dioxide and oxygen, further gases should follow, e.g., methane and hydrogen sulfide.

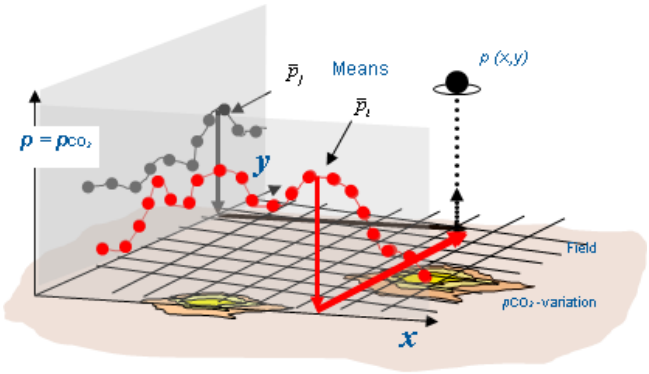

Figure 7: Spatially distributed gas monitoring built up of several membrane sensors. The brown and yellow areas indicate CO2 hotspots underground. The red and grey curves display the averaged measurements of the partial CO2 pressure over x and y.

Glass fiber optical sensors use the effects of stimulated Raman scattering (SRS) and stimulated Brillouin scattering (SBS) for spatially resolved measuring of temperature and strain. Distributed strain measurements can also be performed with polymer optical fibers using optical time-domain reflectometry (OTDR). BAM develops, validates and uses such sensor systems in different areas of application, such as geotechnics, structural engineering, and physical protection.

Combining these two sensor types (membrane sensor and fiber sensor) to a multifunctional sensor offers an innovative and promising approach for spatially resolved monitoring of large-scale areas. Both technologies offer advantageous specifications, which support and encourage their combination:

- Distributed, area-wide applicable measuring system with spatially resolution of all variables
- Scalable and adaptable form of application, depending on monitoring object and problem
- Non-invasive system (no influence on the monitoring object, due to permanent presence of the sensor in the ground)
- No sensitivity against electro-magnetic fields (e.g., lightning and high-voltage lines)
- Applicable in explosive surroundings (no electrical components at the measuring locations)
- High thermal and chemical robustness
- Comparatively reasonable components

The structural combination is accomplished by linkage of the sensitive elements membrane sensor and optical fiber. For this purpose, geogrid materials (Figure 8) act as a carrier material.

Combined data analysis should be investigated and further developed to attain synergy effects, increase the sensitivity and informational value, and address new fields of application. Using sensor data fusion allows in-depth analysis of soil processes and early detection of relevant changes. For instance, the combined analysis of gas concentration, temperature, and strain can enable an indication of very small crack formation and gas emission, with significant higher reliability compared to sole gas measurements.

Figure 8: Geogrid with integrated fiber optical sensors.

 ISBN: 978-1-61208-297-4

Two immediate fields of application are addressed: Landfills produce greenhouse gas and warmth. The combination of both measurement methods should allow a potent landfill monitoring by containment of chemical active areas and leakages.

Underground storage of CO_2 as part of CCS as well as extraction and production of gases from geological areas can lead to mechanical changes of the deck rock (lowering / elevation), with which a regional tension field is build up. Thus gas-leading gaps can be induced, which cause local ground structure changes. The simultaneous measurement of spatially resolved gas concentrations and strain allows the development of an efficient early warning system.

The validation, optimization, and practical demonstration of the overall system are carried out on the BAM Test Site Technical Safety (BAM TTS) [11]. For this purpose, a test field in application relevant scale of 20 x 20 m² is under construction.

VI. CONCLUSION

Safety related monitoring often is necessary in complex scenarios. It requires distinct information to evaluate the situation and to determine the further operation. The combination of several measurands can improve the informative value of a monitoring system in terms of measuring diversity and accuracy.

To present the great potential of such systems, four examples for monitoring in safety relevant scenarios are presented in this paper, which combine multiple application specific sensor techniques. An important result considering each of the examples and multi-sensor systems in general is that data processing and display of the results with focus of the relevant information is crucial. The experiences gained from these projects show that the focus should lay on the final application and end-users should be involved already in the conception of multi-sensor systems. Data-fusion offers broad possibilities, but conditions and objectives should be well defined and expediently applied.

ACKNOWLEDGMENT

The authors thank all participating colleagues from BAM and their project partners. The authors also express their gratitude to the German Federal Ministry of Economics and Technology for funding the research (MNPQ Program; file numbers 28/07 and 17/11 and ZIM Program File KF2201041SM1).

REFERENCES

[1] E. Koeppe, M. Bartholmai, A. Liehrs, and J. H. Schiller, “Radio-based multi-sensor system for person tracking and indoor positioning”, Proceedings of WPNC 2012 - 9th Workshop on positioning, navigation and communication, pp. 180-186, doi: 10.1109/WPNC.2012.6268761

[2] E. Koeppe, D. Augustin, A. Liehrs, and J. H. Schiller, “Automatic 3D Calibration for a Multi-Sensor System”, Proceedings of Indoor Positioning and Indoor Navigation (IPIN), 2012, pp. 1-6, doi: 10.1109/IPIN.2012.6418870

[3] M. Bartholmai and P. Neumann, “Adaptive Spatial-Resolved Gas Concentration Measurement Using a Micro-Drone”, tm - Technisches Messen, 78, 10, 2011, pp. 470-478, doi: 10.1524/teme.2011.0158

[4] P. P. Neumann, S. Asadi, J. H. Schiller, A. J. Li-lienthal, and M. Bartholmai, “Autonomous Gas-Sensitive Microdrone – Wind Vector Estimation and Gas Distribution Mapping”, IEEE Robotics and Automation Magazine, 19, 1, 2012, pp. 50-61, doi: 10.1109/MRA.2012.2184671

[5] P. Neumann, V. Bennets, and M. Bartholmai, “Adap-tive Gas Source Localization Strategies and Gas Distribution Mapping using a Gas-sensitive Micro-Drone”, Proceedings of 16. GMA/ITG-Fachtagung Sensoren und Messsysteme 2012, pp. 800-809, doi: 10.5162/sensoren2012/P5.4

[6] M. Reggente and A. J. Lilienthal, “Using Local Wind Information for Gas Distribution Mapping in Outdoor Environments with a Mobile Robot”, Proceedings of IEEE Sensors 2009, pp. 1715-1720, doi: 10.1109/ICSENS.2009.5398498

[7] T. Goedecke, A. Pettelkau, S. Hohendorf, D. Damm, M. Bartholmai, and M. Farahbakhsh, “Securing of Dangerous Goods Transports by RFID-Tags with Sensor-Functionality and integrated Database “GEFAHRGUT” Information (SIGRID)”, Proceedings of the 17th IAPRI World Conference on Packaging 2010, pp. 639-642, ISBN-13: 978-1935068365

[8] http://www.dgg.bam.de

[9] D. Lazik, S. Ebert, M. Leuthold, J. Hagenau, and H. Geistlinger, “Membrane Based Measurement Technology for in situ Monitoring of Gases in Soil”, Sensors, 9, 2, 2009, pp. 756-767, doi: 10.3390/s90200756

[10] S. Liehr, P. Lenke, M. Wendt, K. Krebber, et al., “Polymer Optical Fiber Sensors for Distributed Strain Measurement and Application in Structural Health Monitoring”, IEEE Sensors Journal, 9, 11, 2009, pp. 1330-1338, doi: 10.1109/JSEN.2009.201835

[11] M. Bartholmai, P. P. Neumann, and D. Lazik, “Multi-functional Sensor for Monitoring of CO_2 Underground Storage by Comprehensive and Spatially Resolved Measuring of Gas Concentrations, Temperature and Structural Changes”, Energy Procedia, 37, 2013, pp. 4033-4040, doi: 10.1016/j.egypro.2013.06.303

 ISBN: 978-1-61208-297-4

Shearing Force Measurement Device Using an Integrated Micro Optical Displacement Sensor

Takuma Iwasaki, Toshihiro Takeshita, Renshi Sawada
Department of Systems Life Sciences
Graduate School of Systems Life Sciences Kyushu University
Fukuoka, Japan
iwasakitakuma@nano-micro.mech.kyushu-u.ac.jp
takeshita@nano-micro.mech.kyushu-u.ac.jp
sawada@mech.kyushu-u.ac.jp

Satoshi Takeuchi, Masutaka Furue
Department of Dermatology
Graduate School of Medical Sciences Kyushu University
Fukuoka, Japan
takeuchs@dermatol.med.kyushu-u.ac.jp
furue@dermatol.med.kyushu-u.ac.jp

***Abstract* — In this paper, the authors propose a novel shearing force measurement device using an integrated micro optical displacement sensor and a frame. The 3 mm x 3 mm square and 0.7 mm thick sensor tip measures the mirror tilt angle on the underside of the frame caused by the shearing force applied to the upper surface of the frame. The authors obtained a linear output change for a single axis shearing force, and expect to be able to detect the magnitude and direction of the shearing force. In addition, it is possible to measure biaxial shearing forces and alter the measurement range and resolution by varying the frame material and shape.**

Keywords — sensor; robot hand; bedsore; tactile sense; shearing force; MEMS;

I. INTRODUCTION

In recent years, developed countries have trended towards super-aging societies, and it is estimated that in 2050 there will be 2 billion people in the world that are 60 years of age or older. The rate of an aging population to productive population will become quarter and younger citizens will have to bear the financial and physical burdens for the aged population. Therefore, in order to alleviate the burden on young people, robots will be needed. Various robots are currently in development and others participate actively in factories, as well as in other areas. These robots are not only necessary in industry, but also for medical welfare, agriculture, and safety system, especially social welfare and livelihood support in the future, as robots can replace humans in various areas of work [1]. However, there are still problems with using robots in human society. The limited tactile sense of robots is one of these problems. Assemblage robots used in factories have been set up to grip specific objects and therefore need only to detect vertical loads applied to their surfaces. However, in general, gripping forces must be determined instantaneously according to the strength of the object to be held. If the robot is unable to detect horizontal forces such as a shearing force, it may drop the object in question. In the field of nursing, it is dangerous to drop human beings after they have been carried to a height. Therefore, emulation of human perception for sophisticated robot manipulation is difficult with only vertical load sensors; a shearing force sensor is also needed.

Certain injuries will also occur more readily in the aged population, one of which is bedsore: a skin lesion that may affect any part of the body after a long time lying in a bed; bony or cartilaginous areas such as elbows, knees, ankles, and the sacrum are the most commonly affected. It is estimated that there are two hundred thousand patients throughout Japan currently, and this number will increase as the population ages. Some causes of bedsores are the local load from the bed, the shearing force between the bed and skin, humidity, and so on [2]. In order to prevent bedsores more reliably, we must detect not only vertical load but also shearing force.

For these reasons, a shearing force sensor is needed. There have been several reports on sensors that can measure both vertical and shearing forces by using electrostatic capacitance change [3-7] or resistance change [8-10], among other techniques. These are soft and thin, which is desirable, but they are not put to practical use as they have problems with hysteresis, drift, creep, and noise. Additionally, the sensors that can measure three axial forces are too large to be embedded in the fingertip of a robot hand.

In this study, we present a new type of shearing force measuring device combining a metallic frame with an integrated micro optical displacement sensor [11] fabricated using micro electro mechanical systems (MEMS) technology. This displacement sensor can measure linear displacement and biaxial tilt angle of an object using one Vertical Cavity Surface Emitting LASER (VCSEL) and four photodiodes (PDs), is downsized drastically compared to the conventional displacement sensor owing to monolithic fabrication and can be utilized for many applications. We believe our sensor will be superior to other shearing force sensors due to its use of optics. In addition, our sensor can be made soft with an elastic frame for embedding in the robot fingertip or a bed.

The purpose of this study is to make sure that we can detect single axis shearing forces using our displacement sensor, and compare experimental results with simulation results using four types of trapezoidal metallic frames.

 ISBN: 978-1-61208-297-4

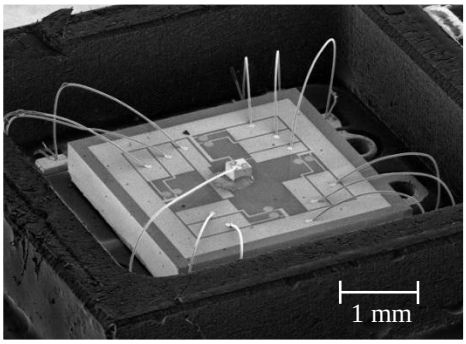

Figure 1. View of displacement sensor

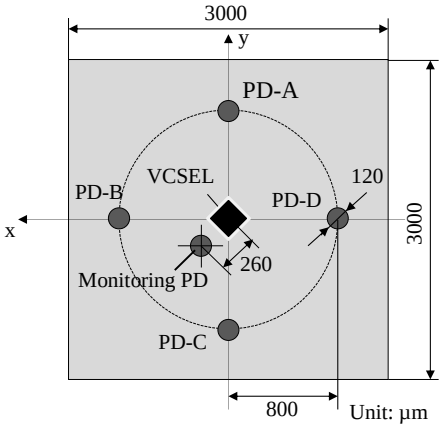

Figure 2. Structure of displacement sensor

II. STRUCTURE AND PRINCIPLE

Our shearing force measurement device applies the integrated micro optical displacement sensor as shown in Fig. 1. The structure of the displacement sensor is described in Section A. The principle of measurement is detailed in Section B.

A. Structure of Displacement Sensor

The sensor has area 3000 µm x 3000 µm and thickness 700 µm. As shown in Fig. 2, a VCSEL in the center of the sensor and four detecting PDs, which apply electrical current according to the intensity received at the PD, are integrated monolithically and arranged in a concentric pattern. The diameter of each PD is 120 µm and the distance of the center from the VCSEL to the center of each outer PD is 800 µm. In addition, a monitoring PD is located near the VCSEL at a distance of 260 µm. This assembly is covered by glass as shown in Fig. 3, and there is a reflective area near the center of the glass. Some of the emitted beam from the VCSEL enters the monitoring PDs after being reflected from the reflective area. In this way, the sensor can obtain feedback for laser output according to temperature change. The VCSEL differs from a normal laser in that the beam is emitted perpendicular to the chip surface; it is superior with respect to production costs, power consumption, and integration capabilities.

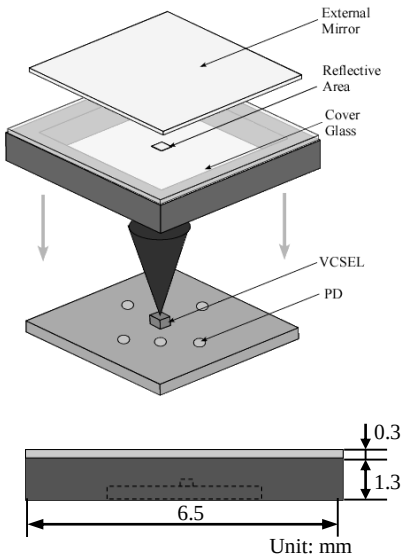

Figure 3. Overall view of the sensor

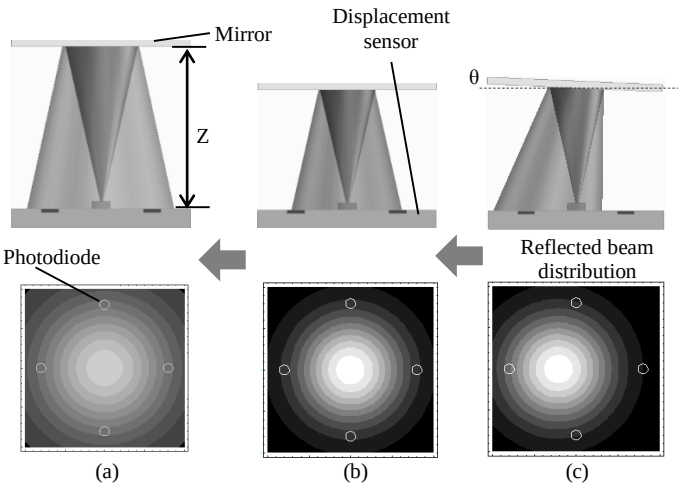

Figure 4. Principle of measurement

B. Operation Principle of Displacement Sensor

The displacement sensor can measure linear displacement and tilt of an object by using the VCSEL, four detecting PDs, and an external mirror attached to the object to be measured beforehand. VCSEL emits beams in a direction perpendicular to the sensor surface, with a certain spread angle. Fig. 4 shows side views of the sensor and mirror, and the corresponding reflected beam distributions on the sensor.

1) Linear displacement: As the distance between the mirror and the sensor changes, the size of the reflected beam distribution — that is, the intensity received at PDs — also changes as shown in Figs. 4 (a) and 4 (b). Fig. 5 shows the relationship between the distance Z and the output *S*, which is given by (1):

 ISBN: 978-1-61208-297-4

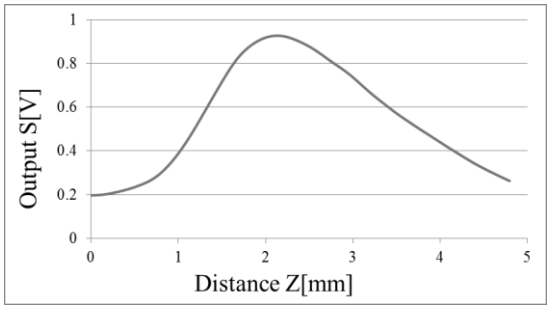

Figure 5. The relationship of output *S* and distance *Z* between mirror and sensor

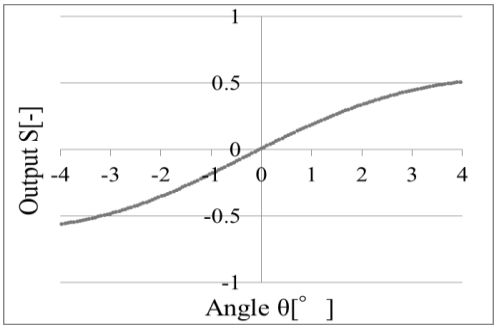

Figure 6. The relationship between output and mirror tilt angle

$$S = P_A + P_B + P_C + P_D \quad (1)$$

where P_A~P_D are the output of PD-A~PD-D, respectively.

When the mirror is close to the sensor, the distribution is small, and only a small amount of the reflected beam enters the PDs. As a result, the output *S* is small. As the mirror moves away from the sensor, the laser beam distribution becomes larger and the PD areas that receive the beam increase proportionately. Therefore, the output *S* increases linearly and peaks when the beam completely enters the PDs. Following this, the output *S* decreases linearly as the intensity weakens with decreasing distance. By using two linear regions on the graph, the sensor can be used to measure linear displacement.

2) Tilt angle: Changes in the tilt angle of the mirror move the reflected beam distribution directionally, as shown in Figs 4 (b) and 4 (c). This causes a difference in the PD intensity. Fig. 6 shows the relationship between tilt angle and the output *S*, which is given by (2)–(3):

$$S_x = \frac{P_A - P_C}{P_A + P_C} \quad (2)$$

$$S_y = \frac{P_B - P_D}{P_B + P_D} \quad (3)$$

In the case of *x*- or *y*-axis rotations, equations (2) or (3) are used, respectively.

For example, when the mirror tilts clockwise as in Fig. 4 (c), the intensity of PD-B increases and that of PD-D decreases. Therefore, the output S_y increases. By using the region where *S* changes linearly, we can determine the tilt angle.

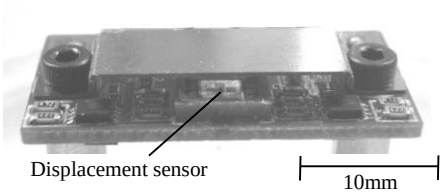

Figure 7. View of shearing force measurement devices

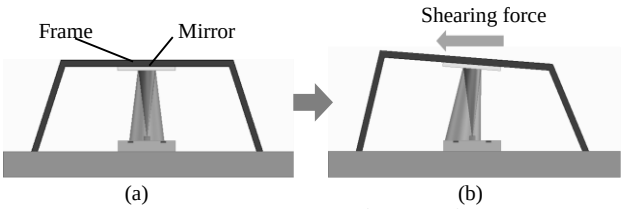

Figure 8. Conceptual diagram of shearing force sensor

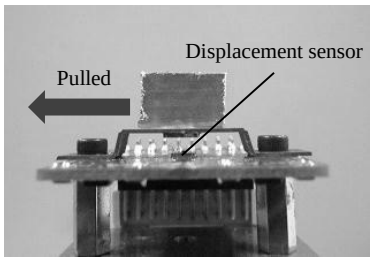

Figure 9. Photograph of the experimental system

C. Structure and Principle of Shearing Force Sensor

Our shearing force measurement device uses the above displacement sensor. The displacement sensor is covered by a trapezoidal fame as shown in Fig. 7. The mirror is attached on the underside of the frame. When a shearing force is applied to the upper surface of the frame, the frame is deformed and the mirror tilts as shown in Fig. 8. By measuring the tilt angle of the mirror with the displacement sensor, the shearing force can be detected. We can change the accuracy and resolution by varying the material and shape of the frame. For example, it is better to use a soft sensor can detect a biaxial shearing force, and by using the principle of measurement of linear displacement, it can detect both normal loads and shearing forces simultaneously. This leads to a reduction of the total component count, which cuts costs.

III. EXPERIMENT

In order to ensure that a single axis shearing force can be measured by using the principle mentioned in the previous sections, we conducted an experiment using metallic frames. The experimental system is shown in Fig. 9. The displacement sensor is in the center of a board, covered by the frame. Applying a shearing force to the upper surface of

 ISBN: 978-1-61208-297-4

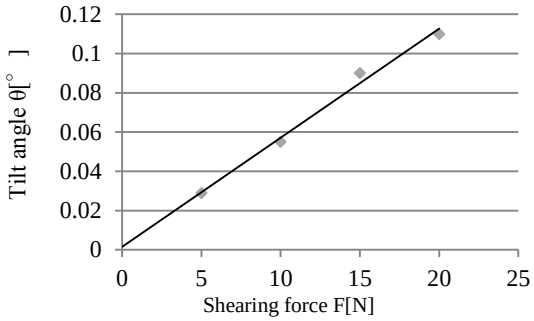

Figure 10. Analysis of the relationship between shearing force and tilt angle with frame (a)

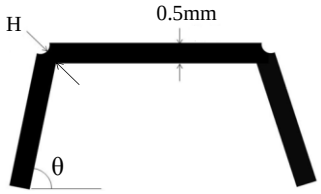

Figure 11. Schematic showing the frame

TABLE I. CHARACTERISTICS OF FRAMES USED IN THE EXPERIMENT

	Material	Young's modulus	Thickness of corners H	Angle of frame sides θ
a	SUS	199 GPa	0.1 mm	70 °
b				90 °
c			0.3 mm	70 °
d	Cu	117 GPa	0.1 mm	70 °
e				90 °
f			0.3 mm	70 °

the frame involved attaching a rectangle object and pulling it side to side with a translation stage; the applied force was measured with a force gauge with 10 mN resolution.

We applied shear loads from 0 N to 20 N to each frame. The loads applied were in the x-axis direction (see Fig. 2); the output *S* was thus given by (3) and the outputs of PD-A and PD-C were not used. Before the experiment, we analyzed the relationship between shearing force and mirror tilt angle by finite element method. We obtained a linear relationship as shown in Fig. 10. Therefore, it is expected that we obtain a linear relationship between the output and shearing force because estimated mirror tilt angle of 20 N falls within the linear area completely as shown in Fig 6. We prepared six types of metallic frames as shown in Fig. 11 and Table 1. We expected the stainless steel frame to deform more readily than the copper frame because the Young's modulus of stainless steel is larger than that of copper. In addition, we expected the frames with a corner thickness of 0.1 mm to be easier to deform than those with 0.3 mm, and that there would be little change in the frame with 90 degree lower corners.

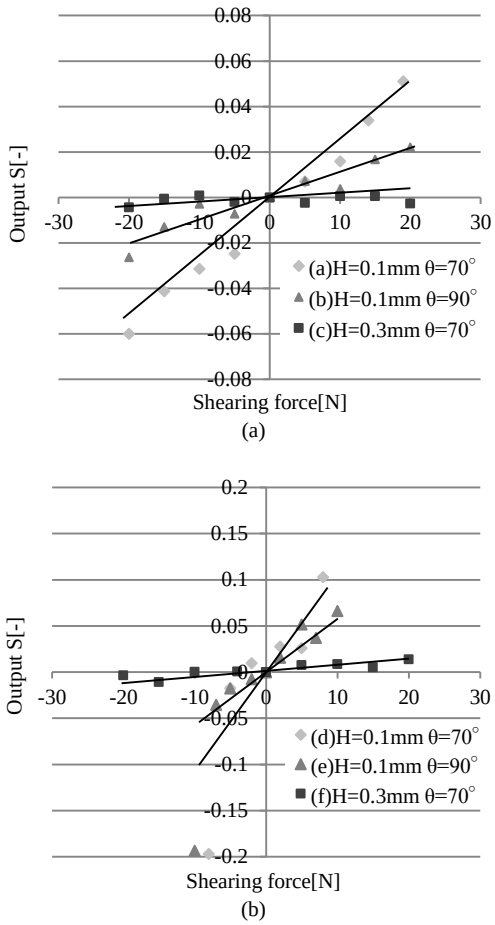

Figure 12. Variations in the output *S* for (a) stainless steel, and (b) copper

As shown in Fig. 12, we obtained a linear increase in *S* for a single axis shearing force as we had expected. As a result, we can determine the magnitude and direction of the single axis shearing force. In addition, we found that the output changes were dependent largely upon the material and shape of the frame. Therefore, smaller shearing forces are likely measurable if a softer material is used for the frame. In the experiment, copper frames with corner thickness 0.1 mm were more likely to collapse, so we did not apply up to the maximum 20 N. As expected, the gradient of the frames with corner thickness 0.1 mm (shown by the light gray points) is much steeper than that of the frames with corner thickness 0.3 mm (black points). When the frame is deformed by applied shearing force, it is essentially identical that the sides and corners of the frame are bended by reaction force as shown in Fig. 13. Therefore, it is thought that the thickness of the corner affects the ease of deformation largely and the gradient of the frames with corner thickness 0.1 mm is much steeper than that of the frames with corner thickness 0.3 mm. Additionally, the gradient of the frame with 70 degree bottom corner angles (light gray points) is steeper than that of the frames with 90 degree bottom corner angles (dark gray points).

 ISBN: 978-1-61208-297-4

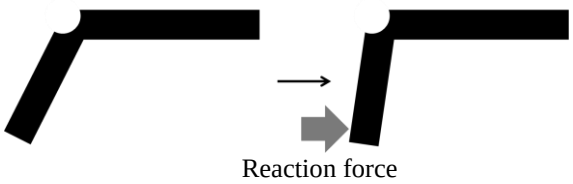

Figure 13. Schematic diagram of deformation

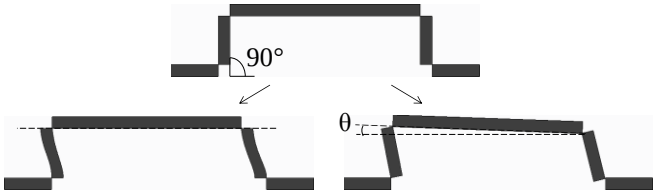

Figure 14. Schematic diagram of frame deformation at (a) the sides, and (b) the corners

We believe there are two reasons for this. The first is that the angle of the side of the frame may not have been exactly 90 degrees, which would cause the mirror to tilt slightly when the frame is deformed. The second is that the corners of the frame were deformed by the shearing force much more than the sides of the frame; this is shown in Fig. 14. When the sides of the frame deform, the upper part of the frame — that is, the mirror — moves in the horizontal direction and the mirror does not tilt. On the other hand, when the corners of the frame deform, the upper part of the frame tilts geometrically, which in turn means that the mirror is tilted. In the case of the frame used in this experiment, the corners are easier to deform than the sides because the sides of the frame are short. Overall, the output gradient of stainless steel frames is steeper than that of copper frames. As shown in Table 1, the Young's modulus of stainless steel is almost twice that of copper; correspondingly, the results show that the *S* values for the copper frame are approximately twice that of those for the stainless steel frame. The outputs of (c) and (f) (black points) were mostly unchanged. This is because the shearing force of 20 N was insufficient for deforming the frame. The outputs of (d) and (e) (light gray and dark gray points) in the results of copper were in part non-linear. This can be explained by the yielding of the frames at a shearing force of about 10 N. The thickness of the corners affects the outputs more than both the tilt angle of the side part of the frame and the frame material. Consequently, we need to set the measurement range according to the strength of the frame.

IV. CONCLUSION AND FUTURE WORK

In this work, we have successfully obtained a linear dependence on a single axis shearing force by combining an integrated micro optical displacement sensor with a metallic frame. The gradient of the linear change primarily depended on the material and shape of the frame. We therefore expect this sensor to be able to detect the magnitude and direction of a single axis shearing force. We also expect to be able to change its resolution and measurement range. It is possible that this sensor can measure biaxial and smaller shearing forces by using the same principle; it could then be embedded in robot fingertips or consumer beds.

REFERENCES

[1] D. Sasaki, T. Noritsugu, and M. Takaiwa: "Development of Pressure Measurement Type Tactile Soft Sensor for Life Assist Robot" , Transactions of the Japan Society of Mechanical Engineers, vol.70, no.689, 2004, pp.77-82.

[2] http://www.mayoclinic.com/health-information (2013/04/03)

[3] F. Zhu and J. W. Spronck, "A capacitive tactile sensor for shear and normal force measurements", Sensors and Actuators A, Volume 31, Issues 1–3, Mar. 1992, pp. 115–120.

[4] H. K. Lee, S. I. Chang, and E. Yoon, "A flexible polymer tactile sensor: Fabrication and modular expandability for large area deployment," J. Microelectromech. Syst., vol. 15, no. 6, Dec. 2006, pp. 1681–1686.

[5] H. K. Lee, J. Chung, S. I. Chang, and E. Yoon, "Normal and Shear Force Measurement Using a Flexible Polymer Tactile Sensor With Embedded Multiple Capacitors", J. Microelectromech. Syst., vol. 17, no. 4, Aug. 2008, pp. 934-942.

[6] H. K. Lee, J. Chung, S. I. Chang, and E. Yoon, "Polymer tactile sensing array with a unit cell of multiple capacitors for three-axis contact force image construction," in Proc. 20th IEEE Int. MEMS Conf., Kobe, Japan, Jan. 21–25, 2006, pp. 623–626.

[7] Z. Chu, P. M. Sarro, and S. Middlehoek, "Silicon three-axial tactile sensor," Sens. Actuators A, Phys., vol. 54, no. 1–3, Jun. 1996, pp. 505–510.

[8] A. Ito, N. Tsujiuchi, T. Koizumi and H. Oshima: "Tactile Information Processing by Distributed-Type Tri-axial Force Sensor for Robot Finger'', The Science and Engineering Review of Doshisha University, vol. 48, no. 3 Oct. 2007, pp. 86-94.

[9] E. S. Hwang, J. H. Seo, and Y. J. Kim, "A Polymer-Based Flexible Tactile Sensor for Normal and Shear Load Detection," Proc. of IEEE International MEMS Conference 2006, Istanbul, Turkey, Jan. 22-26, 2006, pp. 714-717.

[10] K. Kim et al., "3-Axes Flexible Tactile Sensor Fabricated by Si Micromachining and Packaging Technology," Proc. of IEEE International MEMS Conference 2006, Istanbul, Turkey, Jan. 22-26, 2006, pp. 678-681.

[11] T. Takeshita et al., "Characteristics and application of a monoli- thically integrated micro-displacement sensor" ,Joint International IMEKO Symposium, Germany, 2011.

Sensing Method and Fiber Optic Capillary Sensor for Testing the Quality of Biodiesel Fuel

Michal Borecki, Piotr Doroz, Jan Szmidt
Warsaw University of Technology
Institute of Microelectronics and Optoelectronics
Warsaw, Poland
E-mail: borecki@imio.pw.edu.pl

Michael L. Korwin-Pawlowski
Département d'informatique et d'ingénierie
Université du Québec en Outaouais
Gatineau, Québec, Canada
e-mail: michael.korwin-pawlowski@uqo.ca

Andrzej Kociubiński, Mariusz Duk
Lublin University of Technology
Lublin, Poland.
e-mail: akociub@semiconductor.pl

***Abstract*: There are many fuel quality standards introduced by national organizations and fuel producers. Usual techniques for measuring the quality of fuel, as for example cetane index, fraction composition and flash point, require relatively complex and expensive laboratory equipment. Therefore, testing of fuel is not rapid and can be costly. On the fuel user side, fast and low cost sensing of useful state biodiesel fuel is important. For this purpose, we have investigated the sensing method and sensor head that could be cheap in instrumentation as well as in fuel examination, and lead itself to automation. The method presented in this paper is based on fiber optic capillaries with local heating. We have investigated the construction of the sensor that imitates the fuel injection process and of he local heating element, the two critical elements for biodiesel fuel testing. We propose a new capillary optrode construction that enables measuring of time of vapor phase creation. We examine fuels that are mixtures of characterized components of petrodiesel fuel and bio-esters as well as edible rapeseed oil. We show that useful state of biodiesel fuel can be determined from the time of local heating that is required for vapor phase creation and the local time of vapor bubble formation.**

Keywords: biodiesel fuel, fuel quality, useful state of fuel, fiber optic capillaries, fiber optic sensors, capillary sensos.

I. INTRODUCTION

Nowadays, the useful state of diesel fuel is defined by producers by several parameters: cetane number (min 51.0), density (860 to 890 kg/m^3), and distillation temperature T_{90} (max. 360°C), kinematic viscosity at 40°C (3.5 to 5.0 mm^2/s), etc. Other diesel fuel parameters characterize its operability: carbon residue, water and sediment, cloud point, conductivity at 20°C, oxidation stability, acidity, copper corrosion, flashpoint, lubricity, appearance, and color [1]. For the ordinary fuel user such collection of parameters is often too complex for practical use because it requires special laboratory equipment. Therefore, fuel examination is not rapid and can be costly. Moreover, the introduction of biodiesel fuel increases the number of parameters connected with bio component content. In this situation the user requires the simplest possible answer to a question: Is that fuel useful for my engine?

Sensing of useful state of biodiesel fuel is exceptionally important for car fleet owners and farmers. Car fleet owners are interested because of legal regulations and of the possibility of buying poor quality fuel. Farmers are interested because they can produce bio-fuel components for their own use. But the parameters of these components in pure form are not optimal. For example, rapeseed and canola oil have too small cetane numbers and too high viscosities. However, the viscosities of oils decrease with the increase of temperature. For these reasons, in tropical countries the potential of using biodiesel fuels is larger. The use of mixtures of lychee fruit oil with petrodiesel fuel with component shares of 10%, 20%, 30% and 40% are discussed in [2]. It turned out that, despite significant differences in fuel viscosity and flash point performance the observed engine parameters with the prepared mixtures were very similar [3].

In a European study, it was observed that using first generation of biodiesel fuel at low environment temperatures can lead to degeneration of engine parameters [4]. Therefore, production standards for biodiesel fuel were introduced: density at 15°C (ISO3675) and temperature of fluidity for the transitional periods of season and winter (DIN EN 116). The disadvantages of biodiesel fuel can be overcome by fuel processing [5-8] or by using biopetrodiesel fuel mixtures [9].

One of the reasons of low biodiesel fuel mixtures usage by farmers is the absence of low cost device to evaluate its useful state.

Our starting point was to consider the critical points of fuel conversion into energy. The first is the injector of atomized fuel into the combustion chamber by forcibly pumping it through a small nozzle. The second critical point is the exhaust of gases filtered with the diesel particulate filter (DPF). Periodically, the DPF has to be taken up to high temperatures to burn off the matter it has collected [10], which is realized by contact of DPF with a part of fuel vapor, [11].

 ISBN: 978-1-61208-297-4

Typically, fuel is injected into the cylinders just after the vapor fires and the exhaust valve opens. At injection point, the fuel vaporizes and a part of vapor moves down the exhaust to the DPF and cleans it in a precisely controlled injection scheme [12]. Because biodiesel fuel has a higher distillation temperature than petrodiesel fuel, it does not vaporize as fast. Some of the biodiesel fuel can end up adhering to the injector, the cylinder wall or runs past the rings, diluting the engine oil and diluting DPF deposits instead of cleaning it.

Therefore, the examination of vapor creation parameters of biodiesel fuels is critical to evaluate its useful state regardless of the composition of fuel. The methods of spray forming observation in diesel engine have been used [13], but are not good for integration into a sensor device. In this work we present new developments and new applications of on capillary photonic sensors working on the principle of monitoring optical intensity changes in dynamically forced measurement cycles, first postulated in [14]. The sensors use fiber optic capillaries in which the phase of the filling liquid changes locally to gas when forced by local heating, while the propagation of light in the capillary is monitored. Therefore, the sensors examine simultaneously many liquid parameters.

In this paper are presented the idea of the sensor head, the construction of the head, the experimental results of testing biodiesel fuels for their quality for use, and conclusions.

II. IDEA OF SENSOR HEAD

We intend to imitate and examine fuel vaporization in conditions that are close to reality. The fuel injector nozzle diameters are from 50 to 200µm, [15]. Typical temperatures inside the fuel injection nozzle are from 235 to 275°C, the maximum not exceeding 300°C (see Fig. 1) [16]. Since the flame temperatures in the cylinders are about 1500°C and the wall temperatures are under 350°C, we can't replicate the flame temperatures in the sensor device. We have to create a set-up allowing the examination of partial evaporation of fuel which take place in the nozzle and can move fuel into orifice of few hundreds micrometers diameter. Such nozzle can be modeled with two glass capillaries that would allow observation of the direct optical fuel phases and their movement. The capillary with smaller outer diameter can be positioned inside the bigger capillary using glue forming a single-use replaceable optrode [17]. The inner temperature that is needed to create the bubble of vapor can be achieved with a local heater positioned near the capillary. With one end of capillary closed, the local heater can acts as a fuel pump by producing a vapor pressure (see Fig. 2). The creation and movement of the bubble depends on the type of liquid and vapor parameters as well as on the geometry and thermo dynamical conditions.

The faster is the bubble creation from liquid phase, the more probable is the turbulent flow of fuel in the nozzle. Therefore, we have to distinguish two stages of the bubble creation: the time of liquid fuel heating and the time of phase change from liquid to vapor that forms the bubble filling the full cross section of the capillary.

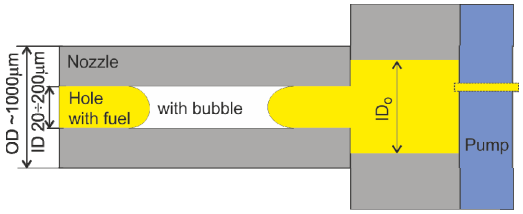

Figure 1. Schematic construction of the nozzle.

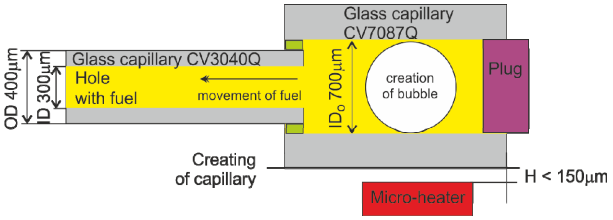

Figure 2. Schematic construction of model of the nozzle.

III. HEAD CONSTRUCTION

The sensor's head consists of two functional blocks: the base and the optrode [18]. The base is used to integrate the microheater, the optical path and for positioning the optrode. The optrode is the replaceable part of the head that imitates the fuel nozzle and enables monitoring of creation of the vapor bubble.

A. Micro heater

The microheater has to supply sufficient heat for the biodiesel fuel to reach 300°C. We examined experimentally and numerically the map of temperatures in the model of nozzle. We used Coventor software, a R300 NEC thermo-vision camera, and InfReC analyzer software. The results for a 4mm×4mm planar micro heater positioned at 50µm under the capillary and dissipating 5W in 30 seconds are presented in Fig. 3. The temperature of surface reached 327°C while the temperature inside the capillary reached 247°C. Sequential simulation showed that the microheater temperature has to be at least 350°C for the assumed distance between the capillary and microheater surface, which is more than can withstand the planar resistors e.g., Vishay High Power Thin Film Wraparound Chip Resistor in 2512 packaging [19].

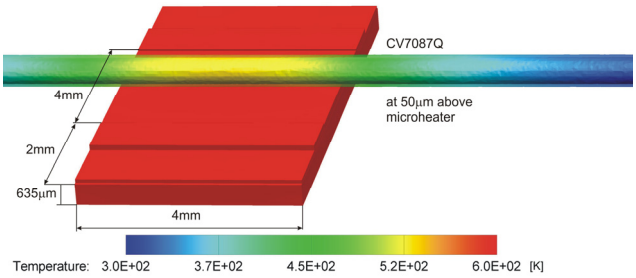

Figure 3. Temperature map in [°K] at 30s of heating for a glass capillary CV7087Q filled with diesel fuel.

 ISBN: 978-1-61208-297-4

Wire heaters can easily work at such temperatures, but such constructions does not provide a constant and repeatable distance between the microheater and the capillary, and they can't replace the planar structures. The most favorable shape of planar microheaters is rectangular with side length from 2mm to 4mm, and the recommended power of heating is 5÷7W. The power density is 1.75W/mm^2, which is also too high for classical hybrid resistors. For the heater current supply the recommended value of resistance is between 10÷50Ω even current dividers from Vishay Current Sensing Bondable Chip Resistors type S.C. [19], are not optimal for the application. We have built different versions of planar microheaters using hybrid technology. With an optimized technology, the parameters of the microheater were stable for temperature shocks from 30°C to 200°C – the resistance changes were low, within 1.5Ω at 30Ω of nominal resistance. The microheater reached 350°C after 30 seconds, dissipating 6W of power, but it should not be powered for more than 60 seconds, because of the possibility of breaking into two symmetrical parts. The next heating cycle with maximum power was safe, when the heater was allowed to cool down to room temperature. In normal condition it required about 2 minutes.

B. *Path of optical signal*

The bubble creation can be observed from outside or inside of capillary with the use of optical fibers [20]. The bubble position can vary in the area of local heating due to variation of fuel composition. Therefore, the observation from outside is not optimal for measuring the bubble creation time. Observation of the bubble creation with two fibers inside the capillary is not optimal for a replaceable optrode set-up, and also complicates the fuel flow. To overcome those problems, we used a modified capillary optrode with a phosphor layer to convert radiation (see Fig. 4). In the presented optrode, the phosphor converts the light from 460nm wavelength of the high power light emitting diodes, to 562nm. Only part of the light radiated in the full angle extent propagates in the inner capillary to the area of examination. The efficiency of light conversion is low.

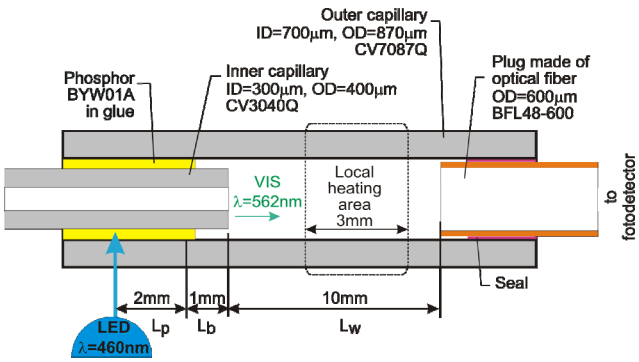

Figure 4. Optrode that uses phosphor to convert outer radiation into light inside capillary.

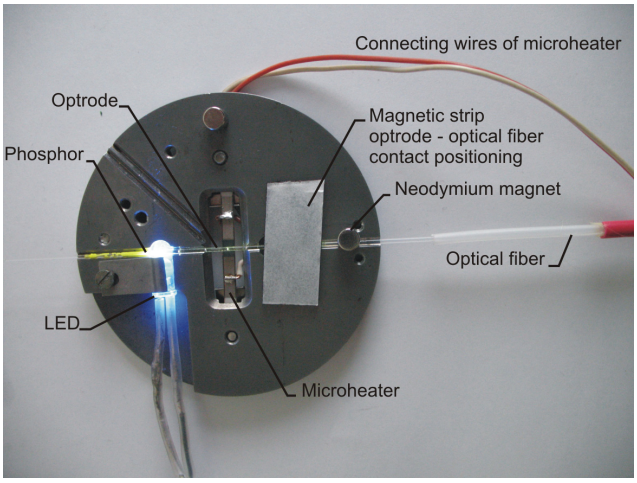

Figure 5. The head construction.

After optimizing the construction, from a L7113QBC-G LED operating at 20mW, we got at the end of the plug made from optical fiber, 111nW for an empty capillary and 0.3µW for a capillary filled with biodiesel fuel. The uncertainty of low signal level in our construction was 10nW.

We optimized the optrode elements position: L_p, L_b and L_w, as well as the method and parameters of phosphor deposition. The optrode was held in position with elastic magnetic strips, while the optical fiber was secured with miniature neodymium magnets. The head construction is presented in Fig. 5.

C. *Optoelectronic signal processing*

As light source driver we built an electronic device that enabled current modulation from DC to 50 kHz at selected frequencies, and was equipped with configurable current limiters to prevent accidental LED burning.

The optoelectronic detection unit of our own construction had an SMA fiber input and consisted of an integrated photo-amplifier and a band-pass filter with amplification and RMS detection. We used the S8745-01, AD8253, UAF42, AD536 and AD8250 components. The optoelectronic unit was connected to a personal computer through an analog input IOtech personal Daq 3000 16bit/1MHz USB data acquisition system. We fed the heater from a laboratory power supply Hameg HM8143 controlled by the analog output from Daq. The view of sensor hardware set-up is presented in Fig. 6.

We also used a Daq 3000 system to monitor the temperatures of the measuring head base and of the surrounding ambient with two LM35DT circuits connected by low pass filters. To operate the system, we designed a script in DASYLab with a 0.01s sampling rate. The script automates the measurements and automatically switched off the heater when the light signal dropped under a specified value corresponding to the point of vapor bubble creation. The script was programmed also to switch off the heater when the maximum heating time was reached, but the bubble did not form. The length of signal registration was 60s.

 ISBN: 978-1-61208-297-4

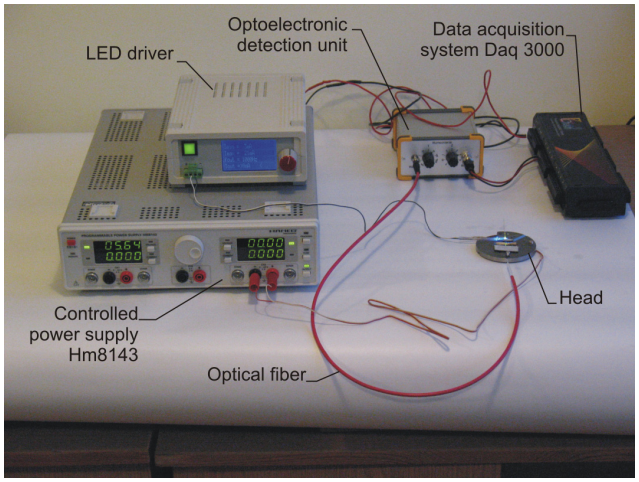

Figure 6. View of experimental set-up

IV. EXPERIMENT RESULTS

In this section are presented the experimental procedure and the results of examination of different biodiesel fuels.

A. *Experiment procedure*

At the start of the experiment the part of the optrode consisting of the CV7087Q capillary was filled with fuel, after which its end was closed. When there were bubbles of gas observed at the initial state of experiment, the optrode and capillary had to be withdrawn [14]. When the capillaries were filled uniformly by the liquid, the initial levels of transmitted signals were measured and used as normalization levels. We normalized the initial signal level to 4 a.u.

As the fuel in the useful state is semitransparent, we expected initially high signal levels and low signal levels when the bubble would appear. The bubble directed the signal from the liquid to the capillary walls. When the transmitted signal decreased rapidly it gave the impulse to switch off the microheater. We terminated the heating when signal dropped under 2.5 a.u. Depending on the thermo-dynamical conditions; the vapor gas phase moved the fuel to the open end with a laminar or a turbid flow. The turbid flow could be detected optically after the experiment as a presence of series of small bubbles in the CV3040Q capillary. We also observed a repeatable presence of a small bubble that remained after heating in the center of the microheater, Fig. 7.

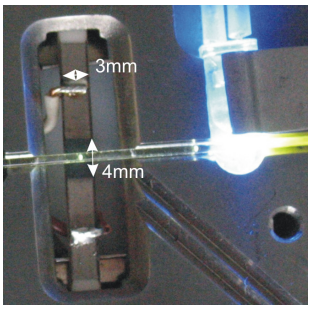

Figure 7. Small bubble remaining after heating in the center of the microheater

We thought that bubble appeared due to structural changes in fuel induced by heating of the components that were added after distillation and some bio-components decomposition, since the bubble was present also after examination of rapeseed oil.

B. *Examination of biodiesel fuels*

We examined 5 fuel mixtures prepared from the same components at different ratios, the commercial 100% biodiesel fuel, as well as edible rapeseed oil (RO). Selected parameters of prepared fuels are grouped in Table 1. The distillation of RO and its parameters can be found in [9].

TABLE I. SELECTED PARAMETERS OF PREPARED FUELS

Parameter	Fuel acronym				
	P2	P12	P14	P17	P21
Base oil [%]	100	90	70	40	0
FAME [%]	0	10	30	60	100
Density at 15ºC [kg/m^3]	832.6	837.4	847.0	862.3	883.2
Temp of flame [°C]	74	75.5	79.5	90	163
Kinematic viscosity at 40ºC [mm^2/s]	3.367	3.432	3.595	3.934	4.509
CI	54.9	57.7	57.5	56.8	*
CN	59.6	57.3	54.9	54.0	51.2
T_0 [ºC]	188.6	195.6	196.7	200.2	*
T_{10} [ºC]	225.7	230.4	242.1	278.1	*
T_{90} [ºC]	345.5	343.6	344.1	345.3	*

Abbreviations used: FAME – Fatty acids methyl esters (bio-component); CI – cetane index, CN – cetane number, T0 temperature of distillation start, T_X – temperature of x% volume of distillation, * - our lab equipment do to allow of such examination.

The laboratory fuel examination prior to the experiment showed that fuels P2-P17 were meeting the norms. P21 did not meet the distillation standards. We made first experiments with P2 fuel with two powers of heating 4W and 6W, (see Fig. 8 and Fig. 9). The examination results showed that increasing the power from 4W to 6W reduced the average time of heating τ from 14.5 seconds to 9 seconds. The differences in time of heating were in agreement with the thermo dynamical properties of the evaluated mixtures.

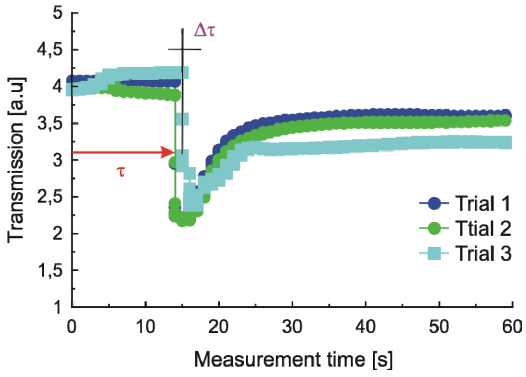

Figure 8. Measurement procedure signals of P2 heated with 4W.

 ISBN: 978-1-61208-297-4

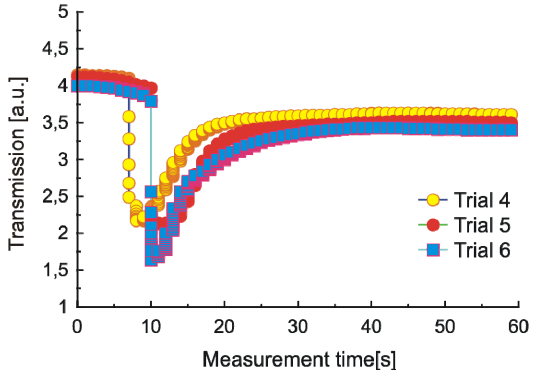

Figure 9. Measurement procedure signals of P2 heated with 6W.

We also observed low values of the times of bubble creation $\Delta\tau$, decreasing from 0.2 seconds for 4W, to 0.1 seconds for 6W. The achieved results were agreement with expectation. The next experiments were made with 6W heating power and their results are presented in Fig. 10 to Fig. 14 and summarized in Table 2.

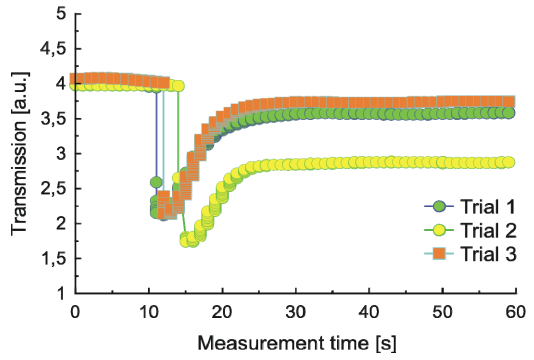

Figure 10. Measurement procedure signals of P12 heated with 6W.

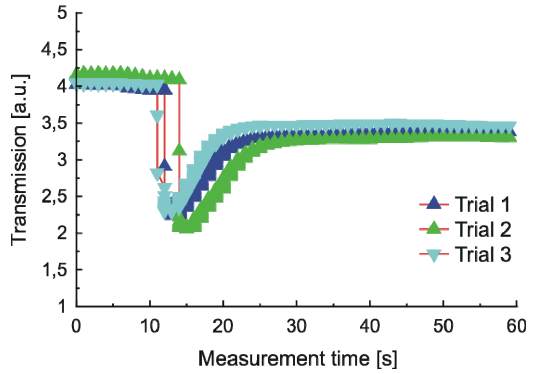

Figure 11. Measurement procedure signals of P14 heated with 6W.

TABLE II. EXAMINED PARAMETERS OF FUELS HEATED WITH 6W

Parameter	Fuel acronym					
	P2	P12	P14	P17	P21	RO
Average τ [s]	9	12.5	13	21.6	22*	13
Average $\Delta\tau$ [s]	0.10	0.13	0.17	0.30	0.2*	0,6
Percent of samples with created bubble	100	100	100	100	33	100

*- no existing the average value, RO - rapeseed edible oil from supermarket

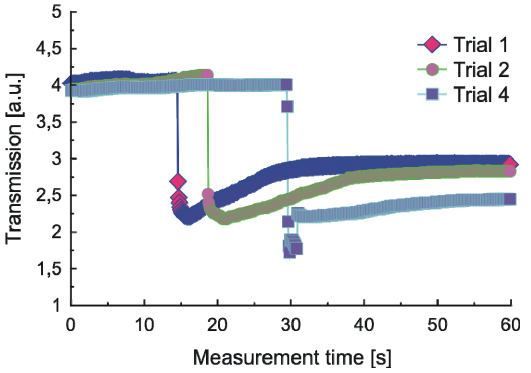

Figure 12. Measurement procedure signals of P17 heated with 6W.

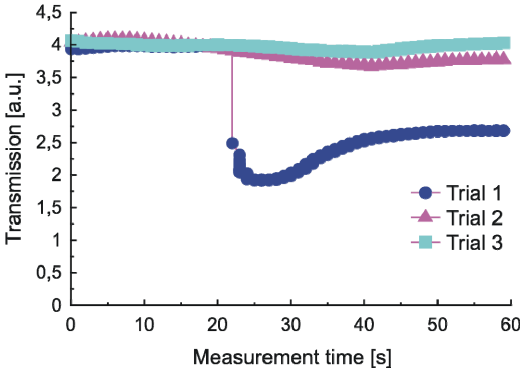

Figure 13. Measurement procedure signals of P21 heated with 6W.

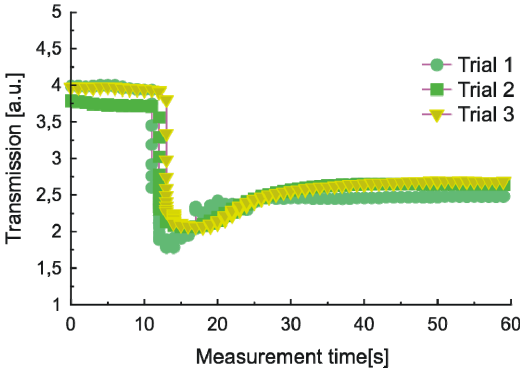

Figure 14. Measurement procedure signals of RO heated with 6W.

From our experiment results we saw that P2, P12 and P14 fuels did not differ significantly. The P17 fuel formed in our heating condition a vapor phase, but the mixture was characterized by very high dispersion of time of heating. Interestingly, the P21 seemed to be a worse fuel than RO, because it required a longer time of heating while occasionally showed a lower time of bubble creation. More over the RO had the lowest τ dispersion, in agreement with its distillation parameters that were close to its boiling temperature, which is not a good property for a fuel.

Therefore, we may set for the parameters of useful state of biodiesel fuel the upper limits of average time of heating, the range of dispersion of time of heating and the upper limit of time of vapor phase creation. The data analysis showed

 ISBN: 978-1-61208-297-4

that in our method the useful state of biodiesel fuel was directly and firmly connected with the gas phase creation.

V. CONCLUSIOSNS

We proposed a sensor working on the principle optical examination of fuel under local heating. Our optoelectronic devices enabled conducting the experiment in lighting room conditions. The results of the measured signals analysis of biodiesel fuels showed the relationship of times of gas phase creation parameters with the useful state of fuel. We showed that the information on useful state of diesel fuel as well as biodiesel fuel could be presented in the form of recommended ranges and times of fuel heating and vapor creation. Because the heating was taking place in a closed capillary, the fuel did not ignite during experiments. We conclude that the proposed construction may be in future the base of commercially marketable instruments.

The future work will consist of optimization of the construction and of the data processing function. The sensor construction needs to be integrated into a complete portable instrument and be built more resistant for use in harsh environments outside of the laboratory.

ACKNOWLEDGMENT

This work was supported by: the European Union structural funds grant InTechFun task 5, “Multi parametric classificatory of liquid biofuels useful state”, NCBiR project N R02 0008 06/2010, “New optoelectronic devices for intelligent classification of organic and biological fluids”, as well as NCN project N N515 362936, “New optoelectronic method of intelligent classification of liquid bio-fuels with the optical capillaries use”

REFERENCES

[1] Department of Industry, Science and Resources, “Setting national fuel quality standards - Discussion paper 4”, in “Operability fuel parameters (petrol and diesel)”, Environment Australia, 2001.

[2] R.D. Misra and M.S. Murthy, “Performance, emission and combustion evaluation of soapnut oil–diesel blends in a compression ignition engine,” Fuel, vol. 90, 2011, pp. 2514–2518.

[3] C. Ketlogetswe and J. Gandure, “Blending Cooking Oil Biodiesel with Petroleum Diesel: A Comparative Performance Test on a Variable IC Engine,” Smart Grid and Renewable Energy, vol. 2, 2011, pp. 165-168.

[4] M. Balat and H. Balat, “A critical review of biodiesel as a vehicular fuel,” Energy Convers Manag., vol. 49, 2008, pp. 2727–41.

[5] N.E. Leadbetter et al. “Fast, Easy Preparation of Biodiesel Using Microwave Heating,” Energy & Fuels, vol. 20, 2006, pp. 2281–2283.

[6] S. Gryglewicz, “Rapeseed oil methyl esters preparation using heterogeneous catalysts,” Bioresource Technology, vol. 70, 1999, pp. 249-253.

[7] http://www.theglycerolchallenge.org/ [retrieved June 1, 2013]

[8] A.R. Sadrolhosseini, et al., “Physical Properties of Normal Grade Biodiesel and Winter Grade Biodiesel,” Int. J. Mol. Sci., vol. 11, 2011, pp. 2100-2111.

[9] W. Gis, A. Zoltowski, and A. Bochenska, “Properties of the rapeseed oil methyl esters and comparing them with the diesel oil properties,” J. of KONES Powertrain and Transport, vol. 18, 2011, pp. 121-127.

[10] M.V. Twigg and P.R. Phillips, “Cleaning the air we breathe – controlling diesel particulate emissions from passenger cars,” Platinum Metals Rev., vol. 53, 2009, pp. 27-34.

[11] B. Kegl, “Numerical analysis of injection characteristics using biodiesel fuel,” Fuel, vol. 85, 2006, pp. 2377–2387.

[12] M. Gumus, C. Sayin, and M. Canakci, “The impact of fuel injection pressure on the exhaust emissions of a direct injection diesel engine fueled with biodiesel–diesel fuel blends,” Fuel, vol. 95, 2012, pp. 486–494.

[13] B. Kegl, M. Kegl, S. Pehan, “Optimization of a fuel injection system for diesel and biodiesel usage,” Energy & Fuels, vol. 22, 2008, pp. 1046–1054.

[14] M. Borecki, M. L. Korwin-Pawlowski, and M. Bebłowska, “A method of examination of liquids by neural network analysis of reflectometric and transmission time domain data from optical capillaries and fibers,” IEEE Sensors, vol. 8, 2008, pp. 1208-1213.

[15] D.L. Siebers and L.M. Pickett, “Injection pressure and oritice diameter effects on soot in DI diesel fuel jets,” in Thermo- and fluid dynamic process in diesel engines 2 - Selected papers from Diesel 2002 conference Valencia, Spain, J.H. Whitelaw, F. Payri, C. Arcoumanis, and J-M. Desantes, Eds., Springer-Verlag, Berlin, Heidelberg, New York, 2002, pp. 109-131.

[16] N. Ladommatos, Z. Xiao, and H. Zhao, “The effect of piston bowl temperature on diesel exhaust emissions,” Proc. IMechE. vol. 219 Part D: J. Automobile Engineering, 2005, pp. 371-388.

[17] M. Borecki, M. Korwin Pawlowski, P. Wrzosek, and J. Szmidt, “Capillaries as the components of photonic sensor micro-systems,” J. of Mater. Sci. and Technol., vol. 19, 2008, pp. 065202.

[18] M. Borecki, M.L. Korwin-Pawlowski, M. Beblowska, J. Szmidt, and A. Jakubowski, “Optoelectronic capillary sensors in microfluidic and point-of-care instrumentation,” Sensors, vol. 10, 2010, pp. 3771-3797.

[19] www.vishay.com, Document Number: 53013, Revision: 25-Aug-09 39, pp. 39-39 [retrieved June 1, 2013].

[20] M. Borecki and M.L. Korwin-Pawlowski, “Optical capillary sensors for intelligent microfluidic sample classification,” in Nanosensors: Theory and Applications in Industry, Healthcare and Defence, T.C. Lim, Ed., CRC Press, Boca Raton, FL, USA, 2011, pp. 215- 245.

 ISBN: 978-1-61208-297-4

Design of Indirect Time-of-Flight Based Lidar for Precise Three-Dimensional Measurement Under Various Reflection Conditions

Junhwan Jang, Sungui Hwnag, Kyihwan Park
School of Mechatronics
Gwangju Institute of Science and Technology
Gwangju, South Korea
e-mail: khpark@gist.ac.kr

Abstract—**In the indirect TOF method, the distance traveled by light can be obtained on the basis of the phase difference between the reference signal and the measured signal. To utilize the lidar as a distance measurement sensor, measuring distance, resolution, and accuracy of the lidar should be considered most importantly. Optical system of the lidar should be optimally designed since a high intensity of measured signal increases the measuring distance and accuracy. Furthermore, electronic circuit design is also considered importantly in addition to the optical system design because the varying signal of the photoelectric current for the measuring distance can cause an inaccurate result of distance measurement. Different amplitudes of the signals due to different distance and object reflectivity cause additional electronic phase delays in the demodulation circuit in addition to the phase delay corresponding to the distance to be measured because of a constant gain bandwidth product limitation. In this study, optical system design, signal processing, and intensity control method are proposed, which can be applied to the lidar to achieve high resolution and linearity performance.**

Keywords- Time-of-flight; Lidar; Intensity control;

I. INTRODUCTION

Time-of-flight(TOF) based lidars are widely used in engineering fields such as robot navigation, automatic guided vehicle, and three-dimensional measurement applications in several industries because they have the advantages of non-contact, wide range, and high precision measurement [1].

Time-of-flight(TOF) methods are classified into direct and indirect TOF methods. For the distance measurement, the direct TOF method directly measures time interval between the emitted and detected signals, which are very short pulsed lights [2][3]. Thus, it requires techniques for generating the short pulsed light and time resolution of picoseconds for obtaining a millimeter resolution, which is hard to be implemented at a low cost. In the indirect TOF method, the distance can be determined by using a phase shift of a modulated light with either a sinusoidal signal or a pulsed signal [4][5]. Since the time interval can be obtained by the phase difference, it does not need techniques that the direct TOF method requires. Therefore, indirect TOF based sensors recently receive attention as 3D imaging systems due to its advantages of compactness and low cost with reasonable accuracy [1].

In the indirect TOF method, the distance traveled by light can be obtained on the basis of the phase difference between the reference signal and the measured signal. The modulation frequency of the signal is inversely proportional to the distance. Therefore, maximum measurable distance and distance resolution are determined by the modulation frequency. In other words, when a higher modulation frequency is used, a shorter measurable distance and a higher distance resolution can be obtained [6].

To utilize the lidar as a distance measurement sensor, measuring distance, resolution, and accuracy of the lidar should be considered most importantly. Optical system of the lidar should be optimally designed since a high intensity of measured signal increases the measuring distance and accuracy. Therefore, it is important to understand how the optical component layout affects the system performances. Optical component design for co-axial and bi-axial mechanisms are considered in this work. Furthermore, electronic circuit design is also considered importantly in addition to the optical system design because the varying signal of the photoelectric current for the measuring distance can cause an inaccurate result of distance measurement. When different colored object are measured, the intensities of the measured signals vary greatly even at the same distance. The different amplitudes of the signals due to different distance and object reflectivity cause additional electronic phase delays in the phase demodulation circuit in addition to the phase delay corresponding to the distance to be measured because of a constant gain bandwidth product limitation. Therefore, it is important to maintain the signal amplitude to be constant. In this paper, optical system design, electronic signal processing, and intensity control method are proposed, which can be applied to the lidar to achieve high resolution and linearity performance.

 ISBN: 978-1-61208-297-4

II. OPERATING PRINCIPLE

In the indirect TOF method, the distance that light travels can be determined using the phase difference between the reference and measured signals, as shown in Fig. 1.

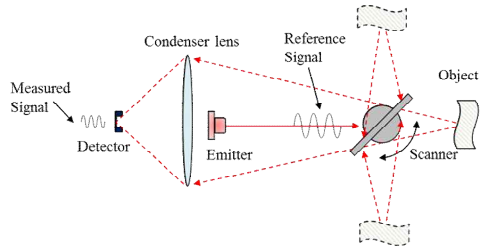

Figure 1. System configuration of the indirect TOF based lidar

When light travels a distance d, light reflected from an object is delayed by the phase, φ. The phase difference between the reference and measured signals is proportional to the distance traveled. When the modulated frequency of the reference signal is f, the distance d is obtained in terms of phase φ and f as

$$d = \frac{c}{2f} \bullet \frac{\varphi}{2\pi} \quad (1)$$

where c (=3 x 10^8 m/s) is the speed of light. According to Eq. (1), the distance resolution is related to the modulated frequency. Hence, the higher the modulated frequency used, the better the distance resolution that can be obtained.

III. THE INDIRECT TOF BASED LIDAR DEVELOPED

A. *Optical system*

To have a high accuracy of distance using the lidar, a high intensity measured signal should be received because the intensity determines the signal to noise ratio. Hence, optical design is one of the most important issues to be considered for design of the lidar for a given mechanical and electronic specifications. However, expanding the size of optical components to obtain high intensity is a limited way due to compact system configuration and various applications. In this section, optical system designs are presented according to detection range and application area.

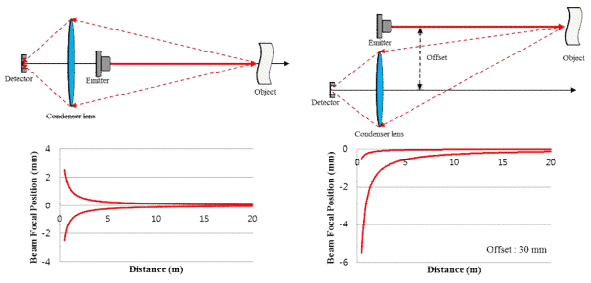

(a) (b)

Figure 2. Optical system layouts of (a) the co-axial and (b) bi-axial types

Typically, there are two types of optical systems, co-axial and bi-axial types. Figure 2 shows the configuration of the co-axial and bi-axial type optical systems. In case of the co-axial type, all optical components, the detector, the condenser lens and the emitter, are on the same optical axis. Figure 2 also shows the results of the ray tracing of a detected beam spot at the focal position [7]. A Ø 50 condenser lens with a focal length of 50 mm was used. As shown in Fig. 2 (a), from the short range to the long range, all reflected signals can be focused on the detector. Hence, the co-axial type optical system is usually utilized with a mirror scanner for 3D applications.

However, the emitter part can make a shade to the focal plane by blocking the center of the condenser lens. Thus, optical power loss is caused by the shadow effect, which decreases the signal to noise ratio and results in a low distance accuracy. In addition, the back beam from the scanning mirror causes an optical crosstalk problem. When there are crosstalk problems, the sensor performance is easily deteriorated. For example, when the reflected signal from the object is weaker than the optical crosstalk signal from the scanning mirror, the distance cannot be obtained. Therefore, it is important to design the emitter part as small as possible without the optical crosstalk problem.

In order to solve the shadow effect of the coaxial type, a bi-axial type optical system is considered. As shown in Fig. 2 (b), the emitter part is located next to the condenser lens. As a result, the problem of intensity loss due to the shadow effect is removed. However, the returning beams are focused not in the detector center in short ranges as shown in Fig. 2 (b) because the condenser lens is not aligned with the emitter. The deviation from the center is more severe when a shorter distance is measured. Therefore, a bigger detector area is required to use for a short distance measurement. This bi-axial type optical system is more suitable for long distance detection since it can receive sufficient reflected beam intensity compared to the coaxial type optical system. However, it has a disadvantage that its structure becomes large in size when a rotating scanner should be used for 2D and 3D applications because the mirror scanner should be at least twice larger than that used in the co-axial type due to the fact that the mirror scanner should cover a cross section areas of the emitted part and condenser lens as well. As an alternative, a gimbal type scanner should be used to move the entire optical system for scanning, which makes the system heavy and large. Figure 3 shows the distance accuracy, obtained from each configuration. The experiment was performed with 40MHz modulation frequency, Ø 50 condenser lens, and a white object. The bi-axial type optical system, which has no intensity loss, is advantageous for long range detection. However, when using the bi-axial type optical system, the short range detection is difficult, and the system becomes complicated. Hence, it is necessary to select an appropriate optical system according to detection range and application area.

 ISBN: 978-1-61208-297-4

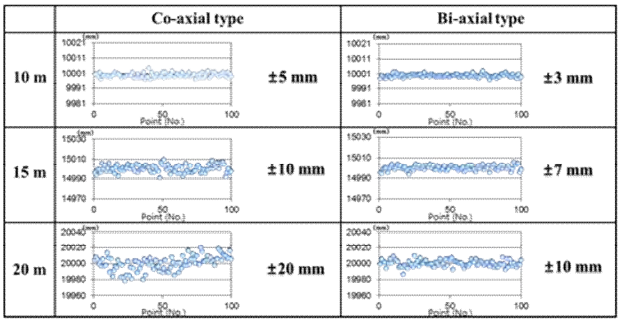

Figure 3. Distance accuracy according to optical system types

B. Demodulation processing

If assuming that a laser diode is modulated with a frequency of ω_{sig} and an amplitude of V_r. A signal emitted from the laser diode, V_{ref} can then be described as

$$V_{ref} = V_r \sin \omega_{sig} t. \quad (2)$$

A signal which is reflected from an arbitrary distance and measured by the photodetector, V_{mea} becomes

$$V_{mea} = \tilde{V}_m \sin (\omega_{sig} t + \varphi_d). \quad (3)$$

Here, φ_d represents the phase difference, which includes the distance information. In addition, $\tilde{V}_m$ is the amplitude of the measured signal, which varies due to the surface reflectivity and measured distance. Thus, using Eq. (1), measured distance can be determined by means of phase difference φ_d. Since high frequency signal gives better resolution according to Eq. (1), usually highly modulated frequency is used as ω_{sig} for high performance of the lidar.

Several demodulation methods have been proposed to obtain φ_d, such as a direct in-phase and quadrature demodulation [8], under-sampling [9], and multiple step phase demodulation methods [10]. In this study, a multiple-step phase demodulation method is used. In this method, another reference signal is needed to shift the frequency ω_{sig} to an intermediate frequency, ω_i. A demodulation reference signal has an amplitude of V_d and a slightly different modulation frequency, ω_d. Then, the demodulation reference signal is described as

$$V_{dem} = V_d \sin \omega_d t. \quad (4)$$

By mixing the measured signal and the demodulation reference signal, the frequency-shifted signal V_i is obtained as

$$V_i = \tilde{V}_m \sin (\omega_{sig} t + \varphi_d) \bullet V_d \sin \omega_d t$$

$$= \frac{1}{2} \tilde{V}_m V_d \cos(\omega_i t + \varphi_d) - \frac{1}{2} \tilde{V}_m V_d \cos(\omega_{sig} t + \omega_d t + \varphi_d). \quad (5)$$

Where $\omega_i = \omega_{sig} - \omega_d$. The second term of the second row in Eq. (5) can be removed by using a low pass filter. Consequently, the filtered output is represented as

$$(V_i)_F = \frac{1}{2} \tilde{V}_m V_d \cos (\omega_i t + \varphi_d) \quad (6)$$

In addition, a reference signal for obtaining φ_d can be defined as $(V_i)_R = \frac{1}{2} V_r V_d \cos (\omega_i t)$ by using the same processing. Then, the phase difference can be determined by means of comparison of $(V_i)_F$ with $(V_i)_R$.

C. Phase detection with the time counting method

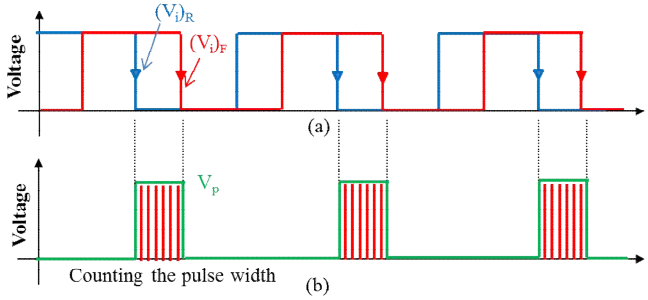

Figure 4. (a) $(Vi)_R$ and $(Vi)_F$ (b) Time counting processing of V_P

The obtained phase difference, φ_d should be changed to analog or digital signals to determine the measured distance via signal processing. The reference and measured signals are first converted to square waves as shown in Fig. 4 (a). Then, a new signal V_p, which is phase difference of two signals, can be obtained by commercial phase detectors. In this study, we used the time counting method[6] because the phase difference can be directly obtained as digital values without the noise effect. In the time counting method, converted square waves are considered as digital signals. In addition, pulse width of V_p is counted by a digital time counting circuit with a high frequency signal as shown Fig. 4 (b). Since the pulse width of V_p is directly measured by a digital processor, the phase difference can be converted to a digital signal without other processing. Moreover, it is not affected by pulse noises because it only measures time. Therefore, the time-counting method is capable of high-resolution and high-speed performance.

D. Intensity control

In the demodulation process for obtaining φ_d by using an analog circuit, many electronic components are implemented for mixing, filtering, amplification, and other types of

 ISBN: 978-1-61208-297-4

processing. Since the amplitude of measured signal, $\tilde{V}_m$ has a wide dynamic range according to distance changes and varying object reflectivity, an additional electronic phase delay $\varphi(\tilde{V}_m)$ is generated in the demodulation processing. In other words, distance errors are caused due to distance changes and varying object reflectivity.

There are primarily two reasons for the additional phase delay. The first reason is due to gain bandwidth product limitation of electronic components because $\tilde{V}_m$ has different voltage inputs according to different distances and object reflectivity. The second reason is a walk error. When measured signal is converted to a square wave digitally by comparing its amplitude with fixed positive and negative threshold values, additional phase delay, $\varphi(\tilde{V}_m)$ is generated according to the varying amplitude in addition to the phase delay corresponding to the distance to be measured. Hence, the real demodulated signal, $(V_i)'_F$ is

$$(V_i)'_F = \frac{1}{2}\tilde{V}_m V_d \cos(\omega_i t + \varphi_d + \varphi(\tilde{V}_m)) \qquad (7)$$

From the Eq. (7), we know that the phase delayof the measured distance becomes different at even the same distance when the reflectivity varies. It is a problem to be considered for the linearity performance of the lidar since a phase error of 1° signifies a 10 mm distance error when 40 MHz frequency is used for the modulation signal, as calculated from Eq. (1). Thus, the electronic phase delay, which causes distance errors must be reduced as much as possible.

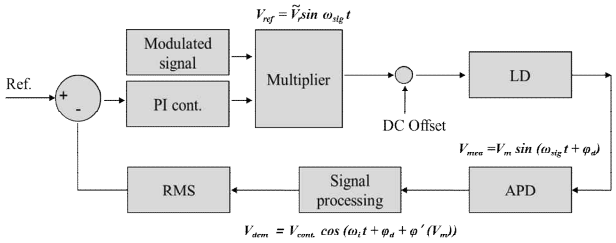

Figure 5. A block diagram of the intensity control method

To reduce the electronic phase delay, an intensity control method is proposed as shown in Fig. 5 [11]. Since the cause of distance errors is basically the varying amplitude of measured signal, in the proposed method, the amplitude of the modulated signal, V_r is controlled by means of a feedback signal to maintain the amplitude of measured signal to be constant. When the amplitude of measured signal reflected from an object becomes smaller than the reference signal of the controller, V_r is increased via the feedback control in order to keep the amplitude of the measured signal constant, and vice versa. Therefore, a constant amplitude, $V_{cont.}$ can be obtained at the detector regardless of the distance change and object reflectivity.

The demodulated signal in the proposed method is then represented as

$$\{(V_i)'_F\}_{controlled} = V_{cont.} \cos(\omega_i t + \varphi_d + \varphi(V_m)) \qquad (8)$$

As indicated in Eq. (8), although a phase delay, $\varphi(V_m)$ is still generated during the demodulation processing, it is constant. Thus, the phase delay does not affect the measured distance because it can be eliminated by shifting the phase of the reference signal, using a known distance.

IV. EXPERIMENTAL RESULTS

For the verification of the performance of the intensity control method, an object located at 3 m was measured with the modulation signal of 40 MHz as shown in Fig. 6.

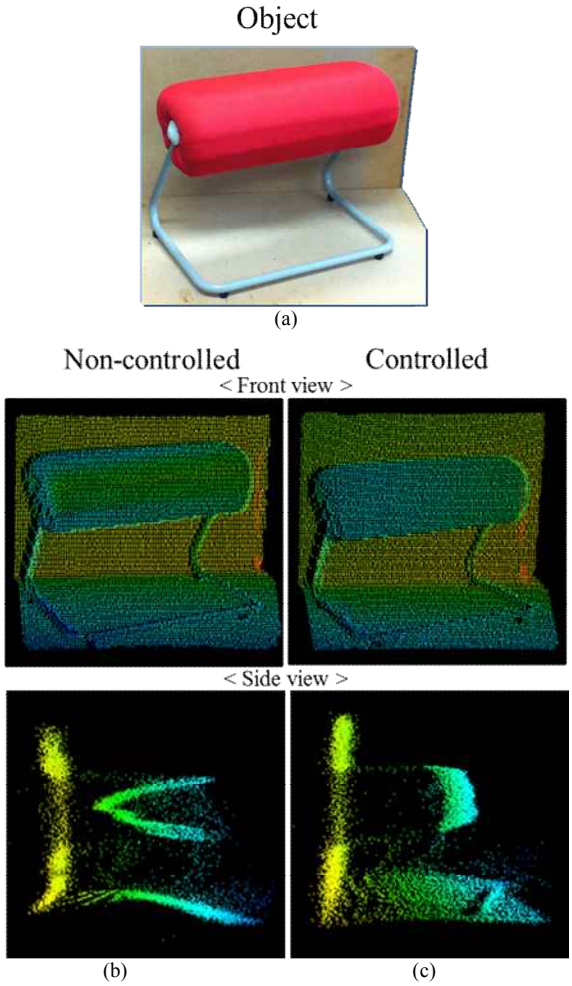

Figure 6. (a) A measured object (b) the non-contolled scanning result (c) the controlled scanning result

Clear difference between non-controlled and controlled results are appeared at short distance because deviation of measured intensity becomes larger when the measured distance get shorter based on the inverse square law of distance[1]. Since the measured intensity also changes according to the laser beam incident angle on the object, the non-controlled scanning result shows shape distortion due to distance errors, caused by the varying amplitude of measured signal, even though the object color is the same. On the other hand, the controlled scanning result shows that the object was scanned without the shape distortion.

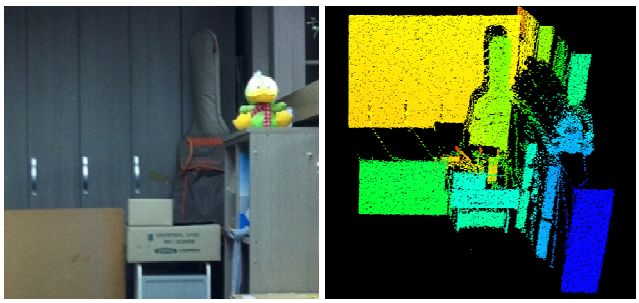

Figure 7. Scanning result for 3D measurement application

For the verification of 3D measurement application, various objects were scanned with the modulation frequency of 20 MHz and a condenser lens of Ø 50 as shown in Fig. 7 In addition, intensity control was applied for the precise measurement. As a result, the scanning results shows that objects were measured without shape distortions although scanned objects have different colors and diverse shapes.

V. CONCLUSION

For precise 3D measurement using the lidar, accuracy, resolution and linearity performances should be considered. In this study, optical system design, signal processing and intensity control method were proposed, which can be applied to the indirect TOF based lidar for high accuracy, resolution and linearity performance.

Optical system is one of the most important factors for the design of the lidar. In this study, appropriate optical systems were considered according to demanded detection range and distance resolution as shown in experimental results.

Demodulation processing and phase detection methods were presented for highly accurate distance measurement. Using the multiple step phase demodulation method, the high frequency modulation signal can be shifted to lower frequency bandwidth. It makes the signal processing easier, and noises are effectively removed during this processing. In the time counting method, analog signals, which have the phase information, can be directly inputted as digital signals. Besides, it is advantageous for noise effect because it only measures time interval corresponding to the phase difference. Therefore, these methods are reasonable for development of high performance lidars at a low price.

Intensity control method was proposed to resolve non-linearity problem caused by varying distance and object reflectivity. As a result, distance errors were significantly reduced, and we could obtain the exact 3D images without shape distortions. The proposed methods are expected to be utilized for other optical sensors as well as lidar sensors.

ACKNOWLEDGMENT

This work was supported by the National Research Foundation of Korea (NRF) grant funded by the Korea government (MEST) (No. 2011-0017876)

REFERENCES

[1] MC. Amann, T. Bosch, M. Lescure, R. Myllylä and M. Rioux, “Laser ranging: a critical review of usual techniques for distance measurement,” Opt. Eng. Vol. 40, No. 1, 2001, pp.10-19.

[2] A. Kilpela, R. Pennala and J. Kostamovaara, “Precise pulsed time-of-flight laser range finder for industrial distance measurements,” Review of Scientific Instruments, Vol. 72, 2001, pp. 2197-2202.

[3] H. Ailisto, et al., “Scannerless imaging pulsed-laser range finding,” Journal of Optics, Vol. 4, No. 6, 2002, pp.337-346.

[4] P. Matteo and S. David, “Figures of Merit for Indirect Time-of-Flight 3D Cameras Definition and Experimental Evaluation,” Remote Sensing, Vol. 3, No. 11, 2011, pp.2461-2472.

[5] S. Bellisai, F. Guerrieri, S. Tisa, “3D ranging with a high speed imaging array,” Ph.D. Research in Microelectronics and Electronics (PRIME) Conference on, 2010, pp.1-4.

[6] Y. Heesun, S. Hajun, P. Kyihwan, “A phase-shift laser scanner based on a time-counting method for high linearity performance,” Review of Scientific Instruments , Vol.82, No.7, 2011, pp.075108-075108-4.

[7] Warren J. Smith, “Modern Optical Engineering,” 4th ed., SPIE press, 2007.

[8] Y. Heesun and P. Kyihwan, “Development of a laser range finder using the phase difference method,” Proceedings of SPIE, Vol. 6049, 2005.

[9] S. Poujouly, B. Journet and D. Placko, “Digital laser range finder: phase-shift estimation by undersampling technique,” IECON/99 Proc. 25th IEEE, Vol. 3, 1999, pp.1312-1317.

[10] Y. Heesun, Y. Woosub, K. Seonggu, H. Jinpyo and P. Kyihwan, “A multiple phase demodulation method for high resolution of the laser scanner,” Review of Scientific Instruments, Vol. 80, 2009, pp.056106 -056106-3.

[11] J. Junhwan, H. Sungui, P. Kyihwan, “Intensity control of a phase-shift based laser scanner for reducing distance errors caused by varying surface reflectivity,” Review of Scientific Instruments , Vol.82, No.12, 2011, pp.126102-126102-3.

 ISBN: 978-1-61208-297-4

Strategies for Realising Long-Term Autonomous Chemical Sensing Devices

Deirdre Cogan, Fiachra Collins, Kate Meagher, John Cleary, Thomas Phelan and Dermot Diamond
CLARITY Centre for Sensor Web Technologies,
National Centre for Sensor Research,
Dublin City University, Dublin 9, Ireland
dermot.diamond@dcu.ie

***Abstract*—Despite decades of intensive research and massive investments in research and development, the unit cost of long-term monitoring of the molecular world of chemistry and biology is still far too high to be practical. This paper reviews the challenges that are preventing the emergence of low cost, reliable chemical sensors and biosensors capable of functioning in a long-term autonomous manner. Strategies for advancing the capabilities of autonomous chemical sensors are discussed, with particular emphasis on direct spectroscopy and reagent based microfluidics for environmental monitoring of nutrients and greenhouse gases.**

Keywords-chemical sensing; biosensing; autonomous sensors; environmental monitoring; nitrate, greenhouse gases, sensor networks

I. INTRODUCTION

In recent years, interest in sensor networks has risen rapidly, driven mainly by the almost ubiquitous availability of wireless communications networks, the increasing power and capabilities of mobile phone platforms, and the need to exploit new sources of data (and hence revenue) beyond conventional phone calls. Phones now can be used to access, generate and exchange audio, video and photo files, and they now have an increasing array of sensors incorporated as standard (e.g., accelerometers, gyroscopes etc.). The increasing interest in new data sources is exemplified by vision statements and strategic movement of very large computing, ICT, network, mobile phone companies into sensor networks. Examples include the Nokia 'Morf' concept, IBM/INTEL activity in Smart Cities, and the HP 'Cense' vision [1].

However, despite the enormous activity both into sensor networks and into the development of improved chemical sensors over the past decade, there has virtually no penetration of chemical sensing platforms into widely distributed sensor network deployments, although the key barriers have been repeatedly highlighted [2,3]. The simple message is that current technologies for autonomous chemical sensing are still not fit for purpose, and do not meet the cost/performance requirements for inclusion in environmental deployments [4].

A striking illustration of the failure to integrate chemical sensing capabilities into widely deployed sensor networks is given by data provided by the Argo project [5], (Fig. 1).

Of the almost 3,600 sensing floats currently active, less than 200 have any chemical sensing capability, and of these, none employ reagent based analysers, and only two are reporting pH measurements. The 'Bio-Optics' sensors (18 locations) are using direct optical colorimetry to infer algal populations from local colour, while the nitrate measurements (27 locations) are all based on direct UV absorbance.

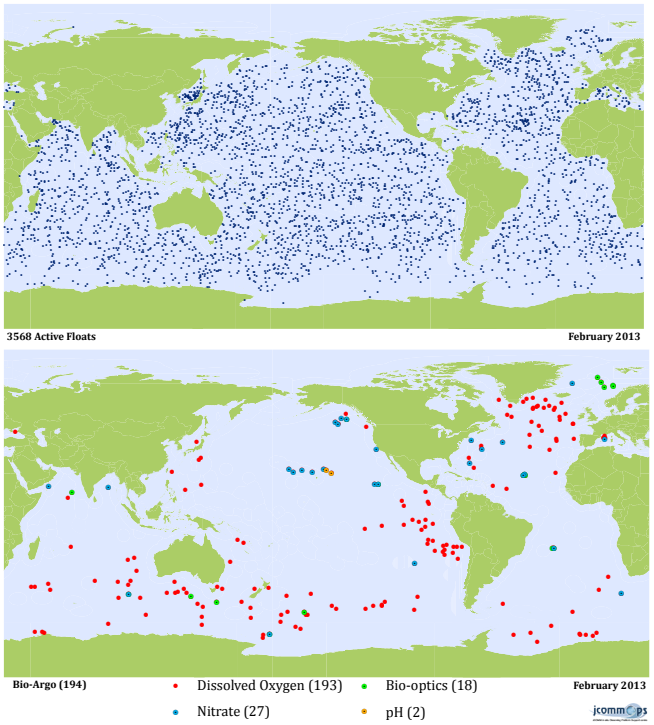

Figure 1: Data from the Agro project website showing the striking difference density of sensor floats reporting temperature and salinity (top, 3568 active) and chem/bio parameters (bottom, 194 active) [5].

II. STRATEGIES FOR ACHIEVING SCALABLE LONG-TERM AUTONOMOUS CHEMICAL SENSING

The clear message from these numbers is that chemical sensors and biosensors do not meet the specifications for these deployments, due to price/performance and reliability issues. In a way, this is understandable, given the rather fragile nature of electrode surfaces modified for chemical sensing purposes, and the extremely hostile nature of the marine environment. The situation on land with

 ISBN: 978-1-61208-297-4

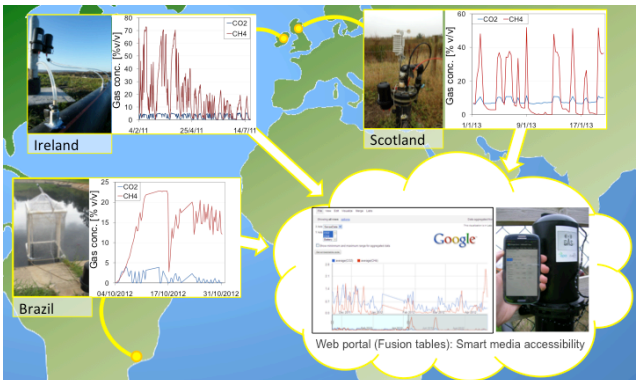

Figure 3: Sample data and photos of deployments of sensing platforms in Ireland, Scotland and Brazil. Data from these deployments is accessed through Cloud-based interfaces like 'Google Fusion Tables'.

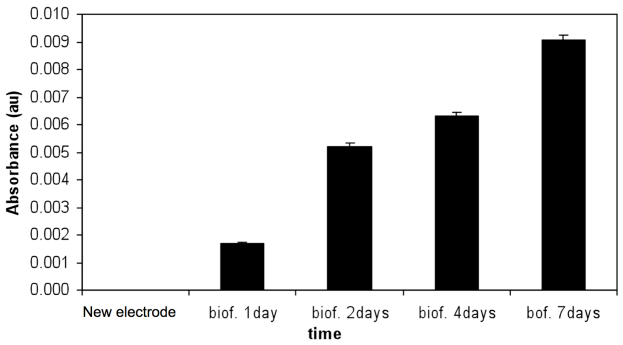

Figure 2: Growth of Biofilm on ion-selective electrode surfaces can be detected within one day of exposure to river water (error bar is standard deviation for n=3 replicates). See [6] for details.

deployments in lakes, rivers, waste water, ground water, is scarcely better. Even though the sensors tend to be much more accessible, scalable deployments demand that the devices must be low cost, and capable of functioning reliably in a totally autonomous manner for long periods of time (several months at least). Unfortunately, our experience is that simple chemical sensors like ion-selective electrodes quickly develop biofilms (Figure 2), and can drastically lose calibration within a few days when directly exposed to river water [6].

Therefore, electrochemical sensors need to be enclosed within a less hostile fluidic environment, and regularly recalibrated to extend the timescale over which they remain functional. This is an essential requirement if chemical sensors are to become part of a scalable sensor network model. However, this also means that the sensor must become part of a more complex fluidic system that can acquire samples, add reagents, perform calibrations with standards, perform cleaning cycles and so on. These functions in turn require control of fluid movement, using pumps and valves, storage of reagents and standards and analytical waste. This pushes the unit cost up to unscalable levels, in the range €15,000-€20,000 or more, with the bulk of the component cost arising from fluid handling [7]. Direct spectroscopic measurements are therefore an attractive option, as direct measurements can be made in the sample, and there is no responsive sensing surface to protect. However, the quality of the analytical information available through direct spectroscopy in the UV-Vis region is limited, mainly due to inability to detect most analytes of interest and lack of specificity for those that do absorb, like nitrate (ca. 190-230 nm) [8].

Direct IR spectroscopy can also be employed, and a number of environmentally important gases can be directly detected with good selectivity and sensitivity using this approach. We have developed very reliable autonomous sensor platforms for monitoring greenhouse gases like CH_4 and CO_2 [9], and deployments of these sensors are currently active in Ireland, Scotland and Brazil. The rugged construction of these autonomous platforms enables long-term in-situ monitoring of gas levels to be performed. The system is remotely deployable with GSM communications and integrated CH_4 and CO_2 infrared gas sensors. A remote server (currently running in our laboratories) receives transmissions from the deployed systems. From here, the data are parsed into the database whereupon it is uploaded onto the online portal (Google Fusion Tables [10]). Figure 3 shows these deployments and presents some sample data in each case in the Google Fusion Tables web interface [11]. So far, >40,000 measurements have been gathered from 6 deployments over a period of >1,000 days.

The web-based monitoring via an online portal enables gas activity to be characterised in a real-time and fully autonomous process. This is particularly important to waste sector activities such as landfilling and anaerobic wastewater treatment plants, where greenhouse gas emissions are required to be controlled and reduced. The autonomous nature of the monitoring platforms, and their high degree of reliability, allow longer term deployments, which is the key

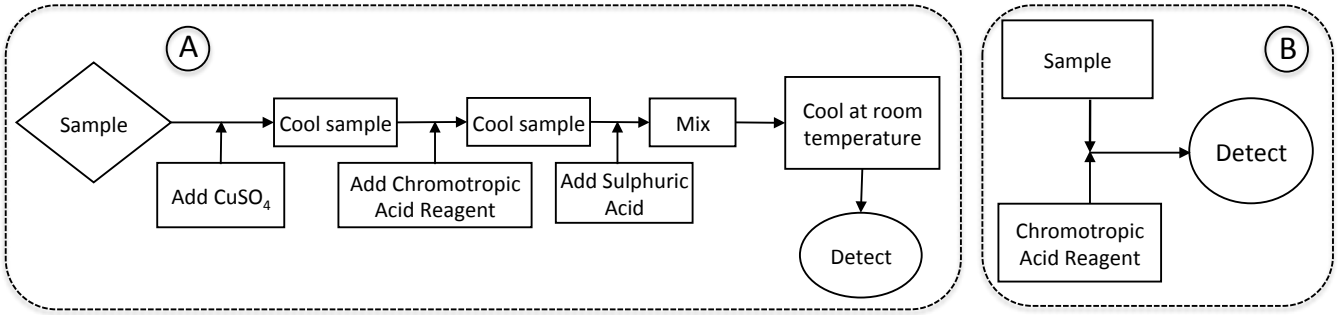

Figure 4: (A) The conventional chromotropic acid method for direct determination of NO_3^-, showing the various stages involved in generating the coloured complex; (B) The simplified chromotropic acid method.

to scalability. Furthermore, the time series data emerging from these deployments permit the identification of numerous events, which otherwise would have been missed using the existing infrequent manual sampling routines, which in turn can provide new insights to natural processes in the environment, and to more effective management of wastewater treatment plants and landfill sites [12,13].

III. REAGENT BASED MICROFLUIDICS

While this success with long-term gas sensing is generating significant interest, we are keen to produce platforms with similar capabilities for monitoring important analytes in water, such as nutrients like phosphate and nitrate. The most successful approach in our experience is to use reliable reagent based analytical methods coupled with optical detection, usually colorimetric based on LEDs and photo-detectors integrated with a microfluidic platform. Provided the reagents employed are stable, and can be mixed reproducibly with the sample under controlled conditions, the colour generated should also be reproducible, and the data therefore reliable, for as long as the reagent lasts. Using microfluidics (which typically involves relatively small sample/reagent volumes), it is relatively easy to perform several thousand assays using as little as 100 mL of reagent.

Previously we reported considerable success with a low cost platform for monitoring phosphate using the well-known 'yellow method' [9]. A key outcome from this work has been the realisation that the best approach is to make the required fluidics design as simple as possible, as this reduces costs and improves overall reliability. For phosphate, the fluidic design could not have been simpler – a 'T' design with one channel for sample and standards, and the other for reagent. For nitrate, the Griess method has been extensively investigated and applied with some success [14-16]. However, the need to use a reduction step (usually through a Cd-reduction column) and the indirect nature of the measurement (involves estimating NO_3^- through subtraction of NO_2^- from total NO_2^- and NO_3^-), makes for a more complex method than is ideal [17].

In terms of direct reagent based methods for nitrate detection, perhaps the best known is based on chromotropic acid [18], in which a yellow colour (λ_{max} ca. 430 nm) is formed when nitrate is mixed with the chromotropic acid reagent in the presence of concentrated sulphuric acid [19]. The various stages in the conventional laboratory version of the method are shown in figure 4 (A) [20]. Obviously, implementing this method in an autonomous fluidic system would be problematic, and, at least in this form, would have little chance of success because of the multiple stages involved, and the very aggressive nature of the concentrated sulphuric acid (>90% v/v). However, we have managed to modify this to a much simpler single reagent addition [21] followed by measurement of the colour using a low cost PEDD photodetector (figure 4 (B)) [22]. Figure 5 shows calibration curves generated using nitrate standards using the simplified method with a UV-Vis spectrophotometer and a prototype fluidic platform comprising two peristaltic pumps (reagent, sample), a mixing junction and integrated PEDD detector. The correlation coefficient in both cases was excellent.

The simplified method was also applied to a sample taken from the Broadmeadow estuary Co. Dublin (found

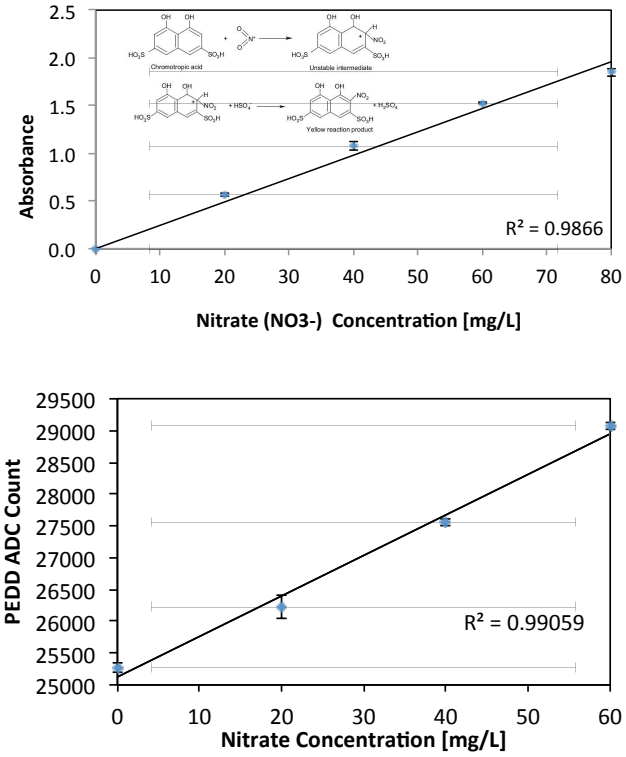

Figure 5: (top) Calibration plot for nitrate standards with a UV-Vis spectrophotometer to validate the simplified chromotropic acid method (scheme for the reaction given in the inset); (bottom) calibration plot generated with a prototype fluidic platform for nitrate detection using the simplified method.

10.18 mg/L) and compared to that of a HACH colorimeter (DR890, HACH LANGE Ireland) (found 10.70 mg/L). Based on these promising initial results, and the fact that the sulphuric acid concentration can be reduced to ca. 50% v/v if a heating stage is integrated into the method, the modified method is now much more amenable for integration into a fluidic platform.

IV. CONCLUSIONS

Direct sensing of key environmental chemical and biological parameters via platforms that require only occasional servicing (months, or years), and are available at a price point that facilitates scaled up deployments remains very challenging. Evidence of penetration of chemical sensors and biosensors into large-scale environmental sensor network deployments is scant due to high cost of ownership and the need for regular maintenance. The most reliable devices currently available operate in 'non-physical contact' mode with the sample. Spectroscopic sensors can be successfully used in long-term deployments to study particular gases, and

 ISBN: 978-1-61208-297-4

measurements of the optical characteristics (scattering, fluorescence, absorbance) can be related to colour, turbidity, algal blooms, nitrate absorbance, while non-contact conductivity provides information on water salinity.

These devices are relatively robust and can be low cost, but tend to provide rather non-specific information about the general condition of the sample. Introducing very selective chemical and biological sensing approaches is much more difficult, for the reasons outlined above. Reagent-based microfluidics appears to be a good option in some cases, provided a suitable colorimetric or fluorescence method is available, and the reagents are stable under the conditions of deployment. Direct exposure of electrochemical sensors is not a good option for long-term water monitoring. Incorporation of these sensors into a microfluidic chip that can perform the required sampling and sample processing, and which exposes the sensors only occasionally to the sample is a reasonable strategy. However, for microfluidics to become adopted more widely for these applications, much lower cost fluid handling strategies that incorporate innovative pumping and valving functions need to be developed.

V. REFERENCES

[1] See for example http://smartercitieschallenge.org, http://research.nokia.com/morph and http://www.livingprinciples.org/sensing-the-future-at-hp-labs/ (last visited April 2013)

[2] D. Diamond, "Internet Scale Sensing", Anal. Chem., vol.76, 2004, pp. 278A-286A.

[3] D. Diamond, S. Coyle, S. Scarmagnani and J. Hayes, "Wireless Sensor Networks and Chemo/Bio-Sensing", Chem. Rev., vol.108, Issue: 2, 2008, pp. 652-679.

[4] D. Diamond, K. T. Lau, S. Brady and J. Cleary, "Integration of Analytical Measurements and Wireless Communications – Current Issues and Future Strategies", Talanta, vol. 75, 2008, pp. 606-612.

[5] see http://www.argo.ucsd.edu/About_Argo.html

[6] A. Radu et al., A. Lewenstam, and D. Diamond, "Diagnostic of functionality of polymer membrane—Based ion selective electrodes by impedance spectroscopy," Analyt. Meth., vol. 1, 2010, pp. 1759–9660.

[7] B. Ziólkowski, M. Czugala and D. Diamond, "Integrating stimulus responsive materials and microfluidics: The key to next-generation chemical sensors", Journal of Intelligent Material Systems and Structures, 27 September 2012, DOI: 10.1177/1045389X12459591.

[8] P. Puitt, "Nitrate Measurement in Less Than 30 Seconds", Water Environment Laboratory Solutions, vol.16, 2009, pp. 1-5.

[9] F. Collins, D. Orpen, D. Maher, J. Cleary, C. Fay and D. Diamond, "Distributed Chemical Sensor Networks for Environmental Sensing", Proc. of the Int. Conf., 'SensorDevices', Nice, France, Aug. 21-26 2011, pp 58-62, ISBN: 978-1-61208-145-8.

[10] see http://support.google.com/fusiontables/answer/2571232?hl=en

[11] F. Collins, J. Cleary, C. Zuliani, C. Fay and D. Diamond, "Distributed Environmental Monitoring, in Autonomous Sensor Networks", ed. Daniel Filippini, Springer Series on Chemical Sensors and Biosensors, Springer (Heidelberg), Vol. 13, 2013, pp 321-363.

[12] F. Collins, D. Orpen, E. McNamara, C. Fay and D. Diamond, "Landfill Gas Monitoring Network – Development of wireless sensor network platforms", SENSORNETS, Barcelona, Spain, Feb. 2013, Accessible from http://doras.dcu.ie/17828/.

[13] C. Fay et al., "Remote real-time monitoring of subsurface landfill gas migration", Sensors, vol. 11, 2011, pp. 6603-6628.

[14] M. Czugala et al., "Optical sensing system based on wireless paired emitter detector diode device and ionogels for lab-on-a-disc water quality analysis", Lab Chip, vol. 12, 2012 pp. 5069-5078.

[15] A.D. Beaton et al., "Lab-on-Chip Measurement of Nitrate and Nitrite for In Situ Analysis of Natural Waters", Environ. Sci. Technol., vol. 46, 2012, pp. 9548-9556.

[16] Greenway, G.M., Haswell, S.J. and Petsul, P.H., "Characterisation of a micro-total analytical system for the determination of nitrite with spectrophotometric detection", Analytica Chimica Acta, vol. 387, 1999, pp. 1-10.

[17] Zhang, J. and Fischer, C.J., "A simplified resorcinol method for direct spectrophotometric determination of nitrate in seawater", Marine Chemistry, vol. 99, 2006, pp. 220-226.

[18] A.L. Clarke, A.C. Jennings, "Soil Analysis, Spectrophotometric Estimation of Nitrate in Soil Using Chromotropic Acid", J. Agric. Food Chem., vol. 13, 1965, pp. 174-176.

[19] L. Bulgariu and D. Bulgariu, "Direct determination of nitrate in small volumes of natural surface waters using a simple spectrophotometric method", Rev. Anal. Chem. Vol. 31, 2012, pp. 201-207.

[20] J. Ryan, G. Estefan, A. Rashid, Eds.; In Soil and Plant Analysis Laboratory Manual; ICARDA: Aleppo, Syria, 2001.

[21] Unpublished results, manuscript in preparation

[22] M. O'Toole K.T. Lau and D. Diamond, "Photometric Detection in Flow Analysis Systems using Integrated PEDDs", Talanta, vol. 66, 2005, pp. 1340-1344.

 ISBN: 978-1-61208-297-4

Design and Characterization of the Seashell Effect Pretouch Sensor Integrated Into Robot Grippers

Liang-Ting Jiang
Department of Mechanical Engineering
University of Washington
Seattle, USA
email: jianglt@uw.edu

Joshua R. Smith
Department of Computer Science and Engineering
Department of Electrical Engineering
University of Washington
Seattle, USA
email: jrs@cs.uw.edu

***Abstract*—The paper presents a short range proximity pretouch sensor device based on the seashell effect inspired by the phenomenon of "hearing the sea" when a seashell is held to the ear. The acoustic theory, design consideration, and the quantitative characterizations of the sensor under different ambient sound conditions are studied. The sensor has a number of practical benefits compared to conventional sonar-based time of flight sensors: (1) easy sensor integration — the sound stimulus source and the detector do not need to be co-located; (2) short-time measurements are not required; (3) no multi-path effects. The sensors are designed and integrated into a robot's gripper, which provides a new source of information for robotic manipulation that complements long range depth sensors and contact-based tactile sensors. Continuous object contour tracking using differential measurements with pairs of the new sensors (one in each robot's fingertip) is demonstrated on objects with different material properties.**

Keywords–pretouch; sensor; acoustic; proximity; non-contact

I. INTRODUCTION

"Pretouch" sensors are non-contact sensors with properties intermediate between long range non-contact sensors (RGB cameras, depth cameras, and laser rangefinders) and contact-based tactile sensors. Previous pretouch sensors based on electric field [1][2][3] and optics [4] have been used in several robot grasping applications, such as robot hand preshaping, gripper servoing, co-manipulation, and, mid-range object imaging. One issue of these sensors is their restricted compatibility for different material properties. Electric field pretouch only works well on materials with high conductivity or dielectric constant, and optical methods (including optical pretouch as well as RGB cameras and depth sensors) are not suited to highly reflective, transparent, or absorbing (black) materials.

The "seashell effect pretouch" sensor [5] we previously proposed relies on mechanical (acoustic) properties rather than electrical or optical properties, and, therefore, is compatible with a set of materials that is orthogonal to those can be sensed by electrical / RF or optical techniques. The effectiveness of seashell effect pretouch was demonstrated with two simple robot grasping applications: (1) pretouch-assisted grasp planning, in which the pretouch sensor is used to exhaustively augment the point cloud of the object provided by a depth sensor operating in sub-optimal conditions, such as with transparent materials or occluded objects; (2) reactive grasping: the detection of extremely compliant objects which can not be sensed by traditional tactile sensors. Recently, we also proposed a unified probabilistic framework to enable automatic exploration with the pretouch sensor to reduce object shape uncertainty before robotic grasping [6].

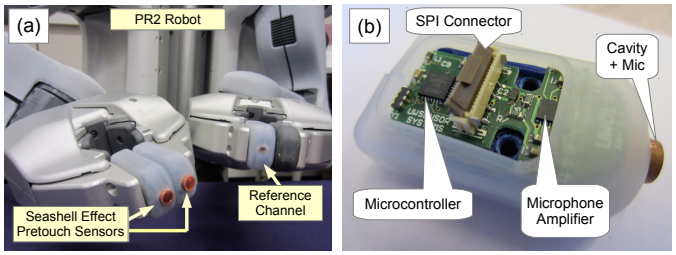

Fig. 1. (a) The seashell effect pretouch sensors installed on the Willow Garage PR2 robot grippers. (b) The sensor system consists of a PCB, a microcontroller, electronic components, a microphone, and an acoustic cavity integrated into the PR2 robot's fingertip.

In this paper, we further discuss in more detail the acoustic theory, design consideration, and the quantitative characterizations of the sensor. We also characterizes the effect of ambient noise power and spectral contents on the sensor performance, and propose an adaptive stimulus generation by deliberately generating white noise, band limited to match the sensor's frequency response. It detects current ambient sound conditions and provides additional band-limited white noise to maintain consistent SNR ratio, and thus guarantee minimum sensor performance, even at low ambient sound levels. We also introduce an embedded sensor system integrated into the PR2 robot's gripper, which eliminates the external power and data cables necessary in prior implementations. This improved implementation has also made it practical to integrate multiple seashell effect sensors in a single robot (one in each finger).

The paper is organized as follows: in Section II, we first review the related work. The acoustic theory is discussed in Section III. The sensor design and considerations are discussed in detail in Section IV, and then the proposed sensor systems is characterized in Section V. In Section VI, we show an example application of the proposed sensor in robotics. Finally, in Section VII, we conclude and discuss the future work.

II. RELATED WORK

The idea of acoustic resonant shift is widely used in highly sensitive mass sensors for chemical and biological environment [7]. A typical acoustic mass sensor uses the fact that the

 ISBN: 978-1-61208-297-4

resonant frequency of an acoustic-wave resonator changes in response to the mass load applied on the resonator's surface. For example, Zhang et al. [8][9] devised a micromachined film bulk acoustic resonator mass sensor built on a micromachined silicon-nitride diaphragm with a piezoelectric thin film and Al electrodes that can operate in vapor and liquid. Its resonant frequency drops linearly with added mass on the surface. The shift of the acoustic resonant frequency is measured from the longitudinal standing wave existing between two faces of the electrodes sandwiching a piezoelectric film, and the mass load and be inferred from the frequency shift.

In the design of our seashell effect pretouch sensor, we design an acoustic system (a closed-open ended cylindrical pipe in our case), in which its resonant frequency is shifted by the reactive radiation impedance (small vibrating air mass) change at the open termination of the pipe caused by the obstacle.

III. Acoustic Theory

The seashell effect is the phenomenon of "hearing the sea" that is observed when a seashell is held to the ear. The sound is the ambient noise amplified (attenuated) with the seashell cavity's acoustic frequency response. Inspired by the fact that the sound of the sea changes as the distance from the seashell to the head varies, a pretouch sensor is essentially an acoustic cavity (an closed-open pipe in our case) attached to a microphone that detects the change in ambient sound spectrum that occurs when the pipe approaches an object. When an object approaches the pipe opening, the sound field between the surface of the object and the pipe opening causes a change in the effective (acoustic) length of the pipe. Perhaps counterintuitively, the effective length of the pipe increases as the sensed object approaches; thus the resonant frequency of the pipe decreases as an object approaches. The similar effects were also studied for the woodwind musical intruments which have keys (buttons) hanging above the tone holes [10]. The key acoustic theory is summarized in this section.

A. End Correction of Cylindrical Pipes

The shift of the resonant frequency caused by the object can be best explained by using the terminologies of acoustic impedance and end correction. The acoustic impedance is defined as: $Z = \frac{P}{U}$, where P and U are the amplitude of the sound pressure and volume velocity, respectively. For an ideal closed-open pipe, the closed end is a rigid termination with infinity acoustic impedance ($Z_c = \infty$). At the open end, the sound wave is small compared to the atmospheric pressure, so the open end acts as a release termination at which the pressure vanishes (p = 0) with zero acoustic impedance ($Z_o = 0$), which gives total reflection in anti-phase. However, the open end is in fact terminated by a radiation impedance. The effect of radiation can be approximated by considering the wave in the pipe accelerating the final layer of the air back and forth as a small mass. The radiation impedance (Z_r) seen by this final layer has a general form of:

$$Z_r = \frac{Z_0}{S}(R + jX) \tag{1}$$

where Z_0 is the characteristic impedance (Z_0 = 415 Ns/m^3 for air at 20 °C); $S = \pi a^2$ is the area of the pipe (m^2), where a is the pipe radius; R and X are functions of the wave number k, the pipe radius a, and most importantly, the geometric configuration in the environment around the opening. R and X represent the similar ratios of the real part of the impedance (acoustic resistance) and the imaginary part of the impedance (acoustic reactance) to the characterisric impedance, respectively. The imaginary part corresponds to the impedance of a mass of a volume of the medium of the size $S\Delta L$, and shifts the position where reflection in antiphase occurs to a virtual plane outside the tube by ΔL, which is usually called *end correction*. The end correction ΔL= $0.8488a$ for a cylinder pipe with infinite flange can be solve analytically using Rayleigh integral for the Helmholtz equation [11], and serves as the upper bound for cylindrical pipes, while ΔL= $0.6133a$ for cylindrical unflange pipe [12] was solved under plane wave assumption (for frequency lower than the first cut-off frequency of the pipe), which serves as the lower bound. End correction for other complicated geometric configurations are usually found by numerical and experimental methods [13].

In our application, we are most interested in knowing the effects of obstacles presenting near the opening, specifically, the distance of the object to the opening. The presented object further restricts the space for sound wave propagation and causes more end correction in addition to ΔL. Dalmont et. al. [14] presented an emperical formula of this additioanl end correction term ΔL_{obj} for this situation:

$$\Delta L_{obj} = \frac{a}{3.5(h/a)^{0.8}(h/a + 3w/a)^{-0.4} + 30(h/d)^{2.6}} \tag{2}$$

where a is the radius of the pipe; h is the distance between the obstable and the pipe opening; w is the thickness of the pipe wall; d is the width of the object. Considering this additional end correction, the effective length of the pipe becomes:

$$L_{eff} = L + \Delta L + \Delta L_{obj} \tag{3}$$

B. Resonance Frequency

The fundamental resonance frequency of the standing wave in a closed-open pipe f_0 can be found by

$$f_0 = \frac{c}{4L_{eff}} \tag{4}$$

where c is the speed of sound. The effective pipe lenght is altered when an object is presented near the opening. Therefore, by measuring the resonance frequency of the pipe, we can inversely infer effective length of the pipe, and then further infer the distance of the object h from experimental data.

IV. Sensor Design

The main sensor hardware consists of a brass open-ended pipe, and a microphone attached to one side of the pipe to form the closed end. The microphone collects the sound pressure at the closed end filtered by the acoustic cavity (i.e., the closed-open pipe). The pipe's fundamental resonant frequency is found by looking for the first maxima in the frequency spectrum. To avoid being confounded by features in the raw (unfiltered) ambient audio itself (including loud ambient sounds), a reference microphone is used to collect

 ISBN: 978-1-61208-297-4

environmental sounds not filtered by the pipe; this background spectrum is subtracted from the actual pretouch sensor channel. This noise cancellation approach substantially improves sensing accuracy. Figure 4 shows the system architecture of our seashell effect pretouch sensor.

A. Acoustic Design

Equations (2), (3), and (4) were employed throughout the acoustic design process. Although the end correction term is based on approximattion and not an exact solution, they serve as useful guiding references. The sensor acoustic characteristics are mainly determined by two geometric parameters: the pipe length L and the pipe radius a. Some considerarions should be taken when designing the two parameters:

(a) As a rule of thumb, we want the plane wave assumption to hold in order to have predictable acoustic behavior. It requires the resonance frequencies in the working range of the sensor to be lower than the first cut-off frequency in the circular pipe (ka<1.8412), so that only the fundamental mode will propagate.

(b) From (2), the end correction caused by the object (ΔL_{obj}) is roughly inversely proportional to the ratio h/a. It means using a larger pipe radius a could increase the amount of end correction changes at different object distances, and thus obtain better frequency resolution in the vertical sensing direction given a fixed pipe length L. Figure 2 shows the end correction values and the estimated resonance frequencies based on (2) and (4). From Fig. 2(a), we can see the frequency drops more at the close range when using larger radius (a=5 mm) compared to when using a small pipe (a=1 mm). This is due to the larger changes of the varying end correction term ΔL_{obj} caused by the object when using a larger radius. However, using a larger radius means the sensor will lose lateral sensing resolution physically, and become harder to integrating into the robot's gripper. Therefore, there is a trade-off when selecting the pipe radius.

(c) In the case of a fixed pipe radius a (fixed end correction ΔL and ΔL_{obj}), using a shorter pipe length L can result in more frequency shift according to (4). Figure 3 shows the shortest pipe (L=2.5mm) has the best dynamic range of the resonance frequency shift. The end correction changes is fixed because it is independent of L. Therefore, the shorter the pipe length L is, the more frequency shifts at the close distances. However, an open cavity is considered as a lumped-element (a mass) as a whole when the length is short compared to the wavelength ($kL_{eff} << 1$) [15], which has a different resonance behavior.

According to the above design considerations and experiments, a pipe length L=5 mm and radius a=2.5 mm was selected for our system, which has a compact size to be embedded on the PR2 gripper fingertip.

B. Hardware Design

A customized Printed Circuit Board (PCB) and fingertip structure was designed to hold all the electronic and mechanical components, including the microphone and the pipe. The cavity used in our system is a 2.5 mm radius / 5 mm length cylindrical pipe attached to a 2.5 mm radius / 3 mm length

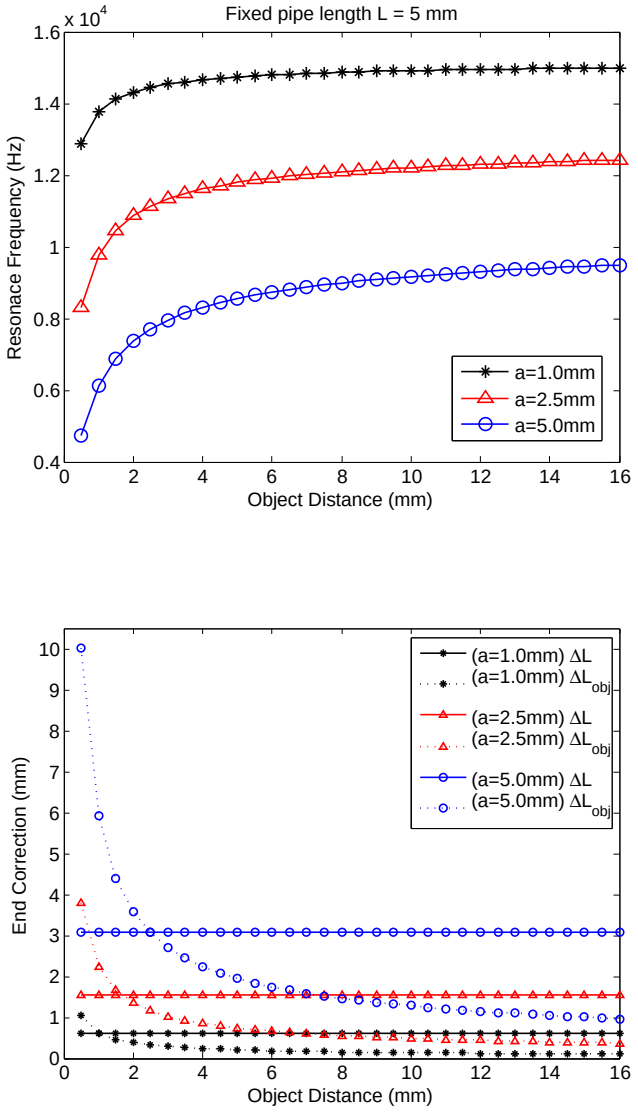

Fig. 2. (Upper:) resonance frequencies of the pipe at different distances with fixed length (L=5 mm) and various radius size. (Lower:) end correction of the pipe at different distances with fixed length and various radius size.

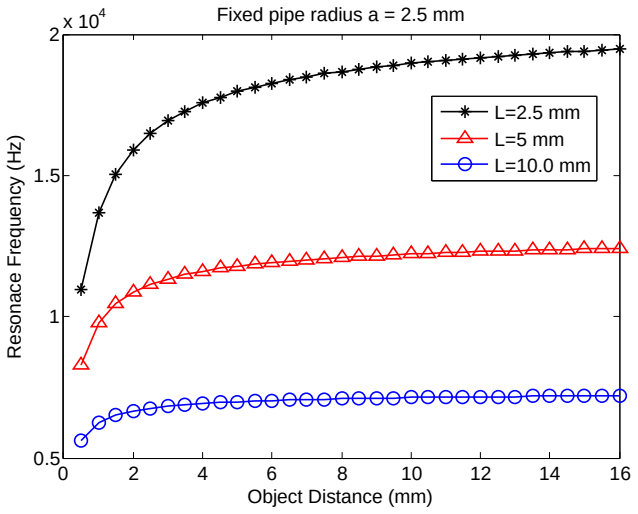

Fig. 3. The computed resonance frequencies of the pipe at different distances with fixed radius size (a=2.5mm) and various pipe length L.

 ISBN: 978-1-61208-297-4

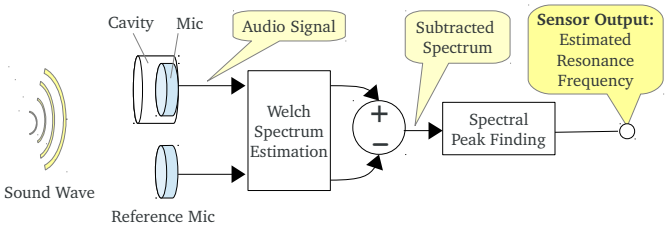

Fig. 4. The system architecture and the signal flow of the seashell effect pretouch sensor system.

microphone, which is compact enough to be embedded in the PR2 gripper's fingertip. Figure 1(b) shows the PCB and fingertip fixture with all the components attached, and Fig. 1(a) shows the completed pretouch sensing fingertip installed on the Willow Garage PR2's gripper. In the current implementation, there are two fingers on one of the grippers as the actual sensing channels, and a reference channel. The microphone for the sensing channel is attached with an acoustic cavity to amplify (attenuate) the ambient sound. The microphone for the reference channel is used to collect the ambient sound for spectrum subtraction. The only difference between the design is that the microphone on the reference channel is not attched to the pipe (acoustic cavity), so it simply collects the ambient (unfiltered) sound. Unlike the previous sensor [5], the new sensor described in this paper is completely integrated into the Willow Garage PR2 robot; all external cables and electronics have been eliminated. The embedded sensor design eliminates the constraints on robot arm motion caused by the external wires and electronics, and thus broadens the applicability of the sensors. The design presented here could also be adpated to integrate the sensor into other platforms.

The sound signal path implementation is decribed here. The pipe cavity filters the ambient noise, and the sound signal collected by an electret microphone (Panasonic WM61-A) is amplified by 40 dB through a low-noise microphone amplifier (Maxim MAX9814), and is sampled by the 8-bit Analog-To-Digital Convertor (ADC) on a 8-bit microcontroller (Atmel ATMega168). The sampled data is then transmitted from the microcontroller to the 8-bit soft soft processor (Xilinx PicoBlaze) residing in the FPGA inside the PR2's gripper via the Serial Peripheral Interface (SPI) communication protocol. Finally the sampled sound data is accessible from the FPGA to Robot Operating System (ROS) in the PR2 robot through the EtherCAT interface. The sampling rate for this whole signal path is 35,700 Hz for each channel. Currently, the sampling rate is limited by the SPI implementation on our circuit board; with more careful SPI design, the sampling rate could be increased up to the limit imposed by the microcontroller's ADC.

C. Signal Processing

The power spectral density of the sound signal from both channels are estimated using Welch spectrum estimation (N_s = 1024; overlap ratio = 70%; Hanning data taper). The spectrum of the reference channel is subtracted from the spectrum of the sensor signal before peak finding, which avoids the effect of loud sounds, outside of the sensor's frequency range, misleading the peak tracking. The peak finding and estimation

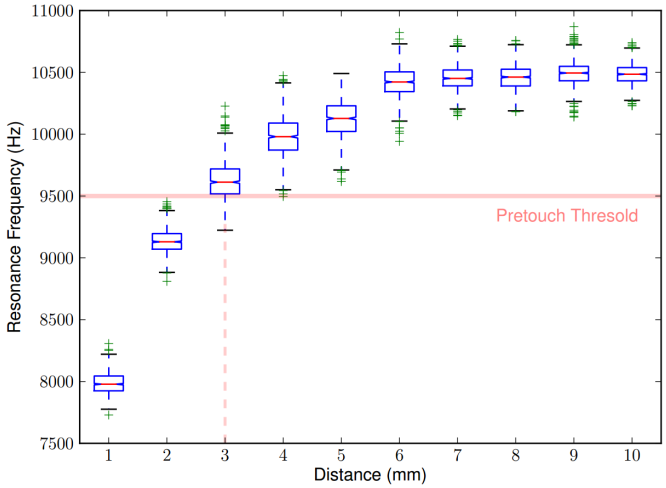

Fig. 5. The box-and-whisker plot of 1000 estimated resonance frequencies at each distance. It represents the sensor characteristics of the sensor with length L=5 mm and radius a=2.5 mm integrated on the robot fingertip.

algorithm we used here is the same as described in [5].

V. Characterization

In this section, we perform a set of experiments to characterize the sensor, including the resonance frequency shift at different object distance and effects of the object materials and ambient noise (the power density and spectral content).

A. Resonance Frequency Shift

The resonance frequency changes with object distance is evaluated by collecting 1000 sensor readings (filtered spectral peak frequency) at various distance from 1 mm to 10 mm. A box-and-whisker plot presents the performance of the sensor (Fig. 5). The resonance frequency drops at close distance starting from 6 mm. Based on experimental data, we select the a threshold at 9500 Hz (the lower quartile at 3 mm), such that the upper quartile at 3 mm is smaller than the lower quartile at 6 mm, so the sensor can be used as a binary sensor.

B. Material Sensitivity

The seashell effect pretouch sensor does not depend on optical or electrical material properties. Instead, it depends on mechanical / acoustic properties. This characteristic makes it a good complement to long range optical depth sensors. For example, seashell effect pretouch can sense highly transparent, reflective, or light-absorbing materials, which are difficult for optical sensors. In this section, we compare the sensor output for several different materials at the same distance. 1000 readings are measured for each object at a distance of 2 mm from the object's surface. The collected data is plotted in Fig. 6. The results show that the readings from materials with more porosity, such as cloth and foam, are more noisy than others. We hypothesize that these materials may acts as absorption or transparent materials depending on their thickness.

C. Effect of Ambient Sound

It is natural to wonder whether seashell effect pretouch could be improved by actively generating sound. Although

 ISBN: 978-1-61208-297-4

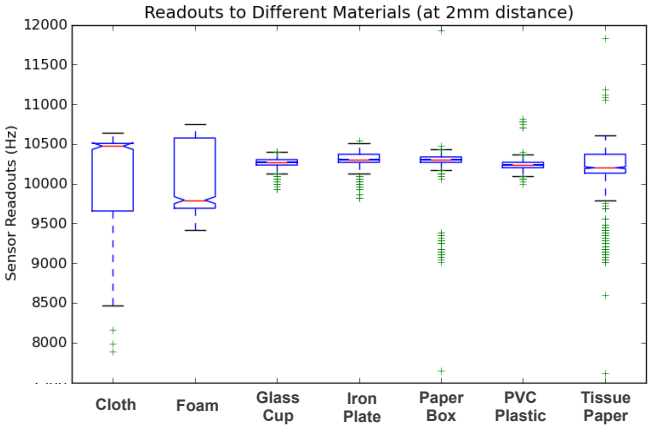

Fig. 6. The box plot of the sensor readouts to different materials. 1000 readouts are measured for each object at 2mm distance.

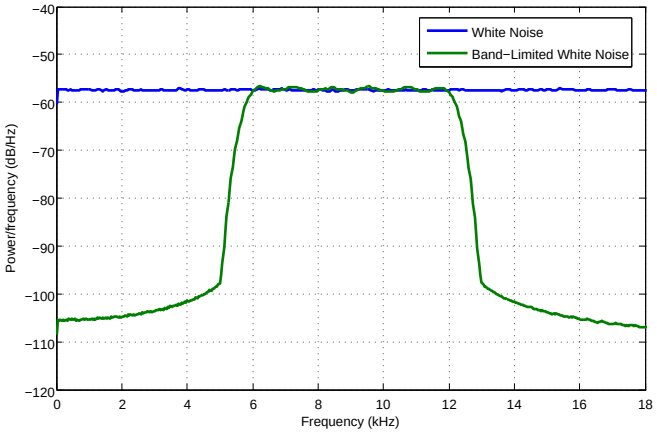

Fig. 7. The spectrum of the two waveforms used for external sound characterization. The bandlimited white noise is the white noise processed by a bandpass filter that attenuates below 6000 Hz and above 12000 Hz.

the passive scheme has the advantage of easy integration, it is desirable to understand how much improvement could be achieved if extra sound is actively generated. In this section, we systematically investigate the effects of deliberately generated sound; we will examine sensor performance as a function of the sound's spectral contents and power density. Finally, we describe an adaptive active sound generation scheme that maintains consistent sensor performace regardless of ambient sound conditions.

The first factor we investigate is the spectral contents of the sound. Two waveforms with different spectral contents are experimented and compared. The first waveform, white noise, has an uniform power spectral density distribution over its frequency band from 0 to 22,050 Hz. Considering the fact that the sensor's resonance frequency is always within a certain range, it is intuitive to hypothesize that providing bandlimited white noise might be sufficient, or even more efficient. Therefore, the second waveform has the uniform spectral density limited within 6,000 - 12,000 Hz (the relevant range, as determined in our previous experiments). The lower and upper bounds were determined by experimental data: the sensor readout is confined to this frequency band for objects in its working range (0 - 10 mm). The waveform is generated by processing the white noise waveform with a bandpass filter. Figure 7 shows the spectral density of the two different waveforms used in this experiment. (For example, 1.5 dB/Hz)

The second factor investigated is the power level of the added sound. During the experiment, we measure the average power density of the sound for 30 seconds without a stimulus, and again for 30s with the stimulus. (The average is computed first over time, and then over all discrete frequency bins.) The difference is computed to find the power increase due to the stimulus. The difference value in units of dB/Hz is the average power density level increased due to the generated sound stimulus. When the waveform is played, the amplitude is adjusted such that the total power received by the microphone is at the target level. Three sound levels are tested: without external stimulus sound, 0.5 dB/Hz stimulus, and 1.5 dB/Hz stimulus. The microphone selected for the sensor system has flat frequency response from a very low frequency (20 Hz) to its highest frequency (20,000 Hz), and the microphone amplifier has flat frequency response over 400 - 20,000 Hz according to the manufacturer's datasheet. Our seashell effect pretouch sensor works in the range of 6,000 - 12,000 Hz, so the effects of the system response of the microphone and amplifier can be considered uniform for both waveforms in this experiment.

Two indicators are defined to characterize the sensor performance: The CNR is defined as:

$$CNR := \frac{\overline{f_n} - \overline{f_1}}{\overline{\sigma(f_i)}}, i = 1..n \quad (5)$$

where i is the object distance in millimeter, n is the farthest distance, f are the measured resonance frequencies, and σ is the standard deviation. This is the frequency difference between the farthest (10mm) and closest (1mm) distance devided by the average of the standard deviation at each distance. It measures the ability of the sensor to distinguish between the farthest and closest distance, subject to sensor variability The second indicator Signal-To-Noise Ratio (SNR) is a measurement of how prominently the peak frequency stands out in the subtracted power spectral density compared with the noise level of the environment. It is defined as:

$$SNR := p_{max} - \overline{p} \quad (6)$$

where p is the power density (dB/Hz) of the spectrum. The higher the SNR is, the more likely the peak (resonance) frequency can be detected precisely in the spectrum. The first measure is useful for characterizing ground truth performance of the sensor. The second measure will be used autonomously to choose the energy of the stimulus. It is necessary for its autonomous use that this measure does not require knowledge of the ground truth.

Using the combination of two different waveforms and three different sound levels, five experimental trials were performed: no stimulus, 0.5 dB/Hz broadband stimulus, 0.5 dB/Hz bandimited stimulus, 1.5 dB/Hz broadband stimulus, and 1.5 dB/Hz bandimited stimulus. For each trial, 1000 readouts were measured at each distance from 1 to 10 mm (in increments of 1 mm). Figure 8 shows the power spectral densities and the computed SNR for the five trials. Whithout providing extra sound stimulus, the peak power is weak compared with the

 ISBN: 978-1-61208-297-4

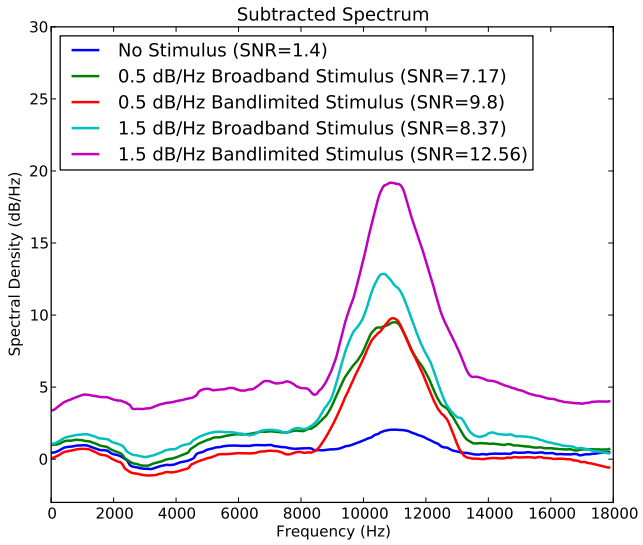

Fig. 8. The subtracted spectrum (spectrum of sensing channel - spectrum of reference channel) at 10mm distance when extra noise is played with different waveforms and different power.

environment sound, so any other noise bursting in the ambient sound can mislead the peak frequency estimation. By providing extra sound, the peak power at around 10,700 Hz is more prominent, so any other smaller peak appearing in the spectrum will not affect the peak frequency estimate. For the same stimulus power constraint, all the power in the bandlmited white noise stimulus falls in the sensor's working range (6,000 - 12,000 Hz), while the broadband stimulus essentially wastes some power (that outside the sensor's working region). Thus for the same allowed stimulus power, the bandlimited stimulus increases the sensor SNR more. Thus, the bandlimited white noise is more efficient, since we want to provide the smallest noise possible, both to avoid annoying nearby people who might hear the stimulus, and to prevent the robot / sensor system from expending unncessary electrical power.

The sensor readouts at each distance from 0 to 10 mm for each of the five cases; the CNR is computed for each case. From Fig. 9, it is clear to see without providing external stimulus noise in a quiet environment, the sensor readings are spread out, with no prominent peaks. When bandlimited white noise is provided at the average power density of 1.5 dB/Hz, the CNR is improved from 0.9 to 10.88 compared to the case without extra noise. (Note that in our prior work [5], noise sources in the robot such as fans appear enabled better performance than the no stimulus case presented here; this data was taken in a quiet room far from the robot.)

Table I shows the performance indices for all the experiment sets. From these results, we can conclude the following: (1) appropriate ambient noise spectrum and level is essential for good sensor performance. (2) the bandlimited white noise is more efficient to imporve the SNR and CNR compared with the white noise at the same power level. (3) CNR is hightly correlated with SNR, which matches the intuition that the more prominent peak will facilitate the peak estimation, and thus the sensor measurement is more accurate. Based on these findings, we propose to implment an adaptive stimulus noise generation

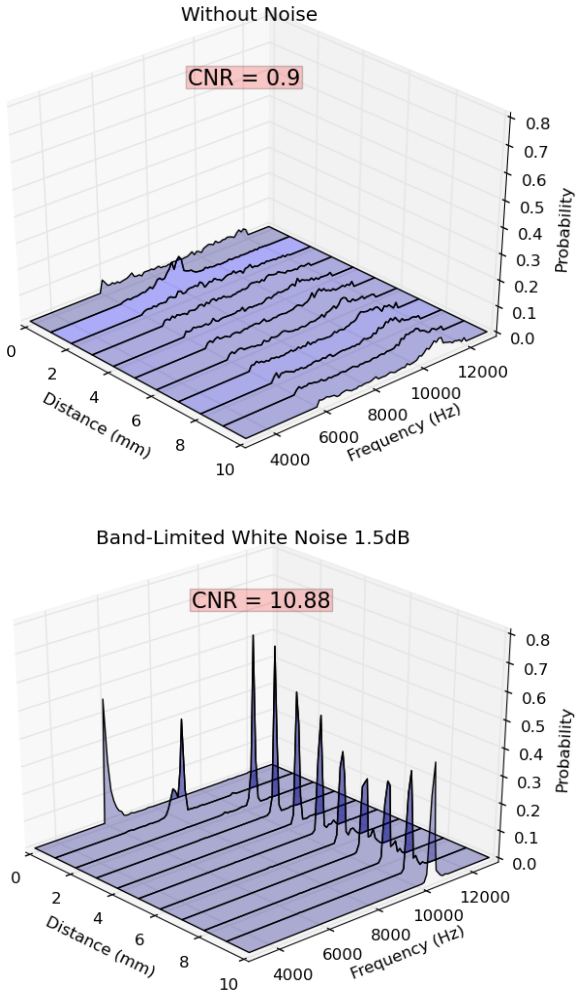

Fig. 9. The sensor model created by collecting 1000 sensor readouts at each distance from 0 to 10 mm for the two cases: (a) In a quiet room without actively providing extra noise. (b) the extra bandlimited white noise provided at 1.5 dB/Hz average spectral power density.

TABLE I. EFFECT OF THE EXTRA NOISE SPECTRUM ON SENSOR PERFORMANCE

Waveform	Stimulus Noise Average Power Density (dB/Hz)	CNR	SNR
No Extra Noise	0	0.90	1.40
White Noise	0.5	6.57	7.17
Bandlimited White Noise	0.5	9,37	9.80
White Noise	1.5	8.45	8.37
Bandlimited White Noise	1.5	10.88	12.56

scheme described in the following section.

D. Adaptive Stimulus Generation

The goal of the adaptive stimulus sound generation scheme is to maintain a consistent and quantifiable sensor performace regardless of ambient noise conditions. Based on the findings from the experiments, bandlimited white noise is selected as the sound waveform of the stimulus sound. We can hypothisize that if the SNR in the sound signal spectrum is kept at a fixed value, the actual sensor measurement performance indicator SNR will also be maintained at a stable level. Since

 ISBN: 978-1-61208-297-4

CNR can only be computed with knowledge of the ground truth sensing situation, it is not the appropriate quantity to control the adaptive stimulus generation. In this particular implementation, a SNR target of 10 was selected, as suggested by the experimental data. A first order closed-loop feedback control is used to monitor the current SNR in the spectrum from the sensor and adjust the bandlimited white noise level with a fixde gain. The goal is to keep the SNR to the targeted value, so that consistent sensor performace can be achieved.

To assess the effectiveness of this approach, the standard deviation of the sensor readouts is computed from the readouts in 60 seconds for both the cases with and without the adaptive stimulus noise generation while the robot's ego noise presents. The standard deviation decreases from 183.59 to 53.56 Hz when the adaptive stimulus is applied. (The discrete frequency bin size is 69.72 Hz). A demonstration of the effectiveness of this scheme can be seen in the video attachment (address in the next section), in which the realtime sensor readouts and the change of stimulus volume are visualized.

VI. APPLICATION IN ROBOTICS: OBJECT CONTOUR TRACKING

The embedded sensor design eliminates the robot arm's motion constraints caused by the external cables and electronics, and thus broadens the sensor's applicability. It also makes it feasible to put one sensor in each of the PR2 robot's fingers. This enables differential distance measurements, and thus allows the robot to orientate its fingertup towards the surface of the object. Using this capability, we present an object contour tracking as an application example to demonstrate the capabilities of the sensor. Two sensors are installed on the same robotic gripper, and the difference between the two sensor readings are used to compute the orientation of the fingertip with respect to the object. Three objects with different material properties are tested: mug (non-conductive material), glass cup (transparent material), and a stainless pot (highly reflective material). The objects are those the previous electric-field and optical pretouch sensors have trouble to sense. These examples demonstrate the PR2 collecting local geometric information enabled by the pretouch sensors, and allows the robot gripper to successfully follow the contour of the objects even if they are transparent or highly reflective.

VII. CONCLUSIONS AND FUTURE WORK

A. Conclusions

This paper demonstrated a novel acoustic pretouch sensor inspired by the well-known seashell effect. As far as we know, this effect has not previously been used to build proximity sensors. We characterize the frequency shift of the sensor at different object distance, and the effect of ambient noise on the sensor performance, including the noise level and spectral content. A stimulus consisting of band-limited white noise with frequency content in the sensor's working frequency range is most effective, compared with a broadband stimulus, or random ambient sound. An automatic adaptive stimulus noise compensation scheme, which detects the current ambient sound condition and provides additional band-limited whitnoise, was proposed to maintain a consistent SNR in the spectrum, and thus achieve the good performance of the sensor invariant to the ambient sound.

The fully-integrated sensor into the robot grippers makes it feasible to put one sensor in each of the PR2 robots fingers for differential distance measurement, and thus enables the object contour tracking application. Compared to to conventional sonar based on time of flight measurements, the technique we presented based on incoherent peak following has a number of practical benefits: (1) The sound stimulus source can be located anywhere—it does not have to be close to the sound receiver, which is an advantage for sensor integration into devices; (2) careful/short-interval time measurements are not required, and (3) our scheme should not be affected by multi-path effects commonly seen when using time of flight sonar methods.

B. Future Work

More applications using the proposed sensor systems are working in progress. For example, the sensor can be integrated with the existing microphones in a mobile phone as a proximity sensor to trigger the lock of the touch screen when the objects (human ears) are close to the microphone to prevent touching the screen by mistake while speaking (current mobile phones use an dedicated light sensor for that purpose).

REFERENCES

[1] J. R. Smith, E. Garcia, R. Wistort, and G. Krishnamoorthy, "Electric field imaging pretouch for robotic graspers," in IEEE/RSJ International Conference on Intelligent Robots and Systems, 2007, pp. 676–683.

[2] R. Wistort and J. R. Smith, "Electric field servoing for robotic manipulation," in IEEE/RSJ International Conference on Intelligent Robots and Systems, 2008, pp. 494–499.

[3] B. Mayton, L. LeGrand, and J. R. Smith, "An electric field pretouch system for grasping and co-manipulation," in IEEE International Conference on Robotics and Automation, 2010, pp. 831–838.

[4] K. Hsiao, P. Nangeroni, M. Huber, A. Saxena, and A. Y. Ng, "Reactive grasping using optical proximity sensors," in IEEE International Conference on Robotics and Automation, 2009, pp. 2098–2105.

[5] L.-T. Jiang and J. R. Smith, "Seashell effect pretouch sensing for robotic grasping," in IEEE International Conference on Robotics and Automation, 2012, pp. 2851–2858.

[6] L.-T. Jiang and J. R. Smith, "A unified framework for grasping and shape acquisition via pretouch sensing," in IEEE International Conference on Robotics and Automation, 2013.

[7] L. Arapan, E. Anderas, I. Katardjiev, and V. Yantchev, "Sensitivity features of thin film plate acoustic wave resonators," IEEE Sensors Journal, 2011, vol. 11, no. 12, pp. 3330–3331.

[8] H. Zhang and E. Kim, "Micromachined acoustic resonant mass sensor," Journal of Microelectromechanical Systems, 2005, vol. 14, no. 4, pp. 699–706.

[9] H. Zhang, M. Marma, S.Bahl, E. Kim, and C. McKenna, "Sequence specic label-free dna sensing using film-bulk-acoustic-resonators," IEEE Sensors Journal, 2007, vol. 7, no. 12, pp. 1587–1588.

[10] J. W. Coltman, "Differentiating sonar reflections from corners and planes by employing an intelligent sensor," Journal of the Acoustical Society of America, 1978, vol. 65, pp. 499–506.

[11] L. V. King, "On the electrical and acoustic conductivities of cylindrical tubes bounded by infinite flanges," Journal of the Acoustical Society of America, 1936, vol. 21, pp. 128–144.

[12] H. Levine and J. Schwinger, "On the radiation of sound from an unflanged circular pipe," Physical Review, 1948, vol. 73, pp. 383–406.

[13] A. R. D. Silva, P. H. Mareze, and A. Lenzi, "Approximate expressions for the reflection coefficient of ducts terminated by circular flanges," Journal of Brazil Society of Mechenical Science and Engineering, 2012, vol. 34, no. 2, pp. 219–224.

[14] J.-P. Dalmont, C. Nederveen, and N. Joly, "Radiation impedance of tubes with different flanges: Numerical and experimental investigations," Journal of Sound and Vibration, 2001, vol. 244, no. 3, pp. 505–534.

[15] D. T. Blackstock, Fundamentals of Physical Acoustics, 1st ed., Wiley-Interscience, 2000.

 ISBN: 978-1-61208-297-4

Carrier Photogeneration During UV-Vis Irradiation on Horizontal and Vertical Metal-Semiconductor Structures Based on Rutile-Phase TiO_2 Nanoparticles

Joel Molina, Carlos Zuniga, Edmundo Gutierrez
Electronics Department,
National Institute of Astrophysics, Optics and Electronics
Santa Maria Tonantzintla, Puebla, Mexico
E-mails: jmolina@inaoep.mx, czuniga@inaoep.mx, edmundo@inaoep.mx

Eunice Mendoza, Jose Luis Sanchez, Erick R. Bandala
Energy and Environment Research Group,
Universidad de las Americas, Puebla
San Andres Cholula, Puebla, Mexico
E-mails: edith.mendozaco@udlap.mx, jluis.sanchez@udlap.mx, erick.bandala@udlap.mx

***Abstract*—In this work, rutile-phase TiO_2 nanoparticles (np-TiO_2) are embedded within a Spin-On Glass oxide matrix (using a simple and economic Sol-Gel method) and the final TiO_2/SiO_2 mixture is directly deposited on stripes of aluminum so that the electronic, physical, chemical and photocatalytic characteristics of the final dielectric structure are obtained and correlated when irradiated with UV-Vis light sources. The I-V characteristics of this simple structure present a reduction in its total resistance when irradiated with UV light (compared to dark conditions), thus revealing a very simple photoresistor with relatively-low quantum efficiency.**

Keywords-TiO_2; nanoparticles; photoresistor; UV light; photogeneration; sol-gel processing; metal-semiconductor.

I. INTRODUCTION

Even though rutile-phase TiO_2 is considered as a very inefficient material in terms of its photocatalytic activity (ability for carrier photogeneration) [1-2], the use and development of this semiconductor material is quite important since the synthesis of TiO_2 usually produces a rutile phase quite easily, with relatively low concentration of impurities and also, economically. On the other hand, the synthesis of anatase-phase TiO_2 is more complicated, usually involving complex chemistry and/or doping with some metal or non-metal elements in order to increase its photocatalytic activity when exposed to UV or visible irradiation [3-6]. Also, using TiO_2 nanoparticles instead of dense TiO_2 thin films is useful in order to increase the contact surface area so that a higher density of photogenerated carriers is expected.

In this work, we embed rutile-phase TiO_2 nanoparticles (np-TiO_2) within an organic SiO_2 matrix and the final mixture of this dielectric structure is deposited on a thin film of aluminum. The final "horizontal" metal-semiconductor structure is then electrically characterized under dark and light conditions (I-V-light) so that the total resistance of a simple aluminum stripe is measured and correlated before and after UV irradiation. Compared to dark conditions, excess carriers are photogenerated within the TiO_2 nanoparticles after light exposure and they are directly transferred to both ends of the aluminum stripe after applying a low potential difference. The highest density of photogenerated carriers is obtained when the $TiO_2/SiO_2/Al$ is irradiated with UV-B light so that the total aluminum resistance is reduced by about 43%. Therefore, this initial device acts like a very simple "photoresistor". Additionally, we also fabricate so-called "vertical" metal-semiconductor-metal structures in order to obtain a solar energy conversion device with the intrinsic ability to self-store must of the converted energy in the form of a rechargeable capacitor. This device then acts like a very simple "photocapacitor" [7-8]. The *state-of-the-art* regarding these latest structures makes use of complex layered structures going from photo-rechargeable textiles for wearable power supplies [9], up to dye-sensitized solar cells (DSSC) connected in series with Li-ion batteries, metal oxides and/or TiO_2 nanotube arrays in order to increase energy conversion efficiency [10-12]. However, because of increasing fabrication complexity and use of a third additional electrode (in order to switch between the functions of energy conversion, storage and output) which consumes extra energy and increase cost of fabrication, a simpler two-electrode device is needed and that requirement is met by our proposed device structures.

This paper is arranged as follows: in Section I, we gave an introduction about the importance of testing simple "horizontal" and "vertical" metal-semiconductor structures which make use of TiO_2 nanoparticles in order to promote energy conversion in "photoresistor" and "photocapacitor" devices. Section II presents the experimental conditions used for fabrication of these structures as well as details about the measurement setup that is used for their physical and photo-electrical characterization. Section III presents and discusses the main experimental results that are found for these structures, thus confirming the ability of np-TiO_2 to act as photocatalytic material for both energy conversion and storage. Finally the main conclusions drawn from all results are highlighted in Section IV, from which we state that it is possible to use the "vertical" structure as a photocapacitor, thus enabling direct storage of solar energy.

II. EXPERIMENTAL

A. *Preparation of Thin FilmsBased on np-TiO_2*

We have used low-organic content or silicate-type spin-on glass (SOG)-based SiO_2 (700B from Filmtronics, Corp.) as a matrix for immobilization of np-TiO_2 (Dupont, R-706 with 93% purity and having an average diameter of 360 nm before embedding). Initially, specific amounts of commercial

 ISBN: 978-1-61208-297-4

np-TiO_2 are suspended in deionized water by hydrolyzing this TiO_2:H_2O mixture in a hot water bath (*baine marie*, 45°C, 30 min) and then, adding SOG-based SiO_2 so that the final TiO_2:SiO_2:H_2O mixture is again subjected to a final hot water bath (*baine marie*, 80°C, 1 hr) in order to obtain an homogeneous suspension. The concentration ratios of TiO_2 (solute) to SiO_2:H_2O (solvent) are 200, 100, 50 and 10 mg/mL and these solutions are labeled as A, B, C and D respectively. The solute concentrations were measured with an analytical balance AG285 from Mettler-Toledo. The final TiO_2:SiO_2:H_2O solutions were directly applied on the surface of clean glass slides (Corning glass 2947, size of 75 mm X 25mm), that were previously metalized with aluminum stripes, and sequentially spinned first at 3000 rpm, 30 sec, and then 4000 rpm, 15 sec in order to obtain uniform layers of np-TiO_2 embedded in SiO_2. After spinning, all films (A-D) were baked for 2 hours using a hot plate at 250°C in N_2 flow (99.99% purity) in order to evaporate mostly water and some of the organic solvents present in the SOG-based SiO_2 matrix. For FTIR characterization, the same processing sequence was followed and the final solution was applied on prime-grade P-type silicon wafers (100) with resistivity of 5–10 Ω·cm in order to eliminate most of the organic and impurity elements present within the Corning glass slides. In order to fabricate "vertical" structures, an additional ultra thin film layer of Titanium (100 Angstroms) is directly deposited atop the already described "horizontal" structures by E-beam evaporation under ultra high vacuum conditions (10^{-7} Torr) and with a very slow deposition rate of 1 Å/sec. Given the ultra low thermal budget required for fabrication of these simple structures, their introduction into large area flexible substrates is expected, thus promoting wide spread use of optimized devices. The fabrication process flows for both structures are briefly summarized, as shown in Fig. 1.

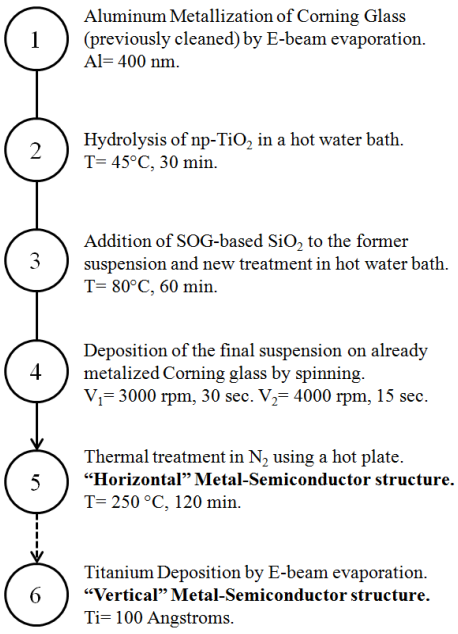

Figure 1. Process flow for fabrication of "horizontal" and "vertical" Metal-Semiconductor structures using np-TiO_2 as photoactive material.

It is important to notice that we did not chemically synthesize the np-TiO_2 used for fabrication of the proposed structures. Instead, we decided to use readily available commercial np-TiO_2 (with rather low purity of 93% and large average diameter of 360 nm) in order to test the ability of this material for carrier photogeneration under light irradiation.

B. Characterization of Materials and Aluminum-Stripes

DLS measurements (Nanotrac Wave, from Microtrac) [13] were done in order to determine the final size distribution of TiO_2 nanoparticles after the embedding process. By using DLS measurement technique, we are able to determine both the size and size distribution profile of TiO_2 nanoparticles in the final suspension before deposition on the glass surfaces. In particular, the size distribution profile for np-TiO_2 is obtained with high accuracy by this system (close to 100% signal intensity), thus giving a direct estimation of the homogeneity of the pn-TiO_2 in the final suspension. Also, thicknesses for all films were measured by profilometry (DEKTAK, V200-SI) after partially etching the TiO_2/SiO_2 film using a strong acid solution composed of diluted HF (HF:H_2O with 1:2 ratio). The crystalline phases of the resulting TiO_2-based films were obtained after XRD measurements using an X-ray diffractometer (Empyrean, from PANalytical), with a scanning step of 0.02°, using Cu-K_α radiation with λ= 1.5406 Å as an X-ray source. The band-gap energies Eg of the resulting films were calculated using optical transmittance data measured with an UV-Vis absorption spectrometer (LAMBDA 3B with double beam from Perkin Elmer, with Corning glass used as substrate) and the Tauc method [14]. Chemical compositional analyses for all films were obtained by FTIR spectrum measurements in absorbance mode with a Bruker Vector-22 system after 5 min of purge in N_2. The samples were measured against crystalline silicon substrate or SOG based silicon dioxide on glass (both were used as references). Finally, the I-V-light characteristics for the Al-stripes (covered with the TiO_2/SiO_2 structure) were obtained using an HP4156B semiconductor parameter analyzer at 300 K.

III. RESULTS AND DISCUSSION

A. Structure's Schematics and Energy Band Diagrams

Fig. 2 shows the 3-D and top view schematics for the first np-TiO_2/SiO_2 structure deposited on Aluminum/Glass. Because of the preparation method (previously discussed), we promote a uniform distribution of the np-TiO_2 within the oxide matrix so that these nanoparticles should have almost the same diameter size and separation in between as well. The aluminum stripes are 18X3 mm^2 in area with thickness of 400 nm. Fig. 3 shows the idealized energy-band diagrams for TiO_2 and TiO_2/SiO_2/Al systems during photogeneration of carriers after irradiation with energies $h\nu \geq Eg(TiO_2)$. In the first band diagram, all physical mechanisms during light irradiation, (1) excitation, (2) relaxation and (3) diffusion are also shown while a small potential difference is developed in the second diagram so that carriers are injected in the metal.

 ISBN: 978-1-61208-297-4

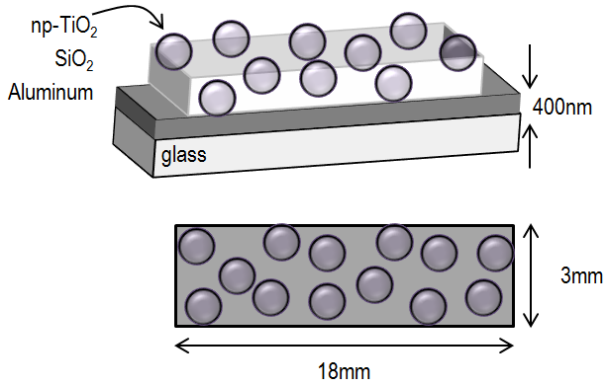

Figure 2. 3D and top views for np-TiO_2/SiO_2 deposited on Aluminum/Glass.

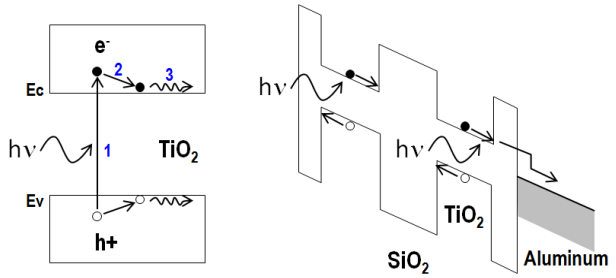

Figure 3. Idealized energy-band diagrams for TiO_2, TiO_2/SiO_2/Al systems.

B. *Dynamic Light Scattering (DLS) and Profilometry*

Fig. 4 shows the averaged particle size for TiO_2 before and after sonication. The dotted arrow shows the nominal average diameter as stated by the manufacturer ~360 nm.

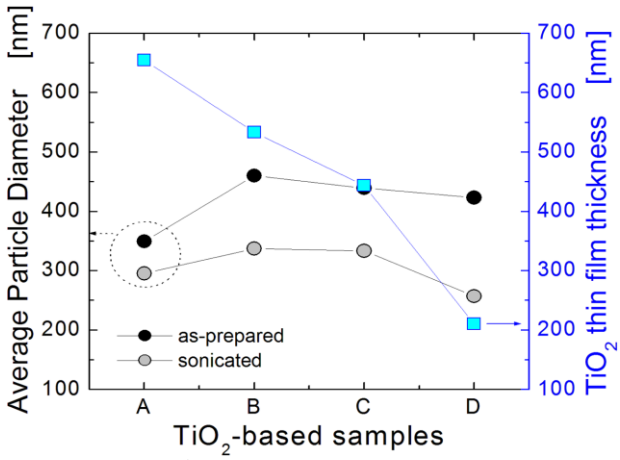

Figure 4. DLS and profilometry data showing the nanoparticle diameter size (before and after sonication) and TiO_2/SiO_2 thin film thickness respectively.

The as-prepared samples present larger particle diameter because of their tendency to agglomerate or aggregate after dispersion and settling within a liquid solution. During bath ultrasonication, dispersion of TiO_2 agglomerates is promoted by overcoming their weaker attractive forces, the final result being smaller np-TiO_2 diameters. The average physical size for sonicated np-TiO_2 is ~300 nm. Fig. 4 also shows the final np-TiO_2/SiO_2 film thickness after spinning deposition and thermal treatment of the prepared suspensions. We notice that thicker np-TiO_2/SiO_2 films are obtained for the more concentrated solutions as expected.

C. *X-Ray Diffraction (XRD)*

Fig. 5 shows the XRD diffraction patterns for all thin films including sample 0 (only SOG-based SiO_2 on glass).

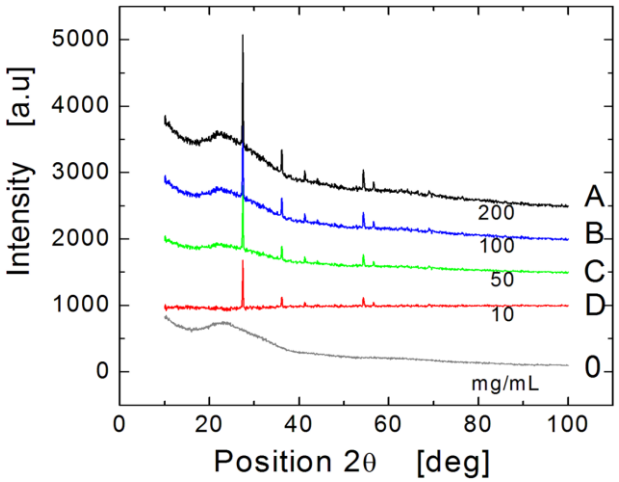

Figure 5. XRD data show existence of rutile phase for TiO_2 nanoparticles.

Samples A-B clearly present the characteristic sharp diffraction peaks for rutile phase TiO_2 including the broad amorphous phase from both the SiO_2 matrix and the glass slide (used for np-TiO_2 immobilization and as mechanical support respectively). Given the relatively high concentration density of np-TiO_2 embedded within the SiO_2 matrix for the A-B samples, it is clear that sharper diffraction peaks will be obtained possibly because of nanoparticles' agglomeration. This effect could be triggered during spinning, which make use of high speed centrifugal forces during step 4 of the process flow; see Fig. 1.

D. *Fourier-Transformed InfraRed (FTIR) Spectroscopy*

Fig. 6 shows typical chemical-bond vibration energies in absorption mode, found in samples A-D for all the range of interest (wavenumbers from 4000 down to 400 cm^{-1}).

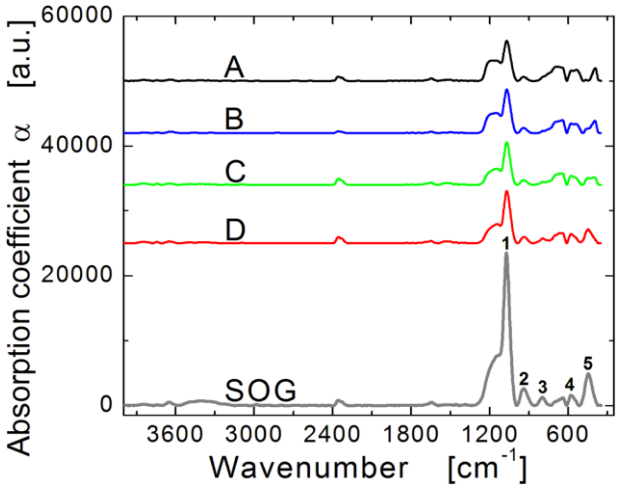

Figure 6. IR spectra (absorbance mode) of TiO_2/SiO_2/glass samples (A-D).

The IR spectra for SOG-based SiO_2 is also included and whose absorption peaks for the Si-O bonds are detected at 1070, 943, 801, 570, and 443 cm^{-1} (peaks 1-5). In order to analyze only the contribution of TiO_2 in the films, the IR spectra of A-D samples must be obtained using only the SOG-based oxide film as reference (SiO_2/glass) at wavenumber between 1600 and 400 cm^{-1} approximately (data in preparation). This way, we are able to eliminate the influence of the highly absorbent peaks related to Si-O bonds (especially those found at 1070 and 443 cm^{-1}).

E. UV-Vis Transmittance Spectroscopy

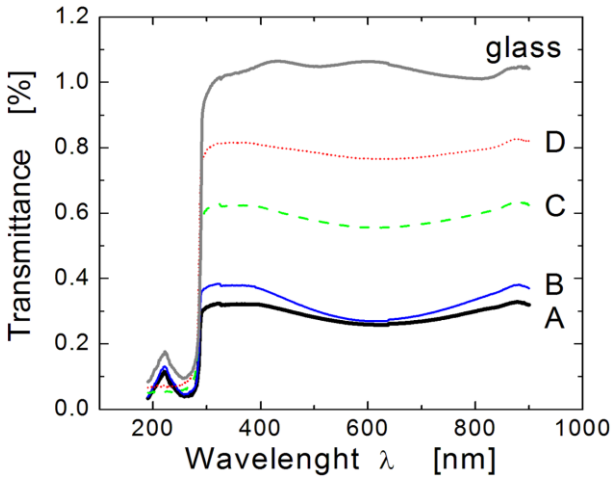

Figure 7. UV-Vis spectra (transmittance) of TiO_2/SiO_2/glass samples (A-D).

Fig. 7 shows the UV-Vis spectra from 190 up to 900 nm region for different np-TiO_2 concentrations (A-D samples), including the spectrum for only the glass substrate. It can be seen that strong absorption occurs at wavelengths λ<290 nm (UV-B regime) for all samples and that transmittance is reduced in direct proportion to the np-TiO_2 concentration as expected. Even though the physical thicknesses for all samples are different (see fig. 4), minimum variations in their optical band gap are expected if we consider different densities for these films. The calculated optical band gap Eg for all A-D samples is at 3.11-3.12 eV. This band gap energy Eg corresponds well with the reported Eg for anatase or rutile TiO_2, between 3.0 and 3.2 eV respectively [15].

F. I-V-Light Characterization

Fig. 8 shows the I-V-Light characteristics of the structure shown previously in fig. 2 (A sample only). Dark, sunlight, sunlight+lamp and UV-B light (~300 nm) conditions were all applied on top of the structures so that surface np-TiO_2 were the first to absorb all possible irradiation coming from these sources. Compared to dark conditions, photogeneration of excess carriers (both electrons and holes) within the TiO_2 nanoparticles is greater after UV-B light exposure and these carriers are directly transferred to both ends of the Al-stripe after applying a low potential difference. During UV-B light irradiation, the total aluminum resistance is reduced by about 43% which represent a moderate change in resistance given by rather low quantum efficiency presented by this structure.

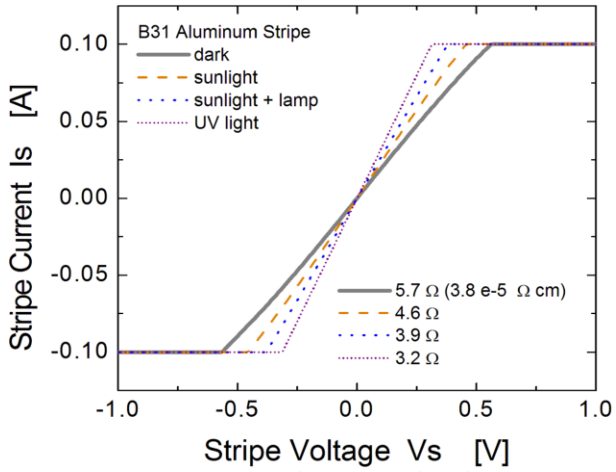

Figure 8. I-V-Light characteristics of Al-stripes before/after light irradiation.

G. Vertical Ti/np-TiO_2/SiO_2/Al/Glass Structure

Previously, I-V-Light characterization for horizontal structures produced a moderate photogeneration of carriers so that the total resistance of an aluminum strip was reduced. However, given that some of the photogenerated carriers will be trapped, recombined or "*lost*" within the SiO_2 matrix or at its interface with np-TiO_2 (any annihilation mechanism), the "*horizontal path*" followed by carriers in the initial structure would reduce their lifetime once they are photogenerated in the np-TiO_2. In order to increase photocarrier lifetime before recombination and thus, increase quantum efficiency during UV-B irradiation, vertical structures are proposed, see fig. 9.

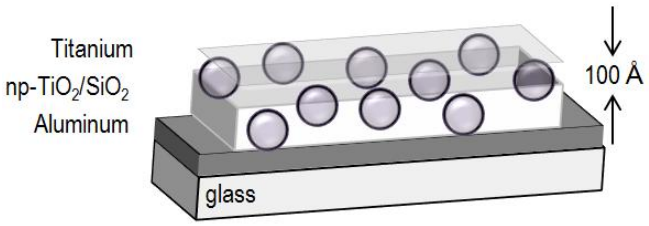

Figure 9. 3D view for a vertical Ti/np-TiO_2/SiO_2/Al/Glass structure where the titanium electrode is 100 Å in thickness, thus being optically transparent.

These vertical structures use Titanium as a gate electrode (only 100 Å in thickness) so that a capacitor in the form of a Metal-Insulator-Metal (MIM) structure is formed. Because of the ultra-thin titanium layer, this gate electrode is highly transparent to all UV-Vis irradiation so that when all carriers are being photogenerated, a vertical transition of these carriers between bottom/top electrodes (by an applied external electric field) would require a shorter distance thus increasing their lifetime before recombination as compared to the horizontal structures. In short, these vertical structures should be able to photogenerate carriers more efficiently and, in contrast with the photoresistor previously described, this MIM structure should be quite similar in function to that of a so-called "photocapacitor" [7-8], where all carriers could be efficiently stored within the dielectric itself right after photogeneration. Thus, a light-driven self-charging capacitor having an efficient storage mechanism of solar energy could

 ISBN: 978-1-61208-297-4

be obtained. The fabrication and testing of this final device is already going on and all results will be soon presented.

IV. CONCLUSIONS

Photocarrier generation during UV-B exposure of rutile-phase np-TiO_2 (embedded within a SiO_2 matrix) in a horizontal np-TiO_2/SiO_2/Al/Glass structure enables a reduction of the total resistance of an aluminum stripe by about 43%. These structures can be fabricated using simple and economic processing techniques, so that immobilization of TiO_2 nanoparticles in a suitable organic matrix for photocarrier generation can be also implemented in vertical Ti/np-TiO_2/SiO_2/Al/Glass MIM structures for more efficient generation of carriers. The vertical structure would act as a photocapacitor, thus enabling direct storage of solar energy.

ACKNOWLEDGMENT

This work was fully supported by the National Council of Science and Technology (CONACyT-Mexico).

REFERENCES

[1] Z. Ding, G.Q. Lu, and P.F Greenfield, "Role of the Crystallite Phase of TiO_2 in Heterogeneous Photocatalysis for Phenol Oxidation In Water", J. Phys. Chem. B, vol. 104, April 2000, pp. 4815-4820.

[2] T.A. Kandiel, R. Dillert, A. Feldhoff, and D. Bahnemann, "Direct Synthesis of Photocatalytically Active Rutile TiO_2 Nanorods Partly Decorated with Anatase Nanoparticles", J. Phys. Chem., vol. 114, February 2010. Pp. 4909-4915.

[3] M.A. Behnajady, N. Modirshahla, M. Shokri, and B. Rad, "Enhancement of photocatalytic activity of TiO_2 nanoparticles by silver doping: photodeposition versus liquid impregnation methods", Global NEST Journal, vol. 10-1, 2008, pp. 1-7.

[4] D.H. Kim, D.K. Choi, S.J. Kim, and K.S. Lee, "The effect of phase type on photocatalytic activity in transition metal doped TiO_2 nanoparticles", Catalysis Communications, vol. 9, March 2008, pp. 654–657.

[5] C.D. Valentin, G. Pacchioni, and A. Selloni, "Origin of the different photoactivity of N-doped anatase and rutile TiO_2", Phys. ReV. B., vol. 70, August 2004, pp. 085116-1, 085116-4 (2004).

[6] O. Diwald, L. Thompson, E.G. Goralski, S.D. Walck, and J.T. Yates, "The Effect of Nitrogen Ion Implantation on the Photoactivity of TiO_2 Rutile Single Crystals", J. Phys. Chem. B, vol. 108, January 2004, pp. 52-57.

[7] T. Miyasaka and T.N. Murakami, "The photocapacitor: An efficient self-charging capacitor for direct storage of solar energy", Appl. Phys. Lett., vol. 85, October 2004, pp. 3932-3934.

[8] C.W. Lo, C. Li, and H. Jiang, "A photoelectrophysical capacitor with direct solar energy harvesting and storage capability", Optical MEMS and Nanophotonics (OPT MEMS), 2010 International Conference on, August 2010, pp. 65-66.

[9] T. Song and B. Sun, "Towards Photo-Rechargeable Textiles Integrating Power Conversion and Energy Storage Functions: Can We Kill Two Birds with One Stone?", ChemSusChem, vol. 6, January 2013, pp.408–410.

[10] X. Zhang, X. Huang, C. Li, and H. Jiang, "Dye-Sensitized Solar Cell with Energy Storage Function through PVDF/ZnO Nanocomposite Counter Electrode", Adv. Mater., June 2013, pp. 1-4.

[11] W. Guo, X. Xue, S. Wang, C. Lin, and Z.L. Wang, "An Integrated Power Pack of Dye-Sensitized Solar Cell and Li Battery Based on Double-Sided TiO_2 Nanotube Arrays", Nano Lett., vol. 12, no. 5, April 2012, pp. 2520–2523.

[12] M.S. Nuckowska, K. Grzejszczyk, P.J. Kulesza, L. Yang, N. Vlachopoulos, L. Häggman, E. Johansson, and A. Hagfeldt, "Integration of solid-state dye-sensitized solar cell with metal oxide charge storage material into photoelectrochemical capacitor", J. of Power Sources, vol. 234, no. 15, July 2013, pp. 91-99.

[13] "Microtrac: Total Solutions in Particle Characterization, NanotracWave", App Note, Microtrac. October 2012, pp. 1-4. http://www.microtrac.com/MTWP/wp-content/uploads/2012/10/Nanotrac-Wave-Temp-Brochure-Ver-9.pdf

[14] J. Tauc, "Optical properties and electronic structure of amorphous Ge and Si", MRS Bulletin, vol. 3, January 1968, pp. 37-46.

[15] J. Dharma and A. Pisal, "Simple method of measurement the band gap energy value of TiO_2 in the powder form using UV/Vis/NIR spectrometer", App Note, Perkin-Elmer Inc. January 2009, pp. 1-4.

 ISBN: 978-1-61208-297-4

Simple Interface Circuit for High-Resolution, Multichannel, Smart Temperature Sensing based on NTC Thermistors

[1, 2] Sergey Y. Yurish
[1] Technology Assistance BCNA 2010, S. L.
[2] International Frequency Sensors Association (IFSA), Barcelona, Spain
e-mail: SYurish@sensorsportal.com

[1, 3] Javier Cañete
[1] Technology Assistance BCNA 2010, S. L.
[3] Universitat Politècnica de Catalunya (UPC, Barcelona) Barcelona, Spain
e-mail: javier.canete@techassist2010.com

***Abstract*—A simple interface circuit for high-resolution, multichannel smart temperature sensing based on NTC thermistors is described in this paper. The circuit is based on the Universal Sensors and Transducers Interface integrated circuit designed by authors, which supplies three different interfacing modes for thermistors and has three popular digital serial interfaces. Such approach lets considerably reduce a time-to-market for various thermistor based sensor systems.**

Keywords-thermistor; universal sensors and transducers interface; temperature sensing

I. INTRODUCTION

Temperature is one of the most widely measured physical quantities in industrial, consumer, and computer applications. Measurement of temperature is critical in various modern portable electronic devices as notebooks, tablets and smart phones to monitoring and control battery and CPU temperatures and compensate oscillator drift. Accurate temperature measurements are also necessary in many other measurement systems such as different instrumentation applications and process control [1, 2].

The modern forecast of *MarketsandMarkets* analysts reports that the market size of temperature sensors in the year 2010 was $3.27 billion and is expected to reach $4.51 billion by 2016, at an estimated CAGR of 5.6 %. In terms of volume, 2.02 billion temperature sensors were shipped in the year 2010 and the number is expected to reach 3.54 billion by 2016, at an estimated CAGR of 10 % from 2011 to 2016 [3]. Due to improved sensitivity, temperature sensors are used in loads of applications such as petrochemicals, automotive segments, consumer electronics, computer peripherals, space applications, and industrial segment. There is a rise in demand for consumer electronic devices, which use microprocessors such as smartphones, media players, cameras and gaming devices that make use of temperature sensors ICs to a greater extent [3].

The most common sensors for measuring temperature are thermocouple, thermistors and resistance temperature detectors (RTDs). Fiber-optic sensors, IR sensors, quartz thermometers and ultrasonic thermometers, while more specialized, are growing in popularity for temperature measurements [4].

Thermistors (THERMally sensitive resISTORS) have a considerably higher sensitivity than other temperature sensors [5]. Thermistors have either a negative temperature coefficient (NTC), that is their resistance value goes down with and increase in the temperature, or a positive temperature coefficient (PTC), their resistance value goes up with an increase in temperature. NTC thermistors are used mainly for temperature sensing applications because they are more stable, while PTC thermistors are typically used for circuit protection applications and as heating elements in small temperature-controlled ovens [6]. NTC thermistors have found a wide application in temperature measurement and control in chemical, food and automobile industries, in measurement instruments, and medicine [7].

A main advantage of thermistors for temperature measurements in comparison with other popular temperature sensors is their extremely high sensitivity [8], for example, sensitivity of -100 $\Omega/^0$C in comparison with 0.4 $\Omega/^0$C for RTDs. It allows to detect miniature variations in temperature, which could not be observed with an RTD or thermocouple. Other advantages of thermistors are the following: low absolute error $\pm$ 0.05 ^{0}C; high resistance value from 30 Ω to 20 MΩ (at 25 ^{0}C); short response time due to low thermal mass; easier to wire (2-wire configuration); miniature size, and low cost [4, 8, 9].

The major tradeoff for these advantages is thermistor's highly nonlinear output and relatively limited operating range typically from - 55 ^{0}C to 300 ^{0}C depending on the type of thermistor. However, special high-temperature sensors, such as chromium oxide ceramic thermistors made by GE Sensing can operate up to 1000 ^{0}C [5].

Typical, average comparative characteristics for common temperature sensors are shown in Table 1.

When thermistors are used in temperature sensing, they must be connected to a corresponding measuring circuit. Very often, the measurement circuits are voltage dividers or bridge circuits. However, due to strongly, exponential type of the thermistor characteristic, a linearization must be used to make their application much easier [7].

With the increasing availability of integrated circuits, the demand for high resolution temperature measurement is now greater than ever [10] .There is no limit to the resolution of thermistors. The limitations are till now in the electronics needed to measure to a specific resolution. They also exist in determining the accuracy of the measurement at a specified resolution [11].

Formerly, the nonlinear resistance vs. temperature characteristic was problematic in analog sensing circuits [12]. Today, however, with the advent of digital and quasi-

 ISBN: 978-1-61208-297-4

digital electronic controls the linearization can be handled via equations in software or lookup tables. This paper is divided into four main parts. The first part contains state-of-the-art review of existing interfacing circuits for thermistors including integrated solutions, available on the modern market. The second part includes a design approach for thermistor sensing systems based on a Universal Sensors and Transducers Interface circuit (USTI). The third part devotes to experimental investigation of designed temperature multisensor system prototype based on the epoxy bead NTC thermistor S861 from EPCOS [13]. The last part of the paper provides conclusions and future research directions.

TABLE I. COMPARATIVE CHARACTERISTIS OF COMMON TEMPERATURE SENSORS

Characteristic	Thermocouple	Resistance Temperature Device (RTD)	NTC Thermistor	Semiconductor Temperature Sensors
Temperature range, ^{0}C	-184 ... +2 300	-200 ... +850	-55 ... +300	-55 ... + 150
Accuracy	< ± 2.2 ^{0}C or ± 0.75 %	< ± 1.9 %	Various, ± 0.05 ^{0}C to 5 ^{0}C	Various, ± 0.5 ^{0}C to 4 ^{0}C
Output Signal	μV	Ω	Ω	Analog (V), Digital (serial), Quasi-digital (frequency, period, PWM, duty-cycle)
Signal Conditioning	• Amplification • Filtering • Cold-Junction • Compensation	• Amplification • Filtering • Current Excitation	• Amplification • Filtering • Current Excitation	No necessary
Linearity	Fair	Excellent	Poor	Good
Precision	Fair	Excellent	Poor	Fair
Sensitivity	Low	Medium	Very High	High
Long-Term Stability	High	High	Low	Medium
Thermal Response Time	Medium to fast	Medium	Fast	Medium to fast
Self Heating	No	Low	High	High
Lead Effect	High	Medium	Low	Low
Cost	Low	High/Moderate	Low	Moderate
Size	Small to large	Medium to small	Small to medium	Small to medium

II. INTERFACING CIRCUITS FOR TERMISTORS: STATE-OF-THE-ART

The use of thermistors for temperature sensing requires some signal conditioning and interfacing hardware to produce an output for the further processing. Let consider main types of such interface circuits.

A. ADC based Thermistor Interfacing

The outputs of most linearizing circuits for thermistors are analog in nature and need to be converted to a digital form before being interfaced to digital instruments or DAQ systems. Digital processing capability (microcontrollers) is available now in many sensor systems at reasonable cost. In addition, such systems contain an excitation current or voltage source, amplifier, lowpass filter, analog multiplexer and high-resolution ADC [2, 14-18]. The temperature resolution in such systems, using tight tolerance thermistors and resistors can be in the order of ±0.01 ^{0}C [10, 14]. Nevertheless a high resolution and small absolute error ±0.3 ^{0}C [14] some such technical solutions are not suitable for multichannel temperature measurements [2, 14-16]; others - contain analog multiplexers [17], which introduce an additional error. In addition, such traditional analog design approach is not suitable for the further smart sensor system integration, especially for technological processes less than 100 nm [19, 20].

B. Temperature-to-Frequency (Period) Converter based Thermistor Interfacing

The use of both: PTC and NTC thermistors in resonant circuits to provide low frequency output is known from the end of 60's [21, 22]. The main advantage of a frequency output is that an ADC is not required. A frequency output is also useful in applications where the sensor conditioning circuitry is combined with a remote temperature sensor [23].

Thermistor interfacing linearization circuits with frequency output based on different kinds of multivibrators are described in [7, 24-26]. In these circuits, different degrees of linearity were obtained over limited ranges of temperatures (see Table 2). An improved converter based on an astable multivibrator with acceptable level of linearization over an increased temperature range 0-86 ^{0}C with sensitivity 21 Hz/ ^{0}C has been reported in [27].

A modified type of a relaxation-oscillator-based temperature-to-frequency converter has been implemented using a delay network and described in [28]. It exhibits linear input/output relation over the wide range -20 ... + 250 ^{0}C with a sensitivity of 14.7 Hz/ ^{0}C. The use of inverse exponential nature of the voltage-time relationship of a charging RC network based on a modified square wave pulse generator for thermistor characteristic linearization is reported in [29]. Although the experiment was done for a temperature range of 5 to 85 ^{0}C, the circuit has been designed for the extended temperature range of -100 to +225 ^{0}C with a sensitive of 9.6 Hz/^{0}C.

The linear temperature-to-frequency converters based on monostable multivibrator on the basis of integrated timer of 555 Series are described in [9, 30] for the temperature range of 270 to +370 ^{0}K with sensitivity of 10 Hz/^{0}K and 3 kHz output frequency corresponds to temperature of 300 ^{0}K [30]. In the circuit reported in [9], as the thermistor resistance varies from 198.3 to 551.2 kΩ, the period of the square wave varies from 22,542 to 61,671 μs.

A linear temperature-to-frequency converter using an integrable Colpitts oscillator is reported in [31] with

 ISBN: 978-1-61208-297-4

sensitivity of 59 Hz /^{0}C and residual nonlinearity less than 2.85 % over the temperature range of -20 to +60 ^{0}C and frequency output approximately from 3.2 to 8 kHz.

TABLE II. COMPARATIVE CHARACTERISTIS OF TEMPERATURE-TO-FREQUENCY CONVERTERS

No	Temperature Range	Sensitivity, Hz/ ^{0}C	Non-linear Error, %	Frequency Range, Hz	Ref.
1.	0... +86 ^{0}C	21	n/a	380...1000	[27]
2.	0...+100 ^{0}C	10	n/a	3000 at 300 ^{0}K	[30]
3.	-20...+250 ^{0}C	14.7	< 0.12	n/a	[28]
4.	-20... +60 ^{0}C	59	2.85	3000...8000 6000 at 298 ^{0}K	[31]
5.	0...+80 ^{0}C	10	< 0.2	2730...3530 3230 at 323 ^{0}K	[26]
6.	-100...225 ^{0}C	9.6	n/a	2745...3514 at +5...+85 ^{0}C	[29]
7.	0...+120 ^{0}C	n/a	< 1	1500...7000	[7]

A temperature-to-frequency/time converter based on the voltage-to-frequency (or time) converter with linearity better then 0.1 % per decade is described in [32].

In comparison with the analog output, the frequency output has many well known advantages [20] including easy optical or pulse-transformer isolation. As rule, all described above temperature-to-frequency converters based on thermistors are well suitable for remote temperature sensing and telemetry. But the problem to convert frequency-to-digital with appropriate resolution and accuracy is still actual.

III. THERMISTOR SENSING SYSTEM DESIGN

The designed universal thermistor based temperature-to-digital converter is based on the novel Universal Sensors and Transducers Interfacing (USTI) integrated circuit [20, 33], in which a three-signal measurement ramp rate method is used for conversion [20, 34, 35]. There are three possible modes for interfacing of thermistors with the USTI IC: resistive measuring mode; resistive bridge measuring mode and frequency measuring mode. Let to consider these methods in details.

A. Resistive Measuring Mode

In this measuring mode the offset, reference and measurand values are converted into three time intervals by internal resistive-to-time converter base on the internal comparator. The unknown resistance of thermistor should be calculated according to the following equation:

$$R_T = \frac{N_T - N_{off}}{N_{ref} - N_{off}} \cdot R_c \qquad (1)$$

where N_T, N_{off} and N_{ref} are the numbers of reference frequency pulses counted during the measurand, offset cancelation and reference measurement stages respectively; R_c is the precision reference resistor. The interfacing circuit for this mode is shown in Fig.1. Design considerations concerning selection of external components (R_0, R_c and C) and charging time are described in details in [20, 34].

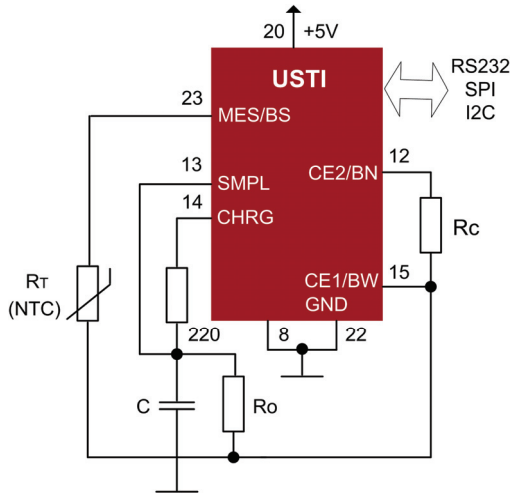

Figure 1. Thermistor interfacing in resistive measuring mode.

The USTI IC has three popular serial interfaces for connection to a master microcontroller, PC or DAQ system: RS232 (master and slave), SPI (slave) and I2C (slave). An example of commands for resistive measuring at SPI communication slave mode is shown in Fig.2.

```
<06><10>; Set up a resistance RT measurement mode
<0E><i><f>; Set the reference value Rc =3011 Ω*
<10><08>; Set the charging time 900 μs
<09>; Start measurement
<03>; Check result. This command returns "0" if the
      result is ready
<07>; Read conversion result in BCD format. Returns
      sign byte and 12 bytes of result in BCD code
* - command format:
<I5><I4><I3><I2><I1><I0><F0><F1><F2><F3><F4><F5>, where
<I5>…<I0> integer part of BCD number;
<F0>…<F5> fractional part of BCD number.
```

Figure 2. Commands for resistance conversion at I2C communication mode.

The further linearization can be handled via nonlinear equations in software (by a master microcontroller or PC) or lookup tables, containing the manufacturer's device characteristics. The custom designed USTI IC for temperature measurement based on thermistors (USTI-TEM) can make the linearization by itself.

B. Resistive Bridge Measuring Mode

Another method of interfacing thermistor to USTI IC is to use a Wheatstone bridge with the thermistor as one arm of the bridge (Fig.3), and the linearization can be made by three-point linearization technique. The selection of R1, R2 and R3 will determine the sensitivity of the circuit as well as the temperature range for which the circuit is best suited.

The resistive sensor bridge is considered as a resistor network with three inputs and one output [20, 35]. The resistance of each input to the output depends on the

measurand. Using each input to turn to charge/discharge a capacitor connected to the bridge output yields three different time intervals. For a full bridge, the ratio between the difference between two time intervals and the third time interval yields the fractional resistance change. This change x for each bridge arm can be obtained by the following way:

$$x = \frac{t_1 - t_3}{t_2} \qquad (2)$$

Design considerations concerning selection of charging time, R and C external components are described in [20, 35].

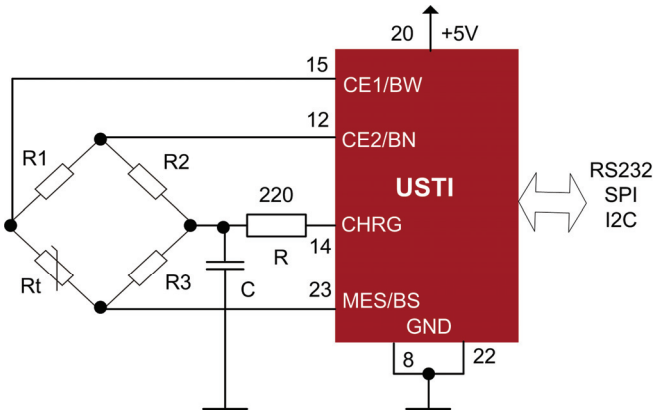

Figure 3. Thermistor interfacing in resistive bridge measuring mode.

An example of USTI's commands for resistance-bridge – to – digital conversion (I2C serial interface, slave mode) is shown in Fig. 4.

```
<06><12>; Set up a resistance-bridge Bx mode
<10><13>; Set the charging time, for example, 20 ms
<09>; Start measurement
<03>; Check result. This command returns "0" if the
      result is ready
<07>; Read conversion result in BCD format. Returns
      sign byte and 12 bytes of result in BCD code
```

Figure 4. Commands for resistive bridge conversion at I2C communication mode.

C. *Frequency Measuring Mode*

The designed universal thermistor based temperature-to-digital converter can work with any known thermistor based temperature–to–frequency (period) converters, described, for example, in [7, 9, 21-32]. In addition to thermistor or resistive bridge interfacing, two such converters can be connected directly to one USTI IC at the same time. The linearization can be made by a thermistor based temperature-to-frequency converter. A three-channel thermistors-based temperature sensing system is shown in Fig.5. Appropriate commands for frequency measurements are shown in Fig.6.

The number of channels can be easily increased by two ways: a time-division channeling method and space-division channeling method. The first one means the use of a digital multiplexer on one of the USTI's frequency input. The second one can be used in SPI and I2C slave communication modes, when appropriate number of USTI ICs is connected to a master microcontroller's bus.

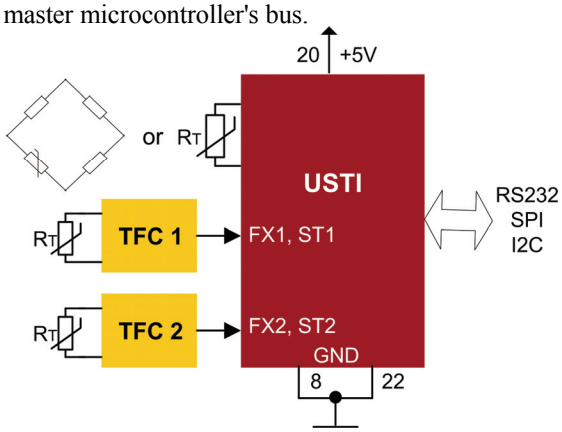

Figure 5. Thermistors interfacing frequency (period) measuring mode
(2 channels plus direct thermistor intefacing). TFC - thermistor based temperature-to-frequency converter.

```
<06><00>; Set up frequency mode in the 1st channel
<02><09>; Set up the relative error, 0.001 %
<09>; Start measurement
<03>; Check result. This command returns "0" if the
      result is ready
<07>; Read conversion result in BCD format
```

Figure 6. Commands for frequency measuremet at I2C communication mode.

IV. Experimental Results and Discussion

A thermistor-based temperature sensing systems consist of the USTI IC and miniature, epoxy resin encapsulated, bead-type thermistor S861 from EPCOS (Fig. 7). Such thermistor is available with the following tolerances: ± 1 %, ± 3 % and ± 5 %, and is suitable for different applications including heating systems, industrial and automotive electronics in -55 ^{0}C to +155 ^{0}C temperature range. It has a nominal resistance R_{25}= 10 kΩ.

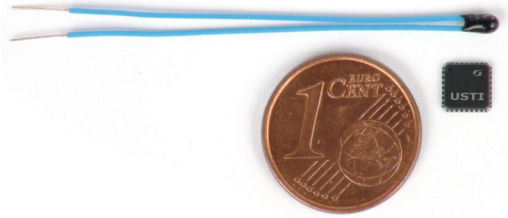

Figure 7. Thermistos S861 (EPCOS) and USTI IC in 5×5 mm MLF package - main components of temperature sensing systems.

The USTI has been preliminary calibrated in laboratory conditions at +23 ^{0}C temperature and 38 % relative humidity with the help of the Universal Counter 53132 A (Agilent). The calibration constant was Δ = 10002491.7979. The following nominals for external components have been selected based on design considerations, described in [33]: R_c= 3011 Ω, R_0=609.86 Ω and C_c = 434.62 nF. The thermistor's and external components' nominals have been

 ISBN: 978-1-61208-297-4

measured by the precise LCR meter Instek LCR-819 with basic accuracy ±0.05 % or better. The real temperature was measured by the true-rms multimeter Fluke 187. Charging time constant was T=956.2 μs, which corresponds to the selected 1 ms time.

The time diagrams on the CHRG USTI's input at +23 ^{0}C temperature measurement are shown in Fig. 8.

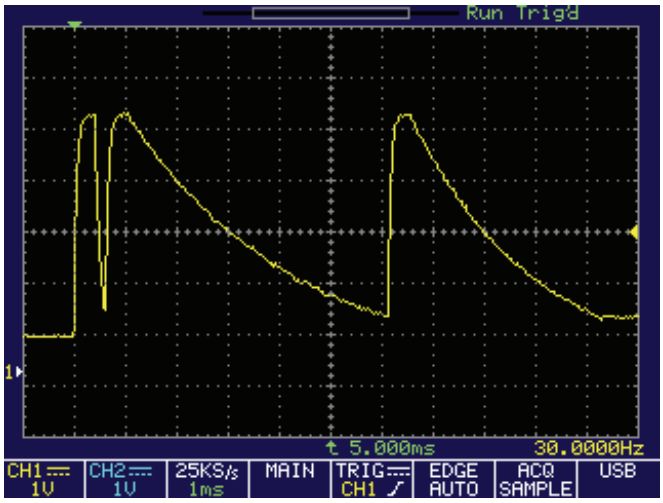

Figure 8. Oscillograms on the USTI's CHRG pin.

The measuring results and calculations based on the R/T thermistor's characteristics are shown in Table 3.

TABLE III. MEASURING AND CALCULATIONS RESULTS

T, ^{0}C	R_{nom}, Ω	R_{min}, Ω	R_{max}, Ω	Error, %	ΔT, ^{0}C	Rx aver, Ω
22	11418	11282	11553	1.2	0.3	-
23	10921	10797	11046	1.1	0.3	10713.84
24	10449	10335	10563	1.1	0.2	-

R_{nom}, R_{min}, R_{max}, Error % and ΔT are calculated parameters for NDT thermistor S861 (EPCOS); $R_{x\ aver}$ is the result of measurement at +23 ^{0}C.

The average resistance of thermistor was 10713.84 Ω, which corresponds to +23 ^{0}C ± 0.3 ^{0}C. It means, that the USTI does not introduce any additional error in the measuring channel, which necessary take into account.

When current flows through a thermistor, it generates heat, which raises the temperature of the thermistor above that of its environment. This of course will cause addition so-called self-heating error in measurement. Typically, the smaller the thermistor, the lower the amount of current needed to self-heat. Certain operating conditions can significantly increase such error, for example, a big number of serial measurements for the further statistical averaging. The increasing of thermistor's resistance due to self-heating effect during 100 serial measurements is shown in Fig. 9. This effect is more pronounced in still air. If the thermistor is located in moving air, liquids or solids, the self-heating error is much lower.

The USTI's error at thermistor's resistance-to-digital conversion has four components: the reference error ~10^{-4} % and three components for appropriate time interval measurements (Fig.8): 1) Time interval for offset cancellation stage; 2) Time interval for resistance reference measurement, and 3) Time interval for thermistor's resistance measurement. Taking into account that USTI measures time intervals with minimum possible relative error:

$$\delta_q = \frac{1}{f_0 \cdot t_x} \times 100\%, \qquad (3)$$

where f_0 = 20 MHz is the reference frequency; t_x is the unknown time interval, we get the following relative error for the mentioned time intervals: 0.025 %, 0.0042 % and 0.005 %. Taking into account that the sensor error is 1.1 %, and based on the rule of neglect of small components of error [36], all these components of the resulting error can be neglected.

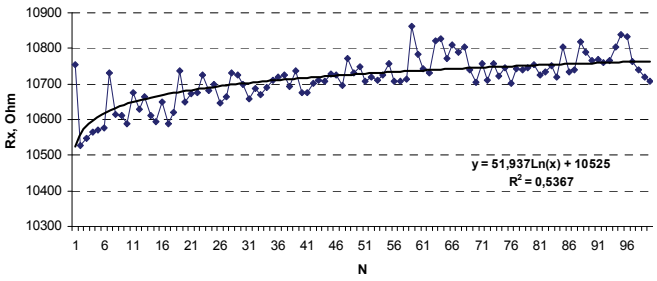

Figure 9. Therimistor's resistance increasing due to self-heating effect..

Let compare the USTI IC with other existing integrated converters for thermistors available. The ispPAC30-based thermistor interface circuit from Lattice Semiconductor offers higher level of integration in comparison with a traditional implementation, which has significantly higher component count [37]. But this converter has only an analog output and needs high-resolution ADC.

The MAX6682 IC converts an external thermistor's temperature-dependent resistance directly into digital form compatible with 3-wire SPI interface. This IC does not linearize the highly nonlinear transfer function of NTC thermistors, but it does provide linear output data over limited temperature ranges, for example, +10 ^{0}C to +40 ^{0}C and 0 ^{0}C to +70 ^{0}C [38].

The MAX6691 four-channel thermistor temperature-to-pulse-width converter measures the temperature of up to four thermistors and converts them to a series of output pulses whose widths are related to the thermistors' temperatures [39]. An external microcontroller must be used to measure accurately appropriate pulse width and pulse space.

The Universal Transducer Interface (UTI) provides interfacing for 1 kΩ - 25 kΩ thermistors and has a microcontroller-compatible period-modulated output [40]. The typical value of linearity is 13 bit.

The number of channels and available interfaces for all mentioned integrated converters for thermistors are shown in Table 4. Only USTI IC has three different, popular serial interfaces and can convert frequency, PWM and period input signals into digital, and support three various measuring

 ISBN: 978-1-61208-297-4

modes for thermistors: resistive, resistive bridge and frequency measuring modes.

TABLE IV. COMPARATIVE CHARACTERISTIS OF INTEGRATED CONVERTERS FOR THERMISTORS

IC	Number of Channels	Output
ispPAC30	1	Analog (V)
MAX6682	1	SPI
MAX6691	4	Pulse-width modulated
UTI	1	Period-modulated
USTI	3	SPI, I2C, RS232

V. CONCLUSIONS

The novel USTI IC designed by authors for multichannel smart temperature sensing system based on thermistors, supports various modes for thermistor interfacing: resistive measuring mode; resistive bridge measuring modes and can work with all existing thermistor based temperature-to-frequency (period, PWM) converters. It has three channels and three popular serial interfaces: RS232, SPI and I2C. The USTI's does not introduce any significant error into a measuring channel, and resulting error of the temperature sensor system is determined only by thermistor's error. Such design approach lets considerably reduce a time-to-market for various thermistor based sensor systems.

REFERENCES

[1] W. Kester, J. Bryant, W. Jung, Temparature Sensors, Analog Devices, 2003.

[2] A. O'Grady, "Building a More Perfect Union: Combining Thermistors and High-Resolution A/D Converters", Sensors Magazine, Vol.17, No.1, 2000.

[3] Temperature Sensor Market, A Study of major Sensor types (ICs, Thermostat, Thermistor, Resistive Temperature Detectors (RTDs), Thermocouple) & Applications, Global Forecast & Analysis 2011 – 2016, MarketsandMarkets, SE 1733, February 2013.

[4] How to Choose the Right Sensor for your Measurement System, Tutorial, National Instruments, July 2012.

[5] J. R. Gyorki, Designing with Thermistors, Design World, 10 March 2009.

[6] Temperature Measurements with Thermistors: How-To Guide, Tutorial, National Instruments, 10 January 2013.

[7] Z. P. Nenova and T. G. Nenov, "Linearization circuit of the thermistor connection", IEEE Transactions on Instrumentation and Measurement, Vol.58, No.2, February 2009, pp.441-449.

[8] D. Potter, Measuring Temperature with Thermistors - a Tutorial, Application Note 065, National Instruments, November 1996.

[9] J. Valvano, "Measuring temperature using thermistors", Circuit Cellar, August 2000, pp.1-6.

[10] P. Lyons and P. Waterworth, "The use of NTC thermistors as sensing devices for TEC controllers and temperature control integrated circuits", Temperature Products, Measurement Specialities, Inc., June 2003.

[11] NTC Termistor Design Guide for Discrete Components & Probes, Quality Thermistor, Inc., http://www.thermistor.com

[12] NTC Thermistor Applications, Spectrum Sensors & Controls, http://www.SpecSensors.com

[13] NTC Thermistors. General technical information, EPCOS, March 2006.

[14] N. M. Mohan, V. J. Kumar and P. Sankaran, "Linearizing Dual-Slope Digital Converter Suitable for a Thermistor", IEEE Transactions on Instrumentation and Measurement, Vol.60, No.5, May 2011, pp.1515-1521.

[15] D. H. Sheingold, Transducer Interfacing Handbook: A Guide to Analog Signal Conditioning, Analog Devices, Inc., 1980.

[16] J. Bishop, "Thermistor temperature transducer-to-ADC application", Analog Applications Journal, Texas Instruments, Inc., November 2000, pp.44-47.

[17] B. C. Baker, Temperature Sensing with a Programmable Gain Amplifier, AN867, Microchip Technology, Inc., 2003.

[18] Temperature Sensor Design Guide, Microchip Technology, Inc., 2004.

[19] S. Henzler, Time-to-Digital Converters, Springer, 2010.

[20] S. Y. Yurish, Digital Sensors and Sensor Systems: Practical Design, IFSA Publishing, 2011.

[21] K. Kraus, "Thermistors as circuit elements in low-frequency circuits", The Review of Scientific Instruments, Vol.39, No. 2, February 1968, pp.216-220.

[22] A. L. Reenstra, "A low-frequency oscillator using PTC and NTC thermistors", IEEE Transactions on Electron Devices, Vol. ED-16, No.6, June 1969, pp.544-554.

[23] Jim Lepkowski, Temperature Measurement Circuits for Emdedded Applications, AN929, Microchip, 2004.

[24] D. Stankovic and J. Elazar, "Thermistor multivibrator as the temperature-to-frequency converter and as a bridge for temperature measurement", IEEE Transacton on Instrumentation and Measurement, Vol. 1M-26, No.1. March 1977, pp. 41-46.

[25] M. Ikeuchi, T. Furukawa and G. Matsumoto, "A linear temperature-to-frequency converter", IEEE Transactions on Instrumentation and Measurement, Vol. IM-24, No.3, September 1975, pp. 233-235.

[26] O. I. Mohamed, T. Takaoka and K. Watanabe, "A simple linear temperature-to-Frequency Converter using a thermistor", The Transactions of the IEICE, Vol. E 70, No.8, August 1987, pp. 775-778.

[27] A. A. Khan and R. Sengupta, "A linear temperature-to-frequency converter using a thermistor", IEEE Transactions on Instrumentation and Measurement, Vol. IM-30, No.4, December 1981, pp.296-299.

[28] A. A. Khan and R. Sengupta, "A linear thermistor-based temperature-to-frequency converter using a delay network", IEEE Transactions on Instrumentation and Measurement, Vol. IM-34, No.1, March 1985, pp.85-86.

[29] R. N. Sengupta, "A widely linear temperature to frequency converter using a thermistor in a Pulse Generator", IEEE Transactions on Instrumentation and Measurement, Vol.37, No.1, March 1988, pp.62-65.

[30] B. Sundqvist, "Simple, wide-range, linear temperature-to-frequency converters using standard thermistors", J.Phys. E: Sci. Instrum., Vol.16, 1983, pp.261-264.

[31] W. S. Chung and K. Watanabe, "A linear temperature-to-frequency converter using an integrable Colpitts Oscillator", IEEE Transactions on Instrumentation and Measurement, Vol.IM-34, No. 4, December 1985, pp.534-537.

[32] D. K. Stankovic, "Temperature-to-frequency/time converson by means of thermistors", Letters to The Editor, IEEE Transactions on Industrial Electronics and Control Instrumentation, August 1974, p. 204.

[33] Universal Sensors and Transducers Interface (USTI) Specification and Application Note, Technology Assistance BCNA 2010, S. L.

[34] S. Y. Yurish, Universal Resistance-to-Digital Converter, in Proceedings of the 2nd International Conference on Advances

 ISBN: 978-1-61208-297-4

in Circuits, Electronics and Microelectronics (CENICS' 2009), Sliema, Malta, 11-16 October 2009, pp.28-33.

[35] S. Y. Yurish, "A simple and universal resistive-bridge sensors interface", Sensors & Transducers, Vol. 10, Special Issue, February 2010, pp.46-59.

[36] P.V. Novitskiy, I.A. Zograf, Error Estimation of Measuring Results, Energoatomizdat, Leningrad, 1991 (in Russian).

[37] ispaPAC30-Based Thermistor Interface Circuit, Application Note AN6032, April 2002, Lattice Semiconductor.

[38] MAX6683 Thermistor-to-Digital Converter, Maxim, 2002.

[39] MAX6691 Four-Channel Thermistor Temperature-to-Pulse-Width Converter, Maxim, 2002.

[40] Universal Transducer Interface (UTI), Datasheet, Smartec, 30 November 2010.

 ISBN: 978-1-61208-297-4

Lab-on-Phone: A Laboratory-on-Phone System

Jorge Mario Garzón Rey, Juan Manuel Soto Valencia, Fredy Segura-Quijano
Departamento de Ingeniería Eléctrica y Electrónica
Centro de Microelectrónica (CMUA) - Universidad de los Andes
Bogotá D.C., Colombia
Email:{jm.garzon131, jm.soto569, fsegura}@uniandes.edu.co

***Abstract*—This paper presents a novel approach defined as "*Lab-on-Phone*" which is a new "*Dielectric Footprint Measure*" platform, specially for food quality control with storage and administration processes over the Internet. It can also be used for other types of products making minimal changes. A small acquisition device, with an inter-digitized capacitor sensor sends measurements to a smartphone via Near Field Communication (NFC) protocol. An Android application installed on the smartphone displays these measurements in a graph and sends them to a web server via Wi-Fi or cellphone network. For example, Lab-on-Phone allows users to know on site the food quality, and to companies, to have a quality control sensor network with a data base and a web server.**

Keywords*—*Near Field Communication (NFC); measurement platform; wireless measure; data acquisition; food quality control; ultralow power sensors; wireless sensors

I. INTRODUCTION

Near Field Communication (NFC) technology, is a wireless communication technology in the frequency range of 13.56 MHz. NFC can be used to transmit information between two NFC devices, to read/write a Radio Frequency IDentification (RFID) card or tag, or to both simulate them [1]. One of the main features of NFC technology is the less than 100 ms set up time, and there is no necessity of pairing. NFC have a communication range of 10 cm and a maximum data rate is 424 kbps.

There is a wide field of applications for the NFC technology in the fields of transport and payment; however, there are a lot of other applications involving NFC technology. American Thermal Instruments created an NFC tag capable of measuring temperature. The tag is read by an NFC-enabled phone with the LOG-IC Mobile App. The application allows monitoring the temperature anywhere and exporting data immediately to anyone via email or can be uploaded to the cloud. It also shows a report of temperatures measured including charts and graphs. The main goal, according to the manufacturer, is to be able to protect critical shipments all the way down to the last mile [2]. A final example of the wide range of NFC applications is SleepTrak, a combo device-application that uses an armband to track symptoms associated with inefficient sleep (recording how active you are during sleep, for example). The armband is read via NFC the next morning, and the app analyzes the data and provides suggestions for better sleep habits [3].

There are a lot of other examples showing that NFC technology is expanding all over the world. According to recent reports from Juniper Research about forecasts for the global NFC market, global NFC retail transaction values are expected to reach $110 bn in 2017 [4]; mobile NFC metro tickets are going to be used by 1 of 8 mobile users in the US and Western Europe by 2016 [5]; and 1 in 4 mobile users in the same region will pay in-store using NFC by 2017 [6]. An analysis made by Frost & Sullivan states that 53 % of phones are going to be NFC-enabled by 2015 [7]. London buses have added NFC technology to their card readers for a contactless payments with debit or credit cards. With a agreements between the bus system and the software industry will be possible to pay a bus ticket with a NFC-enable smartphone [8].

NFC will step smartphones to a new level of interaction and functionality, and will give the users the possibility to use its phones almost in every action that involves money, registration, identification, verification and much more other applications so that practically the only thing they will be carrying in their pockets will be the phone. For example, Google created the concept of an electronic wallet in which all credit and debit cards information are linked to the user Google account and can be accessed at anytime through a computer or a smart phone with Android OS and Google Wallet application. With Google Wallet users can use their NFC-enabled phones as a contactless payment card [9].

In the field of microsensors, there are a great variety and classifications. An alternative is the case of capacitive sensors, which can have a planar geometry based on parallel plates or inter-digitized plates. In this article inter-digitized capacitive sensors are described; they can be useful for measuring changes in the dielectric constant due to contact of any material with the sensor surface.

Inter-digitized electrode capacitive sensors have been used in numerous applications such as soil, grain, and paper moisture content monitoring; rain detection, proximity sensors, touch switches and biomedical sensors. Implementations have been made with several technologies and materials including sensors with printed circuit board technology [10]. The electrode overlapping area or the relative permittivity of the dielectric in the vicinity of the electrodes can be sensed by monitoring the changes in the structures capacitance [11].

Several investigations reported advances in the area of sensors, but left out the area of instrumentation. Most of the works that measure changes in capacitance use sophisticated equipment such as LCR-821 meter, impedance analyzer or similar, that are very expensive, bulky and complex to be used due to their variety of functions. This means that it is important to implement small systems with low cost even if

 ISBN: 978-1-61208-297-4

they are designed for a reduced set of applications.

Having described the NFC protocol characteristics and the advantages and applications of capacitive sensors, this paper aims to develop a generic platform, which can be used in the field in a comfortable and complete way. This platform allows to take measurements with a capacitive sensor and communicate the results to a mobile device, such as a smartphone via NFC protocol. In the mobile platform, the measured data or historical data can be displayed and can be sent to a web server via Wireless Fidelity (Wi-Fi) protocol or General Packet Radio Service (GPRS), allowing multiple people to view the measurements for analysis and perform tracing procedures, almost in real time from any computer with Internet access.

There are previous studies about NFC implantable Medical Devices, which show that NFC technology can be used for data and power transmission to implantable devices without any health consequence [12]. For wireless measurement devices, NFC provides a noninvasive communication interface to smartphones in order to take advantage of their computation capacity and communication flexibility. For example, a generic NFC-enabled Measurement System for remote monitoring is described in [13]. This is a beneficial solution for low-power data acquisition in portable devices [14]. In the case of passive or semi-passive sensors, it is possible to use a batteryless acquisition system by feeding it with the power from the carrier signal of the NFC connection [15].

NFC-enabled phones provide long range Global System for Mobile Communications (GSM) and General Packet Radio Service (GPRS), services that can be used to establish a remote monitoring. Lab-on-Phone advantage is a novel portable platform of Dielectric Footprint Measure for food quality control providing storage and administration over the Internet, it is a small acquisition device with the size of a credit card, with a capacitor sensor that sends measurements to smartphones via NFC protocol. An Android application installed on the smartphone sends sensors information to a web server via Wi-Fi or cellphone network. Lab-on-Phone allows users to get to know on site the food quality, and companies to have a quality control sensor network with a data base and a web server.

In the next section, there will be a description of the system architecture and functionality. In Section III, early results are presented for a system validation based on commercial boards. Finally, Section IV summarizes the presented approach and future works.

II. Lab-on-Phone System Architecture

Figure 1 shows Lab-on-Phone system architecture, including a full chain of acquisition, processing, storage and analysis infrastructure. Lab-on-Phone is itself a multiuser and multipurpose system. The first layer of the system is based on a Measure Card, which is a small acquisition device, the size of a credit card, with a capacitor sensor. The Measure Card is enabled to send measurements to a smartphone via NFC protocol. An Android application installed on the smartphone processes the sensor measurements and gives an on-site result to the user. If the device has a data plan or Wi-Fi access, the measurements are send to a web server through this medium. The web server stores the measurements information from multiple smartphones and controls privacy. Lab-on-Phone also include a set of web applications, which allow accessing data from everywhere and any platform with Internet access.

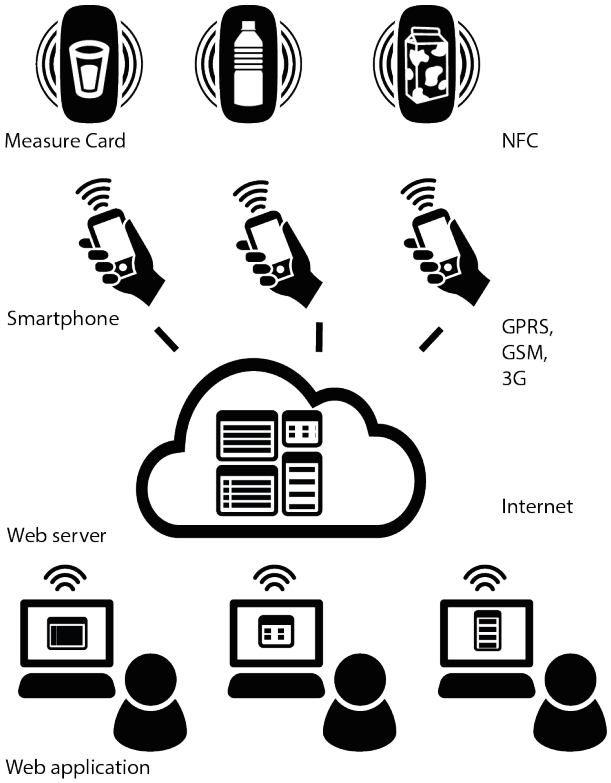

Fig. 1. System Architecture Diagram Block.

The Lab-on-Phone system helps people to have certainty about the quality of the product they buy and will also helps companies to avoid loses. For example, in Latin America, it is common to find adulterated liquors sold as original and there is not an onsite platform to ensure both consumers and authorities about the liquor quality. Although, this paper proposes Lab-on-Phone platform for food quality control; the tool can also be used to find out about the quality of almost any product for final consumers. The governments may take advantage of Lab-on-Phone to detect adulterated liquors suppliers or to have a record of the quality of food and beverages people are having.

A. Measure Card: acquisition system and sensor

The Measure Card is basically a small board with an Interdigitated Capacitor Sensor which sends measurements to a smartphone via NFC technology. An Interdigitated Capacitor Sensor can detect conductivity and dielectric constant of fluids. This type of sensor has a low-cost fabrication process and can be easily integrated with other sensing components. A low power microprocessor reads the sensor using a single slope Analog-to-Digital Converter (ADC) strategy. In other words, the microprocessor measures the discharger time of

 ISBN: 978-1-61208-297-4

the Interdigitated capacitor. The measurement data is stored in a Dual Interface Electrically Erasable Programmable Read-Only Memory (EEPROM - M24LR16E), which is accessed by the microcontroller via Inter-Integrated Circuit (I2C) protocol. This EEPROM memory can also be accessed via NFC communication.

The Measure Card may have an LC sensor, which is a planar coil with an Interdigitated Capacitor, which uses the same strategy of detecting the conductivity and dielectric constant of fluids but it needs a different read strategy based on a self-resonant frequency, meaning the sensor may be wireless. These type of sensor is also inexpensive; so, it can be disposable as well.

The harvesting strategy is possible having a wireless powering via the carrier signal of the NFC technology, this way the proposed Measure Card is a low cost board with Interdigitated Capacitor and it could be batteryless or wireless powering.

The Measure Card implementation uses M24LR16E-A [16], which consist of a dual interface EEPROM connected to an I2C bus and a 20 mm x 40 mm 13.56 MHz etched Radio Frequency (RF) antenna (Figure 2). The integrated circuit (IC) can be feed with the RF energy field of the external device or with an external 1.8 to 5.5 Volts power source. The chip comes with the option of Energy Harvesting; so, the unused energy in the connection and in the command transmission in RF mode can be used to feed another electronic component like a Light-Emitting Diode (LED) or an IC. The RF interface works with the ISO 15693 protocol allowing an NFC device to be able to communicate with it. The minimum data rate is 6.62 kbits/s and the maximum is 52.97 kBits/s.

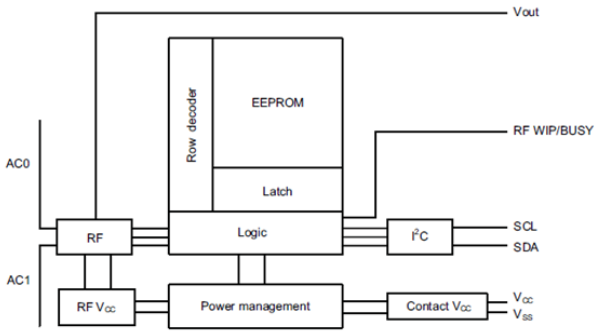

Fig. 2. M24LR16E-A Diagram Block [16]. In the middle can be seen the EEPROM component that can be accessed by an NFC device (left block) or a microcontroller by I2C protocol (right block).

In the Figure 3, the memory area set up is shown. The memory can be divided into the storing area and the configuration area.

The storing area is divided into 16 sectors of 32 blocks of 32 bits. Each sector can be read/write protected in RF or I2C modes with the corresponding Sector Security Status 5-bit registry or the Write Lock_bit registry respectively. In the configuration area, the passwords for read/write protection, the tag identifiers (UID, DSFID, AFI) and the configuration byte are stored.

Sector	Area	Sector security status
0	1 Kbit EEPROM sector	5 bits
1	1 Kbit EEPROM sector	5 bits
2	1 Kbit EEPROM sector	5 bits
3	1 Kbit EEPROM sector	5 bits
12	1 Kbit EEPROM sector	5 bits
13	1 Kbit EEPROM sector	5 bits
14	1 Kbit EEPROM sector	5 bits
15	1 Kbit EEPROM sector	5 bits
	I²C password	System
	RF password 1	System
	RF password 2	System
	RF password 3	System
	8-bit DSFID	System
	8-bit AFI	System
	64-bit UID	System
	8-bit configuration	System
	16-bit I²C Write Lock_bit	System
	80-bit SSS	System

Fig. 3. M24LR16E-A Memory Structure. The registers above represent the data memory divided in sectors. Each one can be write/read protected by its corresponding Sector Security Status (SSS) that can be set in the configuration area (bottom registers).

B. Comunication interfaces

NFC Forum is the world association that established all the set of specifications related with NFC Technology. The set of specifications includes the definition of the NFC Data Exchange Format (NDEF) [17], which defines a format for the exchange of information between NFC applications. There are also defined Record Type Definitions (RTD) that specify the types of the data that can be sent in a NDEF message. The Simple NDEF Exchange Protocol (SNEP) [18] is a high level protocol defined by the NFC Forum for the exchange of NDEF messages between applications. The SNEP works above the Logical Link Control Protocol (LLCP), which defines the way data transmission is made through the physical medium. The LLCP [19] allows two packets transmission modes (Payload Data Units - PDUs): connection-oriented and connectionless. Connection-oriented transport provides a data transmission service with sequenced and guaranteed delivery of service data units unlike connectionless transport, which provides an unacknowledged data transmission service with minimum protocol complexity. NFC Forum has created also specifications for four different tags types.

NFC devices can operate with RFID technologies like ISO/IEC 14443 (Type A and B) used by Mifare Type A (NXP smartcard technology), Calypso (European Cards) or EMV (Europay, Mastercard or Visa cards) cards; JIS6319-4 used by Felica Cards (Sony Smartcard System); ISO15693 used by RFID cards with a range up to 1.5 meters, obviously this will be reduced if the card is read with NFC technology; or ISODEP 14443-4 which is a transmission protocol used in proximity cards used for identification.

The dual interface Memory M24LR16E-A uses ISO15693 standard [16] which allows communication with more than one tag at the same time, but it is not going to be a common

 ISBN: 978-1-61208-297-4

stage of our application. The protocol defines the structure of the requests made by the RFID device, as shown in Figure 4.

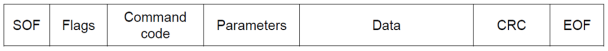

Fig. 4. ISO15693 Request Format.

The first field is the Start Of Frame (SOF), which indicates to the tag, the beginning of a new command. The 8-bit Request_ flags field indicates the tag features of the command and the communication like subcarrier mode, data rate or mode selection. The 8-bit command code field indicates the command to be executed on the tag as well. The parameters, data fields length and information depend on the command to be executed. The next field contains the Cyclic Redundancy Check 16-bit (CRC-16-bit) value, of the previous fields (without the SOF) for content verification at the reception. Finally, there is an End Of Frame (EOF) which indicates the tag the end of the request.

As in the previous case, the response starts and ends with an SOF and EOF frames respectively. The 8-bit Response_ flags field indicates if there was an error, if this is the case, the error information is given in the 8-bit parameters field. The data field carries information related to the request made by the RF device. Next to it, there is a 16-bit CRC for content verification at the RF device. In the Figure 5, the response format the tag sends to the RF device is shown.

Fig. 5. ISO15693 Response Format.

This protocol has defined a lot of commands for reading or writing individual or multiple blocks in the storing area and the configuration area. The main commands used in the application were the following: Read Single Block, Write Single Block, Get system Info, Write sector password, Present sector password, ReadCfg (for reading the configuration byte), WriteEHCfg (for writing the Energy Harvesting configuration), ReadEHCfg (for reading the Energy Harvesting configuration) and WriteDOCfg (for writing the configuration byte).

Data tag acquisition is included with any device with Android OS and NFC technology. The Android OS provides an API for NFC access from the applications [20]. When an NFC tag comes close to the RF radio of the NFC hardware, the operating system automatically parses it and notifies applications designed to manage NFC tags related to it. The API is specifically designed for operations with NFC tags; however, it also has support for other RFID protocols including ISO 15693. For this protocol, the API provides the following methods:

- close() Disable I/O operations to the tag from this TagTechnology object, and release resources.
- connect() Enable I/O operations to the tag from this TagTechnology object.
- get(Tag tag) Get an instance of NfcV for the given tag.
- getDsfId() Return the DSF ID bytes from tag discovery.
- getMaxTransceiveLength() Return the maximum number of bytes that can be sent with transceive(byte[]).
- getResponseFlags() Return the Response Flag bytes from tag discovery.
- getTag() Get the Tag object backing this TagTechnology object.
- isConnected() Helper to indicate if I/O operations should be possible.
- transceive(byte[] data) Send raw NFC-V commands to the tag and receive the response.

After the operating system notifies the application that an ISO 15693 tag has been discovered, the application connects to the tag via the connect() method and start sending commands via transceive() method which receives as input argument the command going to be sent as an array of bytes. This method returns the response given by the tag, after executing the request. For the development of the application, a library with all the commands in the ISO15693 protocol was built.

For sending information through the network the org.apache.http [21] packet available in the Android Development Environment was used. This packet provides the core interfaces and classes of the HTTP components, and deal with the fundamental requirements for using the HTTP protocol, such as representing a message including its headers and optional entity. In order to prepare messages before sending or after receiving them, there are interceptors for requests and responses. The more important classes for communication with a server are HTTPClient, HTTPPost, and HTTPGet. HTTPClient encapsulate a smorgasbord of objects required to execute HTTP requests while handling cookies, authentication, connection management, and other features. HTTPPost can be used to request that the origin server accept the entity enclosed in the request as a new subordinate of the resource identified by the Request-URI in the Request-Line. HttpGet is used to retrieve whatever information (in the form of an entity) is identified by the Request-URI.

In the application, after receiving the data of the measure from the tag an HTTP post request is created with this information. Then the request is executed via an HTTPClient, which sends it to the Internet Protocol (IP) server via internet. Access to the internet can be made via Wi-Fi or a mobile network (GPRS, GSM, 3G, 4G); in that case, if the smartphone has a data plan, the measurements can be sent to the server from anywhere with a mobile network access and can be tracked from any computer with internet almost in real-time. The measure information taken from the tag is stored in a Java Script Object Notation (JSON) object, and then put as an entity in the http request. JSON is a useful format for storing name-value pairs of any type. If the application does not have an available connection to the internet; then the applications waits until it is available to send it to the server.

 ISBN: 978-1-61208-297-4

C. Data storage, information processing

The information acquired from the sensor is stored in any type of external memory (SD Card typically, by default) or in the internal memory, if there is no external memory or if the user opts to store it there. Android provides a very practical set of functions to manage this process. On the other hand, the information send to the server via HTTPPost method is processed in the server side by a PHP algorithm and stored in a MySql database. The database can be viewed from a web page stored in the web server (the same with the PHP code).

D. User interfaces and applications

The platform has two types of user. The first user or field user is the one with the sensor and the phone in the field or site where the measurement is taken. The user puts the card with the sensor in the direct solution or surface where the measurement is desired to be made. Then the user must approach the phone to the sensor. When the phone approaches close enough for NFC communication, the application pop-ups automatically and begin to acquire the measurements from the sensor. The data transmission stops as soon as the user takes away the phone from the card. When the application receives a measurement, it append the actual phone's time and date, the exact position taken from the gps if available, or the approximate position from the local network, and the phone id (which must be registered in the server database). The Android application allows that the user visualize the data in a chart.

The other type of user is the one monitoring the measurements from the web application. It allows visualizing data in the database to different field users and also sending notifications to them. When a user sends data to the server via HTTPPost, it performs a user-password validation before storing data in the database. The web application can only be accessed by registered users.

III. Results

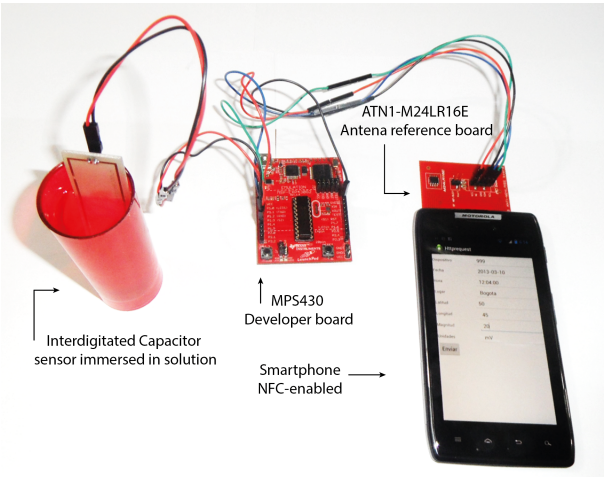

Fig. 6. Implemented acquisition system. From left to right we show the sensor (Interdigitated capacitance) immersed in a solution, a microcontroller and a dual interface EEPROM which is below the phone.

Figure 6 shows the implemented acquisition system using an ANT1-M24LR16E antenna STMicroelectronics reference board, including a MSP430G2553 on a LaunchPab board from Texas Instruments. The Interdigitated Capacitor Sensors was designed and manufactured on the Printed Circuits Board laboratory at Universidad de los Andes.

The Android Application was developed for Android 4.0.3 Version (Ice Cream Sandwich) and tested in a Sony Xperia Sola with the same version of OS, NFC technology, GPS, Wi-Fi, GSM, HSDPA, EDGE, GPRS, Dual-core 1 GHz Cortex-A9 and 512MB of RAM.

For the web server and the database, a LAMP Server was installed in an Ubuntu Server 12.04.1. The apache version of the web server is 2.2.22. The MySql version is 5.5.29. Figure 7 shows an example of web application screenshot where we can observe of measurements sent from the android application, after reading the card via Wi-Fi and 3G. The web application was programmed to update its information every 30 seconds; in no case the transmission overlaped this time, which showed monitoring the measurements made by field users can performed almost instantly.

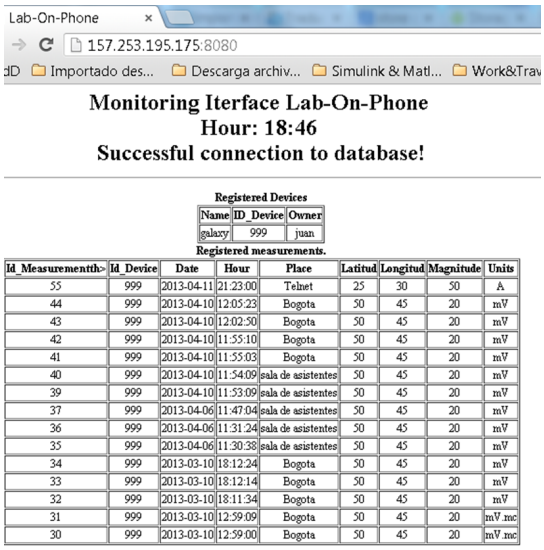

Fig. 7. Web application interface. The measurements send by the phone with information of the place, time, date and device identification are showed in a table. There is also a table showing the registered devices that are allowed to send data to the server.

To validated de implementation we used ethanol (99 %), methanol (99 %) and a traditional Colombian Liqueur (Ethanol 27%) . The sensor was previously characterized using an impedance analyzer HP4194A in order to identify the solutions.

Finally, all the proposed system was tested. For this validation, the acquisition system measure capacitance sensor discharge time. As Table I shows, the system was able to determinate a difference between discharge time for each alcohol. The proposed system was able to successfully identify and differentiate each alcohol.

 ISBN: 978-1-61208-297-4

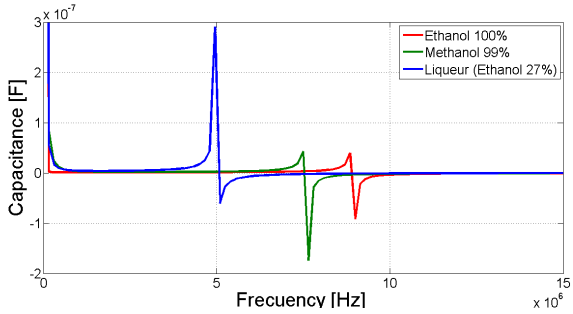

Fig. 8. Capacitance Measurements. The capacitance has a unique peak in a different frequency for each one of the solutions.

TABLE I
DISCHARGE TIMES

Alcohol	Discharge Time [ms]
Ethanol	64 ± 0.5
Colombian Liqueur	69 ± 0.5
Methanol	72 ± 0.5

IV. CONCLUSION AND FUTURE WORKS

This paper presented a novel approach defined as "Lab-on-Phone", that is a new "Dielectric Footprint Measure" platform, specially for food quality control with storage and administration over the Internet. The platform uses the principle of inter-digitized capacitors as the sensor element. For the measurement with the sensor, the system uses the same energy generated by the device NFC component reading card.

The entire measurement chain has been tested in all its phases, including the sensor measurement, data adquision with NFC communication, the mobile application, sending data to the cloud and the application on the server.

The present work does not focus on the development of sensors, but in the development of a novel platform taking advantage of the smartphone benefits.

The stage was developed with NFC commercial kits. As future work, we propose the development of a smaller card that integrates a sensor capacitive coupling, a low-power microcontroller for acquisition and processing, and a dual interface memory that can be accessed by the microcontroller and NFC device. We also propose the use of other types of sensors, such as LC resonators.

ACKNOWLEDGMENT

The authors would like to acknowledge the CleanRoom Laboratory and Printed Circuits Board Manufacturer Laboratory staff at Universidad de los Andes for their support.

REFERENCES

[1] K. Finkenzeller, "RFID Handbook. Fundamentals and Applications in Contactless Smart Cards, Radio Frequency Identification and Near Field Communication," 2010.

[2] A. T. Instruments. Nfc logger. Retrieved: July, 2013. [Online]. Available: http://www.americanthermal.com/products/log-ic/products/nfc/nfc-logger

[3] S. Clark. Sleeptrak nfc sleep monitoring service goes live. NFCworld. Retrieved: July, 2013. [Online]. Available: http://www.nfcworld.com/2011/10/03/310431/sleeptrak-nfc-sleep-monitoring-service-goes-live/

[4] W. Holden. Mobile nfc growth forecast scaled back to 110bn in transactions by 2017 as iphone 5 omits chipset. Juniper Research. Retrieved: July, 2013. [Online]. Available: http://www.juniperresearch.com/viewpressrelease.php?pr=353

[5] D. Snow. Mobile nfc metro tickets to be used by 1 in 8 mobile users in the us and western europe by 2016. Juniper Research. Retrieved: July, 2013. [Online]. Available: http://www.juniperresearch.com/viewpressrelease.php?pr=288

[6] W. Holden. More than 1 in 4 mobile users in the us and western europe will pay in-store using nfc by 2017. Juniper Research. Retrieved: July, 2013. [Online]. Available: http://www.juniperresearch.com/viewpressrelease.php?pr=315

[7] D. Murphy. 53 per cent of phones nfc-enabled by 2015. Mobile Marketing Magazine. Retrieved: July, 2013. [Online]. Available: http://mobilemarketingmagazine.com/content/53-cent-phones-nfc-enabled-2015-says-frost

[8] S. Shead. Nfc is just the ticket for london buses as payments go contactless. ZDNet. Retrieved: July, 2013. [Online]. Available: http://www.zdnet.com/uk/nfc-is-just-the-ticket-for-london-buses-as-payments-go-contactless-/7000008739/

[9] Google. Google wallet. Retrieved: July, 2013. [Online]. Available: http://www.google.com/wallet/index.html

[10] F. Segura-Quijano, J. F. Osma, E. A. Unigarro, and D. A. Sanz, "Low cost wireless passive microsensors for the detection of hazardous," *Sensors and Actuators B*, vol. 178, pp. 26–33, 2013.

[11] D. J. Elton, Z. Hartzog, J. Richard, M. E. Baginski, A. K. Rane, and R. N. Dean, "A capacitive fringing field sensor design for moisture measurement based on printed circuit board technology," *IEEE Transactions on Instrumentation and Measurement*, vol. 61-4, pp. 1105–1112, 2012.

[12] E. Freudenthal, D. Herrera, F. Kautz, C. Natividad, A. Ogrey, J. Sipla, A. Sosa, C. Betancourt, and L. Estevez, "Suitability of nfc for medical device communication and power delivery," in *Engineering in Medicine and Biology Workshop, 2007 IEEE Dallas*, 2007, pp. 51–54.

[13] C. Opperman and G. Hancke, "A generic nfc-enabled measurement system for remote monitoring and control of client-side equipment," in *Near Field Communication (NFC), 2011 3rd International Workshop on*, 2011, pp. 44–49.

[14] O. C.A. and G. Hancke, "Using nfc-enabled phones for remote data acquisition and digital control," in *AFRICON, 2011*, 2011, pp. 1–6.

[15] H. Mika, H. Mikko, and Y.-o. Arto, "Practical implementations of passive and semi-passive nfc enabled sensors," in *Near Field Communication, 2009. NFC '09. First International Workshop on*, 2009, pp. 69–74.

[16] *M24LR16E-R DataSheet. 16-bit EEPROM with password protection, dual interface and energy harvesting: 400 kHz I2C bus and ISO 15693 RF protocol at 13.56 MHz*, 2012.

[17] *NFC Data Exchange Format (NDEF) Technical Specification. NFC ForumTM. NDEF 1.0. NFCForum-TS-NDEF 1.0.*, 2006-07-24.

[18] *Simple NDEF Exchange Protocol Technical Specification. NFC ForumTM. SNEP 1.0. NFCForum-TS-SNEP 1.0*, 2011-08-31.

[19] *Logical Control Link Protocol Technical Specification. NFCForumTM. LLCP 1.1. NFCForum-TS-LLCP 1.1*, 2011-06-20.

[20] Android. Near field communication. Google. Retrieved: July, 2013. [Online]. Available: http://developer.android.com/guide/topics/connectivity/nfc/index.html

[21] T. A. S. Foundation. Httpcomponents. Retrieved: July, 2013. [Online]. Available: http://hc.apache.org/

 ISBN: 978-1-61208-297-4

A New SAW Device Simulator Based on Mason's Equivalent Circuit Model

Aina Heritiana Rasolomboahanginjatovo, Frédéric Domingue, Adel-Omar Dahmane
Département de Génie Electrique et Génie Informatique
Université du Québec à Trois-Rivières
3351, Boul. des Forges, Trois-Rivières, Québec, Canada
rasolomb@uqtr.ca, frederic.domingue@uqtr.ca, adel-omar.dahmane@uqtr.ca

***Abstract*—This paper presents a new simulator capable of frequency and time domain simulations for surface acoustic wave devices such as surface acoustic wave resonators and reflective delay lines. Developed within Matlab and based on the equations of Mason's equivalent circuit model, the proposed simulator allows considerable reduction in simulation durations and does not require high computational resources as existing finite element model tools. It is flexible and reliable. Made up of only six files totalizing 40 kilobytes in size, the simulator can be launched on any computer running Matlab.**

Keywords-surface acoustic wave; resonator; delay line; frequency domain; time domain.

I. INTRODUCTION

Surface Acoustic Wave (SAW) devices have revolutionized the domain of telecommunications by the possibility to design compact and low cost filters [1]. They are widely used as electronic filters, resonators, delay lines, correlators, convolvers or wireless identification systems integrated into modern communication systems. The evolution of telecommunications standards and requirements, especially for low-loss Radio Frequency (RF) filters used in mobile phones, led to the development of high performance SAW devices, which require flexible, precise and efficient models and simulation tools [2].

Several models including the impulse model, the Equivalent Circuit Models (ECM) [3], the Coupling of Modes (COM) model [4], and the matrix models [5] have been proposed for SAW devices. However, only the ECM, the COM approach and the P-matrix model have been developed to maturity [6]. For its part, the impulse model is not reliable. Indeed, it does not take into account second order effects such as propagation losses, reflections and dispersions.

On the other hand, some Finite Element Model (FEM) tools; e.g., COMSOL [7], Coventor [8], ANSYS HFSS [9]; provide 3D view and 3D simulation for SAW devices. However, the higher the number of fingers is, the longer the simulation duration is, and the higher the required computational resources are. Designers are then faced with a challenge to find a compromise allowing them to reduce the computational complexity of the desired FEM simulation. An alternative consists of implementing the ECM into computer tools such as Ansoft, Spice or ADS. But, again, the same problem can occur when the number of fingers is high.

Despite that, the ECMs are particularly efficient for modeling the interaction between the electrical and non-electrical components of SAW devices. The analogies between the electrical and mechanical elements are described by W.P. Mason in [10]. The ECM for one pair of fingers he proposed is presented in [11]. As SAW devices are generally composed of several periodic sections; each section consists of a pair of fingers; Mason's ECM can be easily applied.

From Mason's ECM equations, it is possible to build, with Matlab, functions that compute the S-parameters of each section, set up the links between sections, and then compute the S-parameters of the entire simulated device. Since most of the computations can be modeled by matrix operations, using Matlab should reduce simulation duration. Therefore, this paper presents a new SAW device simulator based on this approach. The simulator has been implemented into a Matlab program to reduce the required computational power.

The paper is organized as follows: Sections II and III describe the operating principle and the design of the proposed simulator. The reliability of the simulation results is demonstrated in Section IV. Section V highlights the main advantages provided by the simulator.

II. MASON'S ECM AND PROPOSED SIMULATOR

A. *Mason's ECM*

SAW resonators and delay lines are composed of three main components, to wit IDTs (InterDigital Transducers), reflectors, and propagation paths. Each IDT and reflector consists of several pairs of fingers. Mason's ECMs for one pair of IDT fingers and reflector fingers are illustrated in Fig. 1 and Fig. 2. The ECM Mason proposed for acoustic propagation paths is depicted in Fig. 3 [12].

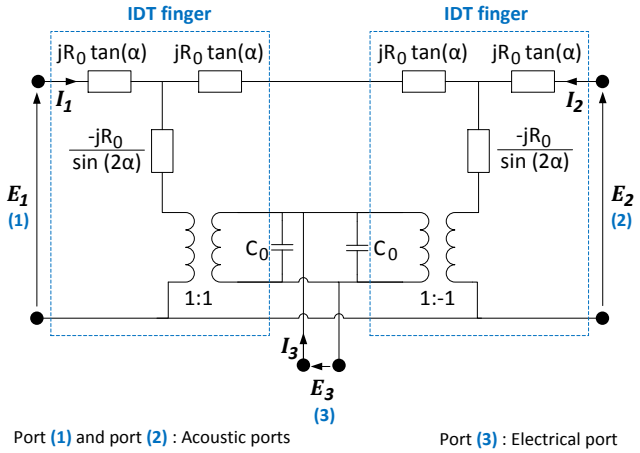

Figure 1. Mason's ECM for one pair of IDT fingers

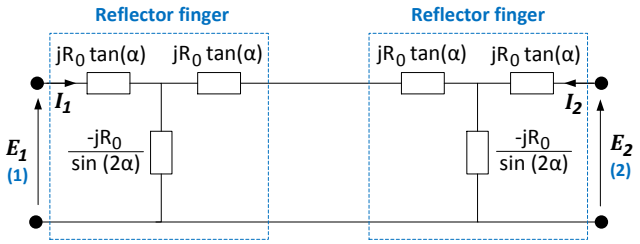

Figure 2. Mason's ECM for one pair of reflector fingers

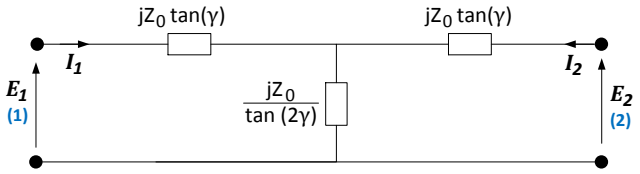

Figure 3. Mason's ECM for one propagation path

R_0 is is the electrical equivalent of the mechanical impedance Z_0. C_0 represents the electrode capacitance per pair of fingers. α and γ are given by :

$$\alpha = \frac{\pi}{2}\frac{f}{f_0} \quad (1)$$

$$\gamma = \frac{\pi f L}{v_{SAW}} \quad (2)$$

where f_0 is the center frequency of the SAW device, L is the length of the propagation, and v_{SAW} is the SAW velocity.

B. *Proposed simulator*

The simulator was developed with Matlab Version 7.13.0.564 (R2011b), and is dedicated to the simulation of SAW resonators and delay lines. The operating principle of the proposed simulator is shown in Fig. 4.

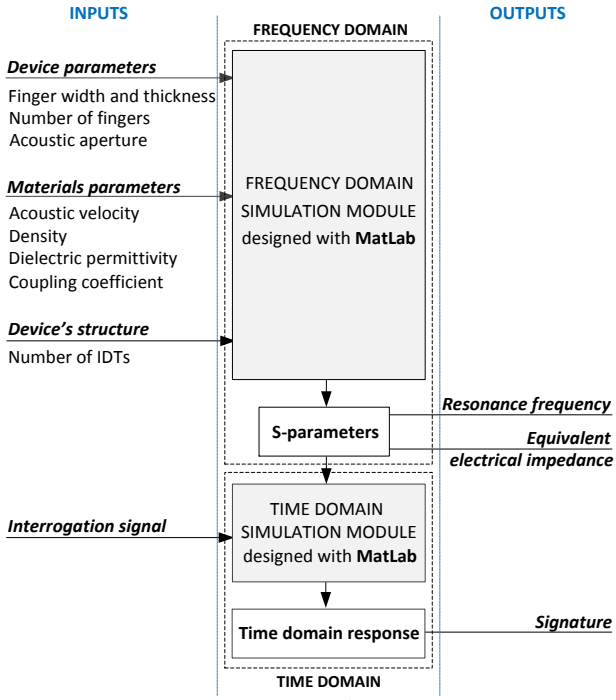

Figure 4. Operating principle of the proposed simulator

The major dimensions and parameters of the device to be simulated are first defined by the user. The simulator offers the possibility to run frequency domain simulations and time domain simulations.

Frequency response, impedance parameters and transfer characteristics are provided by the frequency domain simulation module. These include reflection coefficient S33 at the electrical port for SAW resonators, S21 for SAW delay lines, acoustic impedance and equivalent electrical impedance. The impulse response, which can be considered as a signature for SAW identification tags, is calculated by the time domain simulation module.

III. DESIGN OF THE SIMULATOR

The design method (see Fig. 5) is based on a modular approach. Each element of the simulated device is first represented by its Mason's equivalent circuit. This concerns IDTs, reflectors and propagation paths. Electrical circuit equations are deducted, and then implemented into Matlab functions that extract the S-parameters of each block. Interconnects between blocks are realized by another Matlab function created for this purpose.

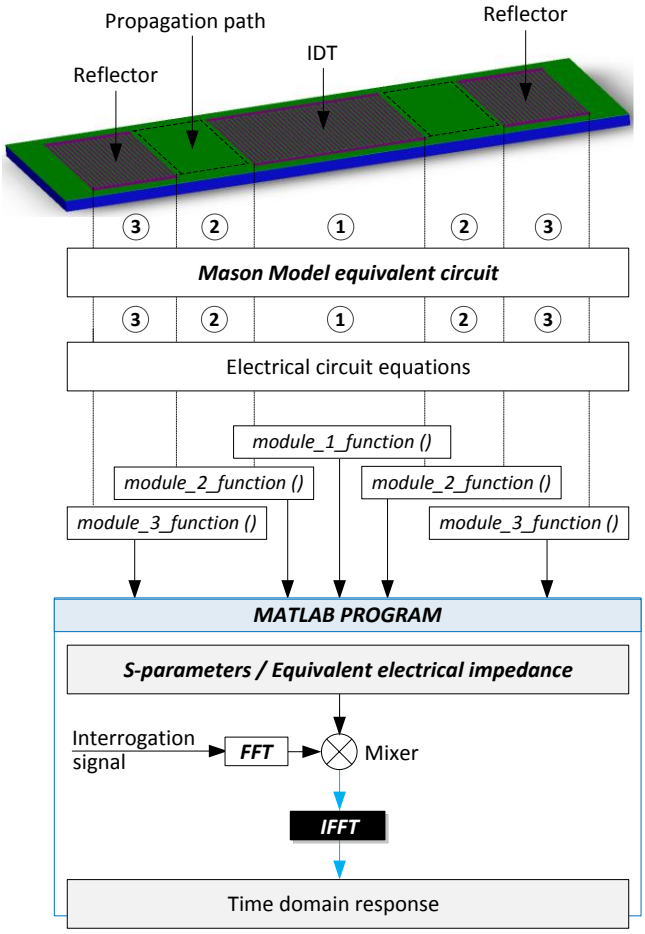

Figure 5. Used approach to simulate a SAW device

The created functions are exported into a Matlab program that computes the S-parameters of the entire simulated device and the equivalent electrical impedance. The results are plotted according to the frequency range set by the user. The time domain simulation capability of the simulator lies in a configurable FFT/IFFT module that predicts the response of the device to a user-defined interrogation signal.

IV. RESULTS

The materials parameters used in the simulations are summarized in Table I. They can be modified by the user, at any time, depending on the properties of the piezoelectric substrate and the metallic layer of the simulated SAW device. The dielectric permittivity of $LiNbO_3$ is given in [12] and the acoustic velocity was extracted from COMSOL simulation.

A. Frequency domain

The first simulated device is a one port SAW resonator. It has the same configuration as the SAW device shown in Fig. 5. The dimensions of each element are presented in Table II. The SAW device was simulated with the proposed simulator and then fabricated. Fig. 6 depicts a comparison between simulation and measurement results.

The results demonstrate the reliability of the simulator. The resonance behavior predicted by the simulator matches well with the measurement results (see Fig. 6). For example, the simulator predicts a resonance frequency of 171.3 MHz when the measured resonance frequency is about 171.4 MHz.

TABLE I
MATERIALS PARAMETERS

Parameter	Value
Piezoelectric substrate	$LiNbO_3$
Substrate Type	Y-cut, Z-propagating
Dielectric permittivity	27.9
Metallic layer	Cu
Acoustic velocity	3 447.7 m/s

TABLE II
DIMENSIONS OF THE SIMULATED ONE PORT RESONATOR

Quantity	Value
IDT and Reflectors	
Number of IDT	1
Number of reflectors	2
Finger width	5 µm
Finger thickness	100 nm
Number of fingers	150
Acoustic aperture	210 µm
Propagation paths	
Length	55 µm

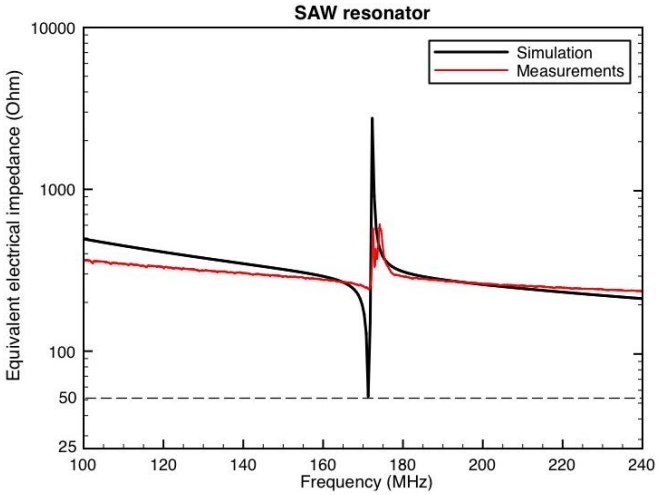

Figure 6. Comparison between simulation results and measurement results

The SAW resonator from which the measurements were taken is not perfectly adapted to 50 Ω. The fabrication process is being improved yet.

B. Time domain

To demonstrate the time domain simulation capability of the simulator, a one port SAW reflective delay line has been simulated. The delay line consists of three reflectors R_1, R_2, and R_3, separated by three propagation paths PP1, PP2 and PP3 (see Fig. 7). The dimensions are summarized in Table III. A short pulse of sinusoidal signal is used as interrogation signal.

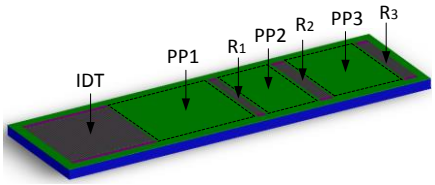

Figure 7. One port SAW reflective delay line

TABLE III
DIMENSIONS OF THE SIMULATED ONE PORT REFLECTIVE DELAY LINE

Parameter	Value
IDT and Reflectors	
Finger width	5 µm
Wavelength λ	20 µm
Finger thickness	100 nm
Acoustic aperture	210 µm
IDT	
Number of fingers	150
Reflectors	R_1, R_2, R_3
Number of fingers	12, 20, 20
Propagation paths	PP1, PP2, PP3
Length	50 λ, 70 λ, 120 λ

 ISBN: 978-1-61208-297-4

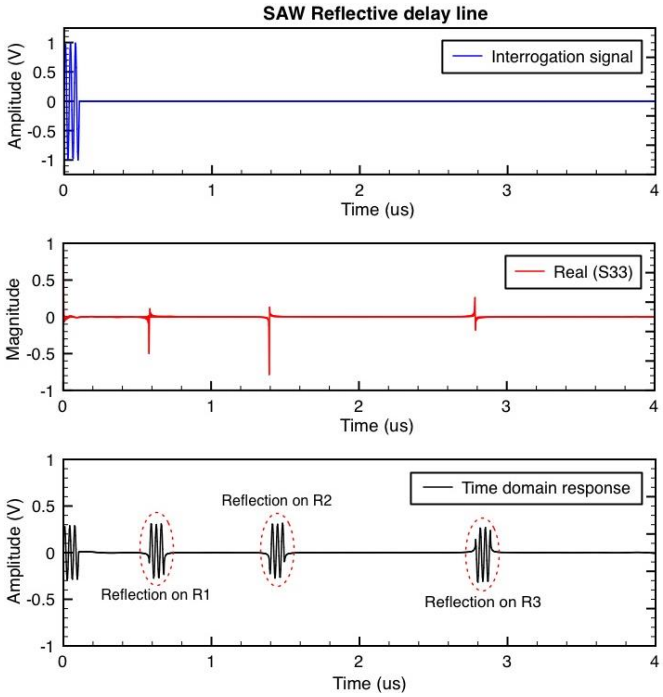

Figure 8. Time domain simulation capability of the simulator

TABLE IV
COMPARISON BETWEEN
EXPECTED RESULTS AND TIME DOMAIN SIMULATION RESULTS

Parameter	Expected result	Simulation result
T_1	0.580 µs	0.580 µs
T_2	1.461 µs	1.428 µs
T_3	2.970 µs	2.912 µs

The time domain response predicted by the simulator is illustrated in Fig. 8. The output signal is composed of four successive short pulses resulting from reflections at the electrical port and on the three reflectors.

The simulation results are compared with the expected results (see Table IV). The expected time delay of the reflection on Ri (i=1, 2, 3) is given by Ti = 2Li / v, where Li is the one-way path length to Ri and v is the acoustic velocity. Good agreement between expected results and simulation results are observed.

V. ADVANTAGES OF THE SIMULATOR

Several one port resonators have been simulated in order to observe the variation of the simulation duration with the number of fingers in each IDT and reflector (see Fig. 9). The same experiment has been carried out on some one port SAW reflective delay lines by varying the number of reflectors (see Fig. 10). The materials parameters and dimensions of the simulated devices are the same as those presented in Table I, Table II, and Table III. The simulation durations were evaluated with the Matlab instruction *tic... toc*.

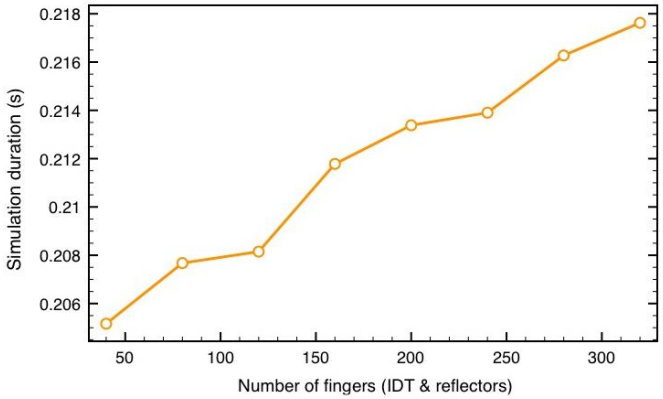

Figure 9. Frequency domain simulation duration

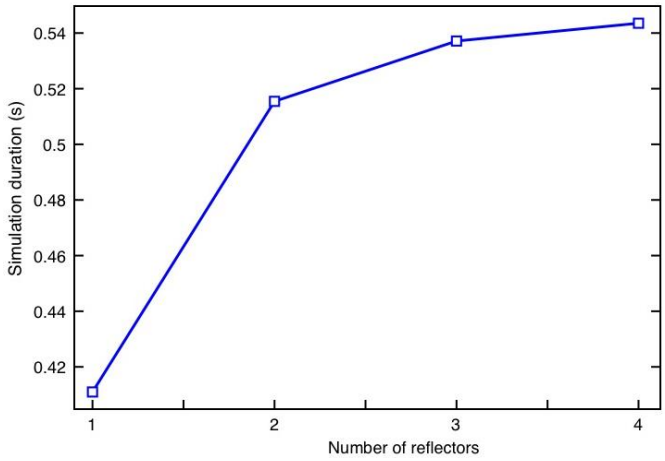

Figure 10. Time domain simulation duration

All simulations were performed using an Intel Core i5-2500 Central Processing Unit @3.30 GHz and 16 gigabytes of RAM. The simulation duration increases with the number of fingers and the number of reflectors. Even for a one port SAW reflective delay line composed of an IDT with 150 fingers and four reflectors with 20 fingers each, the simulation duration is less than one second.

VI. CONCLUSIONS

The proposed new SAW device simulator provides a considerable reduction of the required computational resource and simulation duration. While FEM simulations with COMSOL, or Coventor, or ANSYS HFSS generally last from about ten minutes to several days [13], depending on the complexity of the structure of the simulated device, this simulator allows users to get frequency and time domain simulation results in less than one second.

SAW resonators and SAW reflective delay lines have been simulated. The reliability of the simulator has been demonstrated by comparing simulation results with measurement results. Given that the simulation parameters can be easily modified and a modular approach is used, the new simulator should be able to simulate any SAW device based on the same modules.

 ISBN: 978-1-61208-297-4

AKNOWLEDGMENTS

The authors would like to thank all the members of the LMST team. We especially thank Assane Ndieguene and Issam Kerroum for insightful discussions on acoustic technologies, and Hatem El Matbouly for providing comments on earlier versions of this paper.

REFERENCES

[1] D. C. Malocha, "SAW/BAW Acoustoelectronic Technology for Filters and Communication Systems", IEEE Wireless and Microwave Technology Conference, 2010, pp.1-7.

[2] K. Hashimoto, S. Sato, A. Teshigahara, T. Nakamura, and K. Kano, "High-Performance Surface Acoustic Wave Resonators in the 1 to 3 GHz Range Using a ScAlN/6H-SiC Structure", IEEE Transactions on Ultrasonics, Ferroelectrics, and Frequency Control, vol. 60, no. 3, March 2013, pp. 1-3.

[3] M. Urbanczyk, Z. Waltar, and W. Jakubik, "Interdigital Transducer Analysis Using Equivalent PSpice Model", Elsevier Science B.V. Ultrasonics, vol. 39, 2002, pp. 595 - 599.

[4] K. Hashimoto, T. Omori, and M. Yamaguchi, "Design Considerations on Wideband Longitudinally-Coupled Double-Mode SAW Filters", IEEE Ultrasonics Symposium, 2002, pp. 153 - 157.

[5] G. Kovacs, "A Generalised P-matrix Model for SAW Filters", IEEE Ultrasonics Symposium, 2003, pp. 707 - 710.

[6] J. Munshi and S. Tuli, "A Circuit Simulation Compatible Surface Acoustic Wave Interdigital Transducer Macromodel", IEEE Transactions on Ultrasonics, Ferroelectrics, and Frequency Control, vol. 51, no. 7, July 2004, pp. 783-785.

[7] M. Sadeghi, R. Ghayour, H. Abiri, and M. Karimi, "Design and Simulation of a SAW Filter and a New Approach for Bandwidth's Tuning", 8th IEEE Int. ASICON, 2009, pp. 642-645.

[8] M. Ghahremani et al., "Surface Acoustic Wave Devices for Ocular Drug Delivery", IEEE International Ultrasonics Symposium Proceedings, 2010, pp. 872 - 875.

[9] M. Z. Atashbar, B. J. Bazuin, M. Simpeh, and S. Krishnamurthy, "3-D Finite-Element Simulation Model of SAW palladium thin film hydrogen sensor", in Proc. 2004 IEEE Int. Ultrasonics, Ferroelectrics, Frequency Control 50th Anniversary Conf., pp. 549–553.

[10] W. P. Mason, "Physical Acoustics", vol. 1A, Academic Press, New York, 1964.

[11] W. P. Mason, "Electromechanical Transducer and Wave Filters", Second edition, D.Van Nostrand Company Inc, 1948.

[12] B. A. Auld, "Acoustic Waves and Fields in Solids", vol. I, Wiley, New York, 1973.

[13] A. Stefanescu et al., "Analysis of GaN Based SAW Resonators Including FEM Modeling", Romanian Journal of Information Science and Technology, vol. 14, no. 4, 2011, pp. 334-345.

 ISBN: 978-1-61208-297-4

Wide Dynamic Range Readout for CMOS Pixel Using PWM and Direct Mode Sensing Techniques

Emmanuel Gómez Ramírez, José Alejandro Díaz Méndez, Mariano Aceves Mijares, José Miguel Rocha Pérez and Jorge Miguel Pedraza Chávez.
INAOE
Puebla, México
e-mail: {emmanuelgomez, ajdiaz, maceves, jmr, jpch}@inaoep.mx

Carlos Domínguez Horna
IMB-CNM (CSIC)
Barcelona, España
e-mail: carlos.dominguez@imb-cnm.csic.es

***Abstract*— Dynamic range is a critical figure of merit for image sensors. Then, many researchers have been working to improve this figure. As a result, various techniques have been developed with good results. However, any effort to improve even more the dynamic range is of great value. The multimode method combines more than one technique to use the best part of them. In this paper, a high dynamic range CMOS image sensor using multimode sensing is presented. Dynamic Range as high, as 160 dB is achieved combining PWM and direct mode techniques. The circuit proposed here has one of the higher dynamic ranges reported.**

Keywords-wide dynamic range; CMOS imagers; PWM sensors; continuously operation sensors; multimode sensing.

I. INTRODUCTION

Currently, CMOS (Complementary Metal Oxide Semiconductor) technology allows the integration of complex electronic systems that include devices of various types. For example, optical sensors allow the formation of CMOS imagers that offer several advantages compared to CCD's (Charge-Coupled Device) [1], such as power consumption, low voltage, low cost, etc., which have enabled the creation of imagers that represent single-chip solutions [1].

In a CMOS imager, one of the most important figures of merit is the Dynamic Range (DR) [1] given by (1). The DR permits to differentiate between high and low excitation conditions in general, and, in the case of an imager, to distinguish between lightly and highly illuminated areas.

Then, it is clear that systems with higher DR would resolve extreme conditions without loss of information. As a consequence, nowadays, the increase of DR is an active area of research.

$$DR = 20\log\frac{V_{max}}{V_{min}}\,[\mathrm{dB}] \qquad (1)$$

Many efforts to obtain vision systems with a wide DR have been done. Different techniques to increase the DR have been reported; some of them are reviewed in [2-3], and enlisted here: logarithmic method, capacity well adjustment method, multimode sensors, frequency-based sensors, time-to-saturation sensors, multiple sampling methods, and multiple integration time methods.

As mentioned above, one technique to increase the DR is the multimode sensing system. To enhance the DR, multiple sensing techniques can be used, by taking advantage of the best resolution of each one.

Two types of readout that are used in CMOS imager, i.e., 1) integration-based sensors and 2) direct mode operated sensors, can be combined to improve the system response.

In the first case (i.e., integration-based sensor), photogenerated charges are integrated given a linear response. The current in the order of femtoAmperes can be detected by this method [4], corresponding to very small illumination intensities.

In the direct mode operated sensor technique, the current generated by a Photodiode (PD) is directly converted to voltage. In this case, the current detected is in the order of microA or miliA, corresponding to very high illumination intensities.

Then, a combination of both readout techniques allows detecting the current of a PD from femtoA to miliA.

In this paper, a combination of current integration and direct mode detection methods are used to increase the DR.

This paper is organized as follows: Section II presents the definition and basic assumptions of the multimode technique proposed. Section III presents the results obtained of the proposed circuit. Section IV summarizes the study.

II. PWM - DIRECT MODE TECHNIQUE PROPOSED

A block diagram of the multimode method used is shown in Fig. 1. As it can be seen, the photocurrent from the sensor could be integrated in the upper branch, or could be amplified directly in the lower branch.

In the integration mode, the photocurrent, I_{ph}, obtained in the step 1 is integrated and converted to a voltage ramp, steps 2. In step 3, when the voltage ramp reaches the comparator reference voltage a shot pulse is obtained. In the direct mode, step 4, the I_{ph} is directly fed to an amplifier. Both readout signals are passed into an analog-to-digital converter, and finally, in step, 5 a Digital Word (DW) is obtained proportional to the incident light in the sensor.

 ISBN: 978-1-61208-297-4

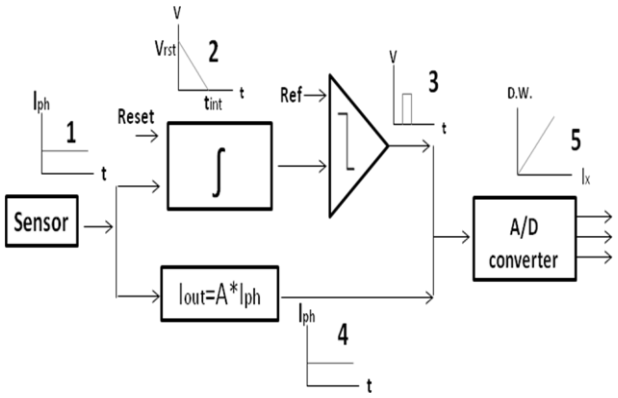

Figure 1. Multimode sensing block diagram.

A. *Pulse Width Modulation Mode Readout*

In integration mode (or lineal mode), the parasitic capacitor of a PD is charged to a reference potential and when light shines on it; this potential decreases almost in a linear fashion, due to the photocurrent discharging the capacitor.

By measuring the voltage drop, the amount of light can be obtained, using (2), where I_{ph} is the photocurrent, T_{int} is integration time, and C_{PD} is the parasitic capacitor of the PD.

$$\Delta V = \frac{I_{ph} T_{int}}{C_{PD}} \qquad (2)$$

In Pulse Width Modulation (PWM) [5] mode, each pixel controls the integration time T_{int}, and can integrate very small signals until an adequate output is obtained.

The circuit shown in Fig. 2 is an example of how to implement the PWM mode. The current is integrated and then compared with the reference voltage.

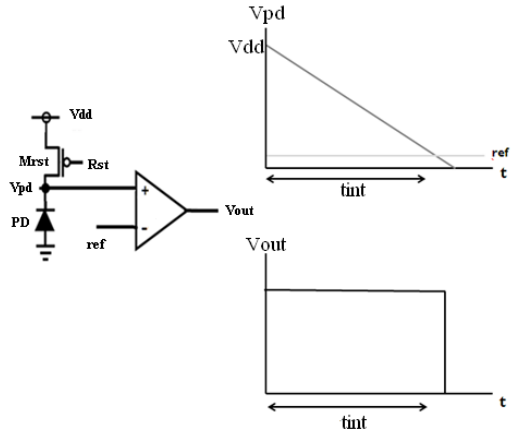

Figure 2. Circuit used to implement the PWM technique. The upper graph shows the Vpd voltage linear decay due to the incident light. The lower graph shows Vout as a function of time.

The PMOS (P-type Metal Oxide Semiconductor) transistor works as a reset switch; on the ON state the PD voltage (V_{pd}) is near V_{dd}. Then, the switch is turned OFF and the incident light produces V_{pd} to decrease linearly.

When V_{pd} reaches the reference voltage, the comparator generates an output voltage pulse. By measuring the width of this pulse, the amount of light shining on the PD can be measured.

The problem with this technique is that pixels working in integration mode have a limited DR at higher levels of photocurrent; this is, the integration time will be too short, and in some cases imperceptible. Then, this technique increases the DR at small light power levels but fails to work adequately with high power levels, as shown in Fig. 3. In other words, low illumination level produces small photocurrent, as the light intensity augment the photocurrent increases reducing the integration time. If the light is intense the integration time will be very difficult to measure.

To solve the high current problem, bright light will be detected by direct current amplification.

B. *Direct Mode Readout*

In direct output mode, the PD current is directly transferred to current mirrors with or without amplification. This architecture suffers from low sensitivity at low level of illumination; however, works fine detecting high illumination levels.

Flipped-Voltage Follower (FVF) in current mode [6] is used to sense the PD current due to its low input impedance and because it can drive large input current variations, as shown in Fig. 4. The FVF is shown in Fig. 4a; in this circuit, the input impedance Z_{in} is very low and given by

$$Z_{in} = \frac{1}{g_{m1} g_{m2} r_{o1}} \qquad (3)$$

where g_{m1} and g_{m2} are the transistor transconductances and r_{01} is the transistor's output resistance of M1.

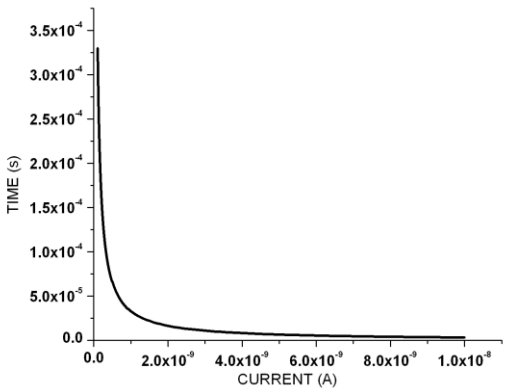

Figure 3. Photocurrent vs integration time, as the current increases the time tends toward zero.

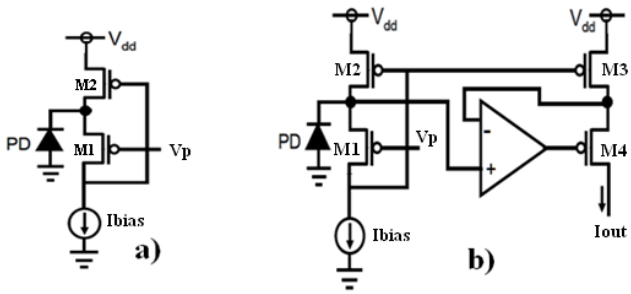

Figure 4. a) Flipped-Voltage Follower in current mode and b) current mirror.

The input impedance is low due to the shunt feedback provided by M2. The output current is given by the expression $I_{out} = I_{ph} - I_{bias}$, where I_{bias} is the bias current provided by the source current in M1, and I_{ph} is the current from PD.

Normally, the current needs to be amplified; so, a current mirror is used and the gain is given by the ratio W/L of the transistors.

To make the mirrored current as accurate as possible is necessary to use an operational amplifier, as shown in Fig. 4b, that keeps the bias voltage equal in both branches.

Fig. 5 compares the fidelity of the current copy with and without operational amplifier topologies. As shown, the advantage of using the operational amplifier is clear.

C. *PWM-Direct Mode Circuit Implementation*

A schematic diagram of the proposed circuit is shown in Fig. 6, which combine both readout topologies: PWM and direct mode. When low illumination is shining on the PD, the PWM mode works, and when bright illumination is received, the direct mode topology comes into operation.

Internal switches, which are controlled by the PWM output, select one or the other topology.

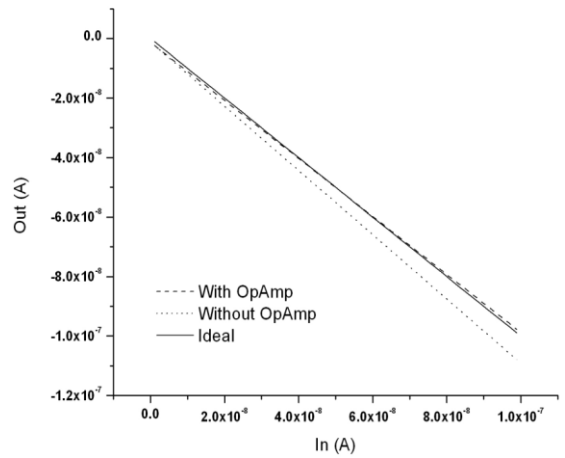

Figure 5. Input and output current comparison in the current mirror with and without operational amplifier.

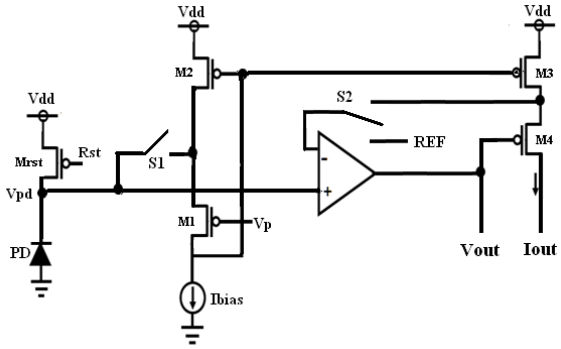

Figure 6. Dual mode circuit, when S1 and S2 are closed the direct mode is activated. On the other hand, when S1 is open and S2 is at the REF voltage the PWM mode is activated.

The PWM output voltage for a single sensor signal is shown in Fig. 7a; when the voltage ramp reaches the voltage reference a step is produced and the voltage gets a constant value. This voltage is then used to switch to the direct mode, and the output current increases to a new value proportional to the current in the sensor, as shown in Fig. 7b.

As displayed in Figs. 2 and 4, an operational amplifier is needed in both topologies. So, sharing the operational amplifier in each pixel to run both techniques reduces the number of transistors and improves the circuit performance.

III. SIMULATION RESULTS

Fig. 8 shows the result of simulations when dull incident light shines on the sensor. As it is shown, the integration time starts when the reset command is triggered and V_{pd} is at V_{dd} (3.3V); then, different V_{pd} voltage ramps are produced by different light intensities. After some time, each ramp reaches the reference (in this case 1.5V). At that moment, the comparator output produces a voltage step.

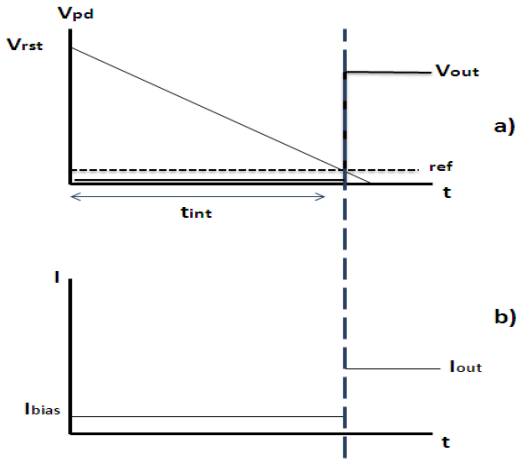

Figure 7. Output voltage and current of the PWM and direct mode sections, in a) the ramp of voltage is shown and after it reaches the reference a constant voltage step is produced. In b) as the PWM mode is active the I_{out} is low, and when the direct mode is activated the Iout increases proportional to the sensor's current.

This voltage step triggers the switches S1 and S2 to start the direct mode, and also it is used to bias the transistor, M4, allowing that the I_{out} increases to a value given by (I_{ph}-I_{bias}).

Fig. 8b shows the PWM output current, as can be seen the current is zero until the voltage reference is reached, then a high current is obtained. The elapsed period can be used to estimate the light intensity. In this case, the input current used was from 20 up to 200 picoA (labels A and B correspond to the lower and the higher intensities respectively).

For example, in this simulation, the first ramp, that corresponds to the intensity B, lasts 0.1ms, as shown in Fig. 8b; the last ramp lasts 0.47 ms (intensity A). Let us suppose that it is the real response of the circuit under illumination, and the light shining on the sensor is monochromatic and is the same for all ramps shown in Fig. 8a. So, we can say that the first ramp would be produced for a more intense beam than that of the last ramp. Furthermore, the beam that produces the first ramp is approximately five times more intense than that of the last ramp.

On the other hand, in Fig. 9, simulation results of a high current regime are shown.

In Fig. 9a, the PWM V_{out} is presented when the input current were from 50 to 500 nanoA (labels C and D correspond to the lower and the higher intensities respectively), comparatively with the results of figure 8a, after certain light intensity is not possible discriminate between the V_{out} ramps (intensities C and D can't be differentiated). In this case, the output current is directly proportional to the current sensor and it is processed by the direct mode circuit. In Fig. 8a, the step of current is constant at a low value, approximately 1.6 microA, and starts at different times; on the other hand, in Fig. 9a, the current steps are variable in amplitude and practically start at the same time. This way, it can be decided when direct mode is working.

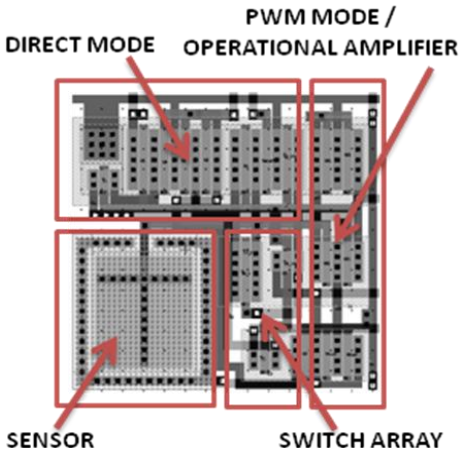

Figure 10. Layout of the PWM and direct mode circuit. The sensor area is 13x13 square microns, and the total area is 50x50 square microns.

The output current, I_{out}, is the addition of I_{ph}-I_{bias} when the output voltage switch to the direct mode and I_{ph} is higher than I_{bias} a detectable I_{out} current is obtained. Thenceforth, the output current is used to estimate the light intensity.

Let us suppose, again, that it is the real response of the circuit under illumination, and the light shining on the sensor is monochromatic and is the same for all output currents. Clearly, the higher current corresponds to the more intense beam.

As mentioned above, both topologies work for different illumination intensities; this allows increasing the DR. PWM topology works at tenuous light and direct current mode topology works at brighter illumination.

The circuit was simulated with HSPICE [7], and implemented in a CMOS technology of 0.5um from MOSIS. Fig. 10 shows, the layout of one pixel.

To measure the robustness of the design against process variations, 4-corners simulation is used submitting the circuit to extreme conditions.

Two examples of 4-corners simulation with 100 and 600 picoA input current (labeled Typ1 and Typ2, respectively) using PWM mode readout are shown in Fig. 11; as it can be seen in the first case (Typ1), there is no difference between the 4 simulations.

In the second case (Typ2), the maximum error was less than 5%, however the variation in the voltage step is 10% approximately.

Fig. 12 presents two examples of 4-corners simulation with 4 and 10 microA input current (labeled Typ1 and Typ2, respectively), in this case direct mode readout is used. In both cases, the worst case variation was 10% reflecting the 10% variations of the Vout.

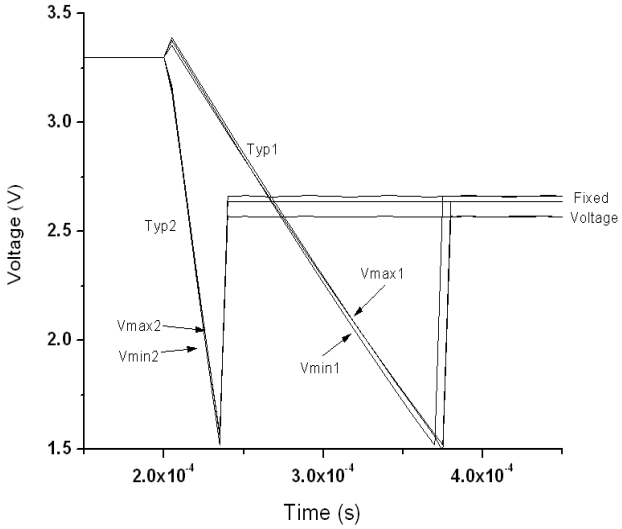

Figure 11. 4-corners simulation for PWM circuit with 100 and 600 picoA input currents, for the low current regimen no difference is observed. The high regime current shows variations of 5% in the ramp voltage and 10% in the voltage step.

 ISBN: 978-1-61208-297-4

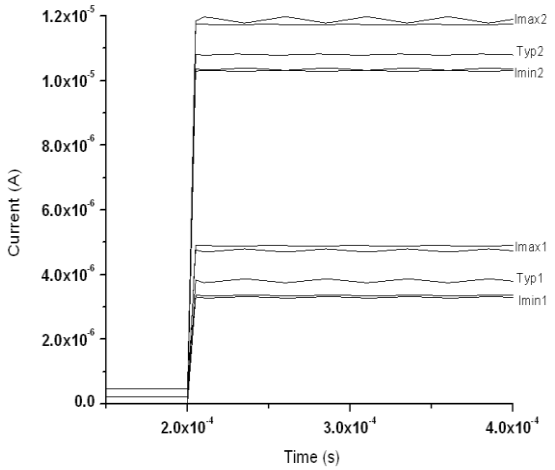

Figure 12. 4-corner simulation for direct mode circuit with 4 and 10 microA input currents, variations up to 10% are obtained.

Fig. 13 presents Vout for PWM circuit and Iout for direct mode circuit; as it can be seen in the low current regimen the PWM works well up to $1X10^{-08}$A; after this value, the output current starts to be registered. Consequently, the DR obtained is 160 dB.

In Table 1, a comparison between different topologies using the multimode techniques to increase DR is presented. From the table is inferred that only one, the Lineal-Logarithmic, reports a higher DR than the one presented here. However, the authors [10] used a smaller technology and they do not report the power consumption.

Other articles present DR that exceeds the one reported here, but these works do not use the multimode technique, neither the same technology [13]. Some reports not even mention the methods or techniques used to obtain a high DR [14].

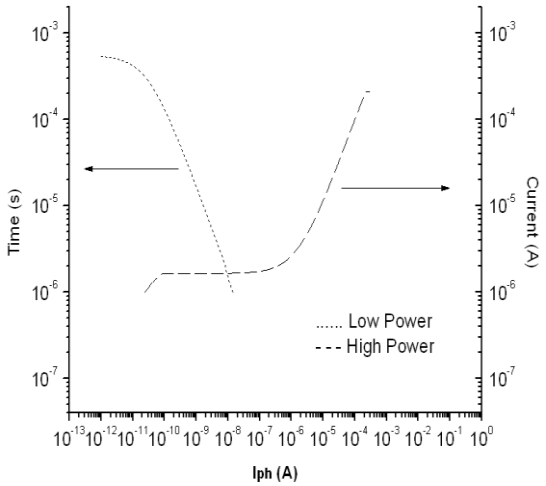

Figure 13. PWM and direct mode range comparison.

TABLE I. MULTIMODE SENSING TECHNIQUES COMPARISON

	Specifications					
	Tech	***DR***	***Area***	***Power consumption***	***Year***	***Ref***
Lineal – Logarithmic	0.35	124	7.5x7.5	---	2005	8
Lineal – Logarithmic	0.18	143	5.6x5.6	61mW y 84mW	2006	9
Lineal – Logarithmic	0.35	200	20x20	---	2006	10
Lineal – Logarithmic	0.35	112	9.4x9.4	---	2011	11
PWM - PFM	0.18	143	30x30	175mW	2011	12
PWM – Direct Mode	**0.5**	**160**	**50x50**	**36uW**	**---**	**This work**

Another advantage of our approach is the lowest power consumption compared with those in Table 1. This is due to the fact that FVF working in current mode consumes negligible power, and has low input impedance.

IV. CONCLUSIONS

A new topology using multimode sensing that increases DR has been demonstrated. PWM and direct techniques were combined to improve the DR obtaining 160 dB.

Using this technique and 0.5 microns CMOS technology, a single pixel circuit was designed, occupying 50x50 square microns of total area. In order to reduce area, an operational amplifier is shared by both techniques.

Compared with other circuits reported in the literature, our approach has one of the highest DR, and the smaller power consumption, as demonstrated by simulation. However, I_{out} variations can be as high as 10%. Nevertheless, we have to mention that we did not yet work to improve these variations.

REFERENCES

[1] J. Ohta, "Smart CMOS Image Sensors and Applications", CRC Press, 2008.

[2] A. Spivak, A. Belenky, A. Fish, and O. Yadid-Pecht "Wide-dynamic-range CMOS image sensors: comparative performance analysis", IEEE Transactions On Electron Devices, vol. 56, no. 11, Nov. 2009, pp. 2446-2461.

[3] D. Park, J. Rhee, and Y. Joo "A wide dynamic-range CMOS image sensor using self-reset technique", IEEE Electron Device Letters, vol. 28, no. 10, Oct. 2007, pp. 890-892.

[4] B. Goldstein, D. Kim, A. Rottigni, J. Xu, T. K. Vanderlick, and E. Culurciello "Cmos low current measurement system for biomedical applications" IEEE International Symposium on Circuits and Systems (ISCAS), May. 2011, pp. 1017-1020.

[5] A.Zarándy, "Focal-Plane Sensor-Processor Chips", Springer, 2011.

[6] R. González, et al. "The flipped voltage follower: A useful cell for low voltage low power circuits design", IEEE Transactions On Circuits And Systems, vol. 52, no. 7, Jul. 2005, pp. 1276-1291.

[7] Synopsys, "HSPICE", URL: http://www.synopsys.com/, 2013.

[8] K. Hara, H. Kubo, M. Kimura, F. Murao, and S. Komori "A linear-logarithmic cmos sensor with offset calibration using an injected charge signal", IEEE International Solid-State Circuits Conference, vol. 1, Feb. 2005, pp. 354-603.

[9] G. Storm, R. Henderson, J. E. D. Hurwitz, D. Renshaw, K. Findlater, and M. Purcell "Extended dynamic range from a combined linear-logarithmic cmos image sensor", IEEE Journal Of Solid-State Circuits, vol. 41, no. 9, Sep. 2006, pp. 2095-2106.

[10] N. Akahane, R. Ryuzaki, S. Adachi, K. Mizobuchi, and S. Sugawa "A 200dB dynamic range iris-less cmos image", IEEE International Solid-State Circuits Conference, Feb. 2006, pp. 1161-1170.

[11] M. Vatteroni, P. Valdastri, A. Sartori, A. Menciassi, and P. Dario "Linear–logarithmic cmos pixel with tunable dynamic range", IEEE Transactions On Electron Devices, vol. 58, no. 4, Apr. 2011, pp. 1108-1115.

[12] C. Posch, D. Matolin, and R. Wohlgenannt "A qvga 143 dB dynamic range frame free pwm image sensor with lossless pixel", IEEE Journal Of Solid-State Circuits, vol. 46, no. 1, Jan. 2011, pp. 259-275.

[13] N. Ide, W. Lee, N. Akahane, and S. Sugawa "A wide DR and linear response cmos image sensor with three photocurrent integrations in photodiodes, lateral overflow capacitors, and column capacitors", IEEE Journal Of Solid-State Circuits, vol. 43, no. 7, Jul. 2008, pp. 1577-1587.

[14] Omron, "German venture company develops highly advanced wide dynamic range cmos image sensor", URL: http:// industrial.omron.fr/fr/news/news/cmos-image-sensor, 2003.

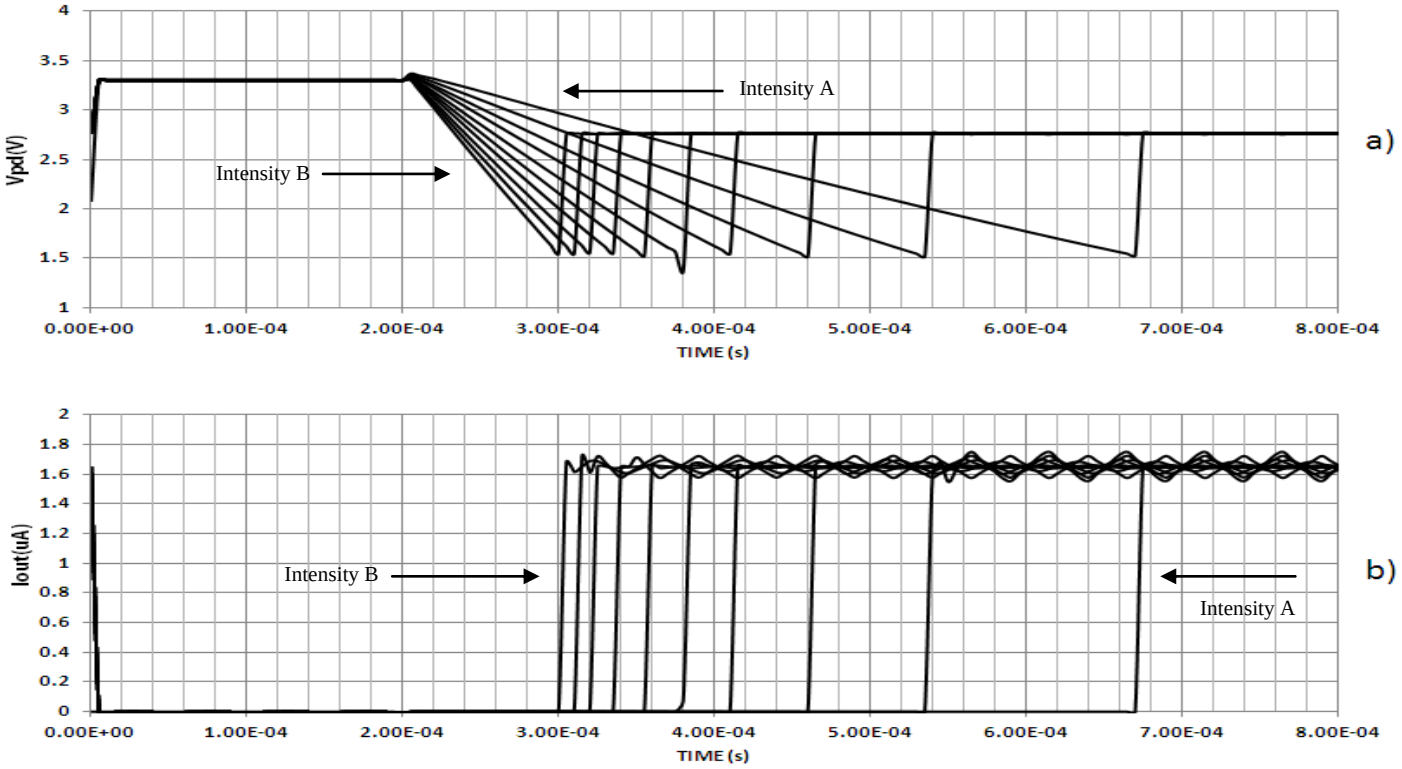

Figure 8. Simulations results of a low intensity light regimen, a) after 200us the Vpd linear decay starts and after reaching the reference a constant voltage is obtained, b) low intensities light sweep presents different integration time proportional to the light intensity.

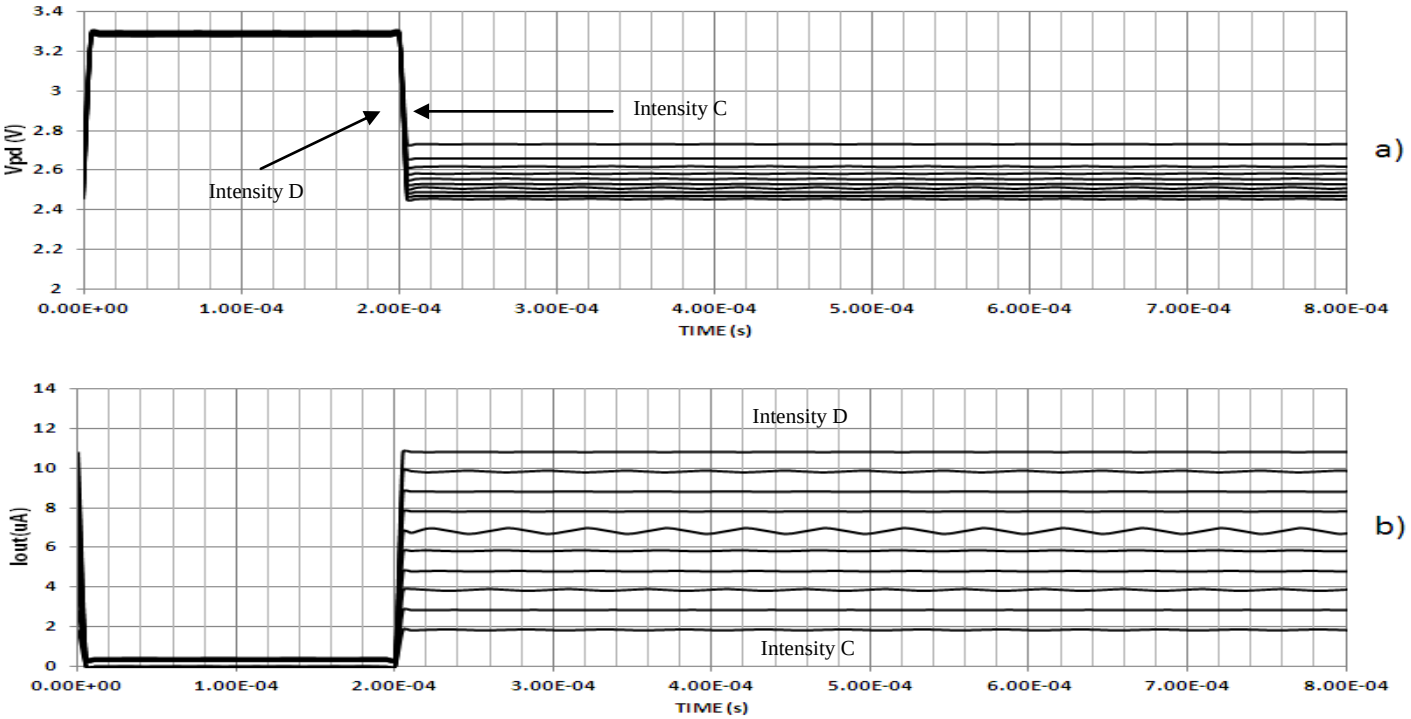

Figure 9. Outputs Simulations results of a high intensity light regimen, a) the Vpd linear decay is too fast and it is not differentiable due to the high current, then b) the current is measured straight forward.

Dual-Band Dipole Antenna for Sensing Applications in ISM Bands

Guy Ayissi Eyebe, Hatem El-Matbouly, Frédéric Domingue
Laboratoire de Microsystèmes et de Télécommunications
Université du Québec à Trois-Rivières
Trois-Rivières, Canada
guy.ayissi.eyebe@uqtr.ca, hatem.el.matbouly@uqtr.ca, frederic.domingue@uqtr.ca

***Abstract*—This paper presents a dipole antenna with dual-band operation designed for sensing applications in ISM bands. The proposed antenna has the advantages of being low profile, low cost, easy to fabricate with a flexible design based on the microstrip antennas. A prototype has been fabricated and tested. The measured results show good gain performance and omnidirectional radiation patterns for all the resonant modes. The proposed structure is suitable for integration with any wireless sensors in the ISM bands.**

Keywords : antenna; dual-band; ISM; wireless; sensors.

I. INTRODUCTION

The exponential growth of wireless communications technology has increased the need for highly integrated RF modules operating in multiple frequency bands. This expansion has been driving the development of dual-band and multiband antennas, in order to integrate numerous frequency bands within the same RF module. Some dual-band or multiband antennas performances reported recently allow achieving wireless applications taking advantage of the free license ISM bands. This includes radiofrequency identification (RFID), wireless local area network (WLAN), wireless sensor network (WSN), and sensing [1-4].

Multiband operation involving 434 MHz, 915 MHz, 2.45 GHz and 5.8 GHz ISM bands has been significantly investigated. The performances reported include dual-band antennas with only one resonant mode inside the ISM bands, and dual-band antennas with the two resonant modes inside the ISM bands. For dual-band antennas with the two ISM resonant modes, most of them operate at 915 MHz – 2.45 GHz, or 2.45 GHz – 5.8 GHz. As single or dual resonant mode, the 434 MHz band has been involved recently in medical applications and passive acoustic sensor, which represents an emerging technology for gas sensors [5]. But amongst the frequency bands listed above, 434 MHz resonant mode is not involved enough in dual-band operation with another ISM resonant mode. Yet, this mode together with the 915 MHz resonant mode can avoid the use of two distinct antennas [6, 7], integrate the UHF RFID function [8] and take advantage of the free license bands for these two functions and others. Dual-band antennas operating in 434 MHz – 915 MHz bands have been proposed in [1] and [2]. The antenna presented [1] consists of a metal plate of 335 mm x 155 mm x 1mm acting as RFID tag antenna while the antenna presented in [2] is a double loop patch antenna ensuring a bidirectional communication between sensors in a wireless sensors network. These antennas are not suitable for sensing applications since the RFID tag proposed in [1] suffers from non-compact configuration and metallic structure, while the double loop antenna proposed in [2] needs a matching network to operate properly.

This paper presents a dual-band dipole antenna with the two resonant modes at 434 MHz and 915 MHz within the ISM bands. The proposed antenna operates in the two free of charge ISM bands to improve sensing possibilities with the same device, and use the sensing application together with another function such as UHF RFID. This antenna has a compact configuration in regards to the resonant modes involved and is very suitable for integration with all the sensors bonded within any package. The proposed antenna structure has the advantages of having high gain with omnidirectional radiation patterns, adjustable design structure and low fabrication cost.

II. ANTENNA DESIGN

Figure 1 presents the picture of the proposed dual-band dipole antenna, fabricated on RO4300 Rogers laminated substrate. The parameters of the substrate are shown in Table I.

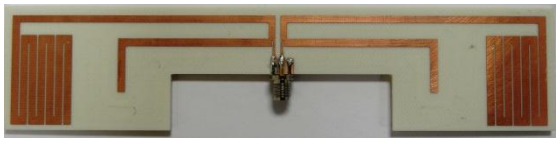

Figure 1. Photograph of antenna

TABLE I

PARAMETERS OF ROGERS RO4300 LAMINATED SUBSTRATE

Parameters	Values
Dielectric constant (ε_r)	3.55
Dissipation factor (tanδ)	0.0027
Dielectric thickness	1.524 mm
Upper layer cooper foil thickness	17 µm

 ISBN: 978-1-61208-297-4

As depicted in Figure 1, each half of the proposed dipole antenna has two arms, in order to achieve ISM dual-band operation.

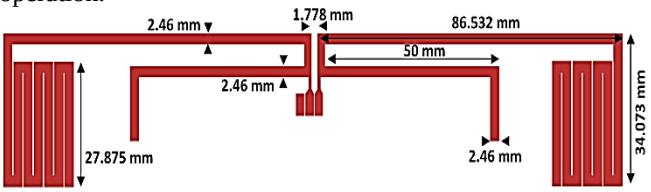

Figure 2. Layout of the proposed dual-band antenna

Given the fact that resonant frequency is inversely proportional to the arm's length, the shorter arm ensures the 915 MHz band operation, whereas the long arm ensures the 434 MHz operation. To achieve a compact configuration, the short arm has been folded down and the long arm has been meandered, so that the antenna is 17.34 x 3.4 x 1.541 (cm). These dimensions have been obtained while taking into consideration the trade-off between the performances of the antenna such as matching levels for each resonant mode, and the compactness of the antenna. Figure 2 shows the layout of dual-band dipole printed antenna with dimensions, designed for matching to a 50 Ω feed line.

III. EXPERIMENTAL RESULTS AND DISCUSSION

Figure 3 shows the simulated and measured S_{11} parameters performed on the prototype shown in Figure 1.

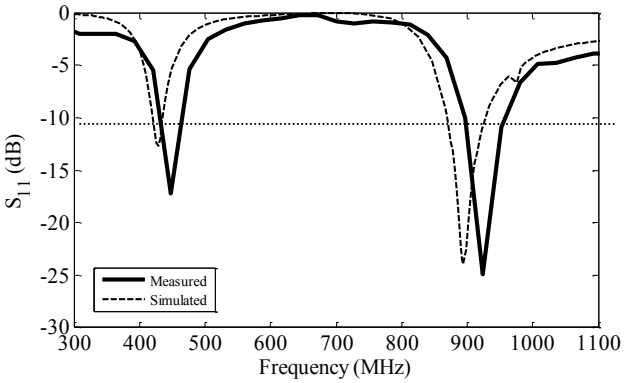

Figure 3. Simulated and measured return loss of the fabricated antenna

The results show a good agreement between simulated and measured results. There are only two distinct resonant modes in the frequency band (300 MHz - 1.1 GHz), the low-band resonant mode is at 448 MHz, and the high-band resonant mode is at 924.3 MHz. The measured return loss is less than -10 dB for (423 – 470 MHz) and for (896 – 956 MHz) bands, which covers the whole ISM bands. To evaluate the far-field behavior of the antenna, radiation patterns have been measured. The radiation patterns have been carried out with the antenna orientated as shown in Figure 4 in regards to the Cartesian axes (x, y, z). Figure 5 and Figure 6 show the cuts of the radiation patterns made in x-z plane, y-z plane and x-y plane at 433.3 MHz for the lower band and 916.6 MHz for the higher band, respectively.

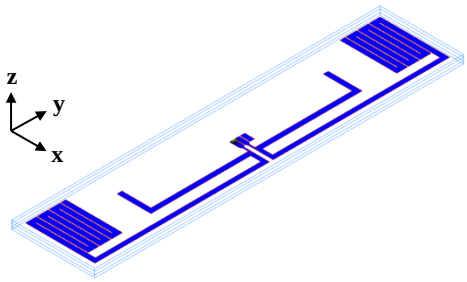

Figure 4. Orientation of antenna in regards to the cartesian axes

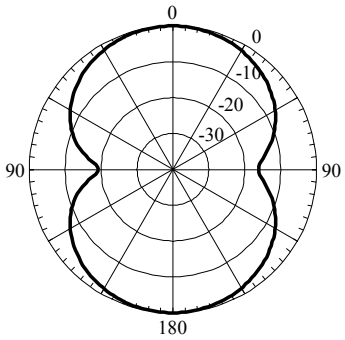

(a)

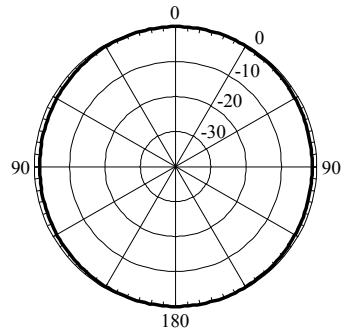

(b)

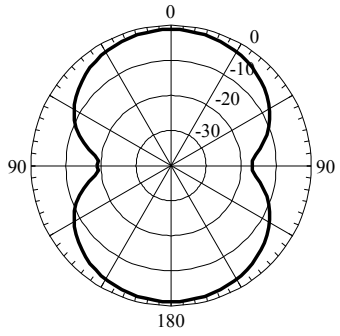

(c)

Figure 5. Measured radiation patterns of the proposed antenna at 433.3 MHz (a) x-z plane at 433.3 MHz, (b) y-z plane at 433.3 MHz and (c) x-z plane at 433.3 MHz

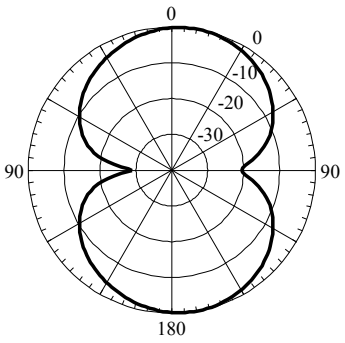

(a)

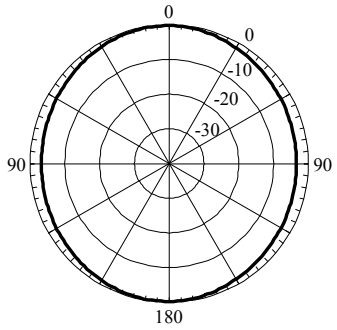

(b)

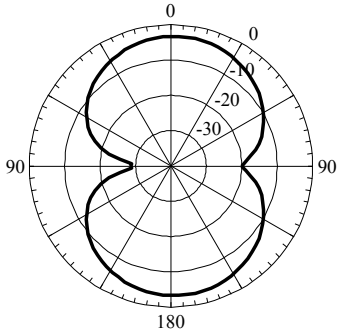

(c)

Figure 6. Measured radiation patterns of the proposed antenna at 916.6 MHz (a) x-z plane at 916.6 MHz, (b) y-z plane at 916.6 MHz and (c) x-z plane at 916.6 MHz

Figure 5 and Figure 6 show omnidirectional radiation patterns as expected with a dipole antenna. The simulated gain across the 434 MHz ISM band is shown in Figure 7 whereas the simulated gain across the 915 MHz band is shown in Figure 8. The proposed antenna exhibits 1.8 dBi of peak gain across the lower band and 2.07 dBi of peak gain across the higher band.

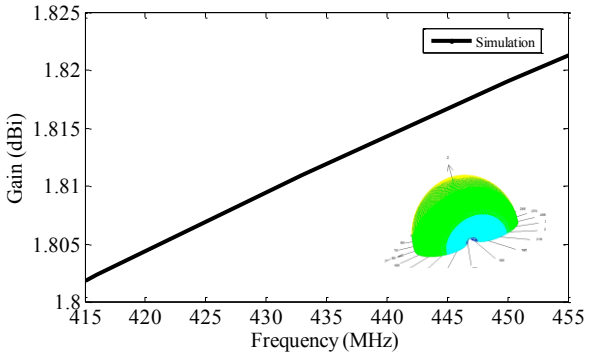

Figure 7. Measure peak antenna gain across the 434 MHz band

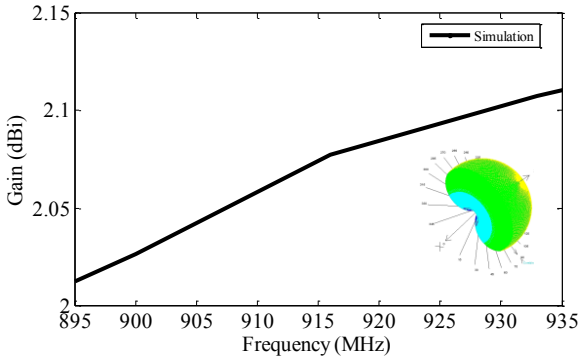

Figure 8. Measure peak antenna gain across the 915 MHz band

Table II summarizes the performances of the antenna for each resonant mode, including simulated peak gain, simulated directivity and simulated efficiency.

TABLE II

SUMMARY OF THE PERFORMANCE OF THE DIPOLE ANTENNA AT 433.3 MHZ AND 916.6 MHZ

Parameter	@433.3 MHz	@916.6 MHz
Gain (dBi)	1.8099	2.0724
Directivity (dBi)	1.9441	2.3719
Efficiency (%)	96.959	93.337

A comparison has been made between the present work and some previous references presenting 434 – 915 MHz dual operation. The results are shown in Table III.

 ISBN: 978-1-61208-297-4

TABLE III

COMPARISON OF PERFORMANCES REPORTED FOR DUAL-BAND OPERATION AT 434 MHZ AND 915 MHZ

Réf.	Types	Dimensions (cm)	Applications
[1]	Metal plate	55.3 x 15.5 x 1	UHF RFID
[2]	Double loop	8 x 3.2 x 0.16	WSN
This work	Dipole	17.3 x 3.4 x 0.15	Sensing UHF RFID

From this comparison, this work proposed a compact configuration in regards to the dimensions of the metal plate antenna reported in [1]. Moreover, the metallic structure is very limited to implement sensing applications and compromises the integration of the antenna proposed in [1] together with a sensor inside the same device. The antenna proposed in [2] is a patch antenna like the one proposed in this paper. It can be easily integrated with any sensor bonded within a package that can be welded on PCB. The antenna reported in [2] has a compact design compared to the antenna proposed in this work but is devoted to bidirectional communication inside a WSN. Thus, it needs a matching network to operate properly, which is an additional constraint in the context of achieving sensing applications with passive devices. The antenna proposed in this work does not need any matching network and can be directly connected to the sensor on a printed circuit board to achieve wireless applications. Like the antenna reported in [1], the proposed antenna can used the 915 MHz band to achieve UHF RFID applications.

IV. CONCLUSION

Dual-band operation with a novel dipole patch antenna has been investigated and a prototype to operate in the 434 and 915 MHz ISM bands has been constructed. The results with the fabricated prototype show good gain and omnidirectional radiation patterns in all the two frequency bands. The antenna is compact in regards to the resonant modes and suitable for sensing applications. The proposed antenna can take advantage of these two ISM bands to improve sensing possibilities with the same device and use the sensing application together with another application such as UHF RFID.

ACKNOWLEDGMENT

This research is partially supported by the Natural Sciences and Engineering Research Council of Canada (NSERC). The authors would also thank the Centre collégial de transfert de technnologie en telecommunications (C2T3) for their support.

REFERENCES

[1] P. Dea-Hwan and M. Kyeong-Sik, "Design for license plate RFID tag antenna with dual resonance to improve identification ratio," in Antennas and Propagation (EuCAP), 2010 Proceedings of the Fourth European Conference on, ed, 2010, pp. 1-4.

[2] S. Genovesi, S. Saponara and A. Monorchio, "Parametric Design of Compact Dual-Frequency Antennas for Wireless Sensor Networks," in Antennas and Propagation, IEEE Transactions on vol. 59, ed, 2011, pp. 2619-2627.

[3] D. Ahbe, S. Beer, T. Zwick, W. Yang and M. M. Tentzeris, "Dual-Band Antennas for Frequency-Doubler-Based Wireless Strain Sensing," in Antennas and Wireless Propagation Letters, IEEE vol. 11, ed, 2012, pp. 216-219.

[4] Z. Zhijun, M. F. Iskander, J. C. Langer and J. Mathews, "Wideband dipole antenna for WLAN," in Antennas and Propagation Society International Symposium, 2004. IEEE vol. 2, ed, 2004, pp. 1963-1966 Vol.2.

[5] I. Kerroum, H. El Matbouly and F. Domingue, "Survey of commercial sensors and emerging miniaturized technologies for safety applications in hydrogen vehicles," in Sensors Applications Symposium (SAS), 2012 IEEE, ed: IEEE, 2012, pp. 1-6.

[6] F. Iacopetti, S. Saponara and L. Fanucci, "Improving Power Efficiency and Reliability in RF Tire Pressure Monitoring Modules," in Electronics, Circuits and Systems, 2007. ICECS 2007. 14th IEEE International Conference on, ed, 2007, pp. 878-881.

[7] D.-S. Lee, Y.-H. Liu and C.-R. Lin, "A Wireless Sensor Enabled by Wireless Power," in Sensors vol. 12, ed, 2012, pp. 16116-16143.

[8] J. M. Boccard and L. M. Reindl, "Printed loop and ceramic antenna for wireless interrogation of SAW resonators on a clamp system," in Systems, Signals and Devices (SSD), 2012 9th International Multi-Conference on, ed, 2012, pp. 1-5.

 ISBN: 978-1-61208-297-4

Miniaturized two-level Controller based on moisture-sensitive Hydrogels

A. Steinke, Th. Frank, A. Cyriax
CiS Forschungsinstitut für Mikrosensorik und Photovoltaik GmbH
D-99099 Erfurt, Germany
asteinke@cismst.de; tfrank@cismst.de; acyriax@cismst.de

C. Bellmann, G. Gerlach
Solid-State Electronics Laboratory
Technische Universität Dresden
D-01069 Dresden, Germany
christian.bellmann@tu-dresden.de; gerald.gerlach@tu-dresden.de

R. Sarwar, H. F. Schlaak
Laboratory of Microtechnology and Electromechanical Systems
Technische Universität Darmstadt
D-64283 Darmstadt, Germany
r.sarwar@emk.tu-darmstadt.de; schlaak@emk.tu-darmstadt.de

***Abstract*— In this paper, we present a novel binary threshold sensor, which is able to use the energy provided directly from the measured relative humidity of the ambient air to mechanically switch an electrical micro contact. This zero-power switch behavior is realized by using the humidity-sensitive volume swelling of a polymer layer as the detection element deflecting a mechanical deformable silicon boss structure, thus closing the electrical contacts of the switch. For the humidity-sensitive sensor switch considered here, a hydrogel blend of 15 wt% poly(vinyl alcohol) (PVA) and 7.5 wt% poly(acryl acid) (PAA) was used. According to first swelling experiments with a prototype the provided deflection of approximately 36 µm of a 20 µm thin silicon flexure plate seems very promising.**

Keywords: binary sensor switch; relative humidity; zero-power; boss structure; hydrogel (PVA / PAAs)

I. INTRODUCTION

The demand for improved processes in industry and the personal environment of humans requires better sensors. As a consequence, sensor industry has been growing in average by 8 % per year since almost three decades. Remarkably, 70 % of all sensors in process control and more than 90 % in building automation are sensors switches acting as threshold switches when changes of particular conditions require dedicated actions. For these purposes, sensors are required, which binarily switch between two pre-defined states. Most of the commercial sensors related to this task are based either on a resistive, a capacitive or an optical measurement principle [1]. Their advantages are a low response time, a high accuracy and a continuous measurement. Unfortunately, they need an electrical processing circuitry as well as an external energy supply to monitor the desired parameter continuously (Fig. 1).

This paper describes another approach for the two point control of relative humidity as water vapor concentration in air and the reduction of the system complexity (compare Fig. 1 with Fig. 2).

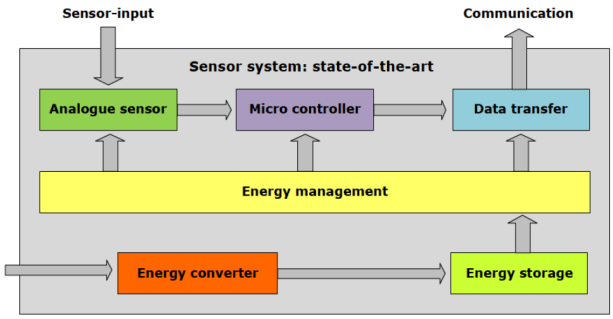

Fig. 1. Signal system of a sensor switch corresponding to the state of the art [7].

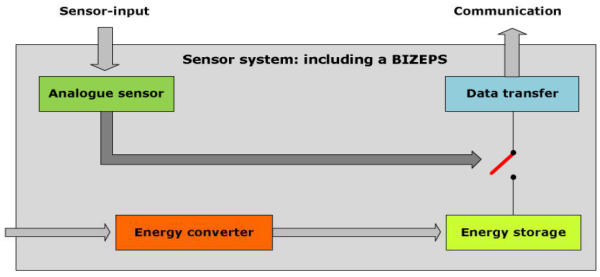

Fig. 2. Signal system of a sensor switch based on the BIZEPS™ platform [7].

 ISBN: 978-1-61208-297-4

We propose a binary zero-power sensor (BIZEPS™) (see Fig. 3) where the humidity causes a transducing element (here a humidity-sensitive hydrogel) to swell. This swelling provides, in contrast to existing solutions, the energy to trigger mechanically an electrical contact. As long as a defined threshold is not reached, the electrical micro contact remains open. The advantages of such polymers are their easy processing technology, their low costs, the adequate availability and the possibility to tailor their properties. The effect of polymer swelling is already used in bimorph sensors [2], biosensors [3] and in sensors for reflectometric interference spectroscopy [4].

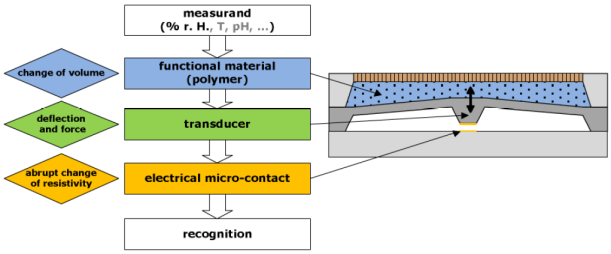

Fig. 3. Operation principle of a binary sensor switch based on the BIZEPS™ platform.

For our intention, two swelling properties can be used. The approach with the largest sensitivity uses the volume increase of the polymer (type B). Due to the absorption of water molecules the polymer swells but remains incompressible. By restricting the free space one can use the resulting high swelling pressure. The second approach uses the bimorph effect, which is based on two connected material layers with different linear expansion coefficients (type A). The expansion of one of the layers due to factors such as temperature or, in our case, humidity, leads to a bending of the bimorph in one direction.

The mechanical part of the sensor switch, which is deflected by the polymer, will be realized with a silicon boss structure as construction part of a thin silicon flexure plate. It offers several advantages:

- The flexure plate shows a suitable compliance with respect to a large enough deflection for the switching movement.
- The boss structure can serve as the switching contact.
- Fast switching needs snap behavior. This can be realized by applying a preload through an oxide layer onto the silicon flexure plate to minimize the effects of the swelling hysteresis.

Due to the expected low contact forces (< 1 mN) provided by the dynamic behavior of the polymer layer, a special contact design has to be applied. Gold nanowires are a promising candidate to minimize the necessary contact force, to decrease the contact resistance and to raise the reliability [5]. They are used in our BIZEPS™ switch as backplate electrode (Fig. 4).

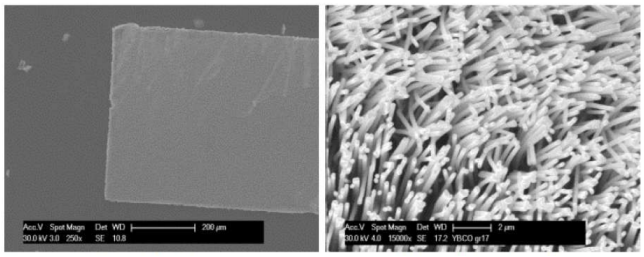

Fig. 4. SEM image (left with low, right with high magnification) of gold nanowires with a density of about 1/µm^2, 200 nm diameter, 10 µm length and an aspect ratio of 90:1 [5].

The gold nanowires are manufactured by optical lithography, galvanic processes and the use of a polycarbonate template which is described more detailed in [6].

II. EXPERIMENTAL

A. *Manufacturing of the humidity sensitive hydrogel*

One key element of the BIZEPS™ platform is the sensitive polymer, which interacts with the parameter to be measured (% r. H., T, pH). Here a hydrogel blend of 15 wt% poly(vinyl alcohol) (PVA) and 7.5 wt% poly(acryl acid) (PAA) in a mass ratio of 4:1 is used. A polymer layer of approximately 20 µm in thickness (measured in dry condition) was created by filling a casting mould of poly(tetrafluorethylen) (PTFE) with the hydrogel solution. PTFE was used because of its very low adhesion force and its hydrophobic behavior. After the evaporation of the solvent, the polymer was annealed at 130 °C for at least 40 min to ensure a high crosslinking. Afterwards, the polymer layer was cut to size.

B. *Sensor prototypes*

1) *Type A – Investigation of the bimorph effect*

The investigation of the swelling pressure caused by the bimorph effect and the resulting deflection was done with the sensor configuration shown in Fig. 5.

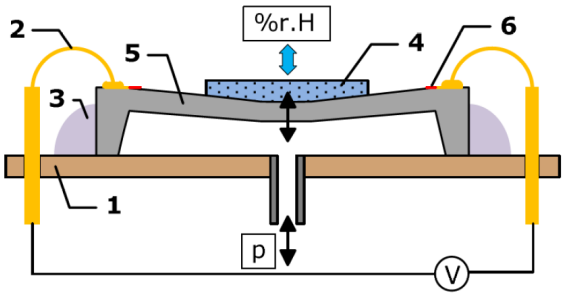

Fig. 5. BIZEPS™ sensor switch based on the bimorph effect (type A): 1. TO8-socket, 2. gold-wire bond, 3. glue, 4. PVA/PAA layer, 5. Si-chip, 6. resistance strain gauge.

A pressure sensor chip with a silicon flexure plate of 3800 x 3800 µm^2 and a thickness of 20 µm was used as basic transducer. A 3 µl drop of the hydrogel blend PVA/PAA was coated directly onto the flexure plate and annealed. It showed a circular shape with a diameter of 2.5 ± 0.8 mm. The

 ISBN: 978-1-61208-297-4

resulting thickness of the polymer layer varied between 5.5 ± 1.2 µm in the middle and 8.8 ± 1.5 µm at the edges. Afterwards, the Si-chip was glued onto a TO8-socket with a small hole which allows varying the pressure to the flexure plate. The electrical contacts between the socket and the resistance strain gauges were done by gold-wire bonding.

The sensor was placed into the conditioning cabinet (Heraeus-Vötsch HC0020) to maintain a constant temperature of about 19.8 °C for 24 hours. During this time the relative humidity φ was reduced in steps from 85 to 10 % r. H. and the voltage output $U_a(\varphi)$ of the resistance strain gauges, which were connected to a Wheatstone bridge, was measured. In the next step, the relative humidity φ was maintained at 10 % and a pressure p between 0 and 40 kPa was applied with a pressure controller (Druck DPI 510) while the resulting output voltage $U_a(p)$ was monitored.

By correlating the characteristic curves of $U_a(\varphi)$ and $U_a(p)$, the dependence $p(\varphi)$ between the pressure and the relative humidity as an approximation of the swelling pressure is obtained. The deflection dependence $w(p)$ of the silicon flexure plate was investigated with a two-beam vibrometer system consisting of a Polytec OFV3001 vibrometer controller and a Polytec OFV502 fiber interferometer. One beam was focused on the edge of the silicon chip while the other one was adjusted to the middle of the flexure plate onto a reflex strip on top of the polymer. This measurement was performed at 10 % r. H..

2) Type B – Investigation of the volume swelling

The influence of the volume swelling to a silicon flexure plate was investigated with the configuration according to Fig. 6.

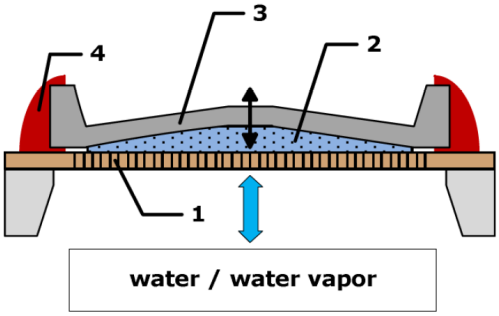

Fig. 6. BIZEPS™ sensor switch based on volume swelling (type B): 1. porous Al_2O_3 membran, 2. crosslinked PVA/PAA layer, 3. silicon chip with a 20 µm silicon flexure plate, 4. silicone glue Scrintec® 901.

For this, the prepared polymer layer was fixed between the sensor chip and a customized porous Al_2O_3 ceramic filter with a thickness of 630 µm using a silicone glue (Scrintec 901). The pores within the ceramic filter was perforated with a laser beam. The average distance between the pores is about 200 µm, their diameter amounts to 50 µm. The filter serves as mechanical restriction for the polymer in the lower direction to lead the volume swelling in the upper direction only deflecting the silicon membrane. On the other side, the porous filter allows the diffusion of the water vapor (and water) into the hydrogel to ensure the sensing function of the polymer layer.

After fabrication, several drops of water were brought into contact with the porous ceramics and the dry polymer. As a result, the water diffused as expected through the holes, and it lead to the volume swelling of the polymer layer. Due to the mechanical stiffness of the ceramic filter the silicon membrane was deflected upward, which was measured by laserprofilometry (µScan, Nanofocus) and a chromatic sensor.

III. Results and Discussion

1) Sensor type A – Investigation of the bimorph effect

The influence of the relative humidity to the hydrogel PVA/PAA coated onto a silicon flexure plate has been studied. According to the results presented in Fig. 7 the silicon flexure plate shows nearly linear deflection up to 23 µm in the range of 10 to 85 % r. H. while the approximated swelling pressure is increasing up to 38 kPa.

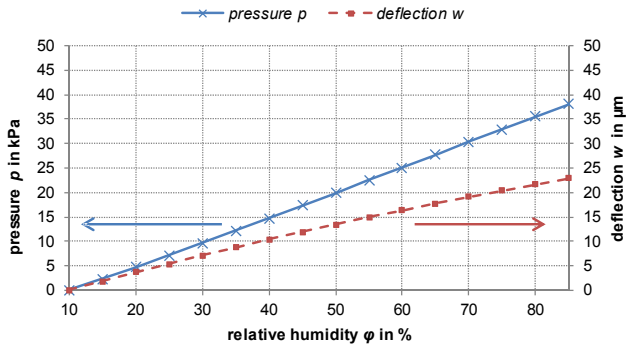

Fig. 7. Influence of the relative humidity on the deflection of a 20 µm silicon flexure plate coated with a PVA/PAA hydrogel blend for the BIZEPS™ sensor of type A based on the bimorph effect.

Because the polymer was not restricted in space during swelling this deflection is mainly caused by the bimorph effect. In detail, by raising the relative humidity, the absorbed water molecules lead to a reduction of the young's modulus and a swelling of the hydrogel fixed to the silicon flexure plate. Because of the geometrical dimensions the polymer expands more in plane than out of plane leading to the deflection of the silicon membrane.

2) Sensor type B – Investigation of the volume swelling

After sensor preparation a first swelling/deswelling cycle was performed. Fig. 8 shows the resulting silicon flexure plate deflection. As can be seen a deflection change of about 36 µm occurs in the range of 10 to 100 % r. H. The initial deflection at 10 % r. H. seems to be caused by a superposition of the bimorph effect resulting from the initial swelling cycle. Nonetheless, the amount of deflection seems to be sufficient for switching devices. The porous ceramic filter operated as expected both as stiff mechanical limitation and element to allow the humidity to penetrate into the hydrogel. However, for applications in fluids, alternative materials like zeolite should be used.

 ISBN: 978-1-61208-297-4

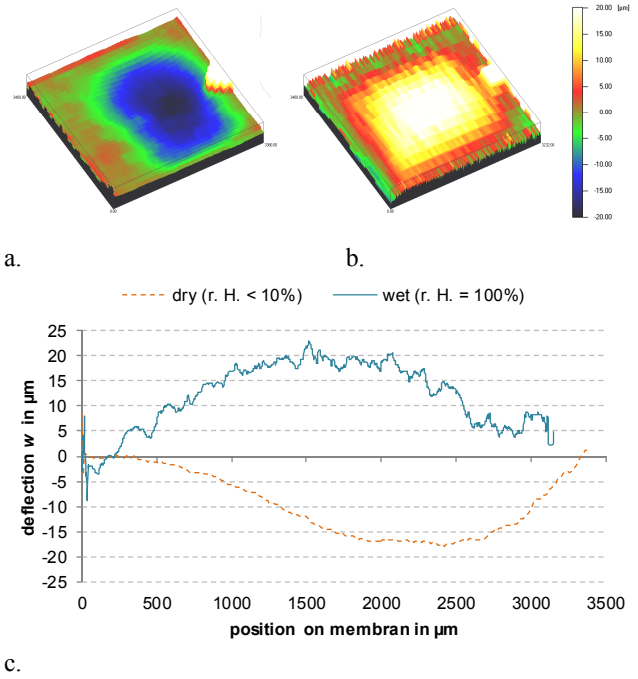

Fig. 8. Overview of the deflection of the silicon membrane in contact with the dry polymer layer (a.) and one line-profile dry (c.) and after contact with drops of water (b.) and on line-profile wet (c.).

3) Suitability of hydrogels for humidity sensor switches

According to the presented experimental results the hydrogel PVA/PAA is a very promising material to provide the required forces to deflect a silicon flexure plate as needed to close an electrical contact. This could be demonstrated both for the volume swelling and for the bimorph effect. However, commercial applications need a more comprehensive investigation of the properties. In particular, several polymer-specific problems have to be considered.

First of all, the fabrication of thin polymer layers which are not coated directly onto the final surface is problematic. This regards the handling, the homogeneity of the layer thickness, the shrinking due to the evaporation of the solvent, the initial swelling and the cross-linking conditions which have to be taken into account. Spin-coating seems to be the more favored technique but did not lead to sufficient results yet, because the layer could not be removed from the used silicon wafer. So far the dipping method with the PTFE casting mould was applied. For an industrial mass production this process shows limited reproducibilty especially when the solvent content in the hydrogel blend is unknown or changingover time.

The second challenge regards the diffusion of water molecules into the hydrogel. The favored all-sided volume swelling is a very slow process.

Another problem is the temperature influence on the maximum saturation vapor pressure and, hence, on the relative humidity as well as the swelling behavior of the polymer.

Swelling and deswelling processes in hydrogels show different time constants which leads to hysteretic behavior during humidity cycles. This hysteresis can be used for the switching behavior of sensor switches but is challenging with respect to the design parameters of the silicon sensor chip and the hydrogel.

Studies on test chips with structured hydrogel of approximately 15 µm revealed that the complete drying (deswelling) is substantially longer than the wetting (swelling). The time until the switch can be switched from the line profile in figures 9 and 10 are not directly derived.

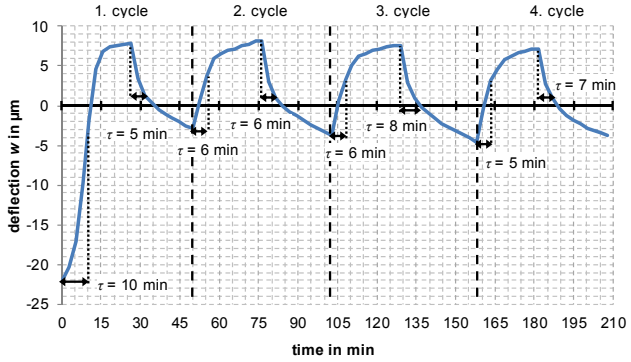

Fig. 9. Line-profil of the deflection of the polymer-coated flexural plate under cyclic wetting / dehumidification (6% ↔ 90% r. H.). Between moisture changes each time 26.3 min.

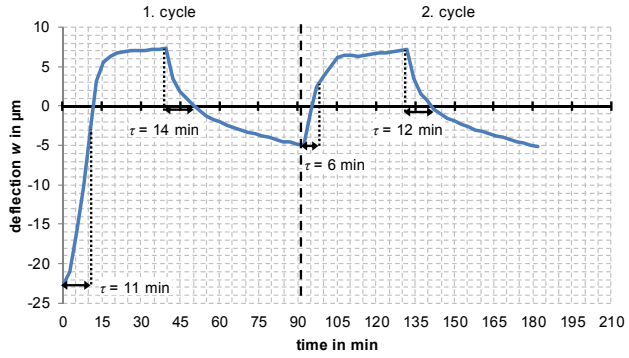

Fig. 10. Line-profil of the deflection of the polymer-coated flexural plate under cyclic wetting / dehumidification (6% ↔ 90% r. H.). Time between changes in humidity respectively 39.5 min to 52.7 min.

For this, the electrode spacing and thus the distance to be covered must be defined first. The time constant τ corresponds to the time when 63% of the final value is reached. According to the measured values of the reversibility within the displayed range is given.

IV. CONCLUSION

The concept of a novel binary zero-power sensor for the monitoring of the relative humidity as water vapor concentration in air was presented. The main advantage of this concept is that the continuous monitoring does not need any external energy supply. Instead, the humidity itself causes the humidity-sensitive hydrogel as basic transducing element to swell and to deflect a silicon flexure plate. Two

 ISBN: 978-1-61208-297-4

swelling-related effects were studied: (type A) the direct volume increase of the hydrogel and (type B) the bimorph effect using the swelling of a hydrogel layer deposited on aflexure plate. The experimental results showed that both effects can provide sufficient deflections of the silicon membrane up to 23 µm with the bimorph effect and 36 µm by volume swelling. A nearly linear correlation between the relative humidity and the deflection was found for the bimorph effect. The estimated swelling pressure amounted to 38 kPa in the range of 10 to 85 % r. H.

ACKNOWLEDGMENT

Financial support from Bundesministerium für Bildung und Forschung (BMBF) (SEMIS, FKZ: 16SV5506K) is gratefully acknowledged.

REFERENCES

[1] Z. M. Rittersma, "Recent achievements in miniaturised humidity sensors – a review of transduction techniques", Senors and Actuators A 96, 2002, pp. 196-210

[2] L.-T. Chen, C.-Y. Lee, W.-H. Cheng, "MEMSbased humidity sensor with integrated temperature compensation mechanism", Sensors and Actuators A 147, Elsevier, 2008, pp. 522-528.

[3] T. Miyata, T. Uragami, K. Nakamae, "Biomoleculesensitive hydrogel"s, Advanced Drug Delivery Reviews 54, Elsevier, 2002, pp. 79-98.

[4] D. Reichl, „Construction, characterization and optimization of an optical sensor system for the reflectometric interference spectroscopy with multicolored LEDs" – „Aufbau, Charakterisierung und Optimierung eines optischen Sensorsystems zur reflektometrischen Interferenzspektroskopie mit mehrfarbigen Leuchtdioden", Dissertation, Eberhard- Karls-Universität Tübingen, 2000.

[5] S. S Baek, R. S. Fearing, "Reducing contact resistance using compliant nickel nanowire arrays", IEEE Transactions on Components and Packaging Technologies, Vol. 31, No. 4, 12.2008.

[6] S. Quednau, H. F. Schlaak, "In-situ generation of arrays of metallic micro-and nanowires in silicon microsystems" – "In-Situ Erzeugung von Arrays aus metallischen Mikro- und Nanodrähten in Silizium-Mikrosystemenen", Mikro-Nano-Integration (GMM-FB 68) – 3. GMM-Workshop, Stuttgart, ISBN: 978-3-8007-3334-7, 03.2011.

[7] Th. Frank, G. Gerlach, A. Steinke, "Binary Zero-Power Sensors: an alternative solution for power-free energy-autonomous sensor systems", Microsyst Technol (2012) 18:1225–1231 DOI 10.1007/s00542-012-1547-4 18.04.2012 - 20.04.2012.

 ISBN: 978-1-61208-297-4

The Development of a Geo-Referenced System for Machine Controlled Construction Equipment

Nicholas Muth
Department of Civil Engineering
Ryerson University
Toronto, Canada
nmuth@ryerson.ca

Mike Chapman
Department of Civil Engineering
Ryerson University
Toronto, Canada
mchapman@ryerson.ca

***Abstract*—This article outlines the motivation and methodology for a reliable, stand-alone, real-time, geo-referencing system for construction equipment. The system consists of a fully integrated Differential Global Positioning System (DGPS)/Inertial Navigation System (INS) Kalman Filter to geo-reference the main body of the construction equipment. Inertial Measurement Units (IMU) attached to each operational joint will provide joint angle information between each link. The IMU information is used in the Denavit-Hartenberg Convention (DH), describing the position of the end-effector in 3D space with respect to the geo-referenced main body of the equipment. There are distinct advantages to this type of approach. It is a more complicated, yet cost-effective, system because lower grade IMUs can be made to perform as more stable IMUs by constant re-calibration using DGPS measurements in a tightly coupled Kalman Filter. It is an autonomous system, unaided by line-of-sight survey based equipment. Finally, it creates a unified model approach for geo-referencing multi-sensor systems that can be applied without accounting for a different set of parameters for each sensor. Preliminary results of a decomposed Kalman Filter to estimate DGPS baselines show a Root Mean Square Error (RMSE) of ±0.003m for variation in successive baseline estimations of stationary receivers.**

Keywords-Geosensor networks; Tracking moving objects; Application of geosensor networks; Localization and tracking using satellites; Movement sensors; Position sensors

I. INTRODUCTION

Construction is an integral part of our overall economy and is of economic significance to many industry sectors and stakeholders. Intense competition, shortages of skilled labor and constant technological advances continue to force rapid change in the construction industry and in support of machine control and Construction Automation (CA) [1].

In order to achieve machine control, considerations must be made regarding equipment operating procedures, construction safety, efficiency, position and navigation. Therefore, machine controlled construction equipment must have the ability to:

- Reference itself in the same coordinate system as the design of the project.
- Navigate in real-time.
- Operate with precision and reliability.
- Position the end-effector accurately.

The research proposed here aims to advance the use of machine control by developing a robust and reliable real-time geo-referencing system for construction equipment focused on the study of an excavator. The geo-referencing system will be a stand-alone system based on the integration of DGPS [2] and INS [3]. The goal of the research is to create a system with centimeter level accuracy in order to achieve Quality Level A standards for precise horizontal and vertical control of utilities, set by the American Society for Civil Engineers *Standard Guideline for the Collection and Depiction of Existing Subsurface Utility Data* [4].

The motivation for research is the potential benefits of a high precision geo-referencing system, including:

- *Safety on the construction site*
- *Optimization of construction tasks*
- *Precision construction/limited accuracy checks*
- *Real-time updating of preliminary survey, design drawings and as-built surveys*

In order to complete the research, the project will be separated into four components. The ***first*** and ***second component***-developing a GPS/INS integrated positioning system to geo-reference the construction equipment body center and relative location of the end-effector with respect to the body center-will be combined in the ***third component*** to create a unified model approach for geo-referencing a multi-sensor system. The ***fourth component*** will be testing system accuracy using one of two approaches: point-to-point comparison of the end-effector position with known locations and comparison of the Digital Elevation Model (DEM) [5] of the construction task with the design of the construction task.

The article has five sections. Section II outlines the current research in real-time geo-referencing systems in the construction environment and the available commercial systems. Section III outlines the methodology of the system including system components (instrumentation, sensors and hardware) and the integration algorithm and architecture for geo-referencing. Section IV outlines work to date, preliminary results of the tightly coupled Kalman Filter decomposed to estimate DGPS baselines and affects this has on the DGPS/INS system. The article concludes with Section

 ISBN: 978-1-61208-297-4

V, by outlining the need for this type of system and stating the overall accuracy goals for geo-referencing.

II. BACKGROUND – GEO-REFERENCING SYSTEMS

The majority of research into absolute, real-time positioning systems has been in Aerial Mapping and Terrestrial Mobile Mapping. The focus of the research is on GPS/INS integration and the argument of centralized versus decentralized integration architecture, which is very well balanced and considered application specific [6].

Aerial navigation is concerned with six degrees of freedom, three position (X, Y and Z) and three orientation (Pitch, Roll and Yaw) components; the same six components needed to geo-reference construction equipment. However, the accuracy of aerial navigation research, in many cases, relies on post-processing even though it is implemented in real-time. One would assume that vehicle navigation is applicable, however, in vehicle navigation it is common to find research on low-order vehicle positioning; navigation that deals with the location of the vehicle, but limits the orientation to two position components (X and Y) and one orientation component (Yaw/Heading) .

A terrestrial multi-sensor GPS/INS system for vehicular mobile mapping conducted by El-Sheimy [7] is worth mentioning due to promising results. The GPS/INS centralized system produced centimeter level accuracy in height.

The majority of studies dealing with positioning construction equipment is in the field of machine control and is based on relative, not geo-referenced, systems. However, large survey companies such as Leica and Trimble, are leading the way in production of off-the-shelf positioning systems for construction equipment. The latest developments include the Leica Powerdigger 3D™ and the Trimble GCS900™.

Powerdigger 3D™ uses a combination of GPS with a pitch, roll and direction sensor to geo-reference the excavator main-body, while the GCS900 ™ system uses a combination of two GPS receivers, a pitch and a roll sensor. Both systems are considered 'black box' integrated, meaning there is no information on the integration algorithm or architecture. There is also no information on the system link between GPS/INS on the excavator body and the end-effector, including the precision of the sensors, the expected accuracy of the ***stand-alone*** system, system testing or field tests.

III. METHODOLOGY

The intent of the research is to design a geo-referencing system based on GPS/INS integration and multiple sensors applicable to several earth-moving machines. However, the focus will be on excavators as they have the most complex range of motion (as many as six degrees of freedom).

The research will be separated into four components:

A. Geo-Referencing the excavator body center.
B. Relative positioning of the Excavator end-effector with respect to the center of the Excavator.
C. Geo-Referencing of the Excavator end-effector.
D. Testing system accuracy.

A. Geo-Referencing of the Excavator Body Center

This section deals with the selection of the instruments, integration algorithm and integration architecture for geo-referencing.

1) Instruments

GPS and INS are the main technologies chosen because of their opposing characteristics. For example, the GPS data latency and signal loss can be accounted for by the high sample rate and high short term stability of INS. Consequently, the INS accumulation of error over time can be accounted for by the high long term stability of GPS. It is this relationship that is the motivation for these sensors to be combined in a geo-referencing system.

Differential GPS (DGPS) using dual frequency receivers will be the specific GPS technique because it can provide many advantages (correcting for several common errors and resolving carrier phase ambiguity) and the centimeter level accuracy desired for this type of positioning.

2) Hardware

Two GPS receivers (base and rover) will be employed; the rover will be fixed to the excavator and the base station set over a known point near the rover. The INS must orient the equipment in three dimensions. This requires three accelerometers and three gyroscopes. The DGPS and INS can be combined in a 'black box' or the hardware of each system run independently and combined on the software level. The research will employ the latter technique because the former makes it difficult to modify the system.

3) Integration Algorithm and Architecture

The integration algorithm will be the Kalman Filter (KF) [8]. It is chosen for its optimum performance, versatility, and ease of implementation obtaining state estimates of a dynamical system in the presence of noisy input sensors. Thus it is the integration algorithm of choice for navigation sensor data.

There are two basic implementation architectures for the KF based on the extent that GPS and INS data aid the others function-tightly coupled and loosely coupled; with no coupling understood as no data feedback from either system.

Tightly coupled, also known as fully integrated or centralized systems, is the chosen architecture because these systems have the best potential accuracy. It requires raw/uncorrelated sensor data. The DGPS will be the main source of navigation because it provides geo-referenced coordinates and will provide constant recalibration of the INS sensors to combat the drifting or unbounded errors of INS over time. The INS, operating at a much higher frequency output, will provide the orientation of the system, as well as, supplement DGPS latency, DGPS outages and smooth transitions between less frequent DGPS measurements.

 ISBN: 978-1-61208-297-4

The result is a non-linear implementation, since both DGPS and INS are non-linear systems. One of the limiting conditions of the KF is the assumption that the system model is linear. Therefore, a method of linearizing the process about some known reference is needed. This is accomplished by implementing an Extended KF (EKF) [9]. The approach has very complex measurement equations, but requires only *one* KF, and thus, is straightforward from the processing point of view.

B. Relative Positioning of Excavator End-Effector

This section deals with the positioning of the excavator end-effector with respect to the excavator body. This includes the types of sensors that will be used to accomplish this, the errors associated with the sensors and a method to propagate the errors to analyze the effect on positioning.

The problem of positioning the end-effector with respect to the equipment main body can be thought of as the positioning a rigid body so it is considered a forward kinematics problem between the relationship of the individual joints of the construction equipment and the position and orientation of the end-effector.

The forward problem is to determine the position and orientation of the end-effector, given the cumulative affect of the joint variables-in an excavator they are simple revolute joints, or the angles between the links (boom, stick and bucket of excavator). The advantage is a single degree-of-freedom of motion for each joint.

Kinematic analysis rigidly attaches a coordinate frame to each link; each coordinate frame must then be related and/or *transformed* in a sequential manner to the inertial frame of reference (excavator center/coordinate frame O_0) as seen in Figure 1. Homogeneous Transformation Matrices (HT) [10] offer the ability to locate any point on construction equipment with respect to the inertial frame and therefore will be used to transform each coordinate frame.

1) The Denavit-Hartenberg Convention

The Denavit-Hartenberg Convention (DH) [10] will be implemented to reduce the number of parameters in the HT from the original six (3 rotations and 3 translations) to four (link length, link twist, link offset and joint angle) by systematically choosing the coordinate frames.

2) Sensors

In order to be a viable option for the private sector, the geo-referencing system must be cost effective and accurate to 1-2cm. For a large excavator (10m boom length) this would require stable sensor accuracy $\leq 0.1°$ arc seconds. This would require high accuracy/stability, high cost IMUs. However, by implementing a centralized KF with constant re-calibration of IMUs, low-grade, high drift rate IMUs can mimic high-grade, low drift rate IMUs. Micro Electronic Mechanical Systems or MEMS sensors built to measure angle/tilt/rotation will be used due to their size (40 to 100mm) and shock limits up to 1000*g*, which is adequate for construction environments.

3) Propagation of IMU Errors

One of the innovations of the relative positioning of the end-effector is the propagation of errors of measurement devices. IMU sensors will be used at each joint with each containing errors. These can be propagated through the network of the excavator to see the effect on geo-referencing, as well as testing the significance of using more/less precise measuring devices.

C. Geo-Referencing the Excavator End-Effector

This is accomplished by developing a unified approach for geo-referencing a multi-sensor system, in this case, composed of DGPS/INS and IMU sensors. The unified approach provides a very important model for sensor fusion in that the model can be applied to sensor data without the need to account for a different set of parameters for each sensor.

The model will be derived for an excavator, but with slight modifications to the transformation matrices, $T_{ee}^{eqp}(t)$ in equation (1), the model be can be used for any type of construction equipment. When the navigation component is supplied by an integrated DGPS/INS system, the equation for the model is of the form (the major steps of equation are shown in Figure 1):

$$r_{ee}^{m} = r_{GPS/INS}^{m}(t) + R_{eqp}^{m}(t)[T_{ee}^{eqp}(t) + a^{eqp}] \quad (1)$$

where *m* is the mapping/absolute reference frame; *eqp* is the INS equipment body reference frame; *ee* is the excavator end-effector reference frame; r_{ee}^{m} is a vector of target point coordinates to be positioned in the absolute reference frame; $r_{GPS/INS}^{m}(t)$ is a vector of the coordinates of the INS center in the absolute reference frame, (estimated by the DGPS/INS integration); $R_{eqp}^{m}(t)$ is the rotation matrix from the INS body frame to the absolute reference frame (estimated by the DGPS/INS integration); $T_{ee}^{eqp}(t)$ are the transformation matrices between the INS body frame and the excavator end-effector (there is a transformation matrix for each joint); a^{eqp} is the translation vector between the INS center and excavator center (constant).

D. Testing System Accuracy

Testing of the system is set to begin in early summer 2013 and will be completed using two methods: point-by-point comparison and Digital Elevation Model (DEM) comparison.

Point-by-point testing will be a comparison of the coordinates of known control points (surveyed by a total station) with those geo-referenced by the excavator.

DEM testing will provide a more dynamic test of the system, closer to the accuracy one would expect from actual operation. It is intended that a human operator will complete

 ISBN: 978-1-61208-297-4

a simple excavation task using a Graphical User Interface (GUI) showing the position of the end-effector as compared to the construction design. After the excavation is complete, a topographic survey will be completed creating a DEM. The DEM, construction design and the actual trajectory measured by the excavator will be compared to quantify human error and assess the accuracy of the system.

In all cases, the excavator will be under human operation.

The success of the accuracy test will be based on the highest accuracy standards. In this case, the American Society of Civil Engineers (ASCE) *Standard Guidelines for the Collection and Depiction of Existing Subsurface Utility Data* [4]-one of the major benefits of this research is construction safety (geo-referencing with respect to safety hazards, i.e., existing underground utilities) and real-time updating of construction records-therefore, the accuracy of the system should strive for the highest quality, or Quality level A, that calls for a vertical accuracy of 15mm [4].

IV. RESULTS

To date, a tightly coupled Kalman Filter (KF) has been developed to integrate the DGPS/INS for geo-referencing the excavator body center. Although a complete DGPS/INS data set, to test the KF, has not been attained, a DGPS data set has been attained. To gain preliminary results, the KF was decomposed to test the DGPS baseline estimation accuracy only.

The DGPS KF utilizes an Extended KF (EKF) design to deal with the non-linearity of calculating the DGPS baseline estimation. The baseline components are estimated using both Course Acquisition (C/A) and Precision (P) code pseudorange and carrier phase observations. Preliminary results show a Root Mean Square Error (RMSE), for variation in successive baseline estimations of stationary DGPS receivers, of ±0.003m with maximum variations of ±0.008m, ±0.005m and ±0.010m in the North, East and Down directions, respectively.

Although the DGPS data is fundamental in the determination of the velocity and position of the excavator center, in order to position the end-effector, orientation of the excavator center, using INS data, must also be solved. Nevertheless, the preliminary results are promising given that in a tightly coupled KF DGPS data is used in comparison with INS to solve the errors of the INS orientation, velocity and position, and consequently, constantly calibrate the INS sensor data.

V. CONCLUSION

The article outlined an ongoing research study in the field of geo-referencing machine controlled construction equipment, the role of geo-referencing in machine control and the benefits it can provide to the overall construction environment.

Geo-referencing using GPS/INS integration has been left to the fields of aerial mapping and terrestrial mobile mapping. Although there has been much research on the integration of GPS/INS using KF, optimal integration architecture is mainly application specific based on motion of the object, processing complexity, flexibility, desired accuracy, integration level, etc. Not only is there a need for the development of a geo-referencing system based on GPS/INS integration, but there is a need to develop optimal integration architecture for construction equipment.

The goal of the research is to develop a stand-alone, robust, reliable, real-time geo-referencing system with centimeter level accuracy, specifically designed for a construction environment. Promising preliminary results for the decomposed Kalman Filter, estimating DGPS baseline components, suggest accuracy goals, on par with ASCE *Standard Guidelines for the Collection and Depiction of Existing Subsurface Utility Data* Quality level A-calling for 15mm vertical accuracy, are achievable.

REFERENCES

[1] Q. Ha, M. Santos, Q. Nguyen, D. Rye, and H. Durrant-Whyte, "Robotic excavation in construction automation," IEEE [Robotics & Automation Magazine]. 2002, vol. 9, is. 1, pp. 20-28.

[2] B.W. Parkinson and P.K. Enge, "Differential GPS," in Global positioning system:theory and applications, vol. II, B.W. Parkinson, and J.J. Spilker Jr., Eds. Washington, D.C.: AIAA, 1996, pp. 3-50.

[3] K.R. Britting, "Inertial navigation systems analysis," New York: Wiley, 1971.

[4] American Society for Civil Engineers(ASCE) Code and Standards Activity Committee, "Standard guideline for the collection and depiction of existing subsurface utility data," ASCE Standard, 2003, ASCE/CI 38-02 [Library of Congress Catalog Card No: 2002034155].

[5] D.F. Maune, "Digital elevation model technologies and applications: the DEM users manual," Bethesda, Maryland: American Society for Photogrammetry and Remote Sensing, 2001.

[6] J. Skaloud, "Problems in direct-georeferencing by INS/DGPS in the airborne environment," In an invited paper to an ISPRS Workshop [Workshop-direct versus indirect methods of orientation, WG III/1, Barcelona], November, 1999.

[7] El-Sheimy, "The development of VISAT - a mobile survey system for GIS applications," PhD Thesis, Department of Geomatics Engineering, University of Calgary, 1996.

[8] R.E. Kalman, "A new approach to linear filtering and prediction problems," Transaction of the ASME—Journal of Basic Engineering. March. 1960, pp. 35-45.

[9] H. W. Sorenson, " Kalman filtering: theory and application," H.W. Sorenson, Eds. IEEE Press, 1985.

[10] R.S. Hartenberg and J. Denavit, "Kinematic synthesis of linkages," New York : McGraw-Hill, 1964.

 ISBN: 978-1-61208-297-4

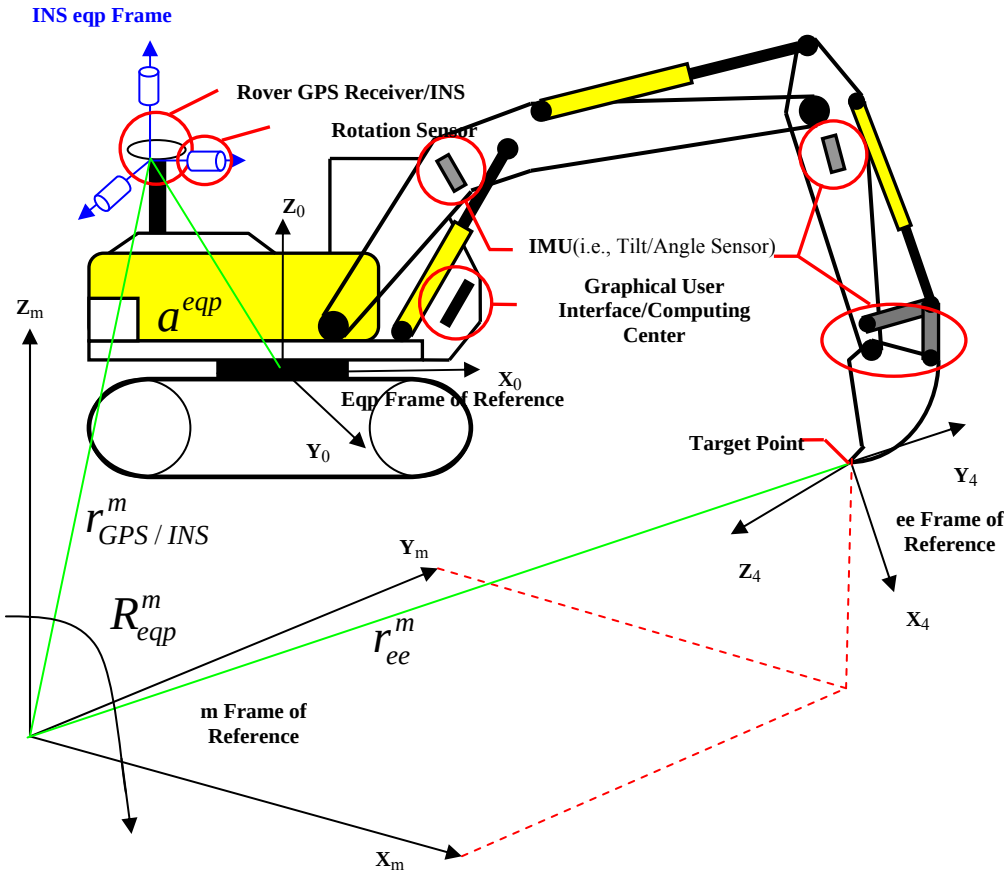

Figure 1. Elements of Geo-Referencing System

Orientation Analysis through a Gyroscope Sensor for Indoor Navigation Systems

Valentina Marotto, Alberto Serra, Davide Carboni
CRS4
Pula, Italy
e-mail: vale@crs4.it, alserra@crs4.it, dcarboni@crs4.it

Mariella Sole, Tiziana Dessi, Andrea Manchinu
GeoWeb Laboratory - Sardegna Ricerche
Pula, Italy
e-mail: sole@crs4.it, tiziana@crs4.it , manchinu@crs4.it

Abstract— **Last years have been characterized by an incredible growth in mobile computing capabilities and sensing technologies, which can leverage the deployment of many location-based applications, ranging from pedometers to navigation system. This work deals with an Inertial Navigation System (INS) able to support users in the navigation in an unknown indoor environment by continuously calculating their motions and their position. The proposed solution is based on integrated use of movement and position sensors. Unfortunately, applications that rely on the use of measures coming from orientation sensors, such accelerometers and digital compasses, are affected by external magnetic interferences thus resulting in inaccurate directional information. This paper focuses on this problem by investigating the use of the gyroscope as the primary determinant of orientation. Several tests have been carried out showing how the proposed method is able to correct the error introduced by the gyroscope both in static position and undergoing rotation, and thus, it is able to provide better orientation information than the compass.**

Keywords-pedestrian navigation; rotation sensors; gyroscope; digital compass; indoor navigation.

I. INTRODUCTION

Nowadays, modern mobile devices, such as smartphones and PDAs in general, come to the market already equipped with sensors able to track them as they move, both in outdoor and in indoor environment. The sensing technologies embedded in such devices make it ideal for a wide range of location-based services, such as navigation applications.

An Inertial Navigation System (INS) uses motion and rotation sensors in order to determine the position, orientation, and velocity of a moving object/user without the need of external infrastructures [1]. This is essential in an indoor environment where common localization systems, such as Global Positioning System (GPS), fail due to severe attenuation or obscuration of the satellite's signal. In inertial navigation systems, localization/orientation estimation is source-independent. The user's position is calculated in relation to a known starting position using a dead reckoning algorithm and the orientation is usually provided by a digital compass embedded in the smartphone. A digital compass sensor provides the orientation of the device relative to the magnetic north of the earth. However, when used in indoor environments, like any magnetic device, it is affected by significant error caused by nearby ferrous materials, as well as local electromagnetic fields. Such errors seriously affect the performance and the accuracy of the system, thus the need to investigate any alternative orientation technique.

The present paper focuses on this problem by investigating the use of a gyroscope for navigation in indoor environment. A gyroscope is a device for measuring or maintaining orientation, based on the principles of angular momentum. The paper is organized as follows: in the next section, we describe the background and related works in the field of indoor navigation systems. Section III provides an overview of the developed application and presents the system architecture. Then, in Section IV, the gyroscope's functionalities are presented and in the next section the gyroscope calibration procedure is described. In Section VI, a comparison between gyroscope and compass behavior is analyzed, and finally, we draw the conclusion in the last section.

II. RELATED WORK

Most mobile navigation systems rely on the use of the digital compass embedded in the smartphone. It is proved that the measurements provided by this sensor are affected by large error, due to the existence of metallic objects and magnetic fields that often compromise the reliability and accuracy of the system. To compensate compass errors, many efforts have been made exploiting different approaches. As experienced by King et al. [2], the measurement errors can vary a lot through the test environment, even if they calibrated the compass in the middle of the operation area. A variation of 1° is measured near the point of calibration, but variations up to 23° are detected a few times in certain points, always close to electromagnetic objects and electronic devices.

Sun et al. [3] proposed a novel approach to provide reliable orientation information for mobile devices in indoor environments that is not affected by magnetic interferences. Pictures of the ceiling of indoor environment are aggregated and computer vision based pattern matching techniques are applied in order to utilize them as orientation references for correcting digital compass readings. Ladetto et al. [4] develop a wearable dead reckoning unit consisting of gyroscope, compass and accelerometer, but they only use the gyroscope for correcting the compass heading errors due to magnetic interferences. In a later work, a pedestrian navigation system was proposed by Ladetto and Merminod [5]. They show that coupling a magnetic compass with a low-cost gyroscope in a decentralized Kalman filter [6]

 ISBN: 978-1-61208-297-4

configuration can limit the errors in the determination of the azimuth of walk. In non-magnetically disturbed areas, the results are close to each other and errors in position are limited. The addition of a gyroscope helps bridging the gap when the compass is strongly disturbed and improves the reliability of the system. Hoshino et al. proposed an extended Kalman filter to combine a magnetic compass and a rate gyroscope for sensor errors compensation [7]. A mathematical model for magnetic compass errors caused by body magnetization is proposed as well as an error model of the rate gyroscope. Barthold et al. [8], exploit the built-in gyroscope in the Nexus S smartphone to address the interference problems associated with the orientation sensor. Many tests were carried out and they proved that integrating the angular velocity output of the gyroscope allows predicting angular orientations to within 6% for test rotations, as well as detecting turns while the phone's orientation was constantly changing. A study to investigate if and how magnetic sensors can be used to replace gyroscopes is conducted by Kunze et al. [9], showing a method to compute angular velocity from 3D magnetic sensor data and discussing its fundamental limitations.

III. APPLICATION FOR INDOOR NAVIGATION SYSTEM

In the context of Indoor Navigation System, we have developed an early prototype of a pedestrian navigation system for indoor environments based on dead reckoning, 2D barcodes and data from accelerometers and magnetometers. All the sensing and computing technologies of our solution are available in common smartphones [10].

The prototype has been further improved by a new algorithm described afterwards (Section V) and now it is able to estimate the correct current position of the user, track him inside the building and provide the best path to achieve a specific destination [11].

The application does not need to connect to any external or pre-installed positioning system such as GPS or Radio Frequency IDentification (RFID), or to use Wireless Fidelity (Wi-Fi) trilateration. The prototype of the proposed system uses just the data from the motion sensors embedded in the smartphone to compute the correct position of the user based on a known initial location, combined with a reference map of the building.

A. Functionality

The initial position of the user, the only certain information on which the system relies on for further calculation, is retrieved by scanning and decoding a geo-referenced datamatrix (2D barcode), placed inside the building, using the built-in camera of the smartphone. Based on the URL encoded in the datamatrix, the application downloads from a dedicated server the indoor vector map for the specific floor, the initial position of the user on the map (corresponding to the point where the user stands when scanning the datamatrix) and a database that stores information about the setup of the building. When the user starts walking, the application draws step by step his position over the downloaded map of the building floor.

The user's position is calculated in relation to a known starting position using a dead reckoning algorithm. In the specific, the application tracks the number of steps taken by the user based on the linear numerical values returned by the smartphone's accelerometers. The acceleration value is the modulus of the accelerations registered in the x, y and z-axes. One step is detected when this module is above a high threshold (*Th_high)* and successively is below a *Th_low* value. To determinate the orientation, only the gyroscope is used thanks to an algorithm of calibration widely described next.

IV. GYROSCOPE

A gyroscope is a device for measuring or maintaining orientation, based on the principles of conservation of angular momentum. It's used primarily for navigation and measurement of angular velocity up to 3 directions: 3-axis gyroscopes are often implemented with a 3-axis accelerometer to provide a full 6 degree-of-freedom (DoF) motion tracking system. There are three basic types of gyroscope:

- *Rotary gyroscopes* are typically composed by a spinning disk or mass on an axle, which is mounted on a series of gimbals; the gyroscope follows the law of conservation of angular momentum, which says that the total angular momentum of a system is constant in both magnitude and direction if the resultant external torque acting upon the system is zero [12];
- *Vibrating Structure Gyroscope* or Micro Electro-Mechanical System (MEMS) contains vibrating elements to measure the Coriolis effect, which states that an object with mass m moving with velocity v, in a frame of reference rotating at angular velocity ω, act a force F_c [13] in a direction perpendicular to the rotation axis and to the velocity of the body in the rotating frame:

$$F_c = -2m(\omega * v) \quad (1)$$

- *Optical Gyroscopes*: they operate on the principle of the Sagnac effect, but, due to the extensive amount of fibre-optic cable needed, optical gyroscopes are mainly used in naval and aviation applications.

Some basic specifications of a gyroscope sensor are:

- *Measurement range*: specifies the maximum angular speed that can be measured by the sensor, is typically expressed in degrees per second $[\mathrm{deg}/\mathrm{sec}]$;
- *Number of sensing axes*: to measure angular rotation, the gyroscope can uses one, two, or three axes. The spatial orientation of a rigid body is thus based on three parameters: *azimuth*, rotation around the z axis; *pitch*, rotation around the x axis; *roll*, rotation around the y axis, as shown in Figure 1;

 ISBN: 978-1-61208-297-4

- *Working temperature range*: from -40˚C to between 70 and 200˚C;
- *Shock survivability*: specifies how much force the gyroscope can withstand before failing. Fortunately, gyroscopes are very robust, and can withstand a very large shock (over a very short duration) without breaking. Generally, this is measured in [g] (1g is the earth's acceleration due to gravity), occasionally is also given the time with which the maximum g-force can be applied before the unit fails;

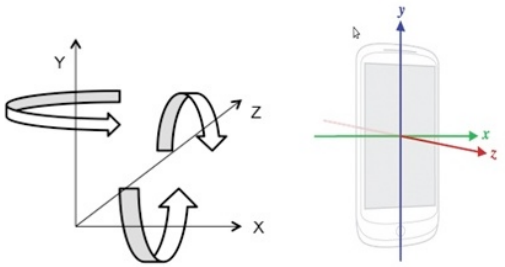

Figure 1. Axes and rotation angles of a smartphone: azimuth (z axis), pitch (x axis) and roll (y axis) parameter.

- *Bandwidth*: the bandwidth of a gyroscope typically indicates how many measurements can be made per second, thus the gyroscope bandwidth is usually intended in $[Hz]$;
- *Angular Random Walk (ARW):* this is a measure of gyroscope noise $[\deg/\sec]$;
- *Bias*: the Bias of a gyroscope sensor is the signal output when it is not experiencing any rotation. The Bias error can be expressed in [deg/sec]. A constant Bias error of ε , when integrated, causes an angular error which grows linearly with time:

$$\theta(t) = \varepsilon * t \tag{2}$$

The aim of this project is to examine the level of accuracy that can be achieved in positioning by using built-in sensors in an Android smartphone. The focus has been put on estimating the position of the mobile phone inside a building only using the gyroscope sensor to determinate the orientation through a specific algorithm of calibration described in the following paragraph.

V. GYROSCOPE CALIBRATION ALGHORITHM

To improve the gyroscope's accuracy we created an algorithm for both still and rotating devices:

- The first part is related to the Bias error when the device is not undergoing rotation. In this case, the constant Bias error of a gyroscope can be estimated by taking a long-term average of the gyroscope's output, which it would be null. Once the Bias is known, it will be subtracted from each value of the gyroscope's output. For this kind of test we have not used any particular equipment, but only the smartphone (Figure 2b) on the level.
- The second part is related to the Bias error when the device is moving.

The equipment used to calculate the real Bias error, when the device is undergoing rotation, is a Stepper Motor (Figure 2a), which converts electrical pulses into discrete mechanical movements. The tests were carried out with a smartphone Samsung Nexus S (Figure 2b). Table I shows the embedded sensors in the smartphone and the angular velocity set in the Stepper Motor.

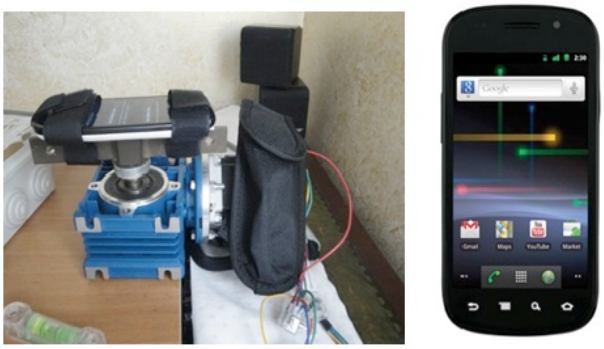

Figure 2. a) Stepper Motor; b) Samsung Nexus S.

TABLE I. SPECIFICATION EQUIPMENT

Embedded sensors in mobile smartphone Samsung Nexus S			
Sensor type		***Manufacturer***	***Quantity Measured***
Accelerometer	KR3DM	STMicroelectronics	Acceleration
Gyroscope	K3G	STMicroelectronics	Angular velocity
Magnetic Field	AK8973	Asahi-Kasei	Magnetic Field
Stepper Motor			
Angular Velocity [rad/s]		0.307876080	

A. Drift Tests

The goal is to find a calibration method for the gyroscope, when the device is not undergoing rotations. In this case, the angular velocity along the three axis should be zero. We calculate the average error of the gyroscope's output along z axis. We have made 4 tests on 1,000, 5,000, 10,000 and 100,000 readings, each composed by 5 sessions (S). This way, we can evaluate how the gyroscope's output changes over time with a constant number of readings.

Table II shows that the average error of the angular velocity is similar for each test and it is independent from the number of readings.

TABLE II. AVERAGE ANGULAR VELOCITY

Session	***Test 1 (1,000 r) μ(z)***	***Test 2 (5,000 r) μ(z)***	***Test 3 (10,000 r) μ(z)***	***Test 4 (100,000 r) μ(z)***
1	-0.00344	-0.00310	-0.00317	-0.00337
2	-0.00321	-0.00329	-0.00328	-0.00361

3	-0.00331	-0.00330	-0,00341	-0.00359
4	-0.00344	-0.00374	-0.00373	-0.00375
5	-0.00290	-0.00288	-0.00291	-0.00319
μ/5	**-0.00326**	**-0.00326**	**-0.00330**	**-0.00350**

The gyroscope's error is completely random and it does not follow a specific error model. For this reason we assume that the Bias is equal to the average error on 1,000 readings. Figure 3 and Figure 4 show how the calibration algorithm improves the accuracy of the output of the gyroscope by subtracting the Bias from each reading.

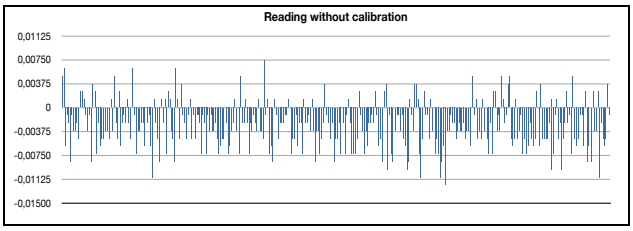

Figure 3. Acquired values from gyroscope without calibration (1,000 readings)

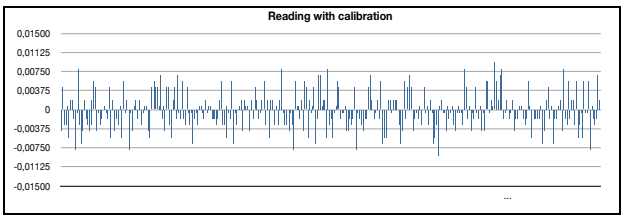

Figure 4. Calibrated values of the gyroscope computed by subtracting the Bias error from each reading (1,000 readings)

B. *Rotation Tests*

To evaluate the error of the gyroscope when the device is undergoing a rotation, a stepper motor is used. It has a constant angular velocity of 0.307876080 [rad/s]. We fixed the device on the stepper motor thus the gyroscope starts reading the angular velocity when the stepper starts moving. We have made three tests with different number of readings (1,000, 10,000, and 20,000). Each test has been done for 10 times as shown in the following Table III.

TABLE III. AVERAGE ERROR OF THE GYROSCOPE COMPARED TO ANGULAR VELOCITY OF THE STEPPER WHILE THE DEVICE IS UNDERGOING A ROTATION AND WITHOUT CALIBRATION

Session	**Moving Test without calibration**			
	Test 1 (1,000 r) μ(z)	***Test 2 (10,000 r) μ(z)***	***Test 3 (20,000 r) μ(z)***	***Stepper μ(z)***
1	0.310910783	0.310656723	0.311009743	0.30787608
2	0.308800393	0.311028093	0.311249073	0.30787608
3	0.310697943	0.310950093	0.311037773	0.30787608
4	0.310861703	0.310756913	0.311065993	0.30787608
5	0.310462643	0.310637243	0.310994773	0.30787608
6	0.309352843	0.310583343	0.311551243	0.30787608
7	0.308340043	0.311504683	0.311021863	0.30787608
8	0.308239443	0.310784043	0.311163783	0.30787608
9	0.310514923	0.310720443	0.310731343	0.30787608
10	0.307767003	0.311079643	0.311277343	0.30787608

As shown in Figure 5, the trend of the blue line, which refers to the 1,000 readings, shows how the average angular velocity acquired by the sensor is significantly different from the trend representing the reference angular velocity.

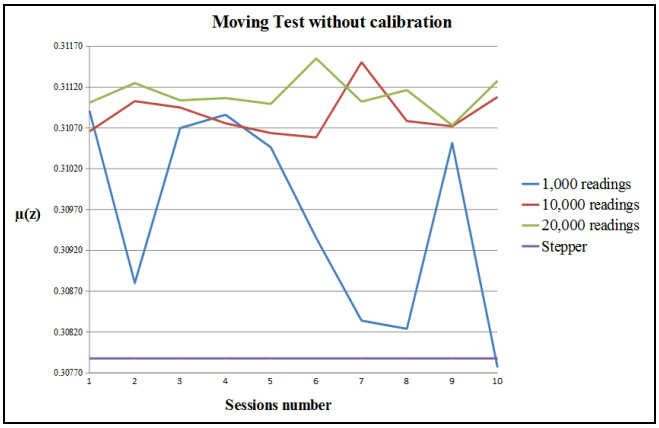

Figure 5. Gyroscope's average angular velocity for 1,000, 10,000 and 20,000 readings compared to the reference angular velocity of the Stepper Motor without calibration

Increasing the number of readings, the red and green line show a more regular trend compared to the blue line, even if they are more shifted upwards than the last one.

The calibration is based on subtracting the Bias error from the average of the number of readings. The following Table IV shows how the averages have changed. Figure 6 highlights how the lines are closer to the reference angular velocity, and this one illustrates and demonstrates the correct algorithm functioning.

TABLE IV. AVERAGE ERROR OF THE GYROSCOPE COMPARED TO ANGULAR VELOCITY OF THE STEPPER WHILE THE DEVICE IS UNDERGOING A ROTATION AND WITH CALIBRATION

Session	**Moving Test with calibration**			
	Test 1 (1,000 r) μ(z)	***Test 2 (10,000 r) μ(z)***	***Test 3 (20,000 r) μ(z)***	***Stepper μ(z)***
1	0.30778804	0.30753398	0.307887	0.30787608
2	0.30567765	0.30790535	0.30812633	0.30787608
3	0.3075752	0.30782735	0.30791503	0.30787608
4	0.30773896	0.30763417	0.30794325	0.30787608
5	0.3073399	0.3075145	0.30787203	0.30787608
6	0.3062301	0.3074606	0.3084285	0.30787608
7	0.3052173	0.30838194	0.30789912	0.30787608
8	0.3051167	0.3076613	0.30804104	0.30787608
9	0.30739218	0.3075977	0.3076086	0.30787608
10	0.30464426	0.3079569	03081546	0.30787608

 ISBN: 978-1-61208-297-4

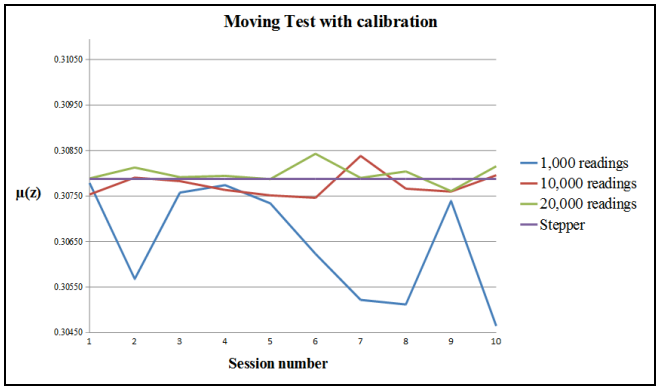

Figure 6. Gyroscope's average angular velocity for 1,000, 10,000 and 20,000 readings compared to the reference angular velocity of the Stepper Motor with calibration

The calibration algorithm has been applied for improving the prototype's functionality of a pedestrian navigation system described in Section III; in this case, is enough to activate the calibration just once at the application's start.

VI. GYROSCOPE VS. COMPASS

Some other tests have been carried out in order to understand if the compass and the gyroscope's error are affected by larger errors in relation to longer paths and if it is possible to find a breakpoint, at which the two errors are comparable. Figure 7 shows the paths inside the building along six different blocks not subjected to electromagnetic pollution, otherwise the compass's output would be been negatively affected.

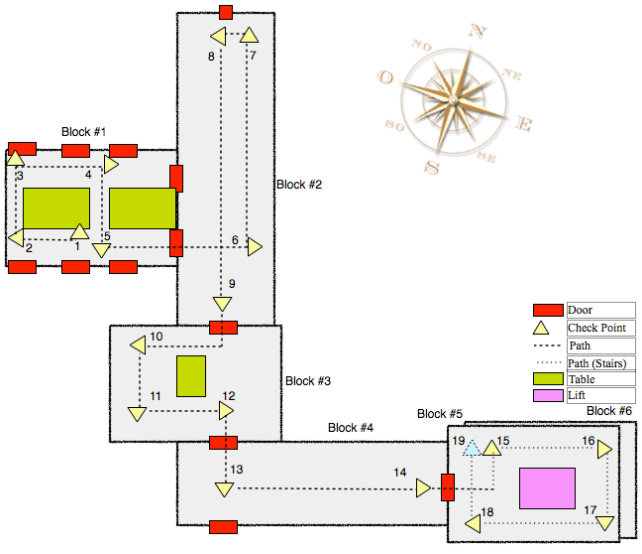

Figure 7. Paths inside a real indoor environment along six different blocks. Each yellow triangle represents a CheckPoint with a predefined orientation

In each checkpoint (described by a numerated triangle), we read the angle rotation of the compass and the gyroscope.

We made 5 paths of different length, starting with the shortest path made of 5 points, and finishing with the longest one made of 19 points, as shown in Table V. The objective is to analyze the absolute error of each sensor as subtracting between the acquired and attempted value. About the gyroscope, the attempted value is a rotation angle composed by a multiple of 90 degrees, while the angle provided by the compass is acquired compared to the real reference system (magnetic north).

TABLE V. REFERENCE PATHS

#Path	*Block1*	*Block2*	*Block3*	*Block4*	*Block5*	*Block6*
1	X					
2	X	X				
3	X	X	X	X		
4	X	X	X	X	X	X

The experimental results have shown how, compared to the gyroscope's absolute error, the compass's absolute error is random and independent from the length of the path, as shown in Figure 8, for a path of 19 checkpoints.

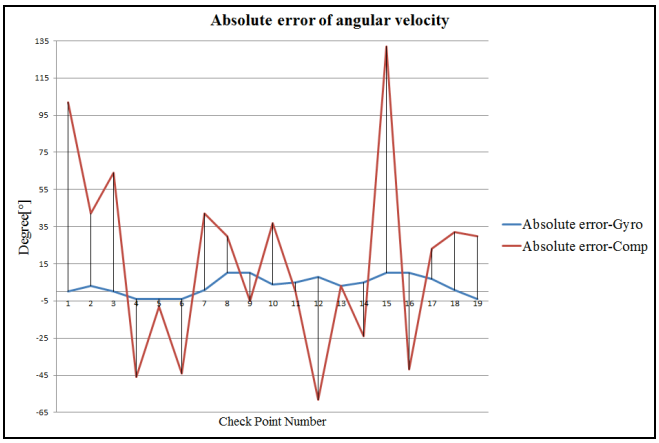

Figure 8. Comparison between the absolute error of Gyroscope and Compass for an indoor path made of 19 CheckPoints

The gyroscope accumulates some errors for rotations in the same verse, while the error decreases for rotation in the opposite verse, resulting in a very small error lying between -4 and 10 degree. The compass's absolute error instead lies between -58 and 132 degrees.

VII. CONCLUSION

The main objective of this paper was to examine the accuracy level that can be achieved in indoor navigation, specifically for the developed prototype [10][11], using exclusively the gyroscope sensor for the orientation. In order to reach the objective, the output from the gyroscope sensor has been analyzed with the device in static position and throughout a rotation. In both cases, the calibration algorithm satisfies the requirement and ensures a better orientation of the used device in indoor environment. Besides, we have

 ISBN: 978-1-61208-297-4

compared the behavior of compass and gyroscope over time and for different paths.

In conclusion, we have established how the gyroscope sensor is better than the compass for indoor navigation, specifically for our mobile application, and how is possible to correct the error introduced from the gyroscope in static position and undergoing rotation.

REFERENCES

[1] A. D. King, "Inertial navigation - forty years of evolution," Handbook of Engineering Fundamentals By Ovid W. Eshbach, GEC REVIEW, vol. 13, no. 3, 1998, pp. 140-149.

[2] T. King, S. Kopf, T. Haenselmann, C. Lubberger, and W. Effelsberg, "Compass: a probabilistic indoor positioning system based on 802.11 and digital compasses," In Proceedings of the 1st ACM International Workshop on Wireless Network Testbeds, Experimental Evaluation & Characterization (WiNTECH), Los Angeles, California, USA, September 2006, pp. 34-40.

[3] Z. Sun, A. Purohit, S. Pan, F. Mokaya, R. Bose, and P. Zhang, "Polaris: getting accurate indoor orientations for mobile devices using ubiquitous visual patterns on ceilings," In Proceedings of the Twelfth Workshop on Mobile Computing Systems Applications (HotMobile '12). ACM, San Diego, CA, USA, February 28-29, 2012, doi: 10.1145/2162081.2162101.

[4] Q. Ladetto and B. Merminod, "In step with INS navigation for the blind, tracking emergency crews," GPS World, vol. 13, no. 10, 2002, pp. 30-38.

[5] Q. Ladetto and B. Merminod, "Digital magnetic compass and gyroscope integration for pedestrian navigation," 9th Saint Petersburg International Conference on Integrated Navigation Systems, Saint Petersburg, Russia, May 27-29 2002, doi:10.3390/s120303720.

[6] Q. Ladetto, Q. Gabaglio, and B. Merminod, "Combining gyroscopes, magnetic compass and GPS for pedestrian navigation," Proc. Int. Symposium on Kinematic Systems in Geodesy, Geomatics and Navigation (KIS 2001), Bariff, Canada, June 5-8 2001, pp. 205-212.

[7] M. Hoshino, Y. Gunji, S. Oho, and K. Takano, "A Kalman filter to estimate direction for automotive navigation," In Proceedings of the IEEE/SICE/RSJ International Conference on Multisensor Fusion and Integration for Intelligent Systems, IEEE, Washington D.C., USA, December 8-11, 1996, pp. 145-150.

[8] C. Barthold, K. Pathapati. Subbu, and R. Dantu, "Evaluation of gyroscope-embedded mobile phones," Conference on Systems, Man, and Cybernetics (SMC), 2011 IEEE International, Anchorage, Alaska, October 9-12, 2011, pp. 1632-1638.

[9] K. Kunze, G. Bahle, P. Lukowicz, and K. Partridge, "Can magneticfield sensors replace gyroscopes in wearable sensing applications?," Published in International Symposium on Wearable Computers (ISWC), October 10-13, 2010, pp. 1-4.

[10] A. Serra, V. Marotto, and D. Carboni, "Indoor pedestrian navigation system using a modern smartphone," In Proceedings of the 12th international conference on Human Computer Interaction with mobile devices and services (MobileHCI 2010), Lisbon, Portugal, September 7-10, 2010, pp. 397-398.

[11] A. Serra, T. Dessì, D. Carboni, V. Popescu, and L. Atzori, "Inertial navigation systems for user-centric indoor applications," In Proceedings of NEM Summit - Towards Future Media Internet, Oct. 2010 Barcelona, Spain.

[12] R. Serway and R. Beichner, "Physics for scientists and engineers," Thomson Learning Inc., Toronto, 5th Ed., 2000.

[13] O. J. Woodman, "An introduction to inertial navigation. Technical report," University of Cambridge, Computer laboratory, Technical report no. UCAM-CL-TR-696, August 2007.

 ISBN: 978-1-61208-297-4

A Coordinated Matrix of RFID Readers as Interactions Input

Maxime Louvel, François Pacull
CEA-LETI MINATEC Campus, Grenoble, France
Email: maxime.louvel@cea.fr ; francois.pacull@cea.fr

***Abstract*—The paper presents a framework to develop applications on a very innovative hardware associating hundreds of rfid readers and a high resolution display within a table. The framework is built on top of a rule-based coordination middleware, which provides mechanisms to handle combinations of events, generated by the rfid readers. The framework offers the basic blocks to fully support the hardware. The paper demonstrates the interest and the possibilities of the framework through simple examples and a more complex scenario. Both illustrate how easy it is to build any kind of interactions with the proposed framework.**

***Keywords*—Coordination Middleware; RFID; Data aggregation.**

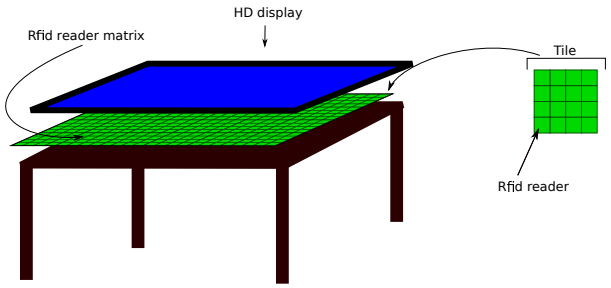

Fig. 1. Description of the table

I. INTRODUCTION

Sensor networks are continuously growing and bringing new designs and usages. The increasing number of devices implied at the same time and the increasingly complex interactions required by the usages does not ease the task of the application programmers. There is a need of a middleware layer, offering as basic bricks high level mechanisms, in order to move most of the complexity from the application to the middleware. This paper illustrates this with an innovative smart table hosting a high resolution display and a matrix of several hundreds of rfid readers. The usage of this table is multiple when it is question of interaction, mediation and collaboration between several users.

The paper is organised as follows. Section II describes the hardware used, an innovative table that allows to detect the identity and the position of rfid tagged objects put on the table and to display arbitrary picture on the HD screen. Section III presents the rule based middleware and the framework built on top, which offers to the application designer the basic interaction involving objects equipped with rfid tags and the 2D graphical engine playing the role of interactive and dynamic tablecloth. Section IV illustrates simple usages of the framework and a more advance scenario. Finally, section V concludes the paper.

II. HARDWARE

To illustrate the capability of our middleware to manage complex events detection, we describe our experiment with an original hardware. This hardware combines a rfid based location system and a HD screen that can be used as classical display.

Fig. 1 depicts the table, composed of two layers. The first layer is a 42" screen able to display with a resolution of HD 1080p. This screen is seen as a classical LCD display and can thus be connected to a computer or a raspberry pi board in this paper. Under this display layer, there is a set of rfid readers organised as a matrix of 6 x 4 tiles, with each tile containing itself a matrix 4 x 4 rfid readers. As a result there are 24 x 16 (384) rfid readers distributed in the table.

This table works with classical rfid tags that can be attached to any physical object. The raw information received is for each rfid reader the set of detected tags. This information is collected via Ethernet. Each tile has its own IP address and gives information for the 16 rfid readers constituting the tile.

There are two interesting functioning modes of this table. In the first mode (push), the tiles are autonomous and send automatically information each time a rfid is seen. In the second mode (pull), each tile can be interrogated in order to have the information.

With this hardware, the applicative fields are quite infinite provided that the middleware offers the required abstraction layer and a powerful mechanism to define the coordination scheme we want to put in place.

III. SOFTWARE

The presented hardware allows a lot of interaction through objects. It needs a high level middleware able to quickly react to the context defined by the set of objects present on the table at the same time. Applications for this hardware typically combine rfid tag location, co-location (several tags), proximity, distance, sequence of tags put on the table. Moreover it is possible to use other interfaces connected to the system (e.g., 3d mouse, cameras). This section firstly introduces the middleware we use. For a more detailed description of this middleware, the reader may refer to [1]. Then the section presents the framework we developed on top to ease the creation of applications using the table.

 ISBN: 978-1-61208-297-4

A. Coordination Middleware

This middleware is an evolution of earlier middlewares [2], [3] specifically designed for lightweight systems. It provides a uniform abstraction layer that eases the integration and coordination of the different components (software and hardware). It relies on the *Associative memory* paradigm implemented in our case as a distributed set of bags containing resources (tuples). Following Linda [4] approach the bags are accessed through the three following operations:

- `rd()` which takes as parameter a partially instantiated tuple and returns from the bag a fully instantiated tuple whose fields match to the input pattern;
- `put()` which takes as parameter a fully instantiated tuple and insert it in the bag;
- `get()` which takes as parameter a fully instantiated tuple, verifies its presence in the bag and consumes it in an atomic way.

For a matrix of rfid readers like the one described above, bags `RawInformation` and `Position` may contain raw data such as `(tagid, tileid, readerid)` or more refined data as `(tagid, posX, posY)`. Depending on the usage (calibration or real application) they both have an interest. Once the location is computed according to the raw data meta-data may be considered from the association between `(physicalTagId, tagId)` or `(tagId, objectId)`.

For actuators, the `put()` operation is used to insert tuples under the form `(actuatorid, function, parameter1, parameter2)`. Once inserted in the bag, it actually triggers the correct action on the physical actuator with the appropriate parameters. The same `put()` operation inserts tuples into bags configuring the readers operating mode or other configuration parameters. Finally, some bags are used to control the videos which are displayed on the table screen.

In addition, bags can be grouped inside objects. For instance an object can model the display on the table and another may handle all the rfid readers.

The operations `rd()`, `get()` and `put()` are used in the Production rules [5] to express the way these resources are used in the classical *pre-condition* and *performance* phases.

Precondition phase: It relies on a sequence of rd() operations to find and detect the presence of resources in several bags. This can be sensed values, result of service calls or states stored in tuplespaces or databases.

The particularity of the precondition phase is that:

- the result of a `rd()` operation can be used to define some fields of the subsequent `rd()` operation;
- a `rd()` is blocked until a resource corresponding to the pattern is available.

Performance phase: It combines the operations `rd()`, `get()` and `put()` to respectively verify that some resources found in the precondition phase are still present, consume some resources and insert new resources. In this phase, the operations are embedded in *distributed transactions*[6]. This particularity ensures several properties that go beyond traditional production rules. In particular it ensures that:

- the conditions responsible of firing the rule (precondition) are still valid in the performance phase;
- the different involved bags are actually all accessible.

These properties are very important since they allow to verify that a set of objects are actually present “at the same time” on the table.

B. Framework

The proposed framework is composed of three objects: *`Rfid`*, *`Display`* and *`2D_Engine`*.

1) Object `Rfid`: This object models the Rfid readers matrix. It contains the following bags:

- `Position(tagId, posX, posY)`: contains the position of the tag (0,0 defines the top left position);
- `LogicalTag(physicalTagId, tagId)`: stores the association of a physical tagId with a more meaningful logical id e.g. (”030209348393”, ”video1”);
- `TagStatus(tagId, status)`: contains the status of a tag: `"in"` if detected by a rfid reader or `"out"` if not seen for a given delay;
- `Mapping(tagId, objectId)`: keeps the association physical object and rfid tag that is attached to it (e.g., an hourglass used to symbolise a timer);
- `Type(tagId, type)`: maintains association of a tagId with a type of tagged object (e.g., physical object, video, action card, badge);
- `Area(areaId, areaDefinition)`: contains areas on the table defined as a set of points defining a polygon;
- `PositionArea(tagId, areaId)`: contains the tagId contained in a given area.

The detection of the tags placed on the table is done by a driver which handles the events sent by the different rfid readers (used in push mode). This information is decoded and the different bags are filled with the corresponding resources. When a tag is detected, the driver computes its position on the table (X,Y) and adds the resource `(tagId, posX, posY)` in the bag `Position`. If several readers detect the same `tagId`, the barycentre is computed. The computation uses as weight the signal strengths of the readers seeing a tag in order to improve the precision of the location. As a rfid reader continuously sends the tag information, a filtering is applied to avoid inserting new resources when it is not necessary. Then, a resource is inserted only when a significant change in the location is effective. In addition, the `status` of the tag, `"in"` if the tag is still on the table or `"out"` if it has been removed (i.e., not be seen for a given delay), is inserted as a resource `(tagId, status)` in the bag `TagStatus` each time the `status` changes.

The bags `Type`, `Area` or `LogicalTag` are configuration bags and their usage is described here after.

 ISBN: 978-1-61208-297-4

a) Introduction to rules: The described middleware allows to express with its rule based language actions to be performed (performance phase) when some conditions (precondition phase) are verified. The actions performed are embedded in transactions enclosed in {}. As `rd()` actions may be included in these transactions, it is possible to ensure that resources found in the precondition are still valid in the performance.

```
1 ["Rfid","TagStatus"].rd(tagId, "in") &
2 # other preconditions
3 ::
4 {
5  ["Rfid","TagStatus"].rd(tagId, "in");
6  # other actions
7 }.
```

Fig. 2. Ensure tag is still there at performance phase

Fig. 2 presents an example of rule, where the precondition and performance part are respectively before and after the `"::"`. To simplify the example, we only show a single operation in the precondition and performance phase but both may contain several additional tokens.

The first token (line 1) reads in the bag `TagStatus` of the object `Rfid` all the tags with status "in". This allows to detect new tags placed on the table and then to manage the corresponding scenario. Line 5 guaranties that the tagId is still on the table when the performance phase executes. Since actions in the performance are embedded in transactions the other actions can only be done if the tag is still there. Note that this approach simplifies a lot the management of events:

- events are detected in preconditions;
- when performances are executed, guaranteeing that the condition related to the event is still valid only requires to add a `rd()` in the performance part.

b) Initialisation rules: Fig. 3 presents an initialisation rule. No precondition is defined, this rule is always executed and only once at the application launch time.

```
1 ::
2 {
3  ["Rfid","LogicalTag"].put("9e7f9cce9","tag_video_table");
4  ["Rfid","Area"].put("zoneA","0,0;0,54,12,54;12,66;66,0");
5  ["Rfid","Type"].put("t_video_presentation_table","video");
6 }.
```

Fig. 3. Initialisation rule

Here we initialise the bags `LogicalTag`, `Area` and `Type`.

In the first bag, we associate the physical tagid `"94e7f89cce9"` to the more user friendly logical tag `"tag_video_table"`. This allows to manipulate in the rules an id that is human readable. In addition, several physical tags can be associated to the same logical tag for backup reason or to offer to several people the possibility to trigger the same action with different objects or cards.

In the second bag, we define a `"zoneA"` as a list of points defining a polygon. This is taken into account by the driver to populate the `PositionArea` bag.

In the third bag, we associate a `type` to a tag. The `type` allows to define a specific context around this tag to verify that it is correctly used. For instance, a tag associated to a voting card cannot be placed everywhere on the table but in a given area. Another usage is to give information to the driver about the sampling frequency for a given tag or if the change in the location is large enough to be reported or not.

c) Defining action area: To better organize the table, area (i.e., zone of the table) can be used. An area is defined by adding a resource `(areaId, areaDefinition)` in the bag `Area`. The `areaDefinition` is a set of points defining a polygon. When the rfid driver detects a new position for a tag, at the same time it inserts the corresponding resource in the bag `Position`, it scans all the defined areas and add the resources `(tagId, areaId)` in the bag `Area`. In the same manner, when the driver inserts a resource `(tagId, "out")` in the bag `Status` it removes all the resources corresponding to the tag in the bag `Area`. This simplifies the application designer's task since she can directly write a rule which starts with a token reading in the bag `Area`.

2) Object `Display`: The second object of the framework manages the displays on the screen. It contains the following bags (non exhaustive list):

- `videoPlayer(playerId, videoname, posX, posY, width, height, orientation, soundTrack)`: this bag accepts only the `put()` operations and launches a video player displaying the video corresponding at filename with the given geometry, with or without soundTrack;
- `video(videoname, status)`: maintains the video status: `started, finished, paused`;
- `videoPlayerCmd(videoname, command)`: accepts only the `put()` operations and the following commands: `"stop"`, `"pause"`, `"resume"`, `"fs_on"`, `"fs_off"` (fs is full screen).

A simple usage of this object is described in Fig. 4. This initialisation rule starts the init video presenting the table on the top left corner of the screen. When the performance is executing, a video player is started and configured to display the video with the resolution (640x480) at position (0,0). The status of the video is set to `"started"`.

```
1 ::
2 {
3  ["Display","video"].put("video_table","started");
4  ["Display","videoPlayer"].put("vlc","video_table",
       "0","0","640","480", "True");
5 }.
```

Fig. 4. Start presentation video of the table

To easily support any kind of video player, the framework uses an external Linux process. The role of this process is to display a video according to a media definition file containing the basic information needed to define the layout, the position, the fact that the sound track is on or off. The display driver saves the PID of the process started in order to interact with it independently of the video player used.

Fig. 5 shows how to stop a video. The precondition waits that the stop card is placed on the table. It then reads the `videoId` of the started video. The performance actually stops the video just by sending the signal `SIGKILL` to the PID playing the video.

 ISBN: 978-1-61208-297-4

```
["Rfid","TagStatus"].rd("tag_stop_video", "in")&
["Display","video"].rd(videoId,"started")
::
{
 ["Display","videoPlayerCmd"].put(videoId, "stop");
}.
```

Fig. 5. Stopping a video with a control card

3) Object `2D engine`: The third and last object of the framework is a 2D engine. It is in charge of displaying the background of the table. It is also in charge of the displayed animations. The current version relies on a Scalable Vector Graphics (SVG) engine to define 2D animations that will be displayed in a simple web browser that is opened in full screen on the table display.

The non exhaustive list of bags is:

- `Background(imagefile)`: When a resource (i.e., an image file) is inserted it replaces the current background of the table;
- `Media(tagId, filename)`: associates a `tagId` to a `filename`;
- `Sprites(spriteId,x,y, svgfile)`: Allows to display a sprite (svg image) at the position `x,y` on the table screen;
- `MoveSpriteGrid(spriteid,x,y,duration, nbsteps,renderlist)`: Allows to define an animation for the sprite defined by `spriteid`. The `duration` of the animation using; `nbsteps` steps and using successively the svg patterns defined in `renderlist`;
- `Visibility(spriteId,percent)`: defines the opacity and the visibility of the sprite.

This object contains in real more than 20 bags that allow not only to define a background but also sprites that can be animated on top of this background. All the svg attributes may be dynamically modified.

The animations are done at the level of the object which returns an html file when invoked through url. This html file is built from static information (templates) present in the file system and contextual information present in the bags. SVG and embedded javascripts take care of the dynamic aspects.

IV. Framework in context

After presenting the framework architecture, this section shows how interactions can be easily encoded with rules, through several examples. It then discusses the interest of the framework compare to other solutions aggregating sensors information. Finally it presents a more complex scenario implemented with the framework.

A. Architecture

Figs 6 presents the current hardware and software setting. It contains the table described in Section II. In addition there are two computing resources: a laptop and a raspberry pi; both embedded inside the table, hidden from the users. The table's screen is connected to the raspberry pi with a HDMI cord,

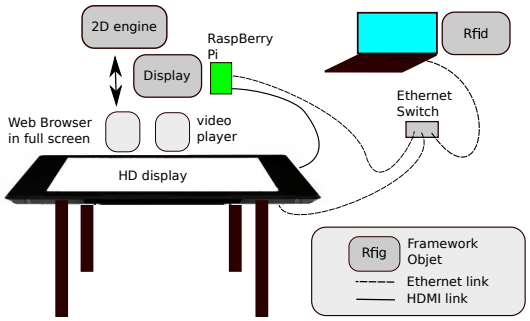

Fig. 6. Global Picture

offering a 1080p HD resolution. The Ethernet switch defines a local area network connecting the matrix of Rfid readers, the raspberry pi and the laptop. From the software point of view, the described objects of the framework are distributed among the two computing resources. The `Rfid` object runs on the laptop, the `2D engine` and the `Display` objects run on the Raspberry pi. In addition a web browser runs on the raspberry pi. It is connected to the `2D engine` object that returns a SVG file according to the current context. The web browser is displayed in full screen on the table display. Video players may be launched on demand on the raspberry pi and displayed on the table screen on top of the web browser.

B. Simple interaction through rules

1) Change the background with a card: In this example (Fig. 7), the background displayed on the screen is changed when a card of type background is put anywhere on the table. The first line of the precondition makes the rule fire only for tags that are known to define a background. Then whenever a card of type background is put on the table (line 2), line 3 finds the filename of the background to render corresponding to the tag id. Then in the the performance phase the action (line 6) changes the background of the table with the content of filename. After the change, it is not necessary to let the card on the table.

```
["Rfid","Type"].rd(tagId, "background")&
["Rfid","TagStatus"].rd(tagId, "in")&
["2D_Engine","Media"].rd(tagId, filename)
::
{
 ["2D_Engine","background"].put(filename);
}.
```

Fig. 7. Rule to change the background when a card is put on the table

You can define as many background as you want, you just need to insert a resource defining the type of your rfid tag as a `"background"` in the bag `"Type"` and a resource to associate the tag id to an image filename in the bag `"Media"`.

2) Display a video at the location of the card: This example aims at starting a video when a card of type video is put. The card's position defines the top-left corner of the video. Fig. 8 gives the rule implementing this scenario. As previously, line 1 and 2 make the rules fires when a video card is put on the table. Line 3 gives the card's position. Finally, line 4 finds the video to be displayed from the tag id. The performance then embeds in one transaction:

- ensuring that the card is still there (line 7);

- starting of the video player with (posX,posY) (line 8);
- saving state "started" for the video (line 9).

```
1  ["Rfid","Type"].rd(tagId, "video")&
2  ["Rfid","TagStatus"].rd(tagId,"in")&
3  ["Rfid","Position"].rd(tagId, posX, posY) &
4  ["Rfid","Mapping"].rd(tagId, videoId) &
5  ::
6  {
7   ["Rfid","TagStatus"].rd(tagId, "in");
8   ["Display","videoPlayer"].put("vlc", videoId, posX,
        posY, "640", "480", "True");
9   ["Display","videoPlayer"].put(videoId, "started");
10 }.
```

Fig. 8. Display video at card's position

3) Play a video at the location of the card or in full screen: This scenario uses two rfid cards, one card to start a video where the card is put and one to display the video in full screen. There are three possible conditions:

1) video card only: display the video where the card is put;
2) both cards: display the video in full screen;
3) full screen card only: do not display anything.

Condition 1 has been detailed in Fig. 8.

Fig. 9 implements condition 2. Lines 1-3 check that both cards are on the table. Line 4 fires when the video has been started (by rule in Fig. 8). The performance phase checks that both cards are still on the table, the video is started an the video player is switched to full screen by adding a resource in the bag `videoPlayerCmd` (line 10).

```
1  ["Rfid","TagStatus"].rd("tag_fullScreen", "in")&
2  ["Rfid","Type"].rd(videoId, "video") &
3  ["Rfid","TagStatus"].rd(videoId, "in")&
4  ["Display","videoPlayer"].rd(videoId, "started")&
5  ::
6  {
7   ["Rfid", "TagStatus".rd(videoId, "in") ;
8   ["Rfid","TagStatus"].rd("tag_fullScreen", "in");
9   ["Display","videoPlayer"].rd(videoId, "started");
10  ["Display","videoPlayerCmd"].put(player, "fs_on");
11 }.
```

Fig. 9. Put video in full screen

It is then necessary to write a rule (Fig. 10) to leave the full screen mode if the full screen card is removed from the table. This rule is triggered when the full screen control card is `"out"` (line 1). As previously, the performance checks the player and the cards' status and adds a resource in the bag `videoPlayerCmd` (line 10).

```
1  ["Rfid","TagStatus"].rd("tag_fullScreen", "out")&
2  ["Rfid","Type"].rd(videoId, "video") &
3  ["Rfid","TagStatus"].rd(videoId, "in")&
4  ["Display","VideoPlayer"].rd(videoId, "started")&
5  ::
6  {
7   ["Rfid", "TagStatus".rd(videoId, "in") ;
8   ["Rfid","TagStatus"].rd("tag_fullScreen", "out");
9   ["Display","VideoPlayer"].rd(videoId, "started");
10  ["Display","VideoPlayerCmd"].put(player,"fs_off");
11 }.
```

Fig. 10. Leave full screen

C. Discussion

This section has illustrated the simplicity of writing interactions with the proposed framework. The detailed examples show how information coming from a set of sensors may be aggregated as a complex distributed event.

This is usually implemented with a publish-subscribe approach[7], where subscribers register to specific events generated by publishers (rfid readers in this paper). This has been applied in the context of sensor networks [8]. With such a system it is possible to write code that would be similar to the precondition part of the rules presented in this section. For instance to react to a tag detected in a specific area or to an external event. However, in a publish-subscribe approach when the system has to react upon a set of events or to be sure that the events are still valid when the actions have to be executed, the amount of additional code is not negligible.

With the framework developed on top of our middleware expressing an event as "one card is put in a specific area" and "another card of a specific type is put at the same time anywhere else" is simply a sequence of rd() tokens.

In addition, defining what to do if a card is put on the table an immediately removed is possible thanks to the distributed transaction offered in the performance phase.

D. Scenario

We described here a simple application based on this framework which uses quite complex interactions between several users around this table. The application allows to collect the opinion of a panel of people to elect the better equipment, concept or decision according to a set of criteria. In the present example the panellists are asked to give their opinions about a set of smartphones according to the following criteria: aesthetic, user interface, size and autonomy. These criteria are noted respectively A, B, C and D and can take the value positive or negative depending on the majority of vote from the panellists. The resulting information is displayed as a Veitch diagram as shown in Fig. 11.

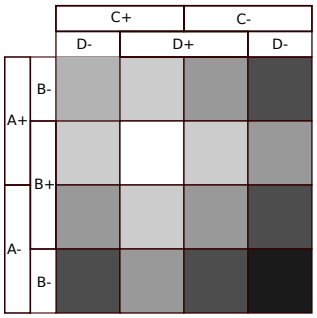

Fig. 11. Veitch Diagram

The white cell contains the best choices that receive 4 positive opinions. The adjacent cell contain choices that receive 3 positive opinions. The darker a cell is, the more negative it is. The black bottom right cell contains the worst choice with 4 negative opinions. This section now details what is an interaction session and gives a few hints on the implementation.

 ISBN: 978-1-61208-297-4

1) Interaction session: At the beginning, each panellist has a badge representing her identity. The master of session presents a smartphone and may display a video on the table by putting the corresponding card on it. Some modifier cards added to the table may modify the display either by switching to fullscreen or by launching a second video player with a 180 rotation to adapt to situation where people are all around the table. In this case, the second video uses the same video flow (without sound track) and is synchronised with the first one. Once the presentation is done, the vote may start. The master of session places the card corresponding to the criterion (e.g., aesthetic) and then the table display shows two areas, one green to collect the badges of panellists liking the smartphone design and one red for those that are not enthusiastic. An additional video or photo specific to this criterion may also be displayed. Then, the master of session triggers the vote by placing an hourglass (tagged with an rfid) on the table. A timer indicates at each corner of the table the remaining time for the vote. Each panellist put her badge on the table according to her opinion. A circle is displayed around the badge to return a feedback to the user. Different modalities may be configured at the beginning of the session to control the vote:

- the duration of a vote phase;
- missing vote is considered as negative or positive;
- a vote is definitive or not.

Once the timer reaches zero the votes are stored for further processing and the master of session can go to the next criterion. When all the criteria have been considered, the master of session can go to the next smartphone. At any moment, the master of session may place a card on the table to display or print current status of the Veitch diagram.

2) Implementation: The full application described here may be implemented by using small variation of the basic interactions involving `Display`, `2D_Engine` and `Rfid` objects presented in the framework section. plus a specific `Veitch` object that contains bag used to store panellists identities, votes and current step in the session (smartphone number and criteria number). The basic settings, configuring a working session, are done through initialisation rules that define modalities such as default value of missing vote or the identity of the panellists. Note that using the proposed framework is very appropriate since adding new features simply requires to add new rules. Existing rules can continue to work without concern. We can for instance, use an initial round getting the identities of the panellists rather than using a configuration rule. This can be done without any other impact that replacing the initialisation rule with the three rules required to obtain the identity of the panellists: i) open identity round with detection of the specific control card, ii) copy each badge id detected to the bag panellist and iii) close identity round by detecting that the specific control card is no longer on the table. This obviously works, with any number of panellists.

V. Conclusion

This paper has presented an innovative hardware and a framework easing the development of applications on top of it. The hardware combines a full HD display and a set of 384 rfid readers allowing to return the location of several tens of object tagged with Rfids.

The framework is built on top of a rule-based middleware relying on production rules and distributed transactions to ease events' combination handling. It uses a driver which maps rfid events into resources stored in bags allowing the resources to be accessible with simple rules, thanks to the middleware. This allows to react to event composing several rfid tags and to embedded event verification in distributed transactions.

To ease the developer task, bags are grouped into three objects to manage the Rfid reader matrix, to start and stop videos and to interact with the 2D engine offering the dynamic background of the table. This paper has shown through simple examples and a more complex scenario how the framework helps designing applications for the proposed hardware.

Future works will take two directions. One is to develop other applications around the decision making field to show that the table plus the framework is a full kit to quickly develop and customize such type of applications. The second is to integrate more external sensors and actuators to the framework. Cameras which can deduce the number of people around the table (e.g., counting the detected faces), sensors computing the distance of the users from the table, voice interface, etc. are informations that once combined with information returned by the table may offer a richer user experience.

Acknowledgement

The authors would like to thank Nicolas Géraud from Dasein Interactions for the numerous advices about the user's interactions of the Veitch application. This work has been partially funded by the FP7 SCUBA project under grant nb 288079 and FUI Rapsodie project under grant nb F1209039V.

References

[1] L.-F. Ducreux, C. Guyon-Gardeux, S. Lesecq, F. Pacull, and S. R. Thior, "Resource-based middleware in the context of heterogeneous building automation systems," in *IECON 2012-38th Annual Conference on IEEE Industrial Electronics Society*. IEEE, 2012, pp. 4847–4852.

[2] J.-M. Andreoli, F. Pacull, D. Pagani, and R. Pareschi, "Multiparty negotiation of dynamic distributed object services," *Journal of Science of Computer Programming*, vol. 31, pp. 179–203, 1998.

[3] D. Arregui, C. Fernström, F. Pacull, G. Rondeau, and J. Willamowski, "Stitch: Middleware for ubiquitous applications," in *In Proc of the Smart Object Conf*, 2003.

[4] N. Carriero and D. Gelernter, "Linda in context," *Commun. ACM*, vol. 32, pp. 444–458, April 1989.

[5] T. A. Cooper and N. Wogrin, *Rule Based Programming with OPS5*. Morgan Kaufmann, July 1988.

[6] P. A. Bernstein, V. Hadzilacos, and N. Goodman, *Concurrency control and recovery in database systems*. Boston, MA, USA: Addison-Wesley Longman Publishing, 1987.

[7] P. T. Eugster, P. A. Felber, R. Guerraoui, and A.-M. Kermarrec, "The many faces of publish/subscribe," *ACM Computing Surveys (CSUR)*, vol. 35, no. 2, pp. 114–131, 2003.

[8] E. Souto, G. Guimarães, G. Vasconcelos, M. Vieira, N. Rosa, C. Ferraz, and J. Kelner, "Mires: a publish/subscribe middleware for sensor networks," *Personal and Ubiquitous Computing*, vol. 10, no. 1, pp. 37–44, 2006.

 ISBN: 978-1-61208-297-4

Combinational Optoelectronic Circuit Based on SiC Technology

M.A. Vieira, M. Vieira, P. Louro, V. Silva, A. Fantoni
DEETC/. ISEL
Lisbon, Portugal
e-mail: mv@isel.ipl.pt

M.A. Vieira ,M. Vieira P. Louro, V. Silva, A. Fantoni
CTS/. UNINOVA
Monte de Caparica, Portugal
e-mail: mv@isel.ipl.pt

Abstract— **The purpose of this paper is the design of simple combinational optoelectronic circuit based on SiC technology, able to act simultaneously as a 4-bit binary encoder or a binary decoder in a 4-to-16 line configurations. The 4-bit binary encoder takes all the data inputs, one by one, and converts them to a single encoded output. The binary decoder decodes a binary input pattern to a decimal output code. The optoelectronic circuit is realized using a a-SiC:H double pin/pin photodetector with two front and back optical gates activated trough steady state violet background. Four red, green, blue and violet input channels impinge on the device at different bit sequences allowing 16 possible inputs. The device selects, through the violet background, one of the sixteen possible input logic signals and sends it to the output. Results show that the device acts as a reconfigurable active filter and allows optical switching and optoelectronic logic functions development. A relationship between the optical inputs and the corresponding digital output levels is established. A binary color weighted code that takes into account the specific weights assigned to each bit position establish the optoelectronic functions. A truth table of an encoder that performs 16-to-1 multiplexer (MUX) function is presented.**

Keywords- SiC Optoelectronic device, photonics, optical communications, MUX/DEMUX; encoders, logic functions.

I. INTRODUCTION

There has been much research on semiconductor devices as elements for optical communication, when a band or frequency needs to be filtered from a wider range of mixed signals or when optical active filter are used to select and filter input signals to specific output ports in WDM communication systems [1, 2].

Optical communication in the visible spectrum usually interfaces with an optoelectric device for further signal processing. Multilayered structures based on amorphous silicon technology are expected to become reconfigurable to perform WDM optoelectronic logic functions [3, 4]. They will be a solution in WDM technique for information transmission and decoding in the visible range [5]. The basic operating principle is the exploitation of the physical properties of a nonlinear element to perform a logic function, with the potential to be rapidly biasing tuned Any change in any of these factors will result in filter readjustments. Here, signal variations with and without front and back backgrounds move electric field action up and down in a known time frame. A truth table support new optoelectronic logic architecture.

II. DEVICE OPERATION

The optoelectronic circuit consists of a p-i'(a-SiC:H)-n/p-i(a-Si:H)-n heterostructure with low conductivity doped layers as displayed in Fig.1. The optoelectronic characterization was described elsewhere [6]. Monochromatic pulsed lights, separately (λ_R=626 nm, λ_G=526 nm, λ_B=470 nm, λ_V=400 nm; input channels) or in a polychromatic mixture (multiplexed signal) at different bit rates illuminated the device.

Independent tuning of each channel is performed by steady state violet optical bias (λ_{bias}= 2300 μW/cm^2) superimposed either from the front and back sides and the generated photocurrent measured at -8V. The device operates within the visible range using as input color channels (data) the wave square modulated light (external regulation of frequency and intensity) supplied by a red (R; 25 μW/cm^2), a green (G; 46 μW/cm^2), a blue (B; 40 μW/cm^2) and violet (V; 150 μW/cm^2) LED's.

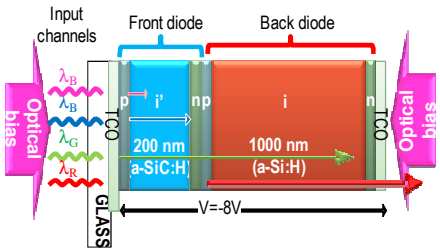

Figure 1. .Device configuration and operation.

III. OPTICAL BIAS CONTROLLED FILTERS

In Fig.2, the spectral photocurrent, normalized to its value without background is displayed, under front (a) and

 ISBN: 978-1-61208-297-4

back (b) violet irradiations and different intensities.

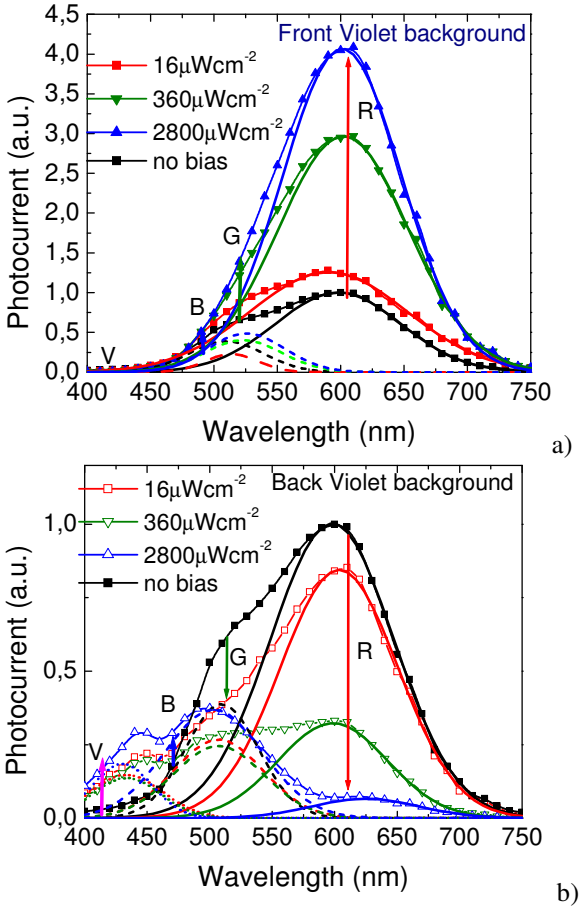

Figure 2. Normalized spectral photocurrent under front (a) and back (b) violet irradiations with different intensities.

A peak fit adjustment to the data was performed (lines) with peaks centered on 630 nm (solid), 520 nm (dash) and 430 nm (dot). Results show that under front violet irradiation, as the background intensity increases, the peak centered at 630 nm (red range) strongly increases while under back light an opposite behavior is observed and the red peak is strongly reduced (see arrows). Under front and back side irradiation, the peak at 520 nm (green range) increases slightly with the intensity. Under back irradiation, a new peak centered at 430 nm appears and increases with the background intensity. So, under front illumination the reddish part of the spectrum is strongly enhanced with the intensity while under back illumination the main enhancement occurs at the violet-blue region. A trade-off between the background intensity and the enhancement or quenching of the different spectral regions, under front and back irradiation, has to be established.

In Fig. 3 the spectral gain (α^V), defined as the ratio between the spectral photocurrents under violet illumination (applied from the front and back sides) and without it, is plotted at 3500 Hz and 2300μWcm^{-2}. As expected from Fig. 2, under back bias the gain is high at short wavelengths and strongly lowers for wavelengths higher than 500 nm, acting as a short-pass filter. Under violet front light the device works as a long-pass filter for wavelengths higher than 550 nm, blocking the shorter wavelengths. Results show that by combining the background wavelengths and the irradiation side the short-, and long- spectral region can be sequentially tuned. The medium region can only be tuned by using both active filters.

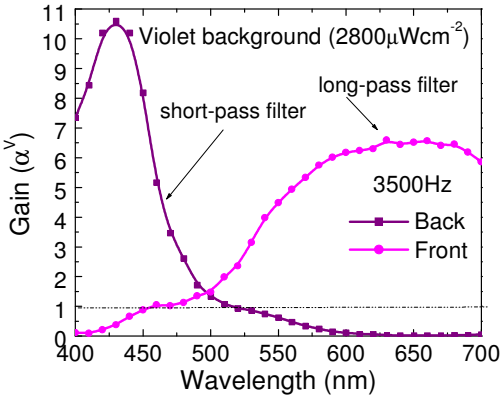

Figure 3. Spectral gain under violet (αV) optical bias, applied from the front and the back sides at 3500Hz.

IV. ENCODER AND DECODER DEVICE

A. *Optical switching*

Four monochromatic pulsed lights separately (red, green, blue and violet input channels, Fig. 4) or combined (multiplexed signal, Fig. 5) illuminated the device at 12000 bps. Steady state violet optical bias was superimposed separately from the front (a) and the back (b) sides and the photocurrent measured. In Fig. 4, the transient signals were normalized to their values without background and added the mean values of the optical gains for each individual channel.

Results show that, even under transient conditions and using commercial LED's as pulsed light sources, the background side affects the signal magnitude of the color channels. As in Fig. 2, under front irradiation, it enhances mainly the spectral sensitivity in the medium-long wavelength ranges (α^V_R=4.7, α^V_G=2.4). Violet radiation is absorbed at the top of the front diode, increasing the electric field at the back diode [7] where the red and part of the green incoming photons are absorbed (see Fig. 1). Under back irradiation the electric field increases mainly near the front p-n interface where the violet and part of the blue incoming channels generate most of the photocarriers (α^V_V=11, α^V_B=1.5). So, by switching between fronts to back irradiation the photonic function is modified from a long- to a short-pass filter allowing, alternately selecting the red or the violet channels.

 ISBN: 978-1-61208-297-4

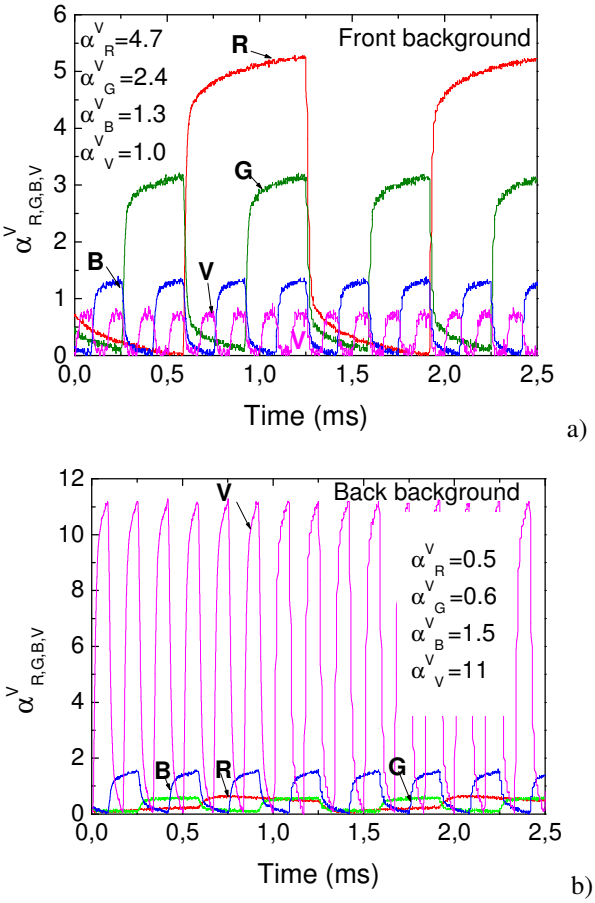

Figure 4. Normalized red (R), green (G) blue (B)and violet (V) transient signals at -8V with violet (400 nm) steady state optical bias applied from the front (a) and from the back (b) sides.

B. *Optoelectronic logic functions*

For an optoelectronic digital capture system, opto-electronic conversion is the relationship between the optical inputs and the corresponding digital output levels.

Fig. 5 displays the normalized MUX signals due to the combination of the input channels of Fig. 4, without and under front (a) and back (b) violet irradiations. On the top the signals used to drive the input channels are displayed showing the presence of all the possible 2^4 *on/off* states. For comparison the MUX signal without optical bias is displayed (dark) in both figures.

Results show that the side of background affects the form and the magnitude of the MUX signal in opposite ways. Under front irradiation, sixteen levels (2^4) are detected and grouped into two main classes due to the high amplification of the red channel (α^V_R>>1; Fig. 4a). The upper eight (2^3) levels are ascribed to the presence of the red channel (R=1), and the lower eight to its absence (R=0), allowing the red channel decoder (8-to-1 multiplexer; long-pass filter function). Since under front irradiation the green channel is also amplified,(α^V_G>1) the four highest levels, in both classes, are ascribed to the presence of the green channel (G=1) and the four lower ones to its lack (G=0).

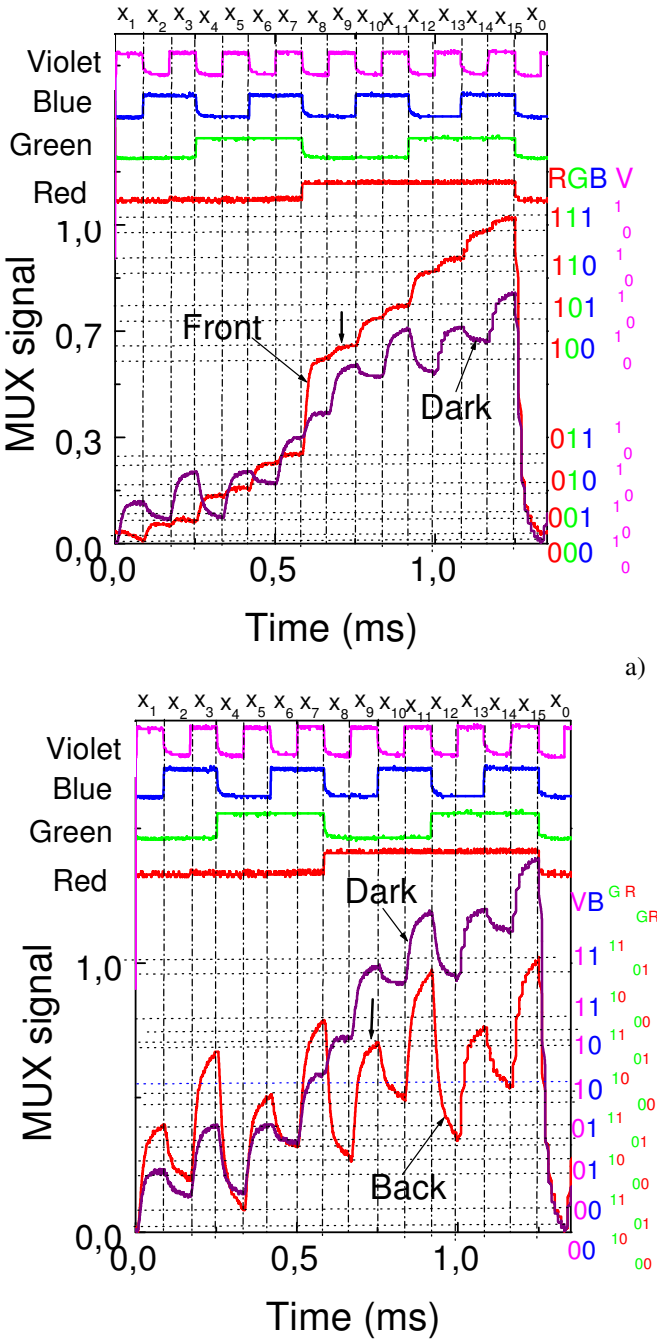

Figure 5. Normalized multiplexed signal under front (a) and back (b) violet irradiation and without it (dark). On the top the signals used to drive the input channels are shown to guide the eyes into the ON/OFF channel states.

The blue channel is slightly amplified, so, in each group of 4 entries, two levels (2^1) can be found: the two higher levels correspond to the presence of the blue channel (B=1) and the two lowers to its absence (B=0). Finally, each group of 2 entries have two near sublevels, the higher where the

 ISBN: 978-1-61208-297-4

violet channels is ON (V=1) and the lower where it is missing (V=0). Under back irradiation, the violet channel is strongly enhanced, the blue channel is slightly and the green and red reduced (α^{V}_{R} and $\alpha^{V}_{G}<1$ and $\alpha^{V}_{B}>1$ and $\alpha^{V}_{V}>>1$; Fig. 4b). The encoded multiplexed signal is, also, made of sixteen sublevels grouped into two main levels, the higher where the violet channel is ON (V=1) and the lower where it is OFF (V=0) (8-to-1 multiplexer; short-pass filter function). Each group the eight sublevels can be grouped in two classes, with and without the blue channel ON. Each of those classes split into four near sublevels, attributed to the presence or absence of the red and green channel. If we consider this red and green output bits "not significant" only four separate levels (2^2) are considered and the logic MUX function is converted into a logic filter function. The violet channel is then decoded.

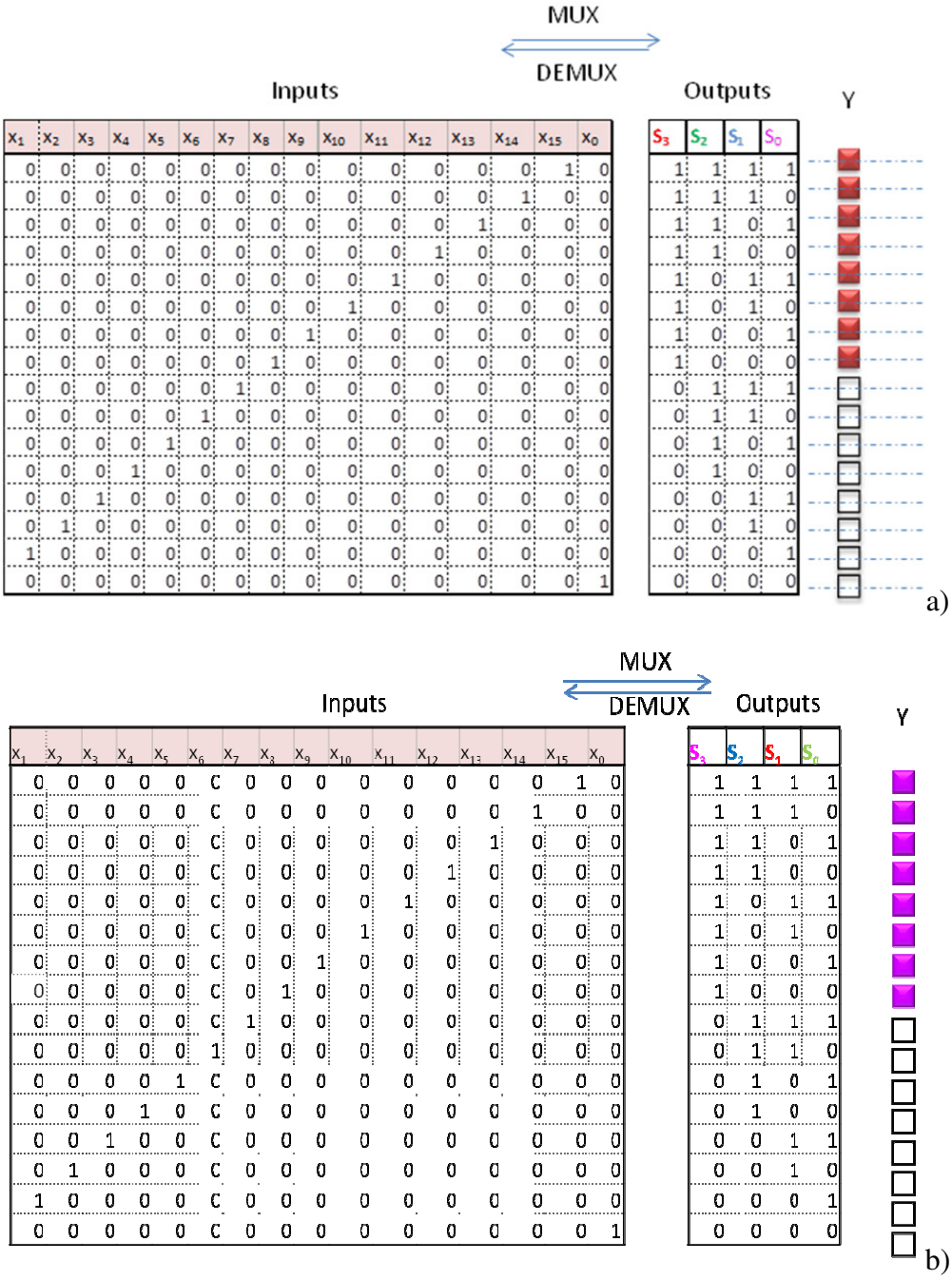

Figure 6. Truth table of the encoders that perform 16-to-1 multiplexer (MUX) function, under front (a) and back (b) violet irradiations.

The binary code is an arithmetic code and so, it is weighted, *i. e*. there is specific weights assigned to each bit position. Due to the different optical gains (Fig. 3), the selection index for those 16-element look-up table are a 4-bit binary [RGBV] code under front irradiation or a 4-bit binary [VBGR] of the form [S_3, S_2, S_1,S_0] where S_n means the color channel (right side of Fig. 5) with n weighted by the amplification factor (Fig. 4). The multiplexer select code represents an address or index, into the ordered inputs.

The truth tables of the encoders of Fig. 5, that perform 16-to-1 MUX function, are shown in Fig. 6. The correspondence between the on/off state of the input channels and the [RGBV] code under front irradiation, and the [VBRG] code under back irradiation are obvious. In the inputs (x_0….x_{15}), the index of each bit, is related to the first (highest) nonzero logic input. Here, the MUX device selects, through the front or back violet backgrounds, one of the sixteen possible input logic signals and sends it to the output ($y=x_S$). In Fig. 6a the output is a 4-bit binary RGBV number that may identify one of sixteen possible inputs. Just as the multiplexer has a binary code for the selection of an input, the demultiplexer (DEMUX) has a similar code for selecting a particular output. The 4-bit output RGBV code allows designing an encoder to transform a four-line-to-sixteen-line decoder. From truth table of Fig. 6a, the Boolean functions for the encoder with inputs x_0 to x_{15} and outputs R, G, B, V is given as:

$$R(S_3)=\sum(8,9,10,11,12,13,14,15);$$
$$G(S_2)=\sum(4,5,6,7,12,13,14,15);$$
$$B(S_1)=\sum(2,3,6,7,10,11,14,15);$$
$$V(S_0)=\sum(1,3,5,7,9,11,13,15).$$

A binary representation for decimal number 9 is in RGBV code "1001" ($2^3+0+0+2^0$) under front irradiation and it corresponds to both red and violet channels ON. Under back irradiation (VBRG code) the binary representation is the same although the weights assigned to each bit position are different (see arrows in Fig. 5). This 4-bit output RGBV code allows us design a 4-to-10 line decoder to transform a decimal number (0 to 9) into a binary code. The 4-bit codes from 1010 through 1111 do not arise from the encoding of the decimal numbers.

V. DATA ROUTER

Whereas the multiplexer is a data selector, the demultiplexer is a data distributor or data router. Just as the multiplexer has a binary code (RGBV) for the selection of an input, the demultiplexer has a similar code for selecting a particular output. In the pi'n/pin device the side of the background is the routing control for the data source. The front and back background acts as selector to select one of the four incoming channels by splitting portions of the input multi-channel optical signal across the front and back photodiodes. This duality of functions is characteristic of decoders and demultiplexers.

Under front background the red channel is decoded due to its higher amplification while under back violet irradiation the violet channel is selected (Figs. 5 and 6). To help to decode the green and blue channels, in Fig. 7 the difference between the multiplex signal under front and back violet irradiation is displayed.

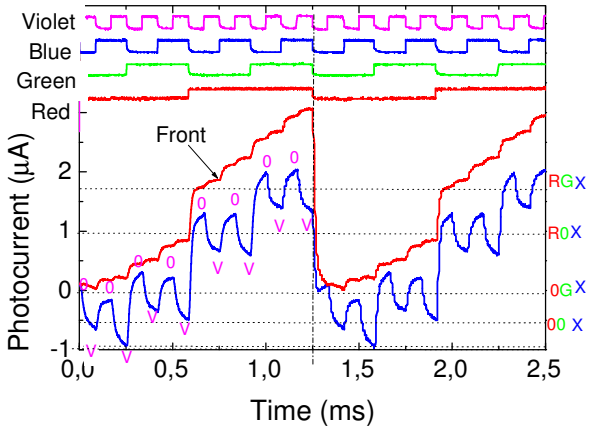

Figure 7. Wavelength difference generation. On the top the signal to drive the input channels guide the eyes.

This difference wavelength generation is a consequence of nonlinear interaction of the device with the front or back backgrounds and the optical channels generation. It weights the red versus violet content of the measured signal, so, it enhances the effect of the routing control and offers a transparent wavelength conversion. The presence of the red channel pushes the difference up and the violet channel pushes it down (right side of Fig. 5). The blue channel does not affect the difference. So, after decoding the red and the violet transmitted information and comparing with difference wavelength generation levels in the same time slots, the green and blue signals can be immediately decoded.

We have used this simple algorithm to perform 1 -to-16 demultiplexer (DEMUX) function and to decode the multiplex signals. As proof of concept the decoding algorithm was implemented in *Matlab* [8] and tested using different binary sequences. In Fig. 8a a random MUX signal under front and back irradiation is displayed and in Fig. 8b the decoding results are shown. On the top of both figures the signals to drive the LED's and the DEMUX signals obtained as well as the binary bit sequences are respectively displayed. A good agreement between the signals used to drive the LED's and the decoded sequences is achieved. In all sequences tested the RGBV signals were correctly decoded.

The DEMUX sends the input logic signal to one of its sixteen outputs, according to the optoelectronic demux algorithm. So, by means of optical control applied to the front or back diodes, the photonic function is modified, respectively from a long- pass filter to pick the red channel to a short-pass filter to select the violet channel, giving a step reconfiguration of the device. The green and blue channels are selected by combining both active long- and

 ISBN: 978-1-61208-297-4

short-pass filters into a band-pass filter. In practice, the decoding applications far outnumber those of demultiplexing. Multilayer SiC/Si optical technology can provide a smart solution to communication problem by providing a possibility of optical bypass for the transit traffic by dropping the fractional traffic that is needed at a particular point.

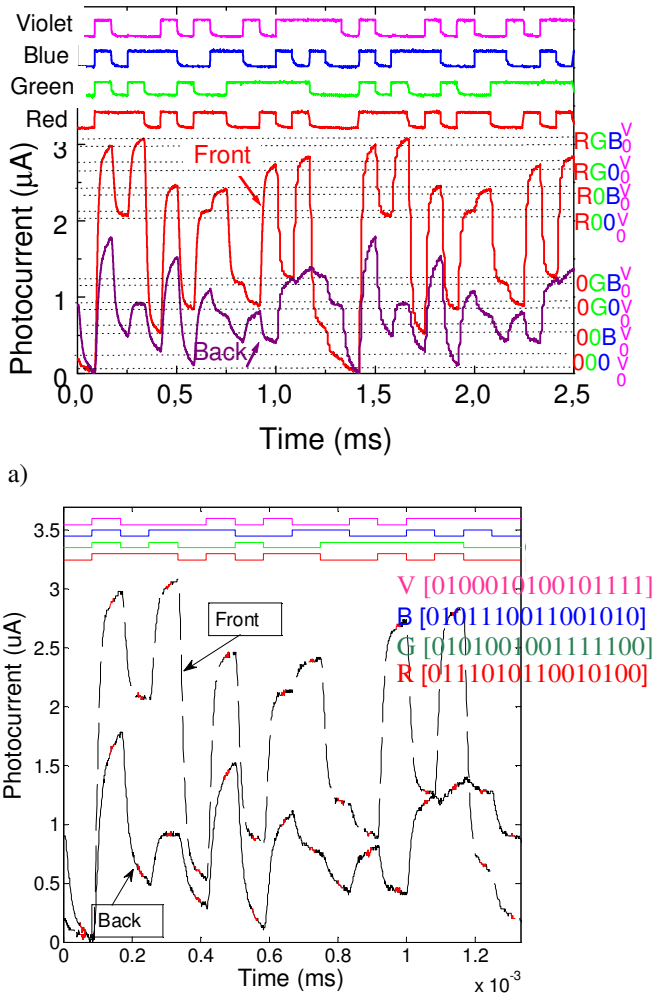

Figure 8. MUX signal under front and back irradiation. On the top a) Signals used to drive the LED's. b) DEMUX signals and decoded RGBV binary bit sequences.

VI. CONCLUSIONS

An optoelectronic device based on a-SiC:H technology is analyzed. The device is able to act simultaneously as a 4-bit binary encoder or a binary decoder in a 4-to-16 line configurations.

A relationship between the optical inputs and the corresponding digital output levels is established. A binary weighted color code that takes into account the specific weights assigned to each bit position establish the optoelectronic functions. A truth table of an encoder that performs 16-to-1 multiplexer (MUX) function is presented. A decode algorithm based on the optical bias control of the device was improved.

More work as to be done in order to execute optical arithmetic micro-operations entirely within the optical domain.

ACKNOWLEDGEMENTS

This work was supported by FCT (CTS multi annual funding) through the PIDDAC Program funds and PTDC/EEA-ELC/111854/2009 and PTDC/EEA-ELC/120539/2010.

REFERENCES

1. C. Petit, M. Blaser, Workshop on Optical Components for Broadband Communication , ed. by Pierre-Yves Fonjallaz, Thomas P. Pearsall, Proc. of SPIE Vol. 6350, 63500I, (2006).
2. S. Ibrahim, L. W. Luo, S. S. Djordjevic, C. B. Poitras, I. Zhou, N. K. Fontaine, B. Guan, Z. Ding, K. Okamoto, M. Lipson, and S. J. B. Yoo, paper OWJ5. Optical Fiber Communications Conference, OSA/OFC/NFOEC, San Diego, 21 Mar 2010.
3. M.A. Vieira, P. Louro, M. Vieira, A. Fantoni, A. Steiger-Garção. IEEE sensor jornal, Vol. 12, NO. 6, (2012) pp. 1755-1762.
4. M.A. Vieira, M. Vieira, P. Louro, V. Silva, A., Applied Surface Science, DOI: 10.1016/j.apsusc.2013.01.020.
5. S. Randel, A.M.J. Koonen, S.C.J. Lee, F. Breyer, M. Garcia Larrode, J. Yang, A. Ng'Oma, G.J Rijckenberg, and H.P.A. Boom.. "ECOC 07 (Th 4.1.4). (pp. 1-4). Berlin, Germany, 2007.
6. M. Vieira, P. Louro, M. Fernandes, M. A. Vieira, A. Fantoni and J. Costa InTech, Chap.19, pp:403-425 (2011).
7. M. Vieira, A. Fantoni, P. Louro, M. Fernandes, R. Schwarz, G. Lavareda, and C. N. Carvalho, Vacuum, 82, Issue 12, 8 August 2008, pp: 1512-1516.
8. M. A. Vieira, M. Vieira, J. Costa, P. Louro, M. Fernandes, A. Fantoni, in Sensors & Transducers Journal Vol. 10, Special Issue, February 2011, pp.96-120.

 ISBN: 978-1-61208-297-4

Detection of Hydrocarbon Oil in Seawater by Light Absorption Analysis

Sangwoo Oh and Moonjin Lee
Maritime Safety Research Division
Korea Institute of Ocean Science & Technology (KIOST)
Daejeon, Republic of Korea
swoh@kiost.ac

***Abstract*—A new optical sensing method is proposed to detect hydrocarbon oil in the sea. As a sensing methodology, a light absorption analysis is used with a laser source and two different types of photodiode sensors. To obtain information about the presence of oil on water and the thickness of oil, the intensity of the penetrating light through the oil–water mixtures is measured. In the experiment, bunker C and lubricating oil are used, and three different lasers having different wavelengths are applied and compared for the selection of an optimal light source. By using a photodiode sensor, we can convert the intensity of the penetrating light through a liquid into an electrical signal. As a result, it is observed that the intensity of the light on the optical sensor decreases with an increase in the oil thickness. Through this relation, both the presence of oil and the thickness of oil can be determined. This result shows the applicability of a hydrocarbon detection sensor.**

***Keywords*—Optical sensor, Hydrocarbon spill detection, Light absorption analysis, Blue laser, Photodiode**

I. INTRODUCTION

A hydrocarbon spill accident in the sea is a major catastrophe that can have bad effects on every life in the ocean. Hence, rapid detection of hydrocarbon and response are very important and helpful for the prevention of environmental pollution.

In response to this need, various types of hydrocarbon spill detection sensors for the ocean application have been developed, and some of them have been applied in a real site [1], [2]. However, these developed sensors have some economic weaknesses. The sensing methodologies of the initially applied sensors are based on laboratory analysis equipment, such as mass spectrometry. These sensors can analyse the detailed components of hydrocarbon as well as the type of hydrocarbon. However, these sensors are mostly large in size and require a long analysis time because of their many processes [3]. Then, an initial type of sensor, sensors that use fluorescence analysis by UV rays [4], and electrical capacitance measurement [5] were developed. These sensors can detect not only the existence of hydrocarbon but also analyse their components down to the parts per million level. However, these sensors are generally not cost effective, and it is therefore very difficult to increase the number of detection points in the ocean. To solve these problems of the existing hydrocarbon spill detection sensors, in this research, we have focused on the development of a sensor, which has advantages of cost-effectiveness with respect to installation and maintenance, and a simple detection mechanism. To realise these requirements, the difference in light absorption between oil and water is used as a sensing principle. Further, by using electro-optical devices such as laser and optical sensor, we have estimated the detection capability of a proposed sensor in this research. To select the optimal wavelength of the laser, three different types of laser are compared and the prototype of the sensor platform is described in the body of paper.

II. SENSOR DESIGN

A. Sensing Principle

In this research, laser is used as a light source, and an optical sensor is used for evaluating the light intensity. These two electric devices are very cheap and easy to use, thus satisfying the aims of sensor development.

This research is partially motivated by existing research on the sensing mechanism [6], where light emitting diodes (LEDs) and light-dependent resistors (LDRs) were used for monitoring oil, with multiple LED/LDR pairs positioned vertically. In this former research, the detection resolution of the oil thickness was on the centimetre scale. However, in the current research, the light source (laser) is positioned underwater and the penetrating light energy is evaluated by the optical sensor above the water surface. Further, the optical sensor is used for directly converting the light intensity into voltage; hence, there is no need for an additional converting process. The changes made to the light source and the optical sensor are different from former research.

The methodology in this research involves the use of (1) a blue laser to illuminate the monochromatic high-powered light to the heavy oil in seawater and (2) an optical sensor to evaluate the intensity of the light that penetrated the oil in seawater. As the sensing principle, the difference in the light absorption rate between oil and water is used.

$$I = I_0 e^{-az} \tag{1}$$

where z = path length
I_0 = initial intensity of light
a = light absorption coefficient

Equation (1) is Beer's law, which describes the light absorption in the seawater [7]. In this equation, the light absorption coefficient is dependent on the type of medium and the wavelength of light. If the light diffuses into different types of media, the decreasing tendency of the light intensity varies. Moreover, the wavelength of light is a major part of the determination of the condition of light absorption. If the light source having a different absorption characteristic between oil and seawater is chosen, using this light source, we can find out the oil existence and the oil thickness.

Normally, it is common sense that a light having a blue wavelength region has considerably selectivity with respect to an absorption rate when it penetrates the oil in seawater. When a blue light diffuses through oil or seawater media, the light is considerably more absorbed in the oil than in seawater. Hence, with an increase in the oil thickness, the possibility of light attenuation in the oil layer increases (see Fig. 1). Therefore, the energy of the penetrating light on the optical sensor will decrease. By using this optical sensing mechanism, we can

 ISBN: 978-1-61208-297-4

monitor the existence and the thickness of oil on the water. Hence, in this research, three different types of lasers (blue, green and red) are compared for the selection of an optimal light source, which has considerable selectivity between oil and seawater.

B. Experiment

To determine the optimal wavelength of the laser, experiments are conducted using three different lasers (473 nm for blue, 532 nm for green and 650 nm for red) with increasing oil thickness (see Fig. 2). For the exact measurement of light intensity, external lights (sunlight and electric light) are blocked by a black box. Further, the oils used in the experiment are lubricating oil and bunker C oil (type A), which can be very harmful when spilt in the ocean.

Two different types of optical sensors are used in the experiment. The first one is a 2 × 2 photodiode array shown in Fig. 3. This sensor can transduce the light intensity to the voltage output. The supply voltage of this sensor is 5.0 V, and the output range is 0.8 V–5.0 V. The gap between the laser and the water surface is 5 cm. The measurements are conducted five times under the same condition at each case of laser. In the measurement of bunker C oil, a 2 × 2 photodiode array sensor is applied to measure the light intensity. The increment in the oil thickness is 0.5 mm, and the experiment is conducted up to a thickness of 2 mm.

In the second experiment, the lubricating oil is used, and the optical sensor having a single photovoltaic photodiode is applied to evaluate the light intensity (see Fig. 4). This optical sensor operated under an unbiased condition and output the current signal. The increment in the oil thickness is 1 mm, and the experiment is conducted up to a thickness of 4 mm.

C. Results

In the first experiment (bunker C oil), the sensor output results obtained using blue, green, and red lasers under conditions of increasing oil thickness are shown in Figs. 5–7. Through these three results, in the case of the blue laser, it is observed that with an increase in the oil thickness, the intensity of the light decreases linearly and the selectivity is the highest among the three laser sources. Hence, the blue laser is the optimal light source for the detection of oil presence and the measurement of the thickness of the bunker C oil.

In the second experiment (lubricating oil), the sensor output results obtained using blue, green, and red lasers under the conditions of increasing oil thickness are shown in Figs. 8–10. Through these three results, in the case of the blue laser, it is also observed that when the oil thickness increases, the intensity of the light decreases linearly and the selectivity is the highest among the three laser sources. Green and red lights generally have a low power output. This implies that these lights are absorbed mostly in the seawater layer. Hence, the blue laser is also the optimal light source for the detection of oil presence and the measurement of the thickness of the lubricating oil.

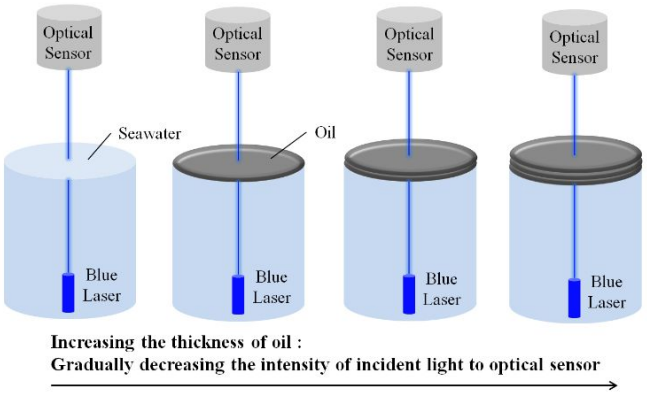

Figure 1. Schematic representation of the sensing mechanism

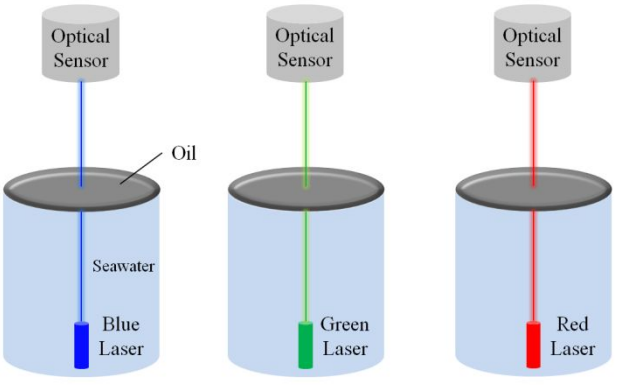

Figure 2. Experimental setup to select a laser as an optimal wavelength light source for the oil-spill detection sensors

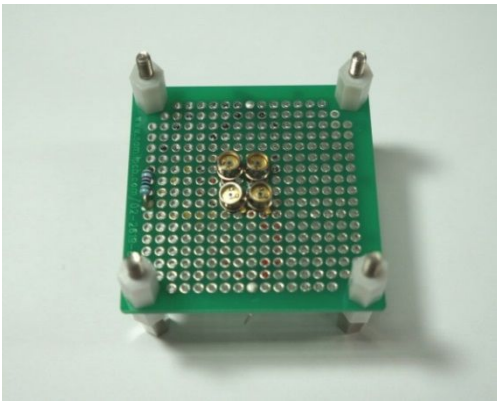

Figure 3. First optical sensor used in the bunker C measurement (2 × 2 photodiode array and voltage output)

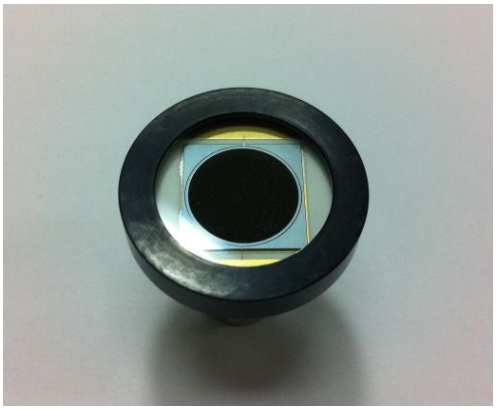

Figure 4. Second optical sensor in the lubricating oil measurement (Single photovoltaic diode and current output)

 ISBN: 978-1-61208-297-4

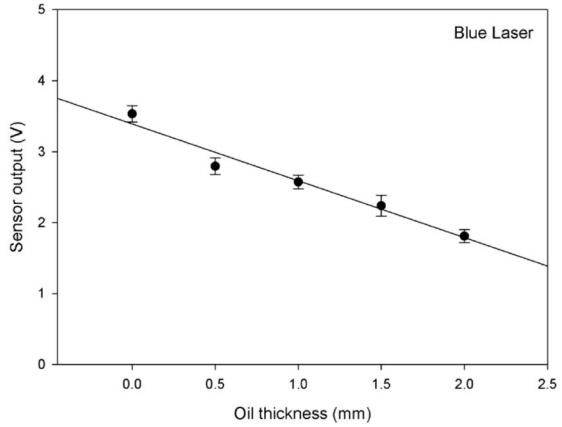

Figure 5. Sensor output results using a blue laser in bunker C oil

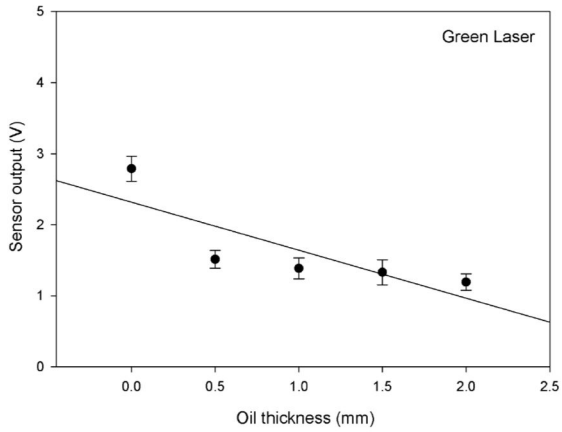

Figure 6. Sensor output results using a green laser in bunker C oil

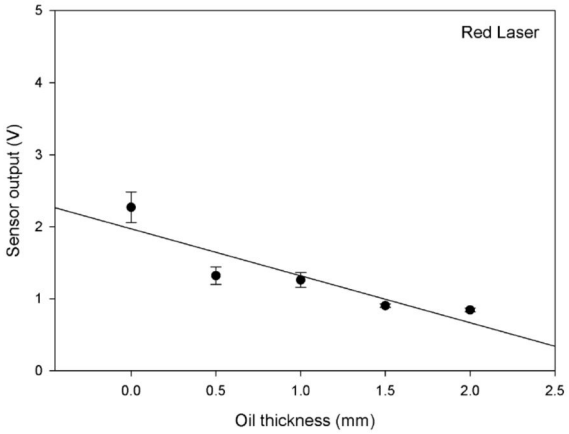

Figure 7. Sensor output results using a red laser in bunker C oil

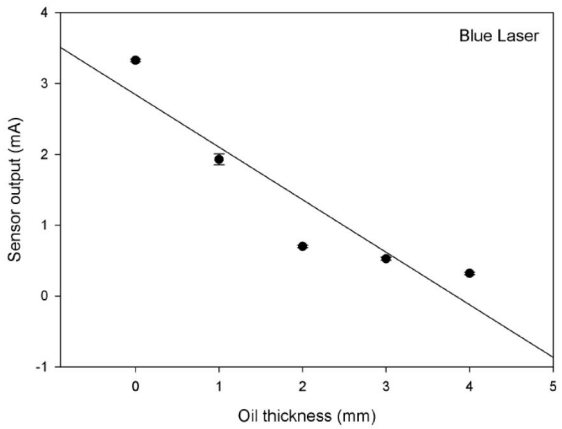

Figure 8. Sensor output results using a blue laser in lubricating oil

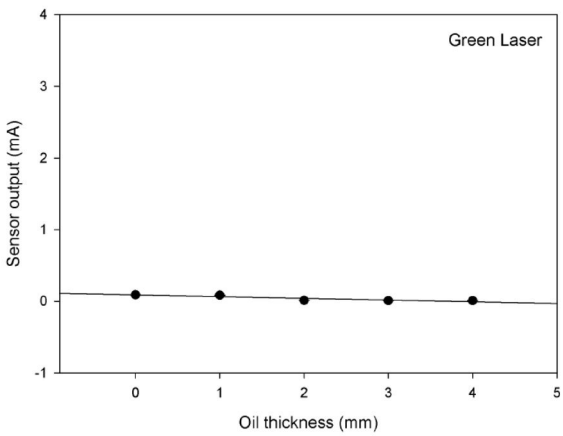

Figure 9. Sensor output results using a green laser in lubricating oil

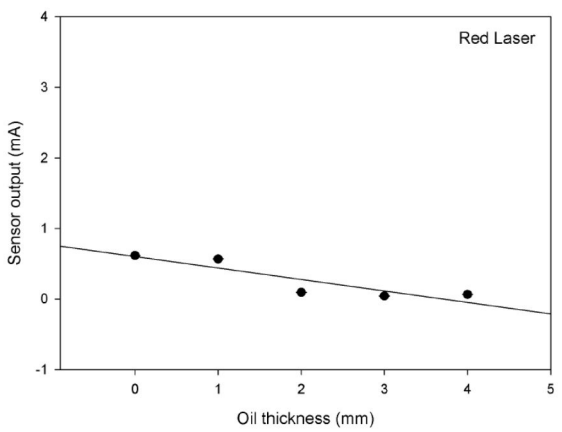

Figure 10. Sensor output results using a red laser in lubricating oil

 ISBN: 978-1-61208-297-4

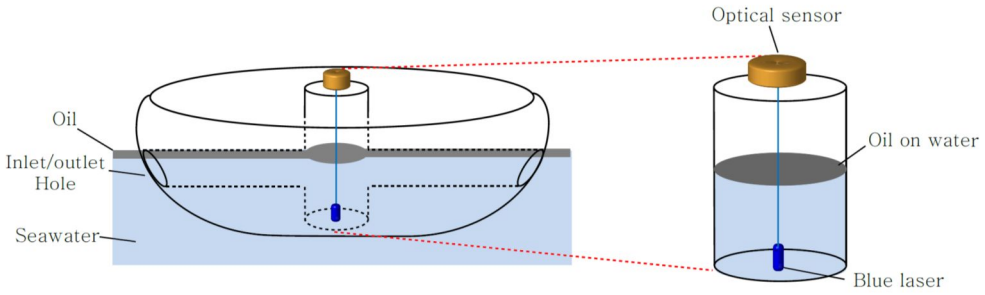

Figure 11. Schematic representation of the sensor platform

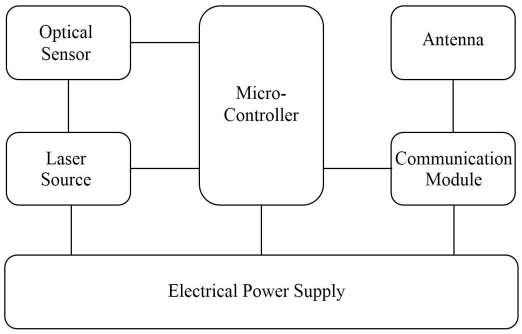

Figure 12. Schematic representation of the sensor architecture

D. Sensor Platform

For the future work, the sensor platform needs to be designed and manufactured in the form of the monitoring buoy. For effective detection on the sea surface, a dish-shaped floater is designed as a sensor platform; through two holes on the water-line side of the floater, the oil can enter and contact the optical detection part of the sensor (Fig. 11). The system architecture of the total sensor is shown in Fig. 12. It consists of the optical sensor, the laser source, the electrical power supply, the main controller and the communication part including the antenna.

III. CONCLUSION

In this research, to find out the optimal wavelength laser, experiments using three lasers and two different oils were conducted and it was concluded that the blue laser was the optimal light source for the detection of oil presence and the measurement of oil thickness.

In this paper, a new optical oil detection methodology was proposed using the difference in light absorption between water and oil using the blue laser and the optical sensor.

ACKNOWLEDGMENT

This work is carried out as a part of the study on "Development of Oil Spill Response Supporting System based on 3-D Oil Dispersion Modelling" and "Development of HNS Spill Response Information Supporting Technologies based on HNS Dispersion Model" under the support by the Korea Institute of Ocean Science and Technology.

REFERENCES

[1] A. MacLean, C. Moran, W. Johnstone, B. Culshaw, D. Marsh, P. Parker, "Detection of hydrocarbon fuel spills using a distributed fibre optic sensor", Sensors and Actuators A, vol. 109, 2003, pp. 60–67.

[2] G. Griffiths, "Review of oceanographic equipment and sensors for the detection and measurement of pollutants", Southhampton Oceanography Center Research and Consultancy Report, no. 99, 2005, pp. 1-24.

[3] G. Reeves, "Introduction to hydrocarbons and monitoring", Common HydroSense Questions and General Information Guide, Arjay Engineering Ltd., 2000, pp. 2-8.

[4] C. Henry, P.O. Roberts, "Background fluorescence values and matrix effects observed using smart protocols in the Atlantic Ocean and Gulf of Mexico", International Oil Spill Conference, Florida, 2001, pp. 1203-1207.

[5] J. Andrews, "Automated marine oil spill detection system development update", Marine Environmental Update, 97(1), US Navy SPARWAR Systems Centre., 1997.

[6] H. Denkilkian, R. Ohannessian, M.S. Chalfoun, M. Joujou, A. Chehab, I.H. Elhajj, "Wireless sensor for continuous real-time oil spill thickness and location measurement", IEEE Transactions on Instrumentation and Measurement, vol. 58, no. 12, 2009, pp. 4001-4011.

[7] E. Friedman, J. Miller, "Photonics Rules of Thumb", 1st ed., SPIE Press, McGraw Hill, 2003, pp. 220-240.

 ISBN: 978-1-61208-297-4

Fiber-Coupled Microcavity Probe for in Vivo Near-Field Sensing

Zachary Ballard, Nichaluk Leartprapun, Jimmy Xu
School of Engineering
Brown University
Providence, USA
e-mail: Zachary_Ballard@brown.edu,
Nichaluk_Leartprapun@brown.edu,
Jimmy_Xu@brown.edu

Jimmy Xu
WCU Program
Seoul National University
Seoul, South Korea
e-mail: Jimmy_Xu@brown.edu

***Abstract*— We report on a new design for near-field sensing based on a fiber-coupled microcavity. The device operates on the bases of sensing in the evanescent near-field zone and offers a robust portable probe solution for in-vivo sensing and diagnostics. In preliminary tests, the first generation device has already demonstrated sensitivity in the range of 10^{-3} and 10^{-4} refractive index units (RIU) and 20 nm/RIU. Using this device, we have also observed, through spectral shift, the binding of a self-assembled monolayer (~ 5 Å thickness) of amino-silane.**

Keywords-Biosensor; Microprobe; microcavity

I. INTRODUCTION

The proliferation of optical bio-sensors has made point of use diagnostics a reality. Label free bio-sensors interact with biological materials often times in bulk solution without the need for any fluorescent bio-markers or dyes, allowing for a more elegant detection or diagnostic protocol [1].

Though many breakthroughs have been made in regard to detection sensitivity, bringing this technology from a lab (optical table) setting into a scalable and robust micro-device remains a challenging problem [2]. Furthermore, there exists a demand for in-vivo or in-situ use for real-time monitoring of cellular environments. Fiber-optic based platforms with sub-micron sized dimensions prove to be one of the more promising technologies due to their needle-like geometries [3]. Despite the functional advantages and published sensitivities around 10^{-4} to 10^{-7} RIU, optical fiber based platforms still remain several orders of magnitude less sensitive than other bio-sensing technologies such as Surface Plasmon Resonance sensors, Whispering Gallery Mode sensors, and interferometric sensors [4]. However, novel fiber-based platforms could increase the capacity for sensitivity and serve as a more robust and low-cost bio-sensor solution. A portable high-sensitivity in-vivo device could have immense impact in driving down the cost of healthcare and guiding vaccine and medicinal distribution networks [5].

This work-in-progress report presents a novel bio-sensor with a probe structure that has the potential for in-vivo or in-situ sensing and probing of bio-environments. This simple, portable, micro-scale device can pick up minute changes, via phase-shift and amplitude change, in its microcavity's immediate vicinity (evanescence zone). It could be used for diagnostics or deoxyribonucleic acid (DNA) and protein assays, and as a possible low-cost tool to aid in the understanding of binding events of specific target molecules. The micro-probe consists of a micro-cavity formed at, and optically coupled to, the tip of an optical fiber, resulting in a compact, simple, and bio-compatible design for refractive index sensing. Preliminary experiments for the first generation device have yielded an initial, non-optimized limit of detection of 10^{-3} to 10^{-4} RIU with 20 nm/RIU.

This manuscript will discuss the fabrication and structure of the fiber-coupled micro-cavity probe, the working principles, and provide experimental validations and preliminary detection capabilities

II. DEVICE DESCRIPTION

The micro-probe is made by tapering hollow borosillicate tubes (1mm OD, .75 mm ID) down to tip diameters of 25-50 µm. The tapering was achieved using a Sutter Instrument P-2000 Micropipette Puller. A 20W Class IV CO_2 laser was used as the heating source while the borosilicate tube was pulled from both sides as shown in Fig. 1. Custom programs were written for the pipette puller to achieve long and gradual tapers. The tapered tips were then melted with a gentle flame from standard butane lighter, whereupon the molten glass forms a solid glass spherical tip due to surface tension. The symmetry of the spherical tips was maintained by constant spinning of the tips during the melting process. The total resulting structure consists of a finely tapered air cavity that extends into a solid glass spherical tip, as seen in Fig. 2.

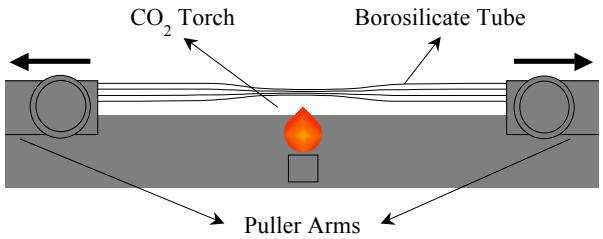

Figure 1. Borosilicate tube tapering process using a Micropipette Puller

Then, standard SMF-28 telecom fibers were stripped, cleaved and inserted into this tapered cavity, eventually becoming wedged. The optical fiber remains stationary due to the cylindrical geometry of the tapered air cavity and

 ISBN: 978-1-61208-297-4

fiber, and can be affixed upon its insertion point with simple epoxy.

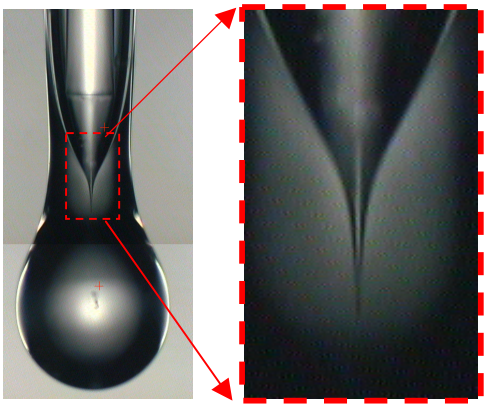

Figure 2. Device structure: (a) SMF-28 fiber (125 μm diameter) wedged in tapered air cavity (410 μm diameter) and (b) tapered air cavity.

The range of spherical tip diameters tested so far were, but not limited to, 300-500 microns.

III. WORKING PRINCIPLES

A. *Fizeau Interferometry*

The resulting spherical probe structure contains two effective reflection surfaces for incident light through the optical fiber [6]. The first interface is between the end of the cleaved fiber and the air cavity, and the second interface is between the edge of the solid glass spherical tip and the outside environment, as shown in Fig. 3. Therefore, when incoming light through the fiber enters the device, the reflection from the second interface recombines with the reflection from the first interface described by the reflection from an effective Fabry-Perot cavity.

The second interface is an effective one that is subjected to change by the material in the evanescence-zone of the probe tip. The spherical tip forms a secondary (weak Q) cavity for the entering light scattered from the sharp air-tip.

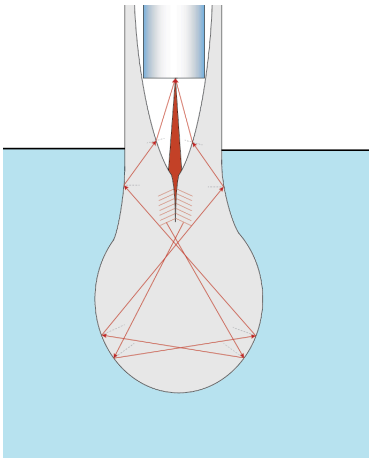

Figure 3. Ray-optics of light propagation in probe geometry.

Surrounding the outer surface of this microcavity is the aforementioned evanescence-zone. A change of material, temperature, or pH, even a minute one, in this zone would effectively change the size of this cavity, which translates into a phase-shift that can be measured from the overall interference pattern.

B. *Use as a Sensor*

Increasing the refractive index of the environment outside of the spherical tip naturally decreases the reflection coefficient for reflections below the critical angle and thus decreases the amplitude of the interference signal. However, this is not the only effect. Experiments show a clear phase change with changing refractive index in exterior environments.

Due to the unique geometry of the sharply tapered air cavity between the two reflection interfaces, this device is able to bend the wave fronts of the fiber-outputted light in such a way that allows for multiple reflections in the spherical silica tip and probe neck, eventually coupling the light back into the optical fiber. This light propagates in the spherical tip with a refractive index, n_1, through a series of reflections with non-normal incident angle, θ_i, allowing the reflections which meet the total internal reflection criteria are greatly affected by the Goos-Hänchen effect [7]. Changing the refractive index, n_2, at the interface along the spherical tip will modulate the Goos-Hänchen shift, thus, shifting the interference pattern by a phase, δ, described by,

$$\tan\left(\frac{\delta_S}{2}\right) = \frac{\left(\sin\theta_i{}^2 - n^2\right)^{\frac{1}{2}}}{\cos\theta_i} \quad (1a)$$

$$\tan\left(\frac{\delta_P}{2}\right) = \frac{\left(\sin\theta_i{}^2 - n^2\right)^{\frac{1}{2}}}{n\cos\theta_i} \quad (1b)$$

where $n = n_2/n_1$.

Treating the device as an effective Fabry-Perot cavity [6], the total reflected intensity could be derived using the Airy Summation Method,

$$I_r(FP) = I_0\left[\frac{r_1^2 + 2\cos(\delta)r_1r_2 + r_2^2}{1 + 2\cos(\delta)r_1r_2 + r_1^2r_2^2}\right], \quad (2)$$

where r_1 and r_2 represent the reflection coefficient of the two interfaces of an asymmetric Fabry-Perot cavity. Substituting $r_1 = -r_2$ into (2) would recover the standard equation for the reflection of a symmetric Fabry-Perot cavity. Fig. 4 shows the model interference patterns produced from (2) for n_2 of air, water, and ethanol. The experimentally obtained interference patterns for the same environment are shown in Fig. 5.

 ISBN: 978-1-61208-297-4

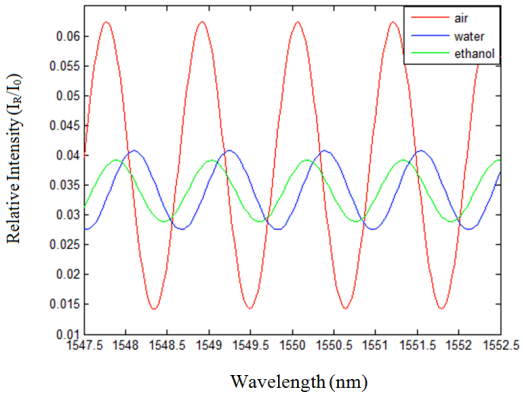

Figure 4. Output of probe model for outside refractive index environments of air, water, and ethanol.

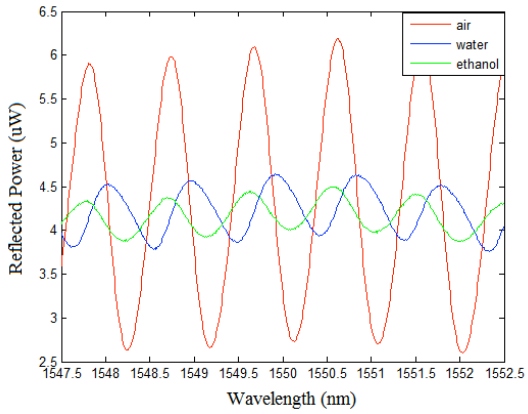

Figure 5. Reflected power (μW) measured for probe during 5 nm sweep in air, water, and ethanol.

This effective F-P model worked remarkably well, despite the complex structure and geometry, and can be used as a tool by which to measure material changes in the probe's immediate vicinity or specific binding events.

IV. EXPERIMENTAL DEMONSTRATION

A. Experimental Set-Up

The experimental set-up to demonstrate the interference properties of the fiber-coupled micro-sphere tip is illustrated in Fig. 6. An Ando AQ4320D Tunable Laser Source was wired to a 2×1 fiber optic coupler. The output of the coupler was sent to the SMF-28 fiber wedged in the micro-sphere tip. The reflected signal from the tip was measured by an Ando AQ6317 Optical Spectrum Analyzer wired to the second output of the coupler.

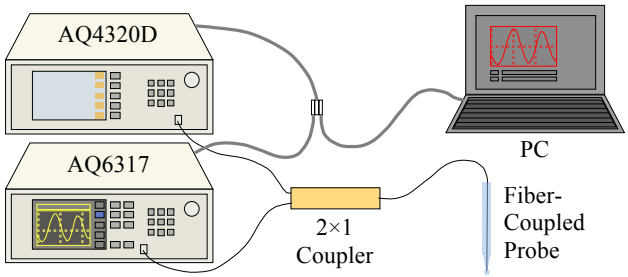

Figure 6. Experimental set-up for fiber-coupled micro-sphere tip interference measurements.

Both the Tunable Laser Source and the Optical Spectrum Analyzer were connected to a PC and controlled by a LabVIEW VI. Spectra collection was also accomplished by the same program.

B. Refractive Index Sensing with Ethanol-Water Mixture

For a quantitative assessment of the sensitivity of this device, the probe was submerged in 0.5 mL DI water and then subsequently submerged in incremental concentrations of ethanol-water mixtures ranging from 0 to 50% volume fraction of ethanol. In each mixture, a 3 nm spectral sweep was performed centered around 1550 nm with 1 mW laser power. The reflected power was measured and demonstrated a red spectral shift with increasing ethanol concentration, as shown in Fig. 7.

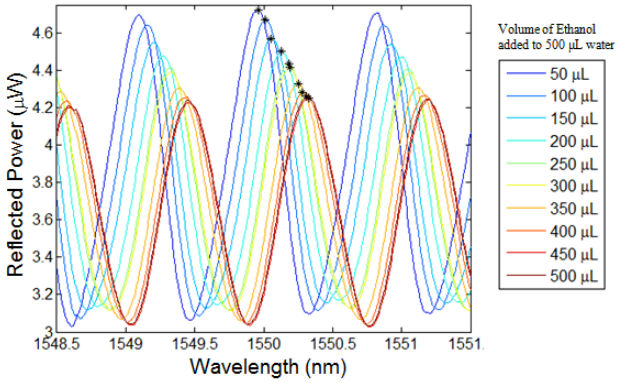

Figure 7. Blue to red shift of interference pattern show incremental 10^{-3} RIU changes in each measured ethanol-water mixture.

The refractive index of each ethanol-water mixture was measured using a Fisher Scientific Abbe Benchtop Refractometer. Fig. 8 plots the peak-to-peak amplitude of the spectrums and the peak wavelength as a function of mixture refractive index. Both the intensity change and spectral shift demonstrated a near-linear change with increasing refractive index, demonstrating a sensitivity of ~10^{-3} RIU, and 20 nm/RIU.

 ISBN: 978-1-61208-297-4

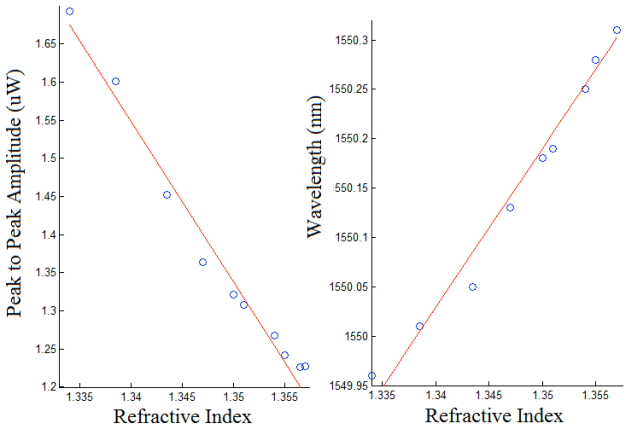

Figure 8. (a) Peak to peak amplitude of the measured interference and (b) the corresponding wavelength at each interference peak (spectral shift).

Deviations from the linearity could be due to temperature fluctuations during testing as well as non-uniform mixing in the ethanol-water samples. Further testing must be done in a flow-system for temperature and mixing control in order to experimentally demonstrate a higher Limit of Detection (LOD).

C. *Monitory Formation of Self-Assembled Monolayer*

The probe surfaces were cleaned in Piranha solution (3:1 v/v of H_2SO_4:H_2O_2) and then placed in a solution of 2% v/v of 3-aminopropyltriethoxysilane (APTES) in acetone [8]. The solution was sealed with a molded polydimethylsiloxane (PDMS) stopper and PTFE thread seal tape to avoid evaporation. Silanization of APTES refers to the binding of APTES molecules onto a substrate surface. It is often used to functionalize silica substrates for selective immobilization of protein bio-targets [9]. The probe was submerged in the solution for 12 hours as continuous 3 nm spectral sweeps, centered around 1550 nm with 1 mW laser power, were taken. The interference patterns obtained during the 12-hour APTES silanization exhibit blue spectral shift, as shown in Fig. 9.

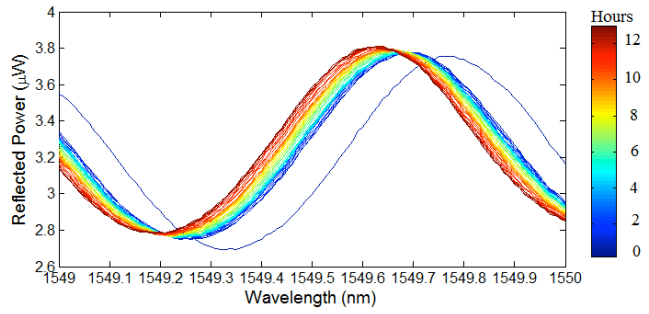

Figure 9. Spectral shift of interference pattern due to silanization during the first 12 hour of incubation.

This result is counter to the spectral shifts observed in typical resonance sensors, caused by an effective lengthening of the optical path due to the presence of the monolayer [10][11][12]. However, this counter-intuitive effect was reproduced in multiple molecular binding experiments, and could be caused by a lessening of optical tunneling into the bulk solution due to the higher Δn between the APTES layer and the bulk solution (assuming that $n_{APTES} > n_{Glass}$).

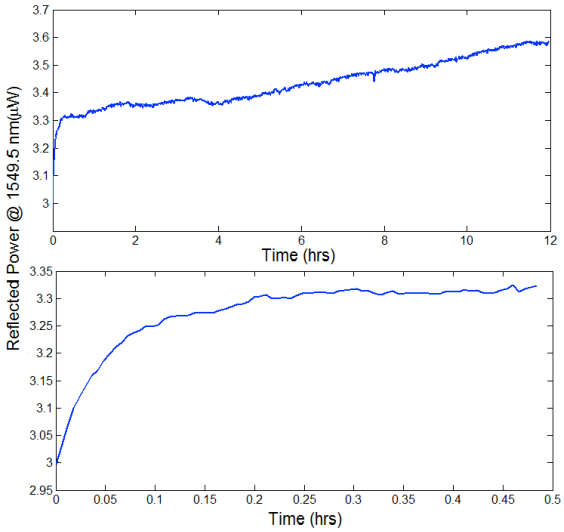

Figure 10. Reflected power at single wavelength during silanization process plotted at (a) the 12-hour incubation period and (b) during the first 30 minutes of incubation.

The reflected power change at 1549.5 nm (rising inflection point) of the interference pattern, shown in Fig. 10, illustrates the self-assembly of the APTES monolayer in the first 30 minutes, and subsequent intermolecular interactions of APTES molecules on top of this monolayer in the 12-hour period after the monolayer formation, resulting in a total spectral shift of ~0.2 nm. This observed monolayer binding time-scale (~30 minutes) agrees with the standard binding protocol time-scale for a 5 Å monolayer formation of APTES on a silica substrate [9].

V. CONCLUSION

Demonstrating the mode coupling between an optical fiber and microcavity sphere works to bring the high sensitivity of microcavity sensors, particularly Whispering Gallery Mode sensors, off of the optical table and into a robust integrated microprobe [13]. The probe design has the distinct advantage of use in vivo without the need of microfluidics or alignment of evanescent coupling, and can be implemented for sample volumes on the order of nano-liters. The first generation microprobes demonstrated sensitivity in the range of 10^{-3} and 10^{-4} RIU and 20 nm/RIU in bulk solutions. In addition, monitoring of the spectral shift during the salinization process confirms a high degree of near-field (evanescent) sensitivity due to immobilized surface molecules as the formation of the 5 Å self-

 ISBN: 978-1-61208-297-4

assembled APTES monolayer was detected in real-time. Thus, the experimental results demonstrates the proof-of-concept that this fiber-coupled microcavity probe can be used for detection of specific immobilized bio-targets, and even has potential use in studying real-time surface reaction kinetics.

Furthermore, though exhibiting sensitivity in bulk solution less than that achieved in other optical biosensors such as Surface Plasmon Resonance sensors, ring resonator sensors and interferometric sensors, which are able to detect down to 10^{-7} RIU, the data recorded thus far is from proof-of-concept hand-made microprobes that are yet to undergo optimization as far as their cavity size and geometric effects on mode coupling [4]. For example, by fabricating smaller diameter spherical tips, we will be able to increase the nm/RIU limit of detection due to a shorter effective cavity length. Similarly, implementing a controlled and mechanical method for melting and shaping the tapered tube, we hope to optimize the geometry of the tapered air cavity and probe curvatures. This optimization could lead to enhanced mode coupling between the fiber and the spherical tip. The geometric variations of the tapered air cavity and probe curvature could allow for tunability between the competing effects of the reflection coefficient modulation and Goos-Hänchen phase shift for the creation of far field and near field sensors respectively.

ACKNOWLEDGMENT

The authors wish to thank Anubhav Tripathi and Domenico Pacifici for their support and helpful discussion for this study. The authors are also very grateful for the guidance of Jin Ho Kim, Gustavo Fernandes, and Carlos Bledt, and the support of ARL, AFOSR, CR Bard Fellowship, and WCU.

REFERENCES

[1] M. A. Cooper, "Label-free screening of bio-molecular interactions."*Analytical and bioanalytical chemistry* 377.5, Nov. 2003, pp. 834-842, doi: 10.1007/s00216-003-2111-y.

[2] F. S. Ligler, "Perspective on optical biosensors and integrated sensor systems." *Analytical chemistry* 81.2, 2009, pp. 519-526, doi: 10.1021/ac8016289.

[3] M. N. Velasco-Garcia, "Optical biosensors for probing at the cellular level: A review of recent progress and future prospects." *Seminars in cell & developmental biology* 20.1. Academic Press, Feb. 2009, pp. 27-33, doi: 10.1016/j.semcdb.2009.01.013.

[4] X. Fan, I. M. White, S. I. Shopova, H. Zhu, J. D. Suter, and Y. Sun, "Sensitive optical biosensors for unlabeled targets: A review." *Analytica chimica acta* 620.1, Jul. 2008, pp. 8-26, doi: 10.1016/j.aca.2008.05.022.

[5] S. Rodriguez-Mozaz, M. J. Lopez de Alda, M. Marco, and D. Barcelo, "Biosensors for environmental monitoring: A global perspective." *Talanta* 65.2, Jan. 2005, pp. 291-297, doi: 10.1016/j.talanta.2004.07.006.

[6] O. R. Ranjbara, et al. "High pressure discrimination based on optical fiber microsphere cavity Fizeau interferometer." *Proc. of SPIE 8421*, Oct. 2012, doi: 10.1117/12.966322.

[7] D. Q. Chowdhury, D. H. Leach, and R. K. Chang, "Effect of the Goos-Häinchen shift on the geometrical-optics model for spherical-cavity mode spacing." *JOSA A* 11.3, 1994, pp. 1110-1116, doi: 10.1364/JOSAA.11.001110.

[8] A. V. Krasnoslobodtsev and S. N. Smirnov, "Effect of water on silanization of silica by trimethoxysilanes." *Langmuir* 18.8, 2002, pp. 3181-3184, doi: 10.1021/la015628h.

[9] M. Zhu, M. Z. Lerum, and W. Chen, "How to prepare reproducible, homogeneous, and hydrolytically stable aminosilane-derived layers on silica."*Langmuir* 28.1, 2012, pp. 416-423, doi: 10.1021/la203638g.

[10] F. Vollmer and S. Arnold, "Whispering-gallery-mode biosensing: label-free detection down to single molecules." *Nature methods* 5.7, Jul. 2008, pp. 591-596, doi: :10.1038/NMETH.1221.

[11] K. M. De Vos, I. Bartolozzi, P. Bienstman, R. Baets, and E. Schacht, "Optical biosensor based on silicon-on-insulator microring cavities for specific protein binding detection-art. no. 64470K." *Nanoscale Imaging, Spectroscopy, Sensing, and Actuation for Biomedical Applications IV* 6447, 2007, pp. 64470K1-64470K8, doi: 10.1117/12.698875.

[12] Y. Guo, et al. "Label-free biosensing using a photonic crystal structure in a total-internal-reflection geometry." *SPIE BiOS: Biomedical Optics* 7188, Feb. 2009, pp. 71880B–71880B12, doi: 10.1117/12.808369.

[13] S. Arnold, S. I. Shopova, and S. Holler, "Whispering gallery mode bio-sensor for label-free detection of single molecules: thermo-optic vs. reactive mechanism." *Optics Express* 18.1, Jan. 2010, pp. 281-287, doi: 10.1364/OE.18.000281.

 ISBN: 978-1-61208-297-4

Development of Shear Horizontal Surface Acoustic Wave Sensor for Detecting Methanol Concentrations in a Direct Methanol Fuel Cell

Jun Kondoh
Graduate School of Science and Technology
Shizuoka University
Hamamatsu-shi, Japan
j-kondoh@sys.eng.shizuoka.ac.jp

Takuya Nozawa and Saburo Endo
Graduate School of Engineering
Shizuoka University
Hamamatsu-shi, Japan

***Abstract*— A liquid phase sensor is realized by using a shear horizontal surface acoustic wave (SH-SAW). The SH-SAW sensor can detect density and viscosity product, conductivity and relative permittivity of liquid. Sensor sensitivity depends on a piezoelectric substrate used. When a 36° rotated Y-cut, X propagating $LiTaO_3$ is used for the substrate, high sensitive detection of electrical properties is possible. In this paper, the SH-SAW sensor is applied to a methanol (MeOH) sensor. First, frequency dependences of the SH-SAW sensor are discussed. The results indicate that the responses of high frequency sensor agree with the perturbation theory. The application of the SH-SAW sensor is MeOH concentration detection in a direct methanol fuel cell (DMFC). As a formic acid is produced during electrode reactions in the DMFC, real fuel becomes binary-mixture solutions of MeOH and formic acid. In this paper, the solutions are also measured. It is found that influence of the formic acid can be neglected by using high frequency SH-SAW sensor. This means that the MeOH concentration is determined from phase shift.**

Keywords-component; SH-SAW sensor; direct methanol fuel cel;, methanol senso; influence of sensor frequency

I. INTRODUCTION

Surface acoustic wave (SAW) devices have a wide range of applications not only in filters, resonators, and oscillators [1], but also in sensors [2] and actuators [3]. Propagating characteristics of a SAW depends on an adjacent medium on a SAW propagating surface. The SAW is mechanically and electrically perturbed, when the adjacent medium physically and chemically changes. When a liquid is loaded on the SAW propagating surface, the SAW is influenced by liquid properties, such as density, viscosity, conductivity, and permittivity. However, to realize a liquid-phase SAW sensor, it is necessary to use a shear horizontal SAW (SH-SAW) to avoid a longitudinal wave radiation into a liquid [4].

A direct methanol fuel cell (DMFC) [5] is operated using a methanol (MeOH) solution. The reactions on the anode and cathode in the DMFC are as follows:

$$CH_3OH + H_2O \rightarrow 6H^+ + 6e^- + CO_2 \text{ for the anode,}$$

$$\frac{3}{2}O_2 + 6H^+ + 6e^- \rightarrow 3H_2O \text{ for the cathode.}$$

As the generation efficiency of the DMFC depends on the concentration of MeOH, the concentration must be known. As the DMFC has an optimum concentration range, monitoring of the MeOH concentration is required. The MeOH concentration is a function of sound speed, viscosity, density, permittivity, and refractive index. The SH-SAW sensor can detect viscosity and density products, and permittivity. The SH-SAW sensor, which is fabricated on 36° rotated Y-cut, X-propagating $LiTaO_3$ (36YX-$LiTaO_3$) can detect the permittivity with high sensitivity [6]. In previous research [6-9], frequency of the SH-SAW sensor was fixed at 50 MHz. In this paper, the SH-SAW sensors with different frequencies are used. The MeOH solutions are measured by changing the temperature. The experimental results are compared with the perturbation theory. Also, influence of a formic acid is discussed.

II. THEORY

Detection mechanism of the MeOH concentration is based on the electrical perturbation [10, 11]. A reference liquid is assumed as nonelectrolyte and expressed as

$$\varepsilon_\ell = \varepsilon_r \varepsilon_0. \tag{1}$$

Here, ε_ℓ, ε_r, and ε_0 are dielectric constant, relative permittivity of the reference liquid, and dielectric constant of free space, respectively. Electrical property of a sample solution is represented by a complex permittivity, ε_ℓ', as follows.

$$\varepsilon_\ell' = \varepsilon_r' \varepsilon_0 - j\frac{\sigma'}{\omega} \tag{2}$$

Here, σ is conductivity of liquid, ω is an angular frequency of the SH-SAW sensor, and $j = \sqrt{-1}$. The prime ($'$) denotes parameter of the sample solution. The SH-SAW is electrically perturbed the change from (1) to (2). The velocity shift, $\Delta V/V$, and attenuation change which is normalized by wave number, $\Delta\alpha/k$, are expressed by the following equations.

$$\frac{\Delta V}{V} = -\frac{{K_s}^2}{2}\frac{(\sigma'/\omega)^2 + \varepsilon_0(\varepsilon_r' - \varepsilon_r)(\varepsilon_r'\varepsilon_0 + \varepsilon_P^T)}{(\sigma'/\omega)^2 + (\varepsilon_r'\varepsilon_0 + \varepsilon_P^T)^2} \tag{3}$$

 ISBN: 978-1-61208-297-4

$$\frac{\Delta\alpha}{k} = \frac{K_s{}^2}{2} \frac{(\sigma'/\omega)\left(\varepsilon_r\varepsilon_0 + \varepsilon_P^T\right)}{(\sigma'/\omega)^2 + \left(\varepsilon_r{}'\varepsilon_0 + \varepsilon_P^T\right)^2} \quad (4)$$

Here, $K_s{}^2$ is an electromechanical coupling coefficient when the reference liquid is loaded on the SH-SAW surface, and ε_P^T is an effective permittivity of the substrate used.

As a MeOH solution is nonelectrolyte, the conductivity can be neglected. Then, (3) and (4) become to

$$\frac{\Delta V}{V} = -\frac{K_s{}^2}{2} \frac{\varepsilon_0\left(\varepsilon_r{}'-\varepsilon_r\right)\left(\varepsilon_r{}'\varepsilon_0 + \varepsilon_P^T\right)}{\left(\varepsilon_r{}'\varepsilon_0 + \varepsilon_P^T\right)^2}, \quad (5)$$

$$\frac{\Delta\alpha}{k} = 0 . \quad (6)$$

Equations (5) and (6) show that the velocity shift does not depend on the frequency and the normalized attenuation change does not changed.

In this paper, the temperature of the SH-SAW sensor was varied. The electromechanical coupling coefficient, effective permittivity, and electrical properties of liquid depend on the temperature. The coupling coefficient is calculated from the phase velocities on free and shorted surfaces. The phase velocity can be calculated by extended Campbell and Jones method for liquid/piezoelectric substrate structure [4, 12]. Kushibiki's material constants [13] and Smith's temperature coefficients [14] of $LiTaO_3$ were used for the numerical calculation. Material constants of MeOH solution were obtained from the chemical handbook [15].

III. EXPERIMENTAL PROCEDURE

A. SH-SAW sensor

The SH-SAW sensor used is shown in Fig. 1. As the SH-SAW on the 36YX-$LiTaO_3$ has large electromechanical coupling coefficient, the crystal was chosen. For generating and receiving SH-SAW, a floating electrode unidirectional transducer (FEUDT) [16] was fabricated on the crystal. The FEUDT was adopted to reduce phase distortion and improve insertion loss [7]. The SH-SAW sensor consists of dual delay lines. The propagating surface of one delay line, channel (Ch.) 1, was metallized and electrically shorted by evaporated gold and titanium films. On the shorted surface, particle displacement only interacts with the adjacent liquid and then the SH-SAW is mechanically perturbed. The other delay line, Ch. 2, has a free surface area where the crystal surface is in direct contact with a liquid. As the electrostatic potential and particle displacement interact with a liquid, the electrical and mechanical perturbations are obtained. The electrical perturbation is detected by detecting differential signals between two delay lines. Center frequencies of the SH-SAW sensors used was 51.5 and 155 MHz. All sensors were obtained from Japan radio Co. Ltd. Design parameters of the SH-SAW sensor used is summarized in Table I. Figure 2 shows a liquid flow cell used.

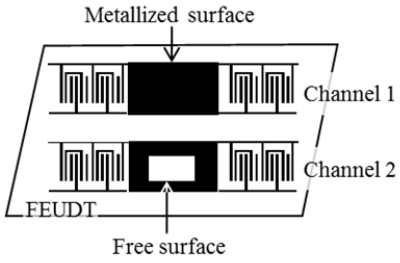

Figure 1. Schematic drawing of the SH-SAW sensor used.

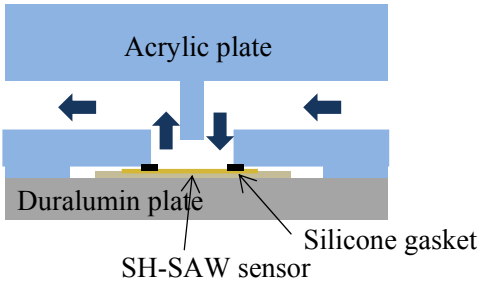

Figure 2. Cross section of the liquid flow cell.

TABLE I. DESIGN PARAMETERS OF THE SH-SAW SENSORS.

	51.5 MHz	155 MHz
Wavelength (λ)	80 μm	26 μm
Aperture	2,000 μm	666 μm
Number of pair	32	32
Distance between FEUDTs	11,000 μm	4,200 μm
Interaction length with liquid	4,000 μm 50 λ	3,000 μm 115.4 λ

B. Experimental setup

A sinusoidal signal from a signal generator (Anritsu MG3601A) is divided. One signal is directly connected to the vector voltmeter as a reference signal. The other is fed to the SH-SAW delay lines via a very high frequency (VHF) switching unit. The phase shift and amplitude ratio between the reference signal and Ch. 1 or Ch. 2 were monitored using a vector voltmeter (HP 8508A). The phase difference and amplitude ratio between the two channels was calculated using a PC. The velocity shift and normalized attenuation change were calculated from the phase difference and amplitude ratio, respectively.

Figure 3 shows the liquid flow measurement system with a peristaltic pump. Flow rate was fixed at 500 ml/min. A part of flow tube and a sample vessel were kept in a temperature-controlled chamber (ESPEC SU-240). The SH-SAW sensor with flow cell and pump were placed outside of the chamber. Temperature was varied from 10 to 80 °C. Temperature on the SH-SAW sensor was monitored using a thermocouple thermometer. The maximum temperature was determined on the basis of the actual DMFC.

 ISBN: 978-1-61208-297-4

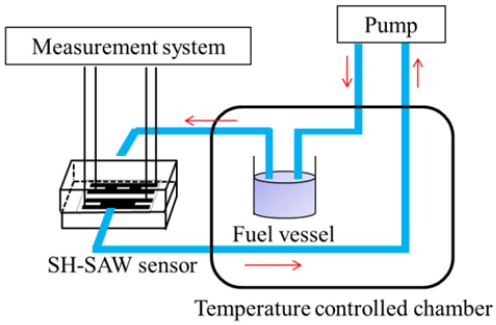

Figure 3. Experimental setup.

IV. RESULTS AND DISCUSSIONS

The MeOH solution of 3 wt% was measured. The concentration was decided on the based on the optimum concentration of a high-power DMFC. In Fig. 4, experimental results and calculated results of the velocity shift using eq. (5) are plotted. Reference temperature was 10 °C. When the temperature is lower than room temperature, the experimental results and theory agree well. However, the results from the 51.5 MHz SH-SAW sensor do not agree with the theory with increasing temperature. In eq. (5), conductivity of the sample is ignored. At high temperature, however, the conductivity cannot be disregarded. The conductivity depends on the temperature and it increases with temperature. In the equations, the conductivity is normalized by the angular frequency. This means that influence of conductivity reduces using a high frequency SH-SAW sensor. Therefore, reasonable results were obtained. We have proposed determination method of methanol concentration without any calibration [9]. The 51.5 MHz SH-SAW sensor was used. As the sensor responses and theory do not agree for the 51.5 MHz SH-SAW sensor, the electromechanical coupling coefficient was corrected. For the 155 MHz SH-SAW sensor, the correction of the electromechanical coupling coefficient is not necessary. The theory can be used to determine the MeOH concentration.

In Fig. 4, the ordinate is the velocity shift. The velocity shift is converted from measured phase shift. Here we compare the phase shift. The results are plotted in Fig. 5. Phase shift depends on the interaction length between the SH-SAW and liquid. The length is shown in Table. I. The converted length in wavelength of the 155 MHz SH-SAW sensor is longer than that to the 51.5 MHz SH-SAW sensor, reasonable results were obtained.

From Figs. 4 and 5, it is found that the best method to determine the concentration of MeOH solution is to use the high frequency SH-SAW sensor. The MeOH solution is liquid fuel for the DMFC. However, during electrode reaction, a formic acid is produced. The formic acid dissolves in the MeOH solution. In our previous research, we proposed the determination method of MeOH concentration of the binary-mixture solution of MeOH and formic acid using the 50 MHz SH-SAW sensor [6]. The

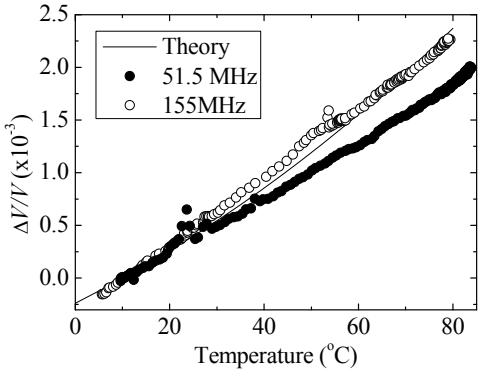

Figure 4. Comparison experimental results of 51.5 and 155 MHz SH-SAW sensors with the perturbation theory.

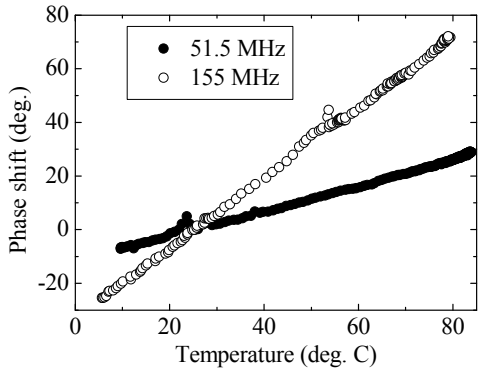

Figure 5. Phase shift as a function of the temperature.

method is complex and both velocity shift and normalized attenuation change are needed. If the MeOH concentration is determined from only the phase shift, a simple measurement system is realized and price will be decreased. Therefore, in this paper, the binary-mixture solutions of MeOH and formic acid were measured using the SH-SAW sensors and compared. The concentration of MeOH solution was fixed at 3 wt%. The value was decided actual value of the DMFC. Liquid was kept at room temperature. Figure 6 shows the velocity shift and normalized attenuation change as a function of concentration of formic acid. The velocity shift of the 155 MHz SH-SAW sensor is almost constant and the attenuation change is smaller than one of the 51.5 MHz SH-SAW sensor. The figure also exhibits that a high frequency SH-SAW sensor must be used to realize a MeOH sensor for the DMFC.

V. CONCLUSIONS

A MeOH sensor for a DMFC is required. In this paper, influences of the SH-SAW sensor for senor responses are experimentally and theoretically discussed. The MeOH solution can be assumed nonelectrolyte when the SH-SAW sensor frequency is high. From the results, the 155 MHz SH-SAW sensor is enough for this application. The advantage of using high frequency SH-SAW sensor is to reduce the influence of the conductivity. For the actual

 ISBN: 978-1-61208-297-4

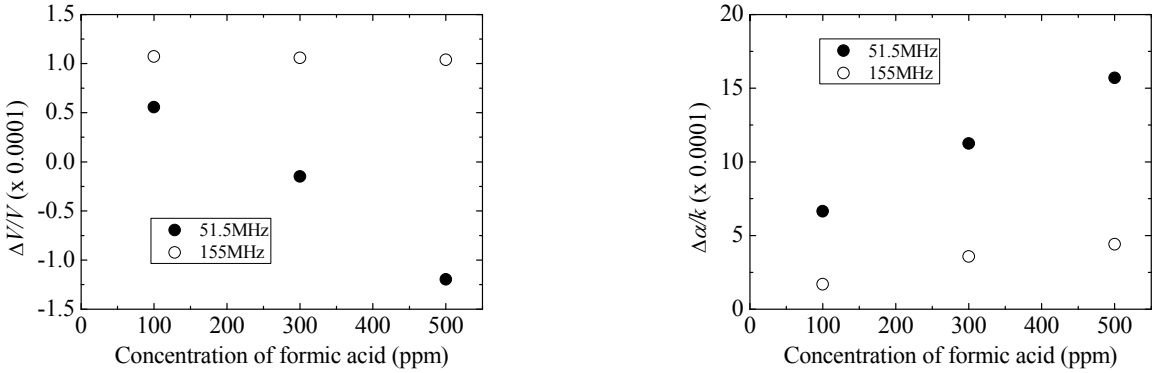

Figure 6. (a) Velocity shift and (b) normalized attenuation change as a function of formic acid conductivity in 3wt% MeOH solution.

DMFC, the formic acid is involved in the fuel solution. Obtained results in this paper suggest the means of the solving. Using the high frequency SH-SAW sensor, the MeOH concentration is determined from only the phase shift. Therefore, low price and simple measurement system will be realized using the high frequency SH-SAW sensor.

REFERENCES

[1] M. Kadota, "Development of Substrate Structures and Processes for Practical Applications of Various Surface Acoustic Wave Devices," Jpn. J. Appl. Phys., vol. 44, pp. 4285-4291, July 2005.

[2] S. Shiokawa and J. Kondoh, "Surface Acoustic Wave Sensors," Jpn. J. Appl. Phys., vol. 43, pp. 2799-2802, May 2004.

[3] N. Yasuda, M. Sugimoto, and J. Kondoh, "Novel Micro-Laboratory on Piezoelectric Crystal," Jpn. J. Appl. Phys., vol. 48, pp. 07GG14-1-07GG14-5, July 2009.

[4] T. Moriizumi, Y. Unno, S. Shiokawa, "New Sensor in Liquid Using Leaky SAW," Proc. IEEE Ultrasonic Symp., October 1987, pp. 579-582.

[5] J. Larminie and A. Dicks, "Kaisetsu Nenryo Denchi System (Fuel Cell Systems Explained)" , transl. H. Tsuchiya, Tokyo: Ohmsha, 2004, pp. 175-204 [in Japanese].

[6] J. Kondoh, S. Tabushi, Y. Matsui, and S. Shiokawa, "Development of methanol sensor using a shear horizontal surface acoustic wave device for a direct methanol fuel cell," Sensors and Actuators B, vol. 129, pp. 575-580, Feb. 2008.

[7] J. Kondoh, Y. Okiyama, S. Mikuni, Y. Matsui, M. Nara, T. Mori, and H. Yatsuda,, "Development of a shear horizontal surface acoustic wave sensor system for liquids with a floating electrode unidirectional transducer," Jpn. J. Appl. Phys., vol. 47, pp. 4065-4069, May 2008.

[8] S. Endo, J. Kondoh. K. Sato, and N. Sawada, "Methanol Sensor Using Shear Horizontal Surface Acoustic Wave Device for Direct Methanol Fuel Cell," Jpn. J. Appl. Phys., vol. 51, pp. 07GC19-1-07GC19-5, July 2012.

[9] J. Kondoh, S. Endo, and T. Nozawa, 2013 Joint UFFC, EFTF, and PFM Symp. (accepted for presentation).

[10] J. Kondoh and S. Shiokawa, "Shear Surface Acoustic Wave Liquid Sensor Based on Acoustoelectric Interaction, Electronics and Communications in Japan Part II, vol. 78, no. 1 pp. 101-112, 1995.

[11] J. Kondoh, K. Saito, S. Shiokawa, and H. Suzuki, "Simultaneous Measurement of Liquid Properties Using Multichannel Shear Horizontal Surface Acoustic Wave Microsensor," Jpn. J. Appl. Phys., vol. 35, pp. 3093-3096, May 1996.

[12] J. J. Campbell and W. R. Jones, "Propagation of Surface Wave at the boundary between a Piezoelectric Crystal and a Fluid Medium," IEEE Trans. Sonics & Ultrason., vol. SU-17, pp. 71-76, April 1970.

[13] J. Kushibiki, I. Takanaga, M. Arakawa, and T. Sannomiya, "Accurate Measurements of the Acoustical Physical Constants of $LiNbO_3$ and $LiTaO_3$ Single Crystals," IEEE Trans. UFFC, vol. 46, pp. 1315-1323, Sep. 1999

[14] R. T. Smith and F. S. Welsh, "Temperature Dependence of the Elastic, Piezoelectric, and Dielectric Constants of Lithium Tantalate and Litium Niobate," J. Appl. Phys., vol. 42, pp. 2219-2230, May 1971.

[15] The Chemical Society of Japan eds., "Kagaku Binran Kisohen II (Chemical Handbook, Basic II)," Tokyo: Maruzen, 1984 (in Japanese).

[16] K. Yamanouchi and H. Furuyashiki, "New low-loss SAW filter using internal floating electrode reflection types of single-phase unidirectional transducer," Electron. Lett., vol. 20, pp. 989-990, Nov. 1984.

 ISBN: 978-1-61208-297-4

Fungicide Residue Identification and Discrimination Using a Conducting Polymer Electronic-nose

Alphus Dan Wilson
Forest Insect and Disease Research
USDA Forest Service, Southern Hardwoods Laboratory
Stoneville, MS, USA
e-mail: dwilson02@fs.fed.us

***Abstract*— The identification of fungicide residues on crop foliage is necessary to make periodic pest management decisions. The determination of fungicide residue identities currently is difficult and time consuming using conventional chemical analysis methods such as gas chromatography-mass spectroscopy. Different fungicide types produce unique electronic aroma signature patterns when headspace volatiles are analyzed using a multi-sensor array within an electronic–nose device. The advantage of electronic-nose sensor devices over conventional methods is that fungicides may be rapidly identified even in the presence of complex plant volatile organic compounds derived from crop foliage that may be present in the headspace mixture. New methods were developed for a conducting polymer type electronic nose device, the Aromascan A32S with a 32-sensor array, to accurately identify and discriminate between fungicide residues types in vitro. The A32S electronic nose distinguished between nine of eleven fungicide types, providing correct identification determinations at frequencies ranging from 84-98%. The distribution of aroma class components, defined by the principal aroma elements detected for each fungicide type analyzed, was determined providing some indications of chemical relatedness between different fungicide aroma classes. The A32S electronic-nose device was capable of providing effective identification and discrimination determinations of most fungicide residue types tested in vitro and has strong potential feasibility for making e-nose fungicide residue determinations on plant (crop) surfaces in the field.**

Keywords- electronic aroma detection; e-nose technologies; volatile organic compounds; fungicide identification

I. INTRODUCTION

The detection and identification of pesticides and other chemical residues on agricultural and landscape plants currently requires time-consuming and expensive chemical analyses [1-4]. This problem has led to delays for crop and land managers who must make frequent crop-management and pest-control decisions involving pesticides applications. Pesticide residues on food crops also are a significant health concern, particularly on vegetables and fruits, which broadly impacts environmental regulatory decisions regarding the safety and legal-sale of food products in commercial markets. The inadequacies of current analytical methods for determining the identities and concentrations of pre-harvest and postharvest crop pesticide residues on the surfaces of food products has produced a strong need for new rapid chemical-detection methods to effectively identify pesticide residues on plants in crop fields and in postharvest storage facilities prior to plant-product introductions into commercial food markets. Thus, a portable electronic analytical gas-sensing device capable of quickly identifying agricultural pesticides on crop surfaces to avoid the high cost of conventional chemical analyses would have high utility.

Electronic-nose (e-nose) devices are designed to produce digital electronic aroma signature patterns (EASPs) derived from sensor-array responses to volatile organic compounds (VOCs) released from chemical sources [5-7]. Unlike other analytical instruments, e-nose devices have the capability of identifying organic samples from the VOCs they release without having to identify individual chemical compounds present in volatile mixtures [8-10]. A variety of different e-nose sensors have been developed including optical sensors [11], metal oxides [12, 13], semi-conductive polymers [14-16], and conductive polymers [17-19] for different applications. The broad agricultural and food industries have utilized electronic aroma detection (EAD) technologies to evaluate food quality and product aromas [20-21], food storage life and freshness [22-24], detect industrial wastes [25-26], diagnose plant diseases [27], and for many other agricultural applications [28-29], including the detection of hazardous agricultural chemicals in the environment [30-32].

The purposes of this study were to 1) determine if an electronic-nose (e-nose) device, the conductive polymer (CP)-type Aromascan A32S e-nose, has the capability of identifying different fungicide residue types in vitro, 2) evaluate the effectiveness (accuracy) of fungicide determinations, and 3) assess whether e-nose aroma data outputs provide some indications of chemical-relatedness between fungicide types from different chemical classes. The fungicide chemical classes tested include polychlorinated aromatic (chlorothalonil), piperazine (triforine), phenylamide (metalaxyl), organochlorine (PCNB), five triazoles (propiconazole, myclobutanil, triadimefon, difenoconazole, and tebuconazole), strobilurin (azoxystrobin), and dicarboximide (iprodione).

This paper is composed of an experimental section describing the materials and methods used in associated with e-nose procedures, followed by results of research findings for CPA e-nose chemical analyses of fungicides residues, and a discussion and conclusions section, based on research

 ISBN: 978-1-61208-297-4

results, to summarize the significance of findings and new discoveries resulting from this research.

II. MATERIALS AND METHODS

A. Collection and storage of fungicide samples

Eleven technical grade fungicides with the following specified common names and formulations, obtained from various pesticide manufacturers, including chlorothalonil (Bravo), triforine (Funginex), metalaxyl (Apron), pentachloronitrobenzene abbreviated as PCNB (Terrachlor), propiconazole (Tilt), azoxystrobin (Quadris), iprodione (Rovral), myclobutanil (Systhane), triadimefon (Bayleton), difenoconazole (Dividend), and tebuconazole (folicur) were utilized in this study. The fungicide azoxystrobin is unique among the eleven fungicides in that it is composed of a mycotoxin secondary metabolite (primarily strobilurin A), produced by mushrooms of the agricaceous fungi *Oudemansiella mucida* and *Strobilurus tenacellus*, common in Czechoslovakian forests.

B. Sample preparation and prerun procedures

Small aliquots (10 µl) of each fungicide type were analyzed separately by placing them into 14.8 ml uncapped glass vials inserted into a 500 ml Pyrex glass sampling bottle no. 1395 (Corning Inc., Corning, NY) fitted with reference air, sampling, and exhaust ports on a polypropylene bottle cap. Reference air entered the sampling bottle through a 3 mm polypropylene tube extending to just above the bottom of the sampling bottle. The sampling bottle was held in the sampling chamber at a constant air temperature of 25 C. The sampling bottle was purged with moisture-conditioned reference air for 2 min prior to building headspace. The sampling bottle was sealed and volatiles from each fungicide analyte were allowed to build headspace and equilibrate for 30 min prior to each run. Reference air was maintained at 4% RH at 25 C. Prerun tests were performed as needed to determine sample air relative humidity compared with that of reference air. A reference library (recognition file) for fungicide types was constructed using neural net training by defining aroma classes using reference databases of known fungicides. This recognition file then was used to identify unknown samples.

C. Instrument configuration and run parameters

All analyses were conducted with an Aromascan A32S (Osmetech, Inc.,Wobum,MA) CP e-nose instrument with 32 sensor capacity in the sensor array and 15 V across sensor paths. The response sensitivities of individual sensors, measured as percent changes in electrical resistance response across sensor paths relative to base resistance (%ΔR/Rbase), varied with the type of plastic polymer used in the sensor matrix coating, the type of ring substitutions used to modify its conductive properties, and the type of metal ions used to dope the matrix to improve and modulate sensor response. Detailed results of analyses that provided prior characterization and calibration of the sensor array were reported previously [27]. The block temperature of the sensor array was maintained at a constant 30 C. Reference air was preconditioned by passing room air sequentially through a carbon filter, silica gel beads, inline filter, and Hepa filter to remove organic compounds, moisture, particulates, and microbes, respectively, prior to humidity control and introduction into the sampling bottle. The flow rate (suction) of sample air at the sampling port was maintained at -702 ml/min using a calibrated ADM 3000 flow meter (Agilent Technologies, Wilmington, DE). Sensor surfaces were purged between runs using a 2% isopropanol wash solution. The instrument was interfaced with a personal computer via an RS232 cable and controlled with Aromascan Version 3.51 software. The instrument plumbing was altered from conventional architecture and specifically configured for static sampling of the headspace by allowing air flow, maintained at 605 ml/min flow rate, coming out of the external vent port of the instrument during analytical runs, and closing the exhaust port on the sampling bottle so that headspace volatiles were taken from a homogeneous static air mass within the sampling bottle.

D. Data acquisition parameters and run schedules

Data from the sensor array were collected at 1 s intervals using a 0.2 detection threshold (y-units), a 15–20 y-max graph scale, and with a pattern average of five data samples taken per run during data acquisition. A uniform run schedule was used consisting of reference air 20 s, sampling time 90 s, and wash 20 s, followed by 90 s of reference air for a total run time of 220 s. A 2 min reference air purge was completed between runs after each sample was removed from the sampling bottle.

E. Construction of reference libraries and validation

An aroma signature reference library was constructed from known fungicide residue types included in this study. All database files were linked to specific (designated) aroma classes defining each sample type or category. The following recognition network options (neural net training parameters) were used for each training session: training threshold = 0.60, recognition threshold = 0.60, number of elements allowed in error = 5, learning rate = 0.10, momentum = 0.60, error goal = 0.010 (P = 0.01), hidden nodes = 5, maximum iterations (epochs) = 10,000, using normalized input data, not actual intensity data. Some parameters were modified for improvement of recognition accuracy. A typical training required 2–35 min, depending on the size of the database applied, using an IBM-compatible personal computer with a minimum of 64 mb of RAM and 350 MHz run speed. Neural net trainings were validated by examining training results that compare individual database files for compatibility or by similarity matches to each specific odor classes by test-assigned odor class distributions among related odor classes included in each library. The specific detailed analytical methods used for identification of unknowns, data processing, and statistical determinations followed the procedures and specifications indicated by Wilson et al. [27].

F. Principal component analysis

Detailed comparisons of relatedness of odor classes (fungicide types) were determined using principal

 ISBN: 978-1-61208-297-4

component analysis (PCA) algorithms provided by Aromascan Version 3.51 software. Three-dimensional PCA was used to distinguish between headspace volatiles released from eleven fungicide residue types in vitro. The mapping parameters for three-dimensional PCA were: iterations = 30, units in Eigen values (%), and with normalized input data.

III. RESULTS

A. Identification of fungicide residue types

The A32S CP e-nose effectively identified nine of the eleven fungicide types tested based on differences in the aroma profiles of headspace volatiles derived from technical grade fungicide samples. Correct identifications of unknown fungicides residues were determined at rates ranging from range 84-98% for all fungicide types except for azoxystrobin and iprodione. Aroma discrimination software could not assign these two fungicide residue types to a principal aroma classification, among all of the aroma profiles present in the aroma reference library, because a large proportional majority of aroma components within the headspace volatiles from these fungicides did not fall into a single aroma class. The aroma components of both fungicide residues were predominantly distributed evenly among the two aroma classes of these two residue types. Thus, ambiguous identity determinations resulted for azoxystrobin and iprodione because a large percentage of aroma components were assigned to primarily two different aroma classes.

B. Discrimination between fungicide types

The aroma profiles of each fungicide type were further evaluated by neural net training validation during the process of creating a diagnostic pesticide library for the selected fungicides. Analysis of data from the sensor array for each aroma class (defined by the principal components present in aroma profiles from each fungicide type) provided a precise breakdown of the aroma class distribution of principal aroma components present in volatiles among the eleven fungicide types (Table I). The aroma class distribution indicated (on percentage bases) the proportion of aroma components, present in the headspace volatiles from each fungicide type, that were in common with principal aroma elements of volatiles from other fungicide types present in the reference library. The amount (percentage) of overlap among principal aroma elements from volatiles of each fungicide type provided an indication of relatedness between the chemical classes or chemical nature of volatiles released from individual fungicide residue types. Nine of the eleven fungicide types were identified correctly with a majority proportion of the aroma profile that was assigned to the principal aroma element characteristic of each fungicide type. The range of aroma class distributions attributed to the principal aroma class characteristic of each fungicide type ranged from 86.3% in difenoconazole to 98.4% in triadimefon. Unusually low proportions of the aroma class distribution profiles of azoxystrobin (57.8%) and iprodione (45.0%) were attributed to their respective principal aroma component. Consequently, these two fungicides residue types were determined as unknown aroma profiles and could not be identified. The proportion of secondary aroma elements attributed to aroma classes (besides the principal aroma element) ranged from 10.3-53.5% for azoxystrobin with three minor aroma elements, and 5.0-41.0% for iprodione with four minor aroma elements.

The number of minor aroma elements found among the aroma class distributions of the nine identified fungicide residues ranged from two to six. The smallest number of minor elements (two) discovered among the fungicides tested was determined for mycobutanil with aroma class distributions ranging from only 2.0-3.2%. The largest number of minor elements (six) was found for tebuconazole with aroma class distributions ranging from only 1.9-10.4%. The highest proportion of minor elements attributed to a single minor aroma class with identifiable fungicides was determined for propiconazole with 26.4% triforine aroma elements, PCNB with 22.5% propiconazole aroma elements, and chlorothalonil with 17.8% propiconazole aroma class elements.

C. Principal component analysis

An analysis of eleven fungicide residue types using PCA by pairwise comparisons of headspace volatiles in all possible combinations provided indications of possible chemical relatedness between fungicides. The results of relatedness between fungicide volatiles were measured using a statistical algorithm called quality factor (QF) analysis that determines the distance between aroma profiles using Euclidean distance units of measurement. The greater the QF value determined from pairwise comparisons of volatiles, the greater the difference (or distance) between the aroma signature profiles of the two aromas being compared. In terms of statistical determinations, a QF value of 2.0 is roughly equivalent to a statistical difference at $P = 0.10$ level of significance. The aroma relatedness among seven fungicide types from different chemical classes varied considerably based on Euclidean distance as indicated in Table II. QF values ranged from 2.4 to >320, indicating a very wide range of chemical differences between individual fungicide residue types. Among the seven fungicides compared, the QF of 2.4 indicated a significantly different, but relatively close aroma signatures between chlorophalonil and propiconazole. The biggest difference, indicated by a QF of >320, showed a strong difference between the headspace volatiles of PCNB and azoxystrobin. Moderate levels of aroma differences were found between chlorothalonil, triforine, and PCNB, between triforine, PCNB, and propiconazole, and between azoxystrobin and iprodione. Intermediate levels of aroma differences were found between chlorthalonil and iprodione, triforine and metalaxyl, metalaxyl and propiconazole, and between PCNB and iprodione. High levels of aroma differences were found between chlorothalonil, metalaxyl, and azoxystrobin, between triforine, azoxystrobin, and iprodione, and between metalaxyl, PCNB, azoxystrobin, and iprodione.

 ISBN: 978-1-61208-297-4

TABLE I. DISTRIBUTION OF ELECTRONIC-NOSE AROMA CLASS COMPONENTS AMONG ELEVEN FUNGICIDE TYPES

Fungicide Types	Aroma Class Distribution (%)[a]										
	Fungicide Types (Chemical common name abbreviations)										
	Chlo	**Trif**	**Meta**	**Pcnb**	**Prop**	**Azox**	**Ipro**	**Myco**	**Tria**	**Dife**	**Tebu**
Chlorothalonil	**90.4**	–	9.7	–	17.8	–	–	–	–	15.8	–
Triforine	–	**92.3**	–	7.2	11.7	16.3	13.2	2.9	–	–	–
Metalaxyl	–	–	**88.8**	–	14.9	8.0	6.4	9.6	11.4	–	–
PCNB	–	10.9	–	**88.1**	22.5	–	–	7.8	–	–	5.6
Propiconazole	–	26.4	7.4	6.5	**86.5**	–	–	–	7.2	14.8	–
Azoxystrobin	–	17.2	–	–	–	**57.8**	53.5	–	10.3	–	–
Iprodione	–	7.5	–	–	–	41.0	**45.0**	–	–	5.5	5.0
Mycobutanil	–	–	2.0	–	–	–	–	**98.4**	–	–	3.2
Triadimefon	–	–	5.3	1.7	–	1.4	–	–	**92.4**	6.5	–
Difenoconazole	–	–	–	3.7	9.3	–	–	–	1.9	**86.3**	5.6
Tebuconazole	3.7	–	–	10.4	–	6.0	9.2	1.9	–	5.9	**91.0**

a. Mean percent aroma class distributions indicated for each fungicide type; read from left to right (by row), not top to bottom. Fungicide abbreviations correspond to fungicide types (column 1).

The relatedness between aroma profiles of volatiles from the seven fungicide residue types, based on 3-dimensional CPA, was graphed in the form of an aroma map that indicates Euclidean distances among the seven fungicide types (Figure 1). The percentages of the total variance for this analysis, accounting for the variability explained by each orthogonal principal component (PC), are as follows: PC 1 = 61.5%; PC 2 = 25.8%; and PC 3 < 7.4%, representing the x-, y-, and z-axis of the aroma map, respectively. A high proportion (87.3%) of the total variance was explained by the first two principal components (PC 1 and PC 2). Two clusters of data points on the aroma map indicated groups of fungicide residue types that were significantly different, but moderately related based on similar aroma elements. The first data cluster consisted of chlorothalonil, propiconazole, and PCNB that had relatively low pairwise QF values of 2.4, 6.2, and 16.9 for each respective combination tested. The second cluster of data points consisted of azoxystrobin and iprodione with a pairwise QF value of 7.7 indicating a moderate level of chemical relatedness based on aroma elements. The fungicide residues of triforine and metalaxyl were highly separated from the two related data clusters, resulting in pairwise QF values ranging from 30.6 to 316.1 for triforine (relative to the other fungicides) and QF values of 75.6 to 317.1 for comparisons of the other fungicides to metalaxyl. However, the pairwise comparison yielding the largest QF value of >320 was between PCNB and azoxystrobin, indicating very large differences in aroma elements and an extremely low level of chemical relatedness.

The five triazole fungicides also were compared together in a separate PCA analysis to determine the e-nose capability of distinguishing between fungicides within the same chemical class. Comparisons of the triazole fungicide residues generally showed lower pairwise QF values that indicated a greater chemical relatedness between fungicides within the triazole class, based on aroma elements, than between fungicides from different chemical classes. The most chemically-related triazoles were difenoconazole and tebuconazole with a QF of 1.3 showing very similar aroma profiles. Most of the other pairwise comparisons between the triazoles resulted in QF values ranging between 20.3 and 86.4 with intermediate levels of aroma differences, but at high levels of statistical differences ($P < 0.001$). The triazole pairs that exhibited the greatest differences in aroma profiles were found between triadimefon and tebuconazole (QF=282.5) and between propiconazole and triadimefon (QF>290). High levels of residue discrimination were determined between the triazole fungicides in all cases except between difenoconazole and tebuconazole ($P < 0.05$).

IV. DISCUSSION AND CONCLUSION

This study has demonstrated that the CP A32S e-nose has the capability of identifying and discriminating between fungicide residue types (in vitro) from several different chemical classes including: polychlorinated aromatics, piperazines, phenylamides, organochlorines, triazoles, strobilurins, and dicarboximides. Additional work is necessary to determine e-nose detection capabilities with other fungicide classes and the feasibility for fungicide residue detection on crop plants in the field.

Electronic-nose aroma data outputs using PCA provided some indications of chemical-relatedness between fungicide types from different chemical classes. Generally, there were greater differences in aroma profiles between fungicides from different chemical classes than between fungicides in the same chemical class, which implied that the higher the

 ISBN: 978-1-61208-297-4

QF values in pairwise comparisons, the greater the chemical differences between fungicides based on aroma profiles (signature patterns) derived from outputs of the e-nose sensor array. However, high levels of discrimination were not only found between fungicides of different chemical classes, but also between some fungicide pairs within the triazole chemical class. These data suggest that aroma chemical characteristics can reflect big differences in the chemical structure and composition of individual fungicides even within the same chemical class. Thus, the e-nose determined aroma characteristics of fungicides, and probably other pesticides, are not always primarily determined by the functional groups and toxophores present (defining the chemical class), but also are determined by other functional groups that are present in the fungicide chemical structure.

TABLE II. RELATEDNESS OF SEVEN FUNGICIDE RESIDUE TYPES BASED ON 3-DIMENSIONAL PCA OF HEADSPACE VOLATILES

Aroma class	*Aroma class*	*QF value*[a]
Chlorothalonil	Triforine	13.7**
	Metalaxyl	125.4***
	PCNB	6.2**
	Propiconazole	2.4*
	Azoxystrobin	109.2***
	Iprodione	59.7**
Triforine	Metalaxyl	30.6**
	PCNB	6.7**
	Propiconazole	9.9**
	Azoxystrobin	109.2***
	Iprodione	316.1****
Metalaxyl	PCNB	178.8***
	Propiconazole	75.6***
	Azoxystrobin	317.1****
	Iprodione	258.9****
PCNB	Propiconazole	16.9**
	Azoxystrobin	> 320.0****
	Iprodione	62.4**
Propiconazole	Azoxystrobin	21.1**
	Iprodione	13.5**
Azoxystrobin	Iprodione	7.7**

a. Quality factor significant difference levels between aroma classes: * = P < 0.05; ** = P < 0.01; *** = P < 0.001; **** = P < 0.0001. The percentages of the total variance, accounting for the variability explained by each orthogonal principal component (PC), are as follows: PC 1 = 61.5%; PC 2 = 25.8%; and PC 3 < 7.4%.

The fungicides azoxystrobin and iprodione were the only two fungicide residue types that could not be identified with the A32S e-nose in the current study. In the case of azoxystrobin, this is a very unusual mycotoxin-type biofungicide (a strobilurin) derived from biological sources (agaric fungi) and not a product of petroleum-based chemical synthesis methods used in the manufacture of most fungicides. The complex structure of azoxystrobin may interfere with the effective detection and discrimination of this secondary fungal metabolite by the sensor array. Some chemical compounds, particularly certain pesticides, cause short- or long-term inactivation of specific sensors in the sensor array as a result of the chemical adhesion and interactions of certain pesticides with the surface of individual sensor types. The pesticides causing the most problems are usually those that are highly polarized or have locally-charged components on the pesticide molecule that react strongly to the surface chemistry of specific sensor types. This also may explain the difficulties in detecting iprodione, which is a dicarboximide that is highly polarized due to the presence of chlorines on the phenyl group and nitrogen groups on the imidazole and carboxamide groups.

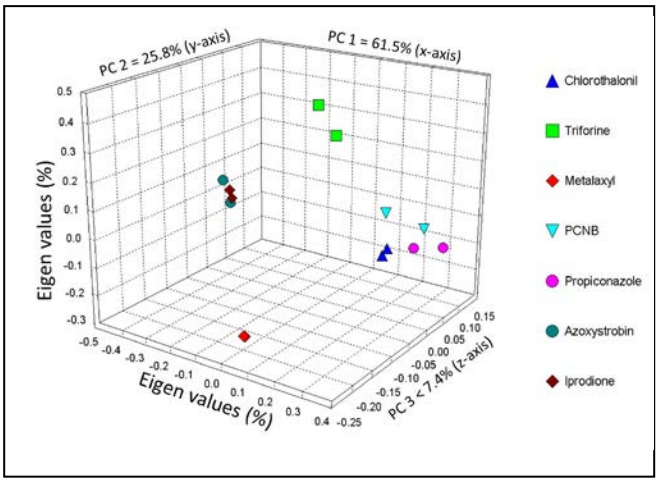

Figure 1. Aroma map showing the relatedness of volatiles from seven fungicide residue types using conductive polymer analysis (CPA).

The available literature on e-nose detection of pesticides is highly limited [4]. A surface acoustic wave (SAW) e-nose previously was used to detect organophosphate (OP) insecticides in ambient air [33] and on vegetables such as different types of chili samples [34].

The next logical step is to determine the feasibility of the e-nose to detect fungicide residues on plant (crop) surfaces in the field. The addition of plant volatiles to the headspace requires the development of new reference libraries to take into consideration all combinations of crop and fungicide types likely applied to a crop during the growing season. All possible combinations of fungicide residues must be accounted for on each crop type. The theoretical logistics of fungicide identifications on crops are quite feasible given that the discrimination of plant volatiles of different plant species has been well established previously [4, 27, 35].

ACKNOWLEDGMENT

The author thanks Mrs. Charisse Oberle for proofreading the manuscript.

 ISBN: 978-1-61208-297-4

REFERENCES

[1] A.D. Wilson, and M. Baietto, "Applications and advances in electronic-nose technologies," Sensors, vol. 9, July 2009, pp. 5099-5148. doi:10.3390/s90705099.

[2] S.O. Obare et al., "Fluorescent chemosensors for toxic organophosphorus pesticides: A review," Sensors, vol. 10, July 2010, pp. 7018-7043. doi:10.3390/s100707018.

[3] A.D. Wilson, "Review of electronic-nose technologies and algorithms to detect hazardous chemicals in the environment," Proc. Technol., vol. 1, 2012, pp. 453-463.

[4] A.D. Wilson, "Diverse applications of electronic-nose technologies in agriculture and forestry," Sensors, vol. 13, February 2013, pp. 2295-2348. doi:10.3390/s130202295.

[5] A. Rizzolo, G. Bianchi, M. Vanoli, S. Lurie, L. Spinelli, and A. Torricelli, "Electronic nose to detect volatile compound profile and quality changes in 'Spring Belle' peach (Prunus persica L.) during cold storage," J. Agric. Food Chem., vol. 61, 2013, pp. 1671−1685.

[6] B. Zhou, J. Wang, and J. Qi, "Identification of different wheat seeds by electronic nose," Int. Agrophys., vol. 26, 2012, pp. 413-418. doi: 10.2478/v10247-012-0-0058-y

[7] J. Lan, B. Liu, Z. Chen, Z. Song, and J. Lin, "Discriminate model of electronic nose for distinguishing volatiles of microbial fermentation bed in swine house," Fujian J. Agric. Sci., vol. 1, 2012, pp. 1–4.

[8] J.P. Santos, M. Alexandrea, and C. Cruz, "Hand held electronic nose for VOC detection," Chem. Eng. Trans., vol. 30, 2012, pp. 181–186.

[9] O.O. Oladipupo, and O.A. Eletta, "Neuro-identification of some commonly used volatile organic compounds using electronic nose," Chem. Process Eng. Res., vol. 2, 2012, pp. 43–53.

[10] D. Gao, J. Ji, J. Gong, and C. Cai, "Quantitative analysis of different volatile organic compounds using an improved electronic nose," Meas. Sci. Technol., vol. 23, Oct. 2012, pp. 205-210. doi:10.1088/0957-0233/23/10/105103.

[11] J. White, J.S. Kauer, T.A. Dickinson, and D.R. Walt, "Rapid analyte recognition in a device based on optical sensors and the olfactory system," Anal. Chem., vol. 68, July 1996, pp. 2191–2202.

[12] K. Brudzewskia, S. Osowskia, and W. Pawlowskia, "Metal oxide sensor arrays for detection of explosives at sub-parts-per million concentration levels by the differential electronic nose," Sens. Actuator B Chem., 2012, vol. 161, pp. 528–533.

[13] M. Baietto, L. Pozzi, A.D. Wilson, and D. Bassi. 2013. "Evaluation of a portable MOS electronic nose to detect root rots in shade tree species," Comput. Electron. Agr., vol. 96, 2013, pp. 117–125.

[14] M. Egashira, and Y. Shimizu, "Odor sensing by semiconductor metal oxides," Sens. Actuators, vol. 13, May 1993, pp. 443–446.

[15] M.E. Meyerhoff, "Polymer membrane electrode based potentiometric ammonia gas sensor," Anal. Chem. vol. 52, Aug. 1980, pp. 1532–1534.

[16] H.S. Yim et al., "Polymer membrane-based ion-, gas- and bio-selective potentiometric sensors," Biosens. Bioelectron., vol. 8, 1993, pp. 1–38.

[17] V. Parra et al., "E-tongue based on a hybrid array of voltammetric sensors based on phthalocyanines, perylene derivatives and conducting polymers: Discrimination capability towards red wines elaborated with different varieties of grapes," Sens. Actuator, 2006, vol. 115, pp. 54–61.

[18] J.V. Hatfield, P. Neaves, P.J. Hicks, K.C. Persaud, and P. Tavers, "Toward an integrated electronic nose using conducting polymer sensors," Sens. Actuators, vol. 18, Mar. 1994, pp. 221–228.

[19] H. Bai, C. Li, F. Chen, and G. Shi, "Aligned three-dimensional microstructures of conducting polymer composites," Polymer, vol. 48, Aug. 2007, pp. 5259-5267.

[20] E.A. Baldwin et al., "Effect of Liberibacter infection (Huanglongbing disease) of citrus on orange fruit physiology and fruit/fruit juice quality: chemical and physical analyses," J. Agric. Food Chem., 2010, vol. 58, pp. 1247–1262.

[21] H. Zhang, and J. Wang, J. "Detection of age and insect damage incurred by wheat with an electronic nose," J. Stored Prod. Res., 2007, vol. 43, pp. 489–495.

[22] E.A. Baldwin, J. Bai, A. Plotto, and S. Dea, "Electronic noses and tongues: Application for the food and pharmaceutical industries," Sensors, 2011, vol. 11, pp. 4744–4766.

[23] Dighavkar, C.; Patil, A.; Patil, S.; Borse, R. "Al-doped TiO2 thick film resistors as H_2S gas sensor," Sci. Technol., 2010, vol. 9, pp. 39–47.

[24] M. Zhang, X. Wang, Y. Liu, X. Xu, and G.; Zhou, "Species discrimination among three kinds of puffer fish using an electronic nose combined with olfactory sensory evaluation," Sensors 2012, vol. 12, pp. 12562–12571.

[25] A.H. Abdullah et al., "Chicken farm malodour monitoring using portable electronic nose system," Chem. Eng. Trans., 2012, vol. 30, pp. 55–60.

[26] L. Dentoni, L. Capelli, S. Sironi, R.D. Rosso, S. Zanetti, and M.D. Torre, "Development of an electronic nose for environmental odour monitoring," Sensors, 2012, vol. 12, pp. 14363–14381.

[27] A.D. Wilson, D.G. Lester, and C.S. Oberle, "Development of conductive polymer analysis for the rapid detection and identification of phytopathogenic microbes," Phytopathology, vol. 94, May 2004, pp. 419–431.

[28] H. Zhang, and J Wang, "Evaluation of peach quality attributes using an electronic nose," Sens. Mater., 2009, vol. 21, pp. 419–431.

[29] R. Labrador, J. Soto, R. Martinez-Manez, and L. Gil, "An electronic tongue for qualitative analyses of anions in natural water," J. Appl. Electrochem., 2009, vol. 39, pp. 2505–2511.

[30] S. Li, A. Simonian, B. A. Chin, "Sensors for agriculture and the food industry," Electrochem. Soc. Interfac., vol. 19, Winter 2010, pp. 41–46.

[31] L. Dentoni, L. Capelli, S. Sironi, R.D. Rosso, S Zanetti, M.D. Torre, "Development of an electronic nose for environmental odour monitoring," Sensors, vol. 12, Nov. 2012, pp. 14363–14381.

[32] H. Kim et al., "Electronic-nose for detecting environmental pollutants: Signal processing and analog front-end design," Analog Integr. Circ. Signal Process., vol. 70, 2012, pp. 15–32.

[33] C. Déjous, D. Rebiére, J. Pistré, C. Tiret, and R. A. Planade, "A surface acoustic wave gas sensor: Detection of organophosphorus compounds," Sens. Actuator, vol. 24, 1995, pp. 58–61.

[34] S. L. Tan, "E-nose screening of pesticide residue on chilli and double-checked analysis through different data-recognition algorithms," Electronics, Robotics,.and Automotive Mechanics Conference, Cuernavaca, Mexico, September 2010, pp. 592-596.

[35] A. D. Wilson, D. G. Lester, and C. S. Oberle, "Application of conductive polymer analysis for wood and woody plant identifications," For. Ecol. Managem., vol. 209, May 2005, pp. 207–224.

 ISBN: 978-1-61208-297-4

Metal-Insulator-Metal Gas Sensor Based on Polarizable Thin Films

Martin Schreivogel, Denis Kunz,
Ralf-Roman Rosenberger
Corporate Research
Robert Bosch GmbH
Stuttgart, Germany
martin.schreivogel@de.bosch.com

Martin Schreivogel, Wolfgang Menesklou, Ellen Ivers-Tiffée
Institute of Materials for Electrical and Electronic Engineering
Karlsruher Institut für Technologie (KIT)
Karlsruhe, Germany

***Abstract*— A new type of Metal-Insulator-Metal (MIM) gas sensor sensitive to low concentrations of hydrogen containing gases is presented. Less than 5 ppm H_2 give rise to significant signal changes compared to pure nitrogen or air. Response times are in the order of several ten seconds. The capacitive structure incorporates two stacked dielectric thin films (SiO_2, Al_2O_3) with a thickness of a few ten nanometers sandwiched between platinum electrodes. The oxides show a distinct polarization mechanism that influences the dielectric properties of the films at elevated temperatures above 200 °C. The devices are characterized by *I-V* measurements and impedance spectroscopy. The mobile species create an additional polarization mechanism that can be influenced by an appropriate DC bias. At low biases the dipoles are moveable in the oxide, so they can change their direction by an applied alternating field. At high biases the dipoles are pinned in one direction and the impedance spectrum of the device corresponds to an almost ideal capacitor with no loss mechanisms. Similar to an externally applied DC bias, species from the gas phase that are adsorbed at the electrode-insulator interface can introduce an electric field in the dielectric thin film influencing the mobility of the species. Thus, the contribution of the polarization mechanism to the impedance depends on the gas atmosphere and the change of its real or imaginary part can be used as sensor signal. Additionally, with this new gas sensor structure one can achieve selectivity for reducing and oxidizing gases by choosing appropriate operating points set by a DC bias.**

Keywords-gas sensor; hydrogen; silicon dioxid; aluminum oxid; polarization; impedance spectroscopy

I. INTRODUCTION

Gas sensors play a major role in monitoring and controlling many kinds of technological processes. One prominent example is the use of hydrogen as a renewable energy carrier for automotive or stationary fuel cell applications. Although there are many optimistic predictions concerning hydrogen based technologies, safety issues remain a critical aspect for hydrogen storage and transport [1]. Therefore, sensing hydrogen leakage with very high sensitivity is essential for the introduction of hydrogen as fuel for commercial applications.

During the last decade different physical mechanisms for the detection of hydrogen have been investigated. To name but a few, there are sensors that use hydrogen partial pressure sensitive optical constants, temperature changes due to different heat conductivities, resistivity changes of metal oxides and field effect devices that detect adsorbed gas species on their catalytically active gate electrode [2-6]. Most of these approaches involve quite elaborate preparation techniques and many different process steps. Furthermore, relatively complex devices still face considerable challenges concerning their long term stability.

We report a new kind of highly sensitive hydrogen gas sensor incorporating a polarizable thin film. The design of the sensor is extremely simple as it is basically a parallel plate capacitor.

At first appearance, one would not expect such a dielectric capacitance with a dense electrode to be gas sensitive. Therefore, after presenting the structure itself and its gas sensitivity in subsection II.A we performed current-voltage measurements (II.B) and impedance spectroscopy (II.C) in order to understand the physical mechanisms. Based on these measurements we propose a first model for the signal mechanism and an equivalent circuit in section II.C and II.D. Finally, we emphasize the potential of the MIM structures for selective gas detection in subsection II.E.

II. EXPERIMENTAL RESULTS AND DISCUSSION

A. Investigated structure and gas sensitivity

Fig. 1 depicts a schematic drawing and scanning transmission electron micrograph (STEM) of the examined metal-insulator-metal (MIM) structure. The two dielectric layers are sandwiched between two dense platinum electrodes. Plasma-enhanced chemical vapor deposited (PECVD) SiO_2 was chosen to promote the adhesion of the following atomic layer deposited (ALD) Al_2O_3. Aluminum oxide is known to show good stability when exposed to gas at elevated temperatures from our former studies [7]. There was no additional annealing step after deposition and the microstructure of the oxide films is amorphous whereas the platinum is polycrystalline, which was shown by the STEM measurements. The layout of the different layers was designed in a way that dielectric breakthroughs are avoided.

In a first step, the effective capacitance (calculated from the measured impedance with the assumption of an RC element as equivalent circuit for the structure) of the MIM structures was measured at a fixed frequency when they were exposed to different gases. The response to different

 ISBN: 978-1-61208-297-4

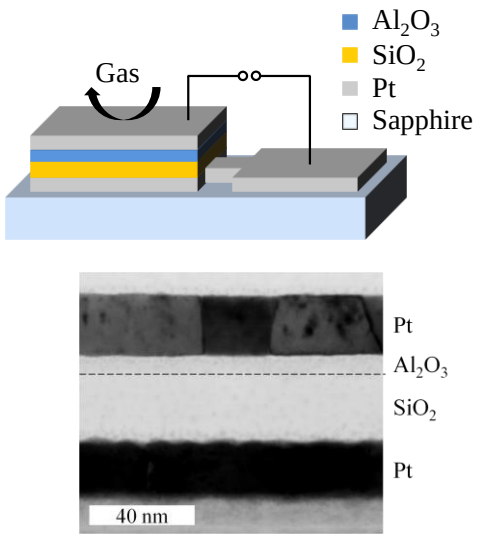

Figure 1. Schematic drawing and STEM micrograph of the examined MIM structure. They consist of a stack of a platinum back contact (20 nm), silicon oxide (23 nm), aluminum oxide (6 nm) and a dense platinum front electrode stacked on a sapphire substrate (to enhance the contrast between SiO_2 and Al_2O_3 a dashed line was added).

concentrations of hydrogen is shown in Fig. 2. The reference gas was pure nitrogen. The devices show a very high sensitivity and presumably it is possible to measure much lower concentrations, because the small signal change between 5 and 20 ppm suggests that the response is already close to saturation in this range (our home designed measurement system is limited to a minimum concentration of 5 ppm).

There was no response observed, when the device was exposed to NO or NO_2. However, there is cross-sensitivity towards other hydrogen-containing gases like C_2H_6 or NH_3.

As mentioned earlier, these clear and steplike hydrogen signals are surprising for a structure like this which incorporates none of the known transducer mechanism usually utilized for gas sensing. Since geometric changes of the dielectric layers can be ruled out as the origin of the capacitance change there has to be a variation of the electric properties of the dielectric thin films due to different gas atmospheres.

To explain these effects and to understand the most interesting gas sensitivity we systematically performed further electrical characterizations that are presented in the following subsections.

B. I-V measurements

One approach to explain the gas sensitivity is an influence of the hydrogen on the electronic or protonic DC conductivity of the dielectric films. Zhu et al. observed a hydrogen-induced increase in the direct current through an amorphous $(Ba_{0.67}Sr_{0.33})Ti_{1.02}O_3$ (BST) MIM structure when it was exposed to hydrogen. They explained it by an induced polarization potential at the electrode-BST interface [8]. To compare their results and validate their theory for our structures we measured the current through the dielectric as

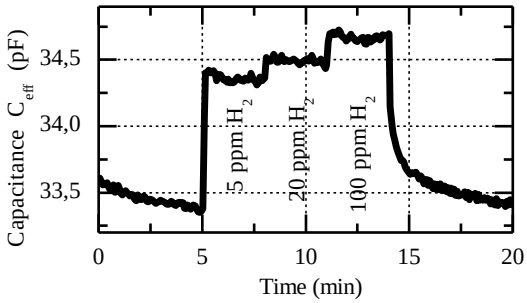

Figure 2. Response of the MIM structure to 5, 20 and 100 ppm hydrogen in nitrogen. The measurement frequency was 100 Hz and the device temperature was set to 350 °C.

function of voltage in pure nitrogen and 100 ppm hydrogen (see Fig. 3). In order to gain information about non-steady state processes we introduced a delay between voltage application and current measurement at each point. By increasing the delay the scan rate was decreased and consequently there was more time for the relaxation of non-steady state processes such as polarization currents. The temperature was set to 350 °C, only at these elevated temperatures the below described effects emerge.

In all the measurements there are distinct current maxima observed. They occur at voltages that are supposed to correspond to the flat band condition in the dielectric layers, that means at these biases the electric field in the dielectrics becomes zero. They occur in both scan directions showing some hysteresis. In nitrogen these maxima are not arranged symmetrically to zero volts. Possible reasons for this could be different work functions of the metal electrodes or fixed charges trapped in one of the oxides.

When the delay between voltage application and current measurement is increased, i.e., the scan rate is decreased, the described maxima vanish. This behavior indicates that there is a contribution to the current that is no continuous leakage current but some kind of polarization current. It should be noticed that the according polarization mechanism arises from the dielectric film itself and can't be explained by the charging of the geometrical capacitance as the time constant is at the order of several seconds.

Another observation that can be made in the current-voltage measurements concerns the effect of hydrogen. At the same scan rate the whole curve seems to be shifted towards lower voltages when exposed to 100 ppm hydrogen. Thus, the hydrogen acts like a voltage offset at the electrode. This offset can be understood as work function change of the platinum at the platinum-dielectric interface induced by adsorbed hydrogen [9]. From literature it is well known that hydrogen is able to diffuse through platinum thin films [10]. This is not the case for gases like NO or NO_2, which explains the observed selectivity towards hydrogen-containing gases for structures with dense front electrodes.

From the *I-V* measurements it can be concluded that the mechanism described by Zhu et al. is not the origin for the gas sensitivity of our structures. However, we got some first

 ISBN: 978-1-61208-297-4

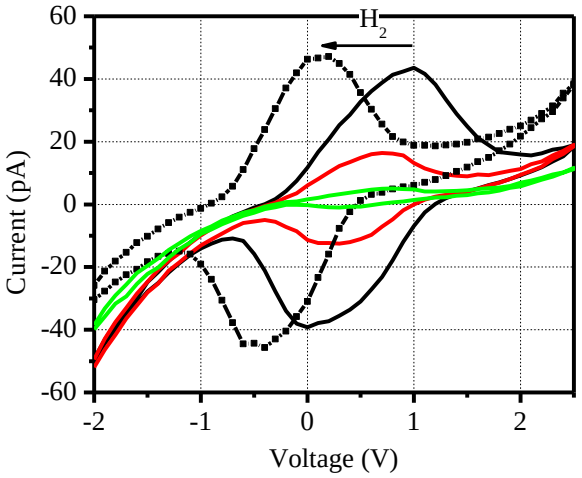

Figure 3. I-V-curves measured on the MIM structures in different gas atmospheres and with different scan rates. The step size of the scan was 100 mV and there was a delay between voltage application and current measurement at each point. The delay was 5 s, 15 s and 60 s (black, red, and green, respectively) for the curves in nitrogen at the right and 5 s for the curve in 100 ppm hydrogen in nitrogen at the left (square symbols).

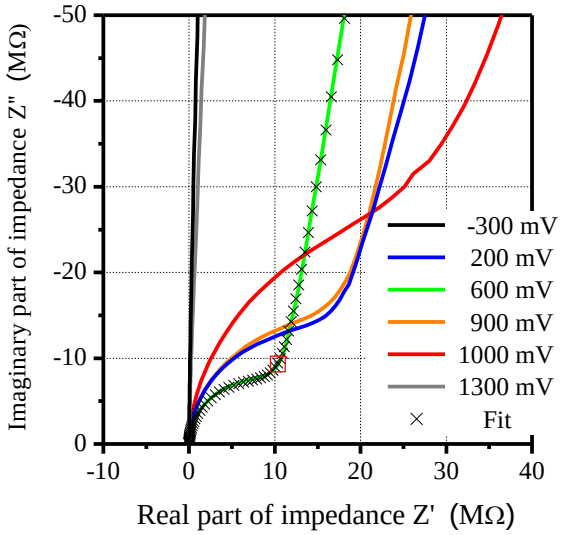

Figure 4. Impedance spectra of the MIM structures at different biases. The measurements were carried out at frequencies from 1 MHz down to 100 mHz (for clarity reasons there is only 1 MHz to 10 Hz depicted; the small red square marks the measured data at 100 Hz.) and at a temperature of 350 °C. The black crosses are fit values corresponding to the equivalent circuit model discussed in subsection D.

ideas of the signal formation mechanism for which an additional polarization mechanism seems to play a major role. Thereby motivated, we performed impedance measurements that are a common technique to characterize dielectric thin films with polarization losses.

C. *Impedance measurements*

In order to gain more information about the nature of the present polarization mechanism we measured the impedance of the structures as a function of frequency. To interpret these impedance spectroscopy data we chose Cole-Cole diagrams, which show the imaginary part Z'' of the impedance as a function of the real part Z', where $Z=Z'+jZ''$. Fig. 4 shows the spectra for different biases applied to the capacitances. In a certain bias range there is clearly an additional polarization mechanism present. It is expressed by the semicircle emerging for small impedances having a minimal radius at a bias of approximately 600 mV. This is in good agreement with the offset of the centre of the *I-V* curves from zero described in subsection B. For biases that are more than about 500 mV away from that value the Cole-Cole plot of the impedance spectrum shows almost a vertical line, which corresponds to an ideal capacitor with small losses. That means the impedance consists basically of a frequency-dependent imaginary part $Z''=-(\omega C)^{-1}$, where ω is the angular frequency and C the capacitance. This implies that there are polarizable species that are free to move when there is no net electric field in the dielectrics. Under these circumstances they contribute significantly to the impedance of the structure with a time constant at the order of 10 s. On the other hand the dipoles are pinned at one side or in one orientation when the magnitude of the applied voltages is relatively high.

The actual microscopic origin of the observed polarization and the relative contribution of the different oxides are subject of current investigations. There are different mechanisms like drifting ionic impurities or the switching of monovalent impurity ions, that are connected to the amorphous structure by non-bridging oxygen ions, imaginable [11]. In both cases the ongoing processes are thermally activated, which explains the need of temperatures above approx. 200 °C to observe the described effects.

The reason for the gas sensitivity of the structures can be examined with impedance measurements as well (see Fig. 5). The adsorbed hydrogen affects the whole frequency range and has the same effect as an additional bias of about 400 to 600 mV (compare to the bias-dependent measurements in nitrogen atmosphere in Fig. 4). This effect is at the same order of magnitude as the shift of the *I-V* curves in Fig. 3.

Additionally, from Fig. 5 the measured gas signal at one specific frequency can be understood in detail. As an effect of the adsorbed gas accompanied by the induced bias offset the influence of the polarization mechanism on the impedance spectra changes. This in general means that both the real and imaginary part of the measured impedance change. From this point of view the first way of plotting the gas signal in Fig. 2 as effective capacitance might be confusing because the assumption of an ideal capacitor for the calculation of the capacitance C_{eff} is invalid. To describe a system like this a little more complex equivalent circuit is necessary. A first suggestion is given in subsection D.

 ISBN: 978-1-61208-297-4

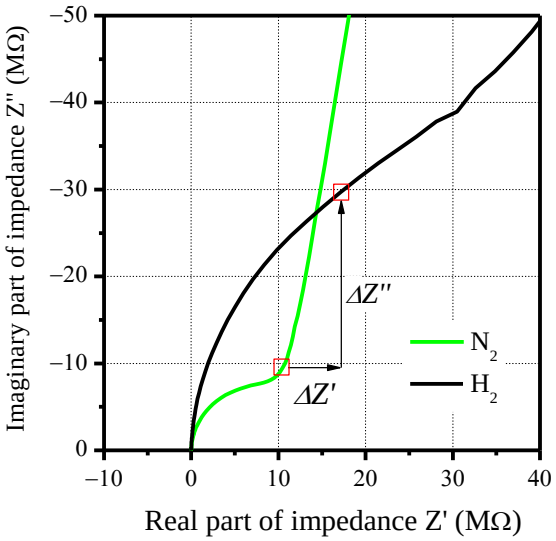

Figure 5. Impedance spectra of the MIM structures in pure nitrogen and 100 ppm hydrogen in nitrogen. In both cases the DC bias was 600 mV and the temperature 350 °C. The small red squares mark the measured data at 100 Hz.

D. Proposed equivalent circuit

In order to quantitatively describe the behavior of the MIM structure it is desirable to use an equivalent circuit model. As a first step we propose the circuit shown in Fig. 6. An impedance spectroscopy specialist might realize that the same electrical behavior can be described by a series connection of two RC elements. Nevertheless, we think that the shown approach is the physically more intuitive one. The physical meanings of the four components are as follows:
C_{geo} is the geometrical capacitance of the structure. Its origin is the charging of the parallel plate capacitor taking into account the bias-independent permittivity of the dielectrics at high frequencies:

$$C_{geo} = \varepsilon_0 \varepsilon_{r,eff}^{hf} \frac{A}{d} = \varepsilon_0 \frac{\varepsilon_{r,1}^{hf} \varepsilon_{r,2}^{hf}}{\varepsilon_{r,1}^{hf} d_2 + \varepsilon_{r,2}^{hf} d_1} A, \qquad (1)$$

where ε_0 is the permittivity of vacuum, $\varepsilon_{r,eff}^{hf}$ is the effective relative permittivity of the dielectric stack at high frequencies, $\varepsilon_{r,x}^{hf}$ and d_x are the relative permittivity and thickness of layer x, with $d=d_1+d_2$ and A is the area of the capacitor. C_{geo} is assumed to be constant for all applied biases and frequencies.

R_{el} is the resistance towards electronic leakage currents through the dielectric materials. It should be noted that in general R_{el} is not ohmic but depends on the applied voltage as there are different electronic conduction mechanisms like Schottky thermoionic emission or Poole-Frenkel conduction imaginable [12].

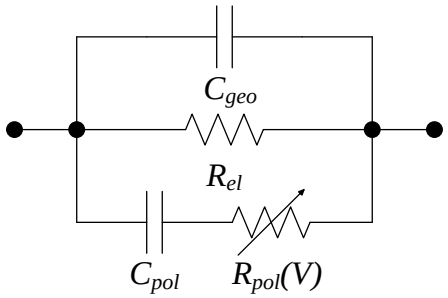

Figure 6. Equivalent circuit model for the MIM structure at elevated temperatures. C_{geo} is the geometrical capacitance, R_{el} the electronic leakage current and C_{pol} and R_{pol} represent the influence of the additional polarization mechanism.

The lower branch of the circuit is intended to describe the additional low frequency gas- and bias-dependent polarization mechanism for biases close to zero. Obviously there has to be an additional capacitance C_{pol} as the polarization allows a higher charge to be stored on the MIM structure at a certain voltage. To improve the agreement of the measured and fitted data one practically uses a so called constant phase element (CPE) instead of an ideal capacitance. The impedance of an CPE includes a correction coefficient n to describe deviations from ideal capacitances like rough electrode surfaces: $Z_{CPE}=((i\omega)^n C_0)^{-1}$ [13].

R_{pol} is implemented to take the polarization losses into account. Furthermore the series connection of C_{pol} and R_{pol} means that there is no continuous current through the lower branch of the parallel circuit. This physically makes sense since the species that are polarized are restricted to the dielectric layers and it is a consequence of the observations in Fig. 3.

In order to describe the observed bias dependence of the polarization, R_{pol} is not a constant, but changes with the bias, which can be seen by the varying diameter of the first semicircle. That means, an increased R_{pol} describes the reduced mobility of the dipoles in high electric fields and it shows a minimum at around 600 mV in nitrogen.

The presented model exemplary was fitted to the curve measured with a bias of 600 mV in Fig. 4. The extracted parameters are listed in Table 1. They all lie in the expected order of magnitude. For example C_{geo} with (1) can be estimated to be approximately (39±8) pF, using reasonable errors for the geometric dimensions (5%) and for the permittivities $\varepsilon_{r,SiO2}^{hf}$ =4.0±0.5 and $\varepsilon_{r,Al2O3}^{hf}$ =7.0±1.0 [14].

TABLE 1. FIT VALUES FOR THE EQUIVALENT CIRCUIT MODEL IN FIG. 6 AND THE IMPEDANCE DATA SHOWN IN FIG. 4 (600 MV)

C_{geo}	R_{el}	$C_{pol,0}$	n	R_{pol}
(33.7±0.5) pF	(13.4±0.4) GΩ	(398±3) pF	0.894±0.2	(13.6±0.1) MΩ

 ISBN: 978-1-61208-297-4

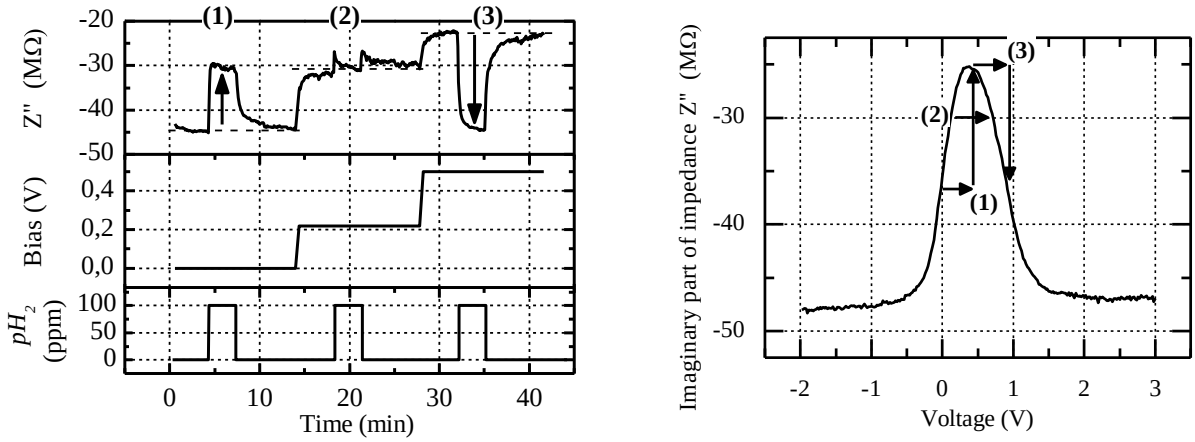

Figure 7. Gas signal - i.e. change in the imaginary part of the impedance - of the MIM structure for 100 ppm H_2 in nitrogen at different biases (left). The different polarities of the signal for different biases can be explained qualitatively by considering the dependence of the imaginary part of the impedance on the bias (right), showing a distinct peak. The horizontal arrows represent a constant voltage offset induced by the hydrogen starting from the externally applied bias.

E. Potential for selective gas measurements

Since it was observed that there is a relatively narrow bias range within which the described polarization mechanism occurs, the operating point, i.e., DC bias, at which the gas measurement is accomplished, obviously plays a critical role. This phenomenon is shown in Fig. 7. Here the imaginary part of the impedance was chosen as signal variable, the real part or the magnitude could be reasonable as well. According to which bias is chosen the gas signal can change its polarity or be completely suppressed. This behavior can be understood by considering the dependence of the impedance on the bias. There is a distinct peak of Z'' at a bias that is supposed to represent flat band condition in the dielectric, which means maximal mobility of the polarizable species. According to which bias is chosen an additional voltage offset caused by the adsorption of hydrogen will lead to an increasing or decreasing impedance and in one special case to no signal at all. It also can be concluded that there is going to be no gas signal for voltages smaller than minus one or bigger than plus two volts.

The described dependence of the working point implies great potential for selectivity of the sensor towards different gases. For example gases that induce a positive voltage offset like hydrogen will lead to a maximal positive gas signal for operating points somewhat below the position of the peak of the impedance.

Inversely, gases that cause negative voltage offsets will lead to maximal signal when the operating point is above the position of the mentioned peak. Of course, it will be necessary to employ porous electrodes to enable the adsorption at the electrode-dielectric interface for other gases than hydrogen.

III. CONCLUSIONS

A new kind of gas sensor that stands out by a very elementary structure, simple fabrication, robustness, and high sensitivity is presented. By choosing the proper operating point impedance signal changes of almost 100 % for 100 ppm hydrogen can be realized. We propose a first equivalent circuit model and are able to explain the observed gas sensitivity with the acquired knowledge of the system. On this basis it is possible to predict a gas-selective operation mode of the device. The calibration of the sensors, the gas selectivity, the long-term stability and the microstructural investigation of the observed polarization mechanism will be subject of our further work.

ACKNOWLEDGMENTS

We would like to thank MicroGaN GmbH for the processing of the samples and the German Federal Ministry of Education and Research for financial support of the publicity sponsored project “InoSens”.

REFERENCES

[1] Y.-H. Chen, C.-Y. Chen, and S.-C. Lee. „Technology forecasting of new clean energy: The example of hydrogen energy and fuel cell,” African Journal of Business Management, vol. 4, 2010, pp. 1372–1380.

[2] P. Tobiška, O. Hugon, A. Trouillet, and H. Gagnaire, “An integrated optic hydrogen sensor based on spr on palladium,” Sensors and Actuators B: Chemical, vol. 74, 2001, pp. 168 – 172.

[3] I. Simon and M. Arndt, “Thermal and gas-sensing properties of a micromachined thermal conductivity sensor for the detection of hydrogen in automotive applications,” Sensors and Actuators A: Physical, vol. 97–98, 2002, pp. 104 – 108.

 ISBN: 978-1-61208-297-4

[4] O. K. Varghese, G. K. Mor, C. A. Grimes, M. Paulose, and N. Mukherjeeb, "A titania nanotube-array room-temperature sensor for selective detection of hydrogen at low concentrations," Journal of Nanoscience and Nanotechnology, vol. 4, 2004, pp. 733–737.

[5] K. I. Lundström, M. S. Shivaraman, and C. M. Svensson, "A hydrogen-sensitive pd-gate mos transistor," Journal of Applied Physics, vol. 46, 1975, pp. 3876–3881.

[6] J. Schalwig, P. Kreisl, S. Ahlers, and G. Muller, "Response mechanism of sic-based mos field-effect gas sensors," Sensors Journal, IEEE, vol. 2, 2002, pp. 394 – 402.

[7] D. Kunz, R. Fix, and A. Martin, "Detection device for detecting gas within operating temperature range of detection device, has electrically conductive metal electrode and rear electrode made of metal or semiconductor material," Patent DE-102009029621 A1, 2009.

[8] W. Zhu, O. K. Tan, and X. Yao, "Amorphous ferroelectric $(Ba_{0.67}Sr_{0.33})Ti_{1.02}O_3$ thin films with enhanced H_2 induced interfacial polarization potential," Journal of Applied Physics, vol. 84, 1998, pp. 5134–5139.

[9] M. Fleischer and M. Lehmann, Solid State Gas Sensors - Industrial Application. Springer series on chemical sensors and biosensors, Springer, 2012.

[10] I. Lundström, H. Sundgren, F. Winquist, M. Eriksson, C. Krantz-Rülcker, and A. Lloyd-Spetz, "Twenty-five years of field effect gas sensor research in Linköping," Sensors and Actuators B: Chemical, vol. 121, 2007, pp. 247 – 262.

[11] F. Argall and A.K. Jonscher, "Dielectric properties of thin films of aluminium oxide and silicon oxide," Thin Solid Films, vol. 2, 1998, pp. 185 – 210.

[12] K. C. Kao, Dielectric Phenomena in Solids - With Emphasis on Physical Concepts of Electronic Processes, Elsevier Academic Press, 2004.

[13] J. R. Macdonald, E. Barsoukov (Editor), Impedance Spectroscopy: Theory, Experiment, and Applications, 2nd Edition, Wiley, 2005.

[14] S. Jakschik, U. Schroeder, T. Hecht, M. Gutsche, H. Seidl, and J. W. Bartha, „Crystallization behavior of thin ALD-Al_2O_3 films," Thin Solid Films, vol. 425, 2003, pp. 216 – 220.

 ISBN: 978-1-61208-297-4

Sensitivity Comparison between Surface Acoustic Wave and Lamb Acoustic Wave Hydrogen Gas Sensors

Assane Ndieguene, Issam Kerroum, Frédéric Domingue
Laboratoire des Microsystèmes et Télécommunications
Université du Québec à Trois-Rivières
Trois-Rivières, Canada
emails: {Assane.Ndieguene, Issam.Kerroum, Frederic.Domingue}@uqtr.ca;

Alexandre Reinhardt
Laboratoire d'Électronique et des Technologies de l'Information,
CEA, LETI
Grenoble, France
email:alexandre.reinhardt@cea.fr;

Abstract— **This paper presents a sensitivity study of acoustic hydrogen gas sensors. The study emphasises on the comparison between sensitivity of Surface Acoustic Wave (SAW) hydrogen gas and new acoustic hydrogen sensors based on Lamb waves. To highlight this comparison, a parametric model based on the variation of mechanical and physical properties of Palladium sensitive layers has been implemented. This results show that SAW wave devices are more sensitive to Young's modulus variations than Lamb Acoustic Wave devices.**

Keywords-acoustic hydrogen sensor; Lamb and surface acoustic waves; FEM; sensitivity.

I. INTRODUCTION

Due to the increasing demand on hydrogen gas sensors for several applications such as automation, transportation, or environmental monitoring, the need for sensitive and reliable sensors with a short response time is increasing [1-2]. The purpose of gas sensors is to analysis residual gas in a reservoir, to insure an optimal security in hydrogen vehicles, or to satisfy the current gas detection requirements. Therefore, in the recent years, the trend has been towards exploiting new emerging sensing technologies. One of most used technologies is the acoustic technology. Most of the developed acoustic sensors are based on Surface Acoustic Waves (SAW) [3-5]. These devices present a good reliability and robustness in harsh environments, combined with low fabrication cost. In addition, SAW devices are passive, that reduces power consumption [6-8]. Recently, some work has been devoted to Lamb wave resonators [9], which is said to exhibit promising performances for biological detection due to their improved mass sensitivity.

In this paper, a sensitivity comparison between SAW and Lamb wave devices is presented, in order to compare their suitability to hydrogen gas sensing.

Because of its high ability to interact with hydrogen molecules, Palladium (Pd) is often used as a sensitive layer to detect the presence of hydrogen gas [10-12] in SAW delay lines. In this work, 3% hydrogen concentration is considered and in this case, the Palladium density and Young's modulus decrease by 2% and 14% respectively with an $\pm 20\%$ error [13-14]. Based on finite element simulations, a parametric study technique has been used to analyze the impact of physical and mechanical parameters variations of a sensitive layer on the frequency of SAW and Lamb wave delay lines.

The different between acoustic modes used to perform the sensitivity analysis is presented in Section 2. In Section 3, the methodology and the finite element models are presented together with a comparison between frequency bands. Section 4 is devoted to the presentation of the obtained results and the analysis. The conclusion will be used to summarize main obtained results and analysis.

II. METHODOLOGY

A. Selected Modes Characteristics

This sensitivity comparison is based on analysing three different modes with different characteristics: two Lamb wave modes using Aluminum Nitride (AlN) membrane - the symmetric S_0 Lamb mode operating at low frequencies and an anti-symmetric A_1 Lamb mode operating at high frequencies above its cut-off frequency – and the Rayleigh mode propagating on the Lithium Niobate ($LiNbO_3$) substrate. The shape of these modes obtained by Comsol is shown in Fig. 1.

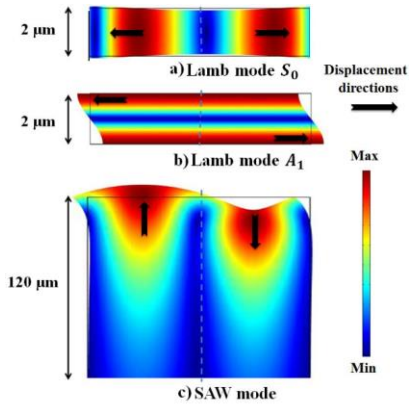

Figure 1. Comparison of the considered vibration modes: (a) S_0 Lamb mode , (b) A_1 Lamb mode and (c) Rayleigh mode substrate deformation

 ISBN: 978-1-61208-297-4

The S_0 Lamb mode corresponds to a compression or an extension of the piezoelectric plate along the propagation direction. Its deformations are homogeneous in the thickness of the plate. The A_1 mode corresponds to shearing in the thickness-direction of the membrane. For a $LiNbO_3$ substrate, the Rayleigh mode corresponds to an elliptic displacement in the sagittal plane and is evanescent in the thickness of the medium.

B. Sensitivity Comparison Method

To perform this comparison, the methodology used is based on a parametric study using Comsol. A model based on small simultaneous variations of sensitive layer properties (Young's modulus and density) is implemented. Initial values for Palladium Young's modulus and density are equal to $E_0 = 174\ GPa$ and $\rho_0 = 12020\ kg/m^3$ respectively. To cover most of the cases, a variation of $\pm 5\%$ for ρ_0 with a step of 0.8% and $\pm 20\%$ for E_0 with a step of 3.1% will be considered in the parametric study. Then, a reduced equation that shows the dependence of the operating frequency to the variations of the studied parameters is established by curve fitting method. This equation will highlight the sensitivity comparison between studied acoustic modes. The following diagram shown in Fig. 2 summarizes the path adopted to establish this equation.

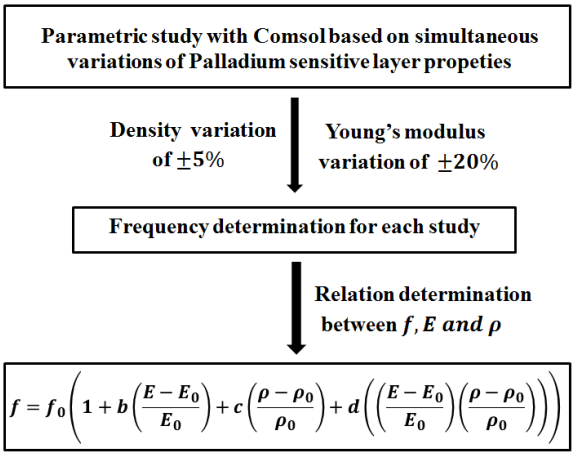

Figure 2. Flow chart summarizing the steps of calculating the relation between the frequency, the density and the Young modulus.

where b is the constant related to the sensitivity of Young's modulus, c is the constant related to the sensitivity of the density and d the interrelationship constant. To determine the equation used as model to perform the sensitivity, another high-order equations (second and fourth order) is explored. This study revealed that the fit and the residuals obtained from high-order equations are better than the established equation in Fig. 2. However, the use of high-order equations is more complex. Thus, for the sensitivity study the equation of first order will be adopted.

C. Finite Element Model Building

A c-axis oriented AlN plate is used for Lamb modes and a Y/Z $LiNbO_3$ cut for SAW mode. The description of the geometries used to perform sensitivity studies is represented in Fig. 3.

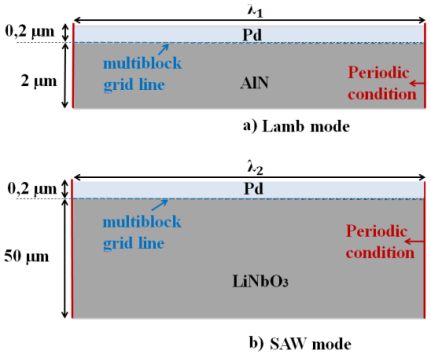

Figure 3. Comsol model proposed for the study of sensitivity: a) Lamb mode and b) SAW mode.

For each studied mode, piezoelectric, linear elastic and electrical models are used. To ensure continuity between blocks, multiblock and conformal mesh are used. Finally, Floquet periodic boundary conditions at the edges of the model are imposed to force a wavelength in the propagation direction.

D. Frequency Band Identification

Sensitivity studies are conducted around the ISM frequency bands: 433 MHz – 435 MHz and 902 MHz – 928 MHz. To design the geometry of the excitation electrodes (period of interdigitated electrodes), the dispersion curves of the first four Lamb wave modes in a 2 µm c-axis oriented AlN plate is plotted, as shown in Fig. 4.

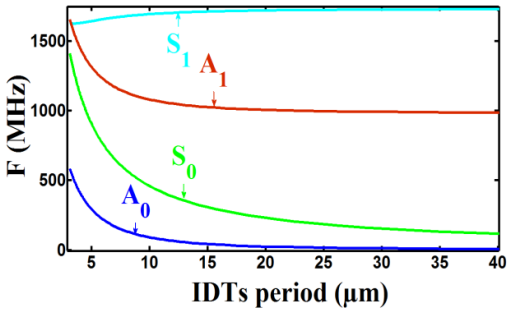

Figure 4. Dispersion curves for a 2 µm c-axis oriented AlN plate.

From these dispersion curves, the S_0 mode operates in the 430 MHz ISM band for electrode period of around 10 µm. The A_1 mode operates in the 920 MHz ISM band for electrode periods around 20 µm. These results are summarized in Table I.

TABLE I. ISM BAND IDENTIFICATION AND FINGERS PERIOD

Modes Selected	*ISM Band (MHz)*	*Fingers period (µm)*	*Wavelength (µm)*
S0	*433.05 – 434.79*	*10*	*20*
A1	*902 – 928*	*20*	*40*
SAW	*433.05 – 434.79 or 902 - 928*	*4 or 1.5*	*8 or 3*

 ISBN: 978-1-61208-297-4

The comparison between SAW and Lamb modes has been done in the same ISM bands frequency.

III. RESULTS AND DISCUSSIONS

A. S_0 Lamb and Rayleigh Mode Sensitivity Comparison

From parametric study proposed in Fig. 2, a relation between frequency and the Palladium various parameters is established, see equation 1.

$$f = f_0\left(1 + b\left(\frac{E-E_0}{E_0}\right) + c\left(\frac{\rho-\rho_0}{\rho_0}\right) + d\left(\frac{E-E_0}{E_0}\right)\left(\frac{\rho-\rho_0}{\rho_0}\right)\right) \quad (1)$$

This equation is used for Rayleigh and S_0 Lamb mode in order to determine the sensitivity of the frequency to the various parameters. The different constants for theses equations are shown in Table II.

TABLE II. S_0 LAMB AND RAYLEIGH MODE SENSITIVITY COMPARISON

Mode sensitivity	*b*	*c*	*d*
S_0	0.0321	-0.1529	0.0027
Rayleigh	0.0421	-0.1070	0.0071

These results show that the Rayleigh mode is more sensitive to changes in Pd stiffness than the S_0 Lamb mode. However, the S_0 Lamb mode is more sensitive to the mass loading effect than the Rayleigh mode. The initial frequency for Rayleigh mode and S_0 Lamb mode are 442 MHz and 476 MHz respectively. In the presence of 3% hydrogen concentration, density decreases by 5% and Young modulus by 20%. The expected frequencies are 440 MHz for the Rayleigh mode and 476 MHz for the S_0 Lamb mode. This shows that the Rayleigh mode is slightly more sensitive (0.45% frequency shift) than the S_0 Lamb mode for which the effect of Pd film stiffening and the mass-loading compensate each other.

B. A_1 Lamb and Rayleigh Mode Sensitivity Comparison

The same analysis was performed to compare the sensitivity between A_1 Lamb mode and Rayleigh mode in the same frequency band.

For each mode, material constants related to the sensitivity properties of the Pd layer are extracted from the set of parametric simulations.

TABLE III. A_1 LAMB MODE AND RAYLEIGH MODE SENSITIVITY COMPARISON

Mode sensitivity	*b*	*c*	*d*
A_1	0.0293	-0.1941	0.0195
Rayleigh	0.0774	-0.2130	0.0078

In this case, the Rayleigh mode is more sensitive to all changes in material properties of the Pd film. In addition, the initial value and the expected value of the frequency are 1082 MHz and 1075 MHz respectively for Rayleigh mode, resulting in a 0.65 % frequency shift. For the A_1 Lamb mode, the initial value is 1154 MHz and the expected value is 1155 MHz, that leads to a 0.09% frequency shift. It is also interesting to note that with the increase in operation frequency, the Rayleigh mode has become more sensitive to added mass and increased stiffness. This is attributed to the decreasing of penetration depth at higher frequency, and therefore a better confinement of vibrations at the vicinity of the sensitive material.

IV. CONCLUSION AND FUTURE WORK

In this paper, the sensitivity comparison between the classical SAW hydrogen gas sensor and future potential hydrogen gas sensors based on Lamb waves was presented. This comparison was performed considering delay lines operating in the ISM bands, at around 430 MHz and 920 MHz. Theoretical evaluations showed that, in the presence of 3 % hydrogen concentration, gas acoustic sensors based on Rayleigh waves are more sensitive to hydrogen than similar Lamb wave sensors. To generalize these results, other comparative studies will be conducted to determine the influence of hydrogen concentration.

REFERENCES

[1] C. Sachs and A. Mack-Gardner, "Safety Aspects of Hydrogen Fuel Cell Vehicles," 18th World Hydrogen Energy Conference, 2010, vol. 78-5, pp. 249-252, Germany.

[2] I. Kerroum, H. El-Matbouly, and F. Domingue, "Survey of commercial sensors and emerging miniaturized technologies for safety applications in hydrogen vehicles," Sensors Application Symposium, 2012, Brescia, Italy.

[3] H. Wohltjen and R. Dessy, "Surface acoustic wave probe for chemical analysis," Analytical chem, 1979, vol. 51, pp. 1458-1475.

[4] A. D'Amico, A. Palma, and E. Verona, "Surface acoustic wave hydrogen sensor," Sensors and Actuators, 1983, vol. 3, pp. 31–39.

[5] W. P Jakubik, M. W. Urbanczyk, S. Kochowski, and J. Bodzenta "Bilayer structure fir Hydrogen detection in a surface acoustic wave sensor system," Sensors and Actuators B, 2002, vol. 82, pp. 265–271.

[6] D. S. Ballantine, R. M. White, S. J. Martin, A. J. Ricco, E. T. Zellers, G. C. Frye, and H. Wohltjen, "Acoustic Wave Sensor – Theory, Design, and Physico-Chemical Applications," Academic Press, San Diego, 1997.

[7] M. F. Hribšek, D. V. Tošić, and M. R. Radosavljević, "Surface Acoustic Wave Sensors in Mechanical Engineering," FME Transactions, 2010, vol. 38, pp. 11-18.

[8] J.D.N. Cheeke and Z. Wang, "Acoustic wave gas sensor," Sensors and Actuators B, 1999, vol. 59, pp. 146-153.

[9] I.Y. Huang and M.C. Lee, "Developpement of a FPW allergy biosensor for human IgE detection by MEMS and cystamine-based SAM technologies,'' Sensors and Actuators B: chemical, 2008, vol. 132, pp. 340-348.

[10] F. Yang, D. K. Taggart, and R. M. Penner, "Fast sensitive Hydrogen Gas Detection Using Single Palladium Nanowires That Resist Fracture,'' Nano Lett., 2009, vol. 9, pp. 2177–2182.

[11] F. A. Lewis, "Absorption of Hydrogen by Palladium Alloys," Platinum Metals Rev., 1970, vol. 14, pp.131-132.

[12] A. D'Amico, A. Palma, and E. Verona, "Hydrogen sensor using a palladium coated surface acoustic wave delay-line," IEEE Ultrasonics Symp, Oct. 1982, pp. 308-311.

[13] M. Z. Atashbar, B. J. Bazuin, M. Simpeh, and S. Krishnamurthy, "3D FE simulation of H2 SAW gas sensor," Sensors and Actuators B, 2005, vol. 111-112, pp. 213–218.

[14] N. R. Krishnan, H. B. Nemade, and R. Paily, "Simplified Finite Element Simulation of a SAW Hydrogen Sensor using COMSOL Multiphysics," Excerpt Proc. COMSOL, 2008, Hannover.

 ISBN: 978-1-61208-297-4

Theoretical Investigation of an Ultrasonic Array Transmitter with Anisotropic Directivity

Sahdev Kumar, Kentaro Ichi, and Hideo Furuhashi
Dept. of Electrical and Electronics Eng.
Aichi Institute of Technology
Toyota, Japan
furuhasi@aitech.ac.jp

***Abstract*— A range sensor based on an ultrasonic array transmitter with anisotropic directivity is investigated theoretically. Although the sound power of an array transmitter with isotropic directivity decreases as the angle of the divergence increases, with anisotropic directivity, the decreases are limited and high power is obtained. The time delay required to control divergence is discussed.**

Keywords-ultrasonic; array sensor; transmitter; range sensor

I. INTRODUCTION

Ultrasonic sound has a number of applications. In particular, it is widely used to measure the distance between two points and in range sensors, which can measure the three-dimensional positions and shapes of various objects [1–4]. Ultrasonic sensors have the advantage of being simple to construct, of being able to perform measurements in optically invisible conditions, and of being relatively non-intrusive when used to monitor daily activities. Since ultrasonic waves traveling through air are spread and absorbed, the range for measurements is limited to a few meters. Some investigations using spark discharge to make high-power ultrasonic transmitter in order to improve the measurable range [3]. However, the frequency is not controllable. We have constructed a high-power ultrasonic transmitter that consists of an array of transmitting elements [4] in order to improve the measurable range. We have constructed a high-power ultrasonic transmitter that consists of an array of transmitting elements and obtained the pressure 144 times higher than that of a single element [4]. The sound frequency is exactly 40 kHz. However, all elements of the array generate ultrasonic sounds that are in phase with each other, and the directivity is narrow. The measurement is thus limited to a small area. Therefore, we proposed an ultrasonic array transmitter in which the phase of the sound is controlled for each element [5], and which has isotropic directivity. As a result of these changes, we showed that the divergence of the directivity is successfully controlled by the phase control, and the directional measurement field covers a wide range. However, the sound pressure decreased significantly with the increase in the divergence. In many cases of measurement in air, a wide area is required in the horizontal direction but not in the vertical direction. Therefore, we consider an ultrasonic array transmitter with wide horizontal but narrow vertical divergence in order to retain a high level of sound pressure.

In the present paper, we discuss the theory of this system and investigate its behavior.

II. ULTRASONIC ARRAY TRANSMITTER

The present paper discusses the array transmitter that was developed in our laboratory. The array has (12 × 12) elements in the XY plane at a distance of 10 mm from each other. Each element has a radius of 4.3 mm, directivity of 100° (-6 dB), and operates at 40kHz.

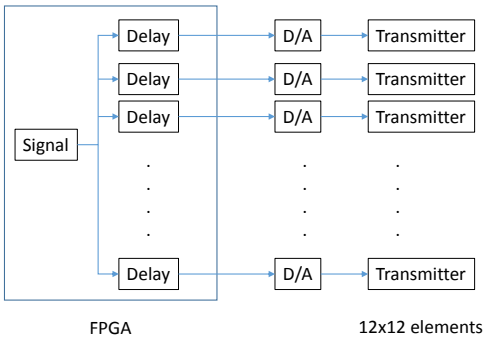

Figure 1. Schematic diagram of the system.

The phase of the signal from each element is controlled by a signal-delay controller, as shown in Fig. 1. The phase delay has been controlled with the sampling rate of 1μs.

III. THEORY

A. Array Transmitter with Isotropic Directivity

There are many transmitting elements at positions $P_i(x_i, y_i, 0)$ in the z = 0 plane and directed toward the z-axis, as shown in Fig. 2 (ultrasonic array).

We now consider an array transmitter with isotropic directivity (the divergences are the same in the *x* and *y* directions). The coordinate system of the divergence is shown in Fig. 3. The sound pressure is obtained by the following equation [5]:

 ISBN: 978-1-61208-297-4

$$|P(x,y,z)| \approx A\frac{1}{r}\left|\sum_i D(\theta_i)\exp\left(-2\pi i\frac{x_i\sin\theta_x + y_i\sin\theta_y + \frac{x_i^2+y_i^2}{2L}}{\lambda}\right)\right| \quad (1)$$

where A is the amplitude of the sound pressure from one element, r is the distance between the origin (i.e., the center of the array) and the observation point $P(x, y, z)$, and θ_x and θ_y are respectively the angles between the vector $\overrightarrow{OP}$ and the yz- and xz-planes. $D(\theta_i)$ is the directivity of the transmitting element

L is the distance between the center of the divergence and the center of the array, as [5]

$$L = \frac{\frac{n-1}{2}d}{\tan\phi}. \quad (2)$$

Here, n × n transmitter elements are located in a square with length of d in the x and y directions. The length of each side is obtained by (n-1) × d, and ϕ is the angle of the divergence.

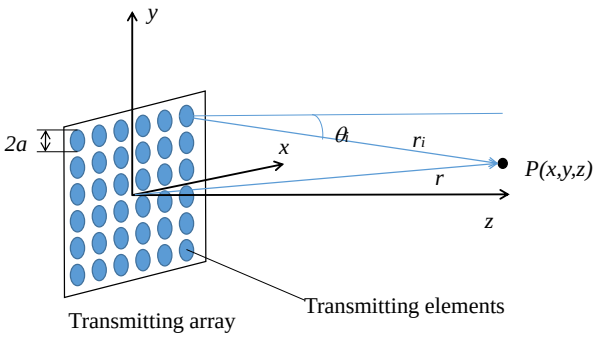

Figure 2. Coordinate system for calculations.

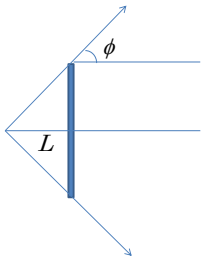

Figure 3. Coordinate system of divergence array transmitter with isotropic directivity.

Such a sound wave is obtained by applying a time delay for each element as follows [5]:

$$\Delta\tau_d \approx \left(x_i^2 + y_i^2\right)\frac{1}{2\upsilon L}, \quad (3)$$

where υ is the velocity of the sound wave.

B. *Array Transmitter with Anisotropic Directivity*

We next consider an array transmitter with anisotropic directivity (the divergences are different in the x and y directions). Figure 4 shows this coordinate system and the angle of divergence.

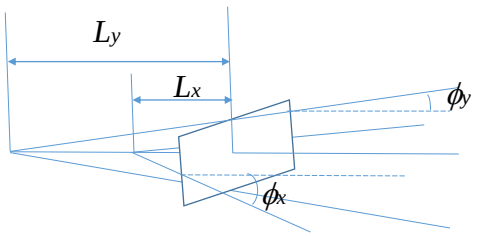

Figure 4. Coordinate system of divergence array transmitter with anisotropic directivity.

Here, ϕ_x and ϕ_y are the angles of the divergence in the x and y directions, respectively, and L_x and L_y are the distances between the center of the array and center of the divergence in the x and y directions, respectively. They are calculated as follows:

$$L_x = \frac{\frac{n-1}{2}d}{\tan\phi_x}, \quad (4)$$

$$L_y = \frac{\frac{n-1}{2}d}{\tan\phi_y}. \quad (5)$$

By modifying (1), the following equation is obtained for an array transmitter with anisotropic directivity:

$$|P(x,y,z)| \approx A\frac{1}{r}\left|\sum_i D(\theta_i)\exp\left(-2\pi i\frac{x_i\sin\theta_x + y_i\sin\theta_y + \frac{x_i^2}{2L_x} + \frac{y_i^2}{2L_y}}{\lambda}\right)\right|. \quad (6)$$

The time delay applied to each element is

$$\Delta\tau_d \approx \left(\frac{x_i^2}{L_x} + \frac{y_i^2}{L_y}\right)\frac{1}{2\upsilon}. \quad (7)$$

IV. RESULTS

Figure 5 shows the directivities of an array transmitter in which all the elements are in phase, as calculated using (1). The elements have a radius of 4.3 mm, and the transmitting elements are located in squares with lengths of 10 mm in the x and y directions. The sound pressure is normalized by A/r.

 ISBN: 978-1-61208-297-4

Figure 5(a) is the 2D image, and Fig. 5(b) is the result along with the x-axis. The sound pressure is normalized by A/r such that the normalized sound pressure of a transmitter with one element is 1. A sound pressure 144 times higher than that of a single element is obtained, and it has a directivity of ±2 deg. Note that this directivity is too narrow for some applications.

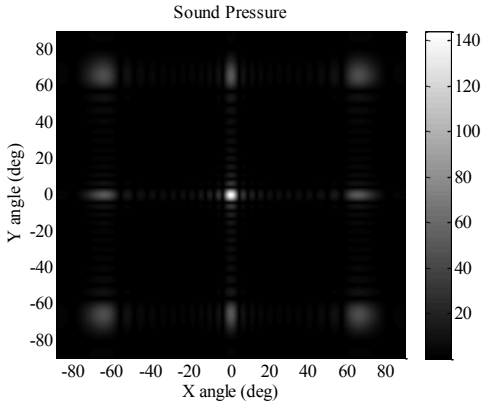

(a) 2D image.

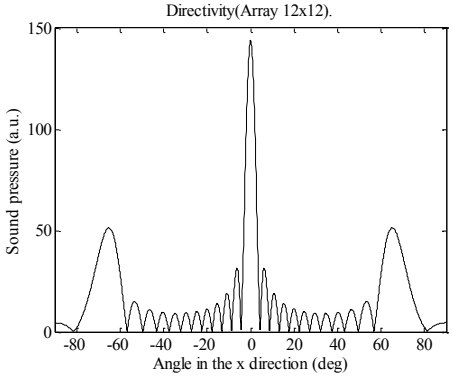

(b) In the *x* direction.

Figure 5. Sound pressure of the arry transmitter in phase. The sound pressure is normalized by A/r.

Figure 6 shows the directivities of an array transmitter in which the divergence of the directivity is controlled, as in (1). The angle of the divergence used in the equation is 20 deg in the *x* and *y* directions. The sound pressure is normalized by A/r.

The length L is calculated to be 155 mm. The time delay is calculated by (3), and it is 0 to 1.45 ms. Although the angle of divergence is about ±20 deg, the sound pressure is only 1/20th that of a single element, and it is 7 times lower than that of an array transmitter that is in phase.

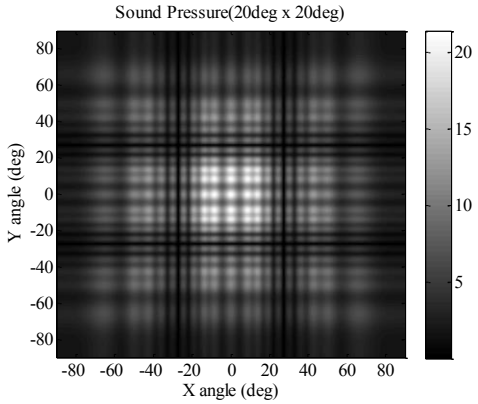

(a) 2D image.

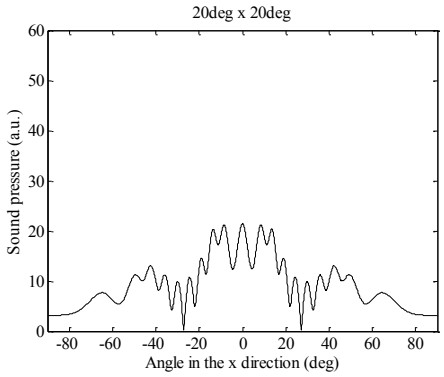

(b) In the *x* direction.

Figure 6. Sound pressure of the arry transmitter with isotropic phase. The sound pressure is normalized by A/r.

Figure 7 shows the directivities of an array transmitter for which the anisotropic directivity is calculated by (6). The angle of divergence used in the calculation is 20 deg and 5 deg in the *x* and *y* directions, respectively. The sound pressure is normalized by A/r.

The angle of divergence is about 20 deg and 5 deg in the *x* and *y* directions, respectively. The peak pressure is about 48 times higher than that of a single element transmitter and 2.5 times higher than that of an array transmitter with isotropic directivity. The measuring area at the distance r=30 m is ±10 m horizontally and ±2.6 m vertically.

Figure 8 shows the dependence of the sound pressure on the angle of the divergence in the *y* direction. The angle of the divergence in the *x* direction is changed. The sound pressure decreases with an increase in the angle of divergence for the isotropic array transmitter ($\phi_x = \phi_y$).

 ISBN: 978-1-61208-297-4

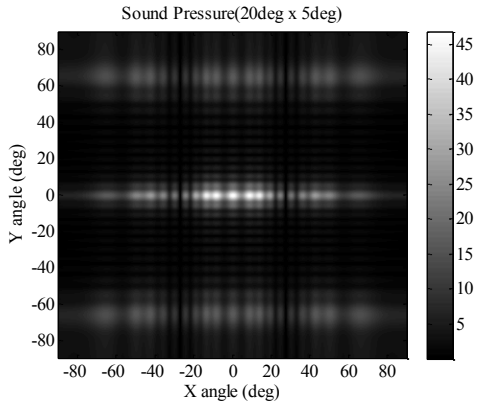

(a) 2D image.

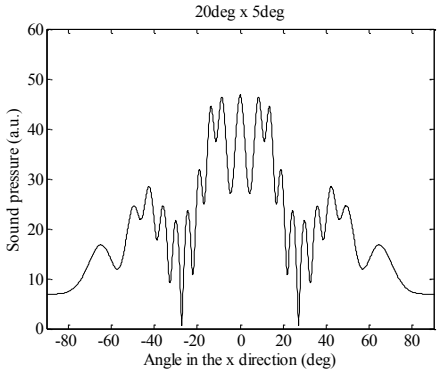

(b) In the *x* direction.

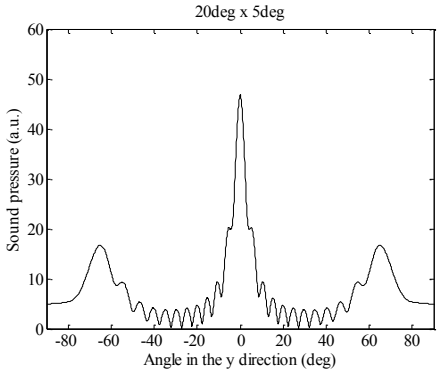

(c) In the *y* direction.

Figure 7. Sound pressure of the arry transmitter with anisotropic directivity. $\phi_x = 20$ deg and $\phi_y = 5$ deg.

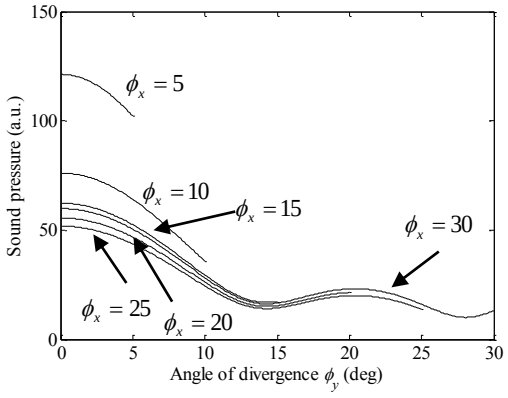

Figure 8. Dependences of sound pressure on the angle of the divergence in the *y* direction

However, by using an anisotropic array transmitter, the decrease of the peak power can be controlled. The sound pressure is about 50 times higher than that of a single element when the vertical angle of divergence is kept within 5 deg for an array transmitter with a wide horizontal divergence

V. CONCLUSIONS

An ultrasonic array transmitter with anisotropic directivity has been proposed and its characteristics have been investigated theoretically. The signal phase of each of the elements was changed, and the divergences were successfully controlled. By making the directivities anisotropic, a high sound pressure with a wide range of measurement was obtained. The detailed investigations comparing the simulation results with experimental results of actual device is now in progress.

REFERENCES

[1] P. N. Keating, T. Sawatari, and G. Zilinskas, "Signal processing in acoustic imaging", Proceedings of the IEEE, 67, 1979, pp. 496-510.

[2] L. J. Griffiths, and K. M. Buckley, "Quiescent pattern control in linearly-constrained adaptive arrays", IEEE Trans. Acoustic, Speech and Signal Processing, ASSP-35, 1987, pp.917-926.

[3] E. Martinson, and J. Delsing, "Electric spark discharge as an ultrasonic generator in flow measuremsnt situations", Elsevier- Flow Measuremnt and Instrumentation, Vol.21, 2010, pp 394-401.

[4] S. Kumar, K. Ichi, and H. Furuhashi,"Theoretical Investigation of High-Power Ultrasonic Array Transmitter for a Range Sensor in Air", Proceedings of the ICIT 2013 - 2013 IEEE International Conference on Industrial Technology, 2013, pp. 1190-1195.

[5] S. Kumar, K. Ichi, and H. Furuhashi, " Theoretical Investigation of Divergence Control of Directivity On Ultrasonic Array Transmitter", SICE Annual Conference 2013, 2013, in press.

 ISBN: 978-1-61208-297-4

Intelligent Monitoring of Subjects with Severe Disorder of Consciousness

Luigi Flotta, Francesco Riganello
Istituto S. Anna – Research in Advanced Rehabilitation
Crotone, Italy
l.flotta@istitutosantanna.it
f.riganello@istitutosantanna.it

Walter G Sannita
Dept. of Neuroscience, Ophthalmology and Genetics
University of Genova, Genova, Italy
Dept. of Psychiatry
State University of New York, Stony Brook , NY, USA
wgs@dism.unige.it

***Abstract* — We describe an integrated system for continuous acquisition, storage, handling and analysis of clinical and functional data from subjects in the vegetative or minimally conscious states. Data from different sources are stored in a centralized database and analyzed off-line by commercial or open source tools. Custom modules have been developed in order to convert proprietary data formats to the standard SQL data format. The centralized database is directly accessible when the patient's clinical record and data are needed to support decision (diagnosis, prognosis, selection of rehabilitation protocols) as well as in the patients' monitoring or for research purposes. The system is supported by web and open source technologies and interfaced with advanced support systems; it allows an integrated view of clinical and functional data flows.**

Keywords-severe disorder of consciousness; autonomic nervous system; intelligent monitoring; decision support system.

I. INTRODUCTION

Patients in vegetative or minimally conscious states need constant monitoring and a continuous stream of clinical/neurobiological information is required for appropriate healthcare by the medical and nursing staff and to optimize the rehabilitation therapy [1,2]. In the framework of the rehabilitation protocol, patients are also given sensory stimuli in order to improve their responsiveness to the environment and reduce isolation; responses to stimuli can vary and depend on the ortho/parasymphatetic functional balance in the autonomic system [3].

A. Structure of the article

The article includes the following sections: Acquisition and integration systems summarizing the system and its use, The decision support system, describing the main tools for analysis, Summary.

II. ACQUISITION AND INTEGRATION SYSTEM

The data acquisition and integration system (Figure 1) is implemented to record:

- Biometric and biological functional data and environmental information;
- Heart Rate and measures of Heart Rate Variability (HRV) in the time and frequency domains;
- Information about the individual neurorehabilitation program and training protocols.

Data collected by automated sensors are numerical measurements represented in ASCII (American Standard Code for Information Interchange) format that have minimal memory footprint and impact on the network requirements, so to make a standard 100 Mb LAN sufficient to sustain the system efficience.

The system is deployed on a LAN environment not accessible via web from unauthorized users. The chances of the patient's data leaking are, therefore, limited and the system complies with the modern standards of information security.

The system is neither a remote health monitoring system, nor a telemedicine system; it is intended to support the daily work and research activities of the specialized public/private institutions dedicated to the treatment of subjects with severe Disorder Of Consciousness (DOC). One main goal is to collect over time a very large dataset of biological data from patients with severe DOC and their (statistical) correlations with environmental data and clinical condition. Purpose is to use these data and their relations to obtain objective diagnostic criteria, predict early and accurate prognosis of patients and define therapeutic pathways.

The centralized database is hosted on a PostgreSQL [22] instance, version 9.2, and its main tables, namely:

- *Gateway* – wireless access point that collects and forward to the database the data from sensors;
- *Sensors* – collecting information from environment and patients;
- *BiologicalMeasurements* – storing biological data;
- *EnvMeasuremtes* – storing environmental data.

For security reasons, the centralized database is installed on a server different than the web-server.

A. Biogical and environmental data

A hard/software system with Hx24 high-availability acquires biometric and environmental raw data measured by a series of traditional or innovative wireless sensors. The system includes a gateway connected to the LAN (Local Area Network) to detect environmental data (ambient temperature, environmental humidity, light intensity, noise, etc.). Wireless sensors are positioned at proper locations on

 ISBN: 978-1-61208-297-4

the patients and measure biometric parameters such as body temperature, heart rate and systolic/diastolic blood pressure, breathing, pO2, pCO2, spontaneous movements, voice, eye movements and blinking, to be transferred to the gateway. All data are forwarded to a server that collects the byte stream and stores it, after appropriate transformations, in the centralized data base for further processing or sends data to user interface software (example in Figure 2). The system is operative and already collected about 1GB of data. Measures are from sensors detecting/quantifying: Environmental Temperature, Light, Humidity, Noise, Body Temperature, Heart Rate, Oximetry and Eyes blinking.

B. Heart Rate Variability

Heart Rate Variability (HRV), i.e., the heart rate fluctuations around the mean value over the time sample, mirrors to a substantial extent the cardiorespiratory control system and is regarded as a reliable index of the sympathetic/parasympathetic functional interplay [4] and intrinsic influence on heart rate. HRV is also thought to provide independent information on the autonomic nervous system and its functional integration with the brain, to reflect the action of physiological factors modulating the heart rhythm and homeostatic adaptation to the changing conditions, and to describe modulation by Central Autonomic Nervous network (CAN) [5]. CAN influences heart rate adaptation through multiple connections (inputs from sensory and baroreceptors within the heart and great vessels, respiratory changes, vasomotor regulation, thermoregulatory system and changes in endocrine function and neuroendocrine interaction) [6]. There is indication that the autonomic system may also mediate patterns of brain activation of varying complexity. HRV is thought to reflect the organization of affective, physiological, cognitive, and behavioral elements and is emerging as a possible descriptor of the brain functional organization contributing to homeostasis and homeostatic responses [6]. The basic objective of the survey is to identify patterns of correlation between the HRV data and functional models available today for the CAN.

Heart signals (EKG) can be recorded continuously by non-invasive techniques and analyses in the time or frequency domains can extract HRV information; the method is now established in the functional investigation of the CAN and has proved reliable in the study of subjects with severe DOC. Records of responses are obtained either from a Nexus 10 or from a Nexus 32 (Mind Media, NL). Nexus systems provide outputs in .edf file format that are transferred through web application to the server for storage in the central database and retrieval off-line for further processing.

C. Rehabilitation data

These data are obtained by clinical observation according to established rating scales filled by the medical and nursing staff. The scales now in use are:

- The Coma Recovery Scale Revisited – CRS [7];
- The Wessex Head Injury Matrix – WHIM [8];
- The Levels of Cognitive Functions – LCF [9];
- The Nociception Coma Scale – NCF [10].

Dedicated web applications have been developed to enable medical and nursing staff to fill in each scale item with the appropriate values. Data are stored in the central database and integrated with the information for further processing and correlative studies.

III. THE DECISION SUPPORT SYSTEM

The Decision Support System is composed mainly of **R**, an Open Source statistical package, extended with custom modules [12]. Classical techniques of statistical analysis are used, such as the *Bayesian Statistics*, *Data Mining*, *Neural Network*, *Linear Regression*, etc [12].

In the following sections, we briefly describe the main objectives of our statistical analysis.

A. Ambient Intelligence

Analyses of information from environmental and biometric sensors follow a straightforward strategy, with major focus on spontaneous variability or in response to changes in the environment [13-15]. Sources of variation are manifold and can reflect changes in the functional status or in responsiveness as well as the existence of residual endogenous mechanisms of self-regulation or circadian/ultradian cycles. For patients in vegetative or minimally conscious state, changes can also depend on interaction with the staff or relatives and effects of the procedures of nursing and rehabilitation services, or reflect endogenous mechanisms [16]. The rationale for the analysis of each vital parameter aims at assessing the existence of cyclic or non-cyclic changes and at correlating each parameter or pattern of variation with environmental changes [17].

Investigation in this field has several goals:

- To verify whether circadian/ultradian pattern of change are partially preserved or have recovered to a significant extent in individual subjects;
- To recognize processes to be relied on as prognostic indicators;
- To identify changes in the vital parameters related to contingent events and indicative of residual/recovered responsiveness or of use when customizing the rehabilitation treatments according to tolerability;
- To to achieve an integrated model of analysis and prediction.

The regression analysis (to identify relationships among variables), the Neural Network (a sophisticated pattern detection algorithm using machine learning techniques to generate predictions), the Clustering/Segmentation processes (to create groups for applications), the Association Rules techniques (to detect related items in a dataset) are widely used for performing above investigations [18].

 ISBN: 978-1-61208-297-4

B. *Parameters and Analysis*

Two main lines of analysis were identified:

1) Stimuli Response Distribution Analysis

The stimulus conditions to be administered to patients with severe DOC (Disorder Of Consciousness) can be characterized in order to activate simple or complex functions of the auditory or visual sensory channels (including highly integrated extrinsic eye mobility, e.g., the visual pursuit response) or the somatosensory system.

Analyses are purported to distribute the recorded HRV descriptor values vs. the response, by selecting at pre-determined conditions and time points the parameters qualifying as possible biomarkers. The obtained distribution is classified by Data Mining techniques and/or Linear Regression and/or Sequence Association tools (to detect causality and association between time-ordered events) in order to assess the subject's state of consciousness (e.g., vegetative vs. minimally conscious states) or identify and monitor stimulus- or environment-related changes or spontaneous fluctuations over time.

Statistical techniques used include: the regression analysis, the Neural Network, the Clustering/Segmentation processes, the Association Rules techniques.

2) Central Autonomic Nervous System (CAN)

HRV provides independent information on the CAN and its functional integration with the brain [19-21]. The basic objective of the survey is to identify patterns of correlation between the HRV data and functional models available today for the CAN. Parameters "representing" CAN are reported in table 1.

Statistical techniques used include: the regression analysis, the Neural Network, the Clustering/Segmentation processes, the Association Rules techniques.

IV. SUMMARY

The functional state/recovery of CAN recovery, the impact of ambient condition and/or changes, sleep quality, circadian symphato/vagal alternance, organization of the brain electrophysiological activities, infra-ultra/circadian rhythms, and responsiveness to stimuli are fundamentals in the rehabilitation project of patients with severe DOC.

The development of *acquisition and integration systems* will provide the information needed to design effecient tive plain of protocol for the observation, rehabilitation and monitoring of patients with severe DOC. The approach will contribute in the process of acquiring new knowledge on the neural mechanism underlining recovery in these patients and help planning better rehabilitative routines.

REFERENCES

[1] Royal College of Physicians, The vegetative state: guidance on diagnosis and management. Royal College of Physicians (Ed.). RCP Publications Department , 2003.

[2] The Multi-Society Task Force on PVS, "Medical aspects of the persistent vegetative state", New England Journal of Medicine vol. 330, pp.1499-1508, 1994.

[3] F. Riganello, A. Candelieri, M. Quintieri, D. Conforti, and G. Dolce, "Heart rate variability: an index of brain processing in vegetative state? An artificial intelligence, data mining study", Clinical Neurophysiology, vol. 121, pp. 2024-2034, 2010.

[4] Task Force of the European Society of Cardiology and the North American Society of Pacing and electrophysiology of Circulation, "Heart rate variability: standard of measurement, physiological interpretation, and clinical use", Circulation, vol. 93, pp. 1043-1065, 1996.

[5] F. Riganello, G. Dolce, and W. G. Sannita, "Heart rate variability and the central autonomic network in the severe disorder of consciousness", Journal of Rehabilitation Medicine, vol. 44(5), pp. 495-501, 2012.

[6] F. Riganello, S. Garbarino, and W. G. Sannita, "Heart rate variability, homeostasis, and brain function: a tutorial and review of application", Journal of Psychophysiology, vol. 26(4), pp. 178-203, 2012.

[7] J.T. Giacino, K. Kalmar, and J. Whyte, "The jfk coma recovery scale-revised: measurement characteristics and diagnostic utility", Arch. Phys. Med .Rehabil., vol. 85(12), pp. 2020-2029, 2004.

[8] S. Majerus, M. Van der Linden, and A. Shiel, "Wessex head injury matrix and glasgow/glasgow-liège coma scale: a validation and comparison study", Neuropsychol. Rehabil., vol. 10, pp. 167-184, 2000.

[9] C. Hagen, D. Malkmus, and P. Durham, "Levels of cognitive functioning", Ranchos Los Amigos Hospital (Ed.). Ranchos Los Amigos Hospital, Downey, CA, 1972.

[10] C. Schnakers, C. Chatelle, A. Vanhaudenhuyse, S. Majerus, D. Ledoux, M. Boly et al., "The nociception coma scale: a new tool to assess nociception in disorders of consciousness", Pain, vol. 148(2), pp. 215-219, 2010.

[11] S. Tufféry, Data mining and statistics for decision making. Wiley, 2011.

[12] J.P. Marques de Sa. Applied statistics using SPSS, Statistica, Matlab and R. Springer, 2007.

[13] A. Candelieri, D. Conforti, F. Riganello, and W. G. Sannita, "Data mining for the analysis of psychophysiologica variation to stimuli in vegetative state patients", Proc. of airo 2010, xli giornate di lavoro airo 2010, Villa S. Giovanni (RC), September 2010.

[14] A. Candelieri, G. Dolce, F. Riganello, and W. G. Sannita, "Data mining in neurology", In Knowledge-oriented application in data mining, Funatsu K & Hasegawa K (Eds.), pp. 264-276, 2011.

[15] A. Candelieri, M. D. Cortese, F. Riganello, and W.G. Sannita, "Functional status and the eye-tracking response. A data mining classification study in the vegetative and minimaly conscious states", Proc. Heathinf Rome, pp. 138-141, 2011.

[16] F. Riganello, G. Dolce, M. D. Cortese, and W. G. Sannita, "Responsiveness and prognosis in the severe disorder of consciousness", In Brain damage: causes, management and prognosis, Schäffer AJ & Müller J (Eds.) pp. 117-135, 2010.

[17] L. Pignolo, F. Riganello, G. Dolce, and W. G. Sannita, "Ambient intelligence for monitoring and research in clinical neurophysiology and medicine: the Mimerica* project and prototype", Clinical EEG and Neuroscience, in press: [Epub ahead of print], 2013.

[18] M. F. Hornick, H. Marcadé, and S. Venkayala, Java data mining. Morgan Kaufmann, 2007.

[19] M. L. Ryan, C. M. Thorson, C. A. Otero, T. Vu, and K. G. Proctor, "Clinical applications of heart rate variability in the triage and assessment of traumatically injured patients", Anesthesiology Research and Practice, 2011, doi:10.1155/2011/416590.

[20] J. J. Sollers, T. A. Sanford, R. Nabors-Oberg, C. A. Anderson, and J. F. Thayer, "Examining changes in hrv in response to varying ambient temperature", IEEE Engineering in Medicine and Biology, May 2002, vol. 21, pp. 30-34.

 ISBN: 978-1-61208-297-4

[21] A. L. Hansen, B. H. Johnsen, J. F. Thayer, "Relationship between heart rate variability and cognitive function during threat of shock", Anxiety Stress Coping, vol. 22, pp. 77-89, 2009.

[22] PostgreSQL DBMS, version 9.2, http://www.postgresql.org/, [retrieved: April, 2013].

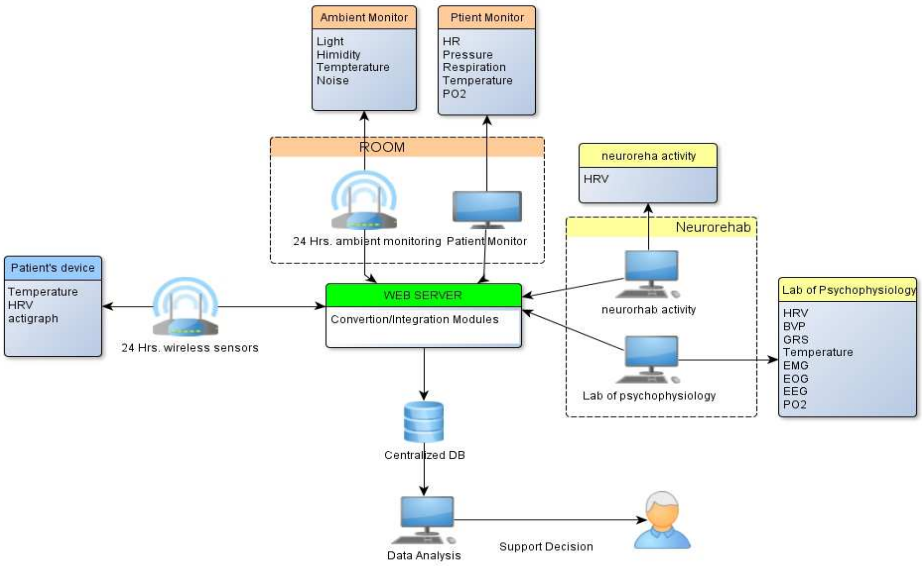

Figure 1. The architecture of the acquisition and integration system.

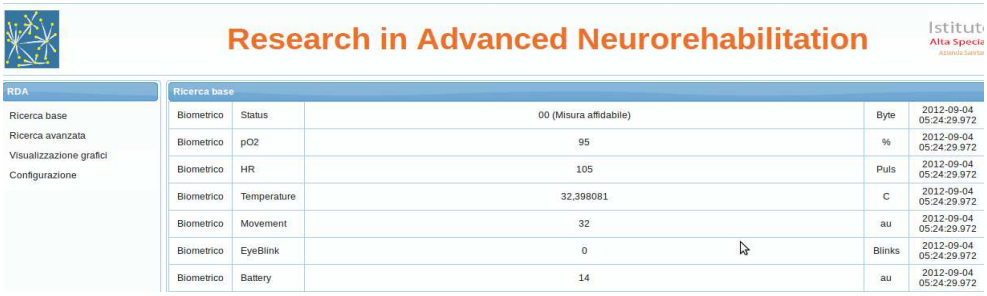

Figure 2. Some biological data acquired by the system.

Statistical Parameters	Mean RR interval (Mean RR [*ms*]); Standard deviation of RR values (STD RR [*1/min*]); Mean Heart Rate (Mean HR[*1/min*]); Standard deviation of heart rate values (STD HR [*1/min*]); Square root of the mean squared differences between successive RR intervals (RMSSD) [*ms*]); Number of successive RR interval pairs that differ more than 50 ms(NN50); NN50 divided by the total number of RR intervals(pNN50 [*%*]); The integral of the RR interval histogram divided by the height of the histogram (HRV triangular index); Baseline width of the RR interval histogram Frequency-Domain (TINN [*ms*]);
Spectral Parameters	Peak frequency in *FFT* and *autoregressive spectra* of Very Low Frequency (VLF), Low Frequency (LF) and High Frequency (HF) band [*Hz*]; Power Spectrum of VLF, LF, HF and Total in FFT and autoregressive spectra [*ms2*]; % of VLF, LF, HF in FFT and autoregressive spectra *[Spectral band [ms2]/total power [ms2] × 100%];* Ratio between LF and HF band powers **(**Ratio LF/HF**)**; normalized unit of LF (nu LF) and normalized unit of HF (nu HF), in FFT and autoregressive Spectra, [*Spectral band [ms2]/(total power [ms2] − VLF [ms2*]];
Nonlinear	The standard deviation of the Poincarè plot perpendicular to (SD1) and along (SD2) the line-of-identity, [ms]; Approximate entropy ApEn;Sample entropy SampEn;Correlation dimension;Detrended fluctuation analysis DFA (ά1Short term fluctuation slope and ά2 Long term fluctuation slope);
Galvanik Skin Responce	Measure of the electrical conductance of the skin. It's is used as an indication of psychological or physiological arousal.
Actigraphy	Monitoring of rest/activity cycles.
Blood Volume Pulse	Measured by a process called photoplethysmography, which produces a graph indicating blood flow through the extremities.

Table1: Principal parameters extracted for the ANS analysis

A Prototype for Blood Typing Based on Image Processing

Ana Ferraz, Filomena Soares
R&D Centre Algoritmi
University of Minho
Guimarães, Portugal
Ana.Ferraz@algoritmi.uminho.pt
Filomena.Soares@algoritmi.uminho.pt

Vitor Carvalho
EST, Polytechnic Institute of Cávado and Ave
Barcelos, Portugal & R&D Centre Algoritmi
University of Minho, Guimarães, Portugal
vcarvalho@dei.uminho.pt

***Abstract*—This paper presents a new methodology for blood phenotyping based on the plate test and on image processing techniques to determine the occurrence of agglutination (between blood sample and reagent). A portable device for ABO-Rh blood typing and blood phenotying that automates all the analysis procedure, including mixture/centrifugation, reading and interpretation of results is presented. The system was tested with donor blood samples.**

Keywords - blood type determination; phenotyping; image processing techniques; prototype.

I. INTRODUCTION

The process of determination of blood types is essential before administering a blood transfusion, but in some cases, due to the risk of the individual´s life, it is necessary to quickly administer blood [1-3]. In these emergency situations, there is no time to determine the blood type and so the procedure is to administer the blood type O negative (universal donor) [1-3]. Nevertheless, due to some incompatibilities transfusion reactions may occur that could lead to the death of the patient [3].

Before performing a safe blood transfusion, certain compatibility tests, named pre-transfusion tests, must be undertaken, namely [4-6]:

1. Determine the A, B, AB, O (ABO system) and Rhesus (Rh) type of the patient;
2. Perform the reverse test: reverse grouping of ABO typing of the patient;
3. Perform the Rh (C, c, E and e) and Kell (K) phenotyping for detecting the presence of antigens in the blood of the patient. The search of other antigens can also be performed, but only in few situations [7];
4. Perform the screening of antibodies to detect the presence of significant antibodies. If antibody screening is positive, an identification of the antibody must be performed to allow the selection of the compatible blood;
5. Verify the results with previous data, if available;
6. Select the erythrocytes of the donor and perform the cross match.

The determination of ABO and Rh type can be performed in tube [8], plate [8], micro-plates [2], or gel centrifugation [9]. Due to the fast response time, the tube and the plate tests are those used in emergency situations. The micro-plates and gel centrifugation tests are more accurate than the tube or plate tests, but they require expensive and heavy devices.

This work aims to develop a prototype able to automatically perform the pre-transfusion tests necessary for a safe blood transfusion. This device is based on a previous version of the equipment developed by the authors [10-13] and it automates the reading, centrifugation and interpretation of results of all the pre-transfusion tests previously mentioned. The prototype presented is able to determine ABO and Rh blood typing and blood phenotyping.

It is important to mention that currently these tests are performed manually or at least semi-automatically, which may occur in errors in the testing procedure, the reading and interpretation of the results, being sometimes fatal to the patient [14, 15].

Apart from the present section, the paper is organized with more four sections. In Section II, the phenotyping determination is described, presenting the image processing techniques applied. The prototype developed is presented in Section III and in Section IV the results of the phenotyping ABO and Rh tests with the prototype developed are discussed. Finally, Section VI presents the conclusions and the directions for future work.

II. PHENOTYPING DETERMINATION

A methodology was developed regarding the pre-transfusion tests for determining the ABO and Rh type, based on the plate test and image processing techniques [13, 16-18].

This work is focused on the phenotyping tests Rh (C, c, E and e) and Kell (K), based also on the plate test [8]. The phenotyping determination is obtained through image processing techniques applied to the target image. The plate test method was employed due to its reliability and fast response time suitable in emergency situations.

The procedure used in the phenotyping is described in [19], where it can be observed that it requires centrifugation to separate the blood from the plasma and red blood cells, which is a costly and complex process.

 ISBN: 978-1-61208-297-4

The proposed system is able to perform the centrifugation in a simple approach. After separating the blood and obtaining the plasma, six slides are considered, one for each of the phenotypes tested. In each slide, it was added a drop of the respective reagent TransClone Anti-RH1 (D), TransClone Anti-RH2 (C), Transclone Anti-RH3 (E), TransClone Anti-RH4 (c), TransClone Anti-RH5 (e) and TransClone Anti-Kel1 (K) [19], and a drop of blood of the patient. The mixture was manually performed using a glass rod in each slide. An image of the sample (mixed blood/reagent) was acquired and sent to the computer for further processing. The presence (or absence) of agglutination in each sample was determined through image processing techniques. The classification algorithm used in the analysis is implemented to work with blood samples after its centrifugation. The camera used to capture the images was a Sony Cyber-shot DSC-S750 of 7.2 Megapixel with 3X Optical Zoom (35-105 mm eq.) and 5 point auto focus [20].

To process the images, in order to determine the blood phenotyping as well as ABO-Rh, an algorithm was developed using IMAQ Vision software from National Instruments [21]. The algorithm developed is presented in Figure 1, as a flowchart [21-23]. The image captured is segmented, the localization of each of the wells is obtained and then the mixture reagents/blood is quantified, among others, with the standard deviation value.

In Figure 1 are presented the image processing techniques applied: image selection and storage, extraction of the color planes of the image, application of thresholds and fill holes, removal of small and border objects, and analysis. The original image is retrieved and luminance planes are removed, pattern and geometric matching is used to identify the imagine reference and containers position; finally the quantify function is employed determining the blood type in analysis.

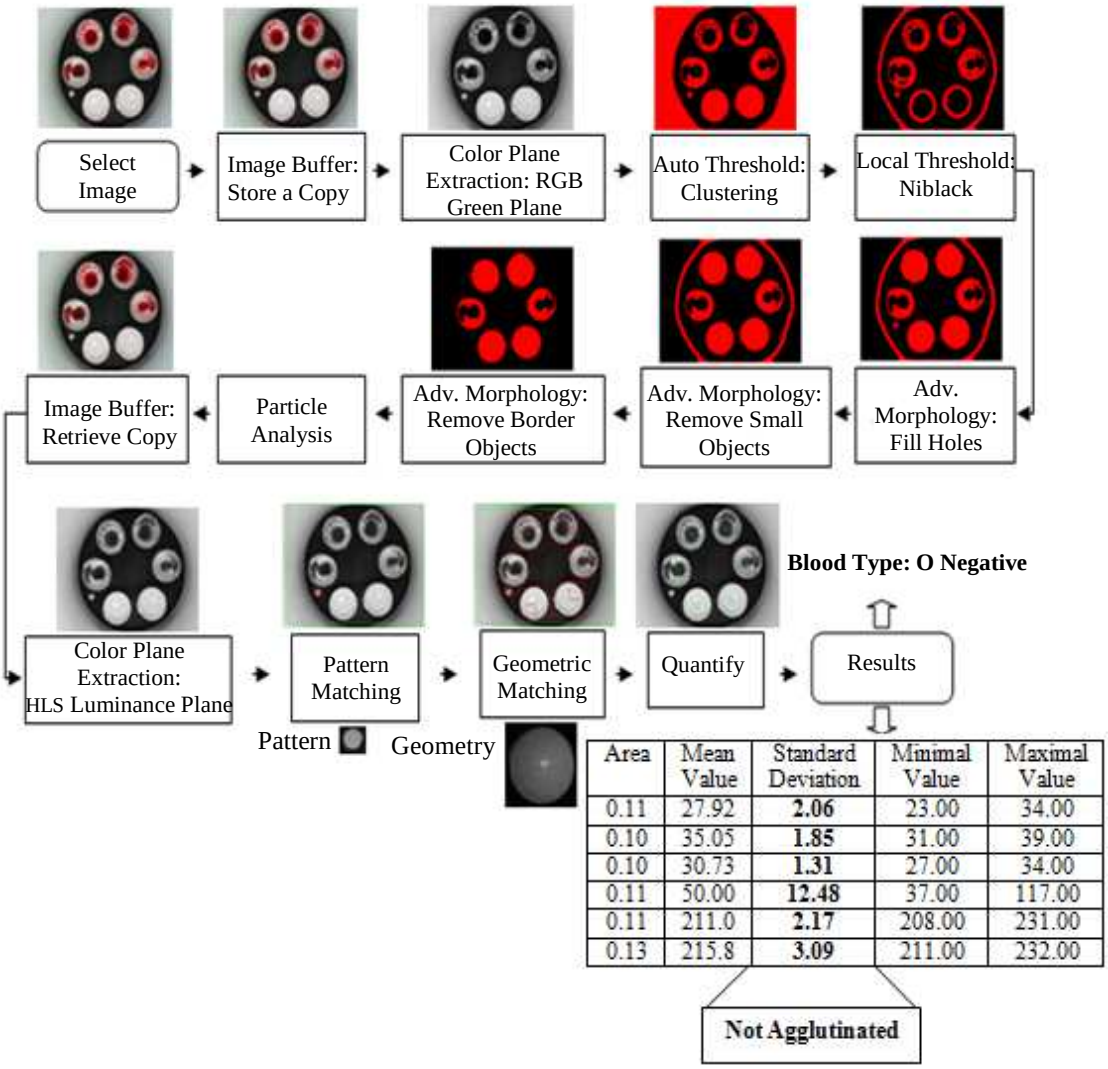

Figure 1. Flowchart of the algorithm developed for the prototype.

 ISBN: 978-1-61208-297-4

III. AUTOMATIC AND PORTABLE SYSTEM DEVELOPED

The proposed system was developed to automatically determine the human blood type of a patient (phenotyping and ABO-Rh). An important requisite of the developed system was its portability (small and easy to transport to any place) in order to be used in emergency vehicles and other services. Thus, the analysis can be performed outside the clinical analysis laboratory and the results can be sent to the hospital through Wi-Fi or GSM.

The system developed has 30 cm of height and 10,5 cm of diameter (Figure 2). It has an AC motor that allows the mixture and the centrifugation. The motor rotational speed is adjustable depending if the test performed is a mixture (low speed) or a centrifugation (high speed). The motor can spin the plate test with the six containers and mixture the blood and reagent, or spin the plate and centrifuge the blood for obtaining the plasma. When the test is performed the motor is stopped, the LEDs switch on and then an image with all the necessary data is captured. The image is processed and the result of the test is given. At the end the LEDs switch off. The whole procedure is illustrated in the flowchart of Figure 3.

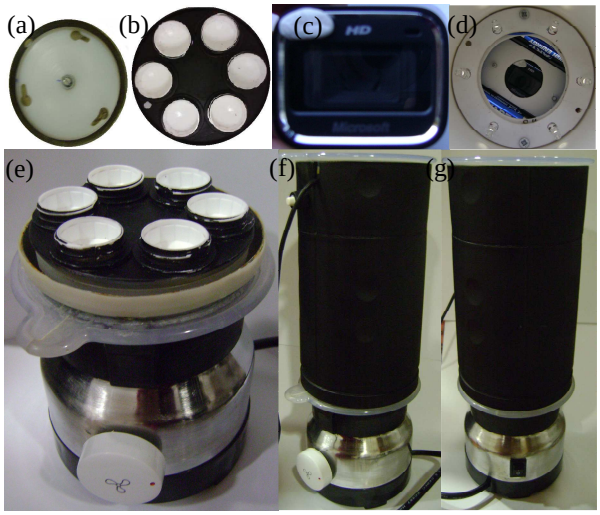

Figure 2. Portable System developed: (a) base of the system where piece with containers fits into the system, (b) piece with containers for mixture of blood and reagents, (c) web camera used to capture the image, (d) LEDs around and web camera in the centre, (e) base of the system that promote the mixture, (f) final system with button to change velocity, (g) final system with switch to switch on/off the system.

The user friendly application where all the image processing techniques are included as well as the classification algorithm was developed in C# Language and XAML (Figure 4).

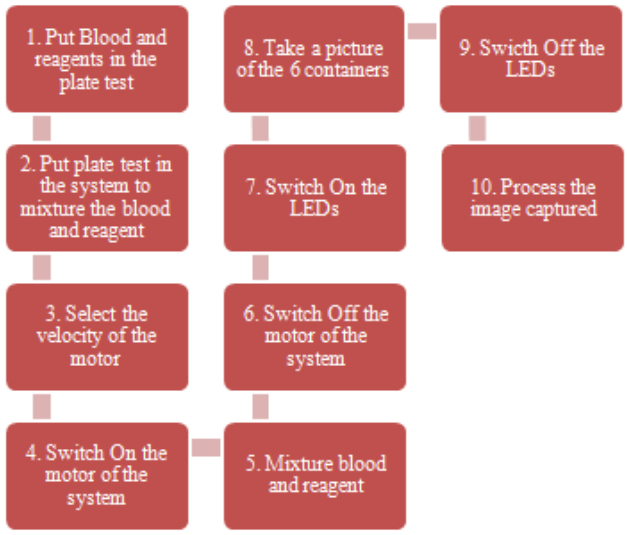

Figure 3. Flowchart of the system developed.

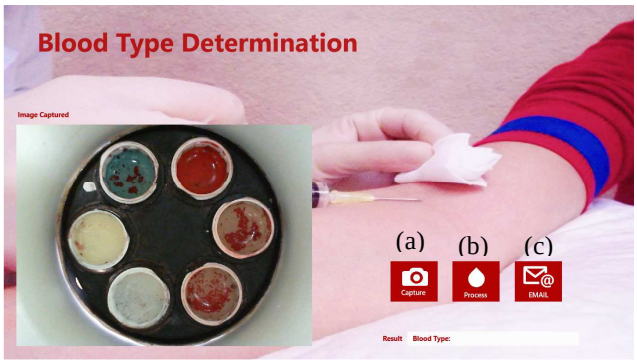

Figure 4. Application Developed. (a) Button to capture the image. (b) Button to process the image captured. (c) Button to send the results message.

This application contains a button to capture the original image with the six containers, Figure 4 (a), a button to process the original image and give the blood type result, Figure 4 (b), and finally a button to send a message to the laboratory with the blood type result, Figure 4 (c).

IV. RESULTS OBTAINED WITH THE DEVELOPED SYSTEM

This section presents the results of phenotyping tests (A) and the results of ABO and Rh tests (B), obtained with the prototype developed. The blood samples tested were from donors from the Portuguese Blood Institute (IPST).

A. Results of phenotyping tests

The methodology presented in this paper was tested and validated using several blood phenotypes from donors. This subsection presents the obtained results when applying the image processing techniques developed in images captured after the procedure of plate test (Section II). Figure 5 shows

 ISBN: 978-1-61208-297-4

six original images corresponding to the mixture of blood and the respective reagent, TransClone Anti-RH1 (D), TransClone Anti-RH2 (C), Transclone Anti-RH3 (E), TransClone Anti-RH4 (c), TransClone Anti-RH5 (e) and TransClone Anti-Kel1 (K), captured by the camera. Figure 6 shows the images obtained after the application of image processing techniques and in Table I are summarized the quantified results.

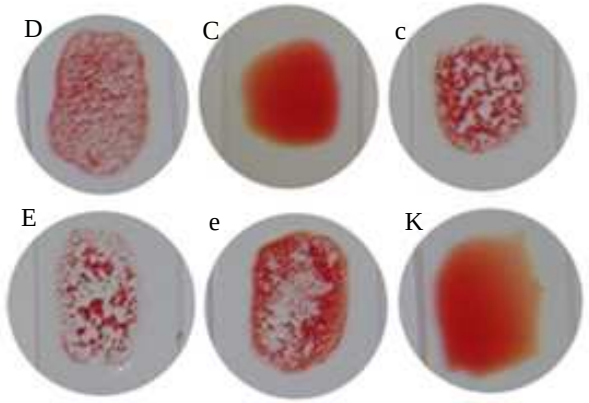

Figure 5. Images captured of blood/reagent mix for determination of Rh and Kell phenotype.

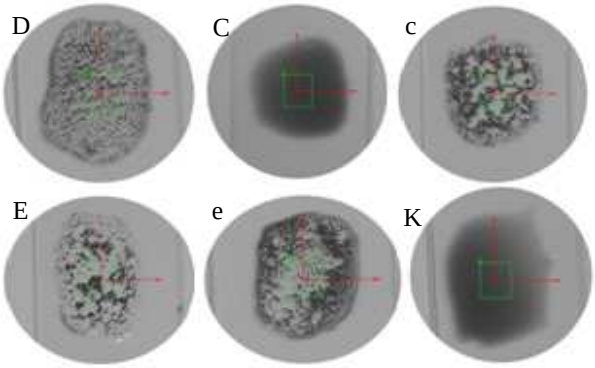

Figure 6. Results of the application of the developed algorithm through the images of Figure 4.

TABLE I. RESULTS OF THE DEVELOPED ALGORITHM THROUGH THE IMAGES OF FIGURE 5

Figure 6	Area	Mean Value	Standard Variation	Minimal Value	Maximal Value
D	3,19	118,36	**29,09**	21,00	181,00
C	2,08	59,24	3,08	51,00	71,00
c	1,98	118,69	**39,32**	20,00	184,00
E	2,67	125,20	**44,91**	15,00	195,00
e	3,75	131,88	**29,30**	25,00	195,00
K	3,18	67,31	5,70	55,00	86,00

Analyzing Figure 5, one can see that agglutination occurred in images corresponding to phenotype test D, c, E and e (Standard Variation values highlighted in bold), and agglutination does not occur in the remaining images C and K. It can be observed in Table I, that when agglutination occurs, images D, c, E and e of Figure 6, present a standard deviation value higher than 16 (threshold established in previous studies [13] to detect the occurrence of agglutination). The standard deviation value is the threshold for determining the occurrence or non occurrence of agglutination. Thus, standard deviation value above 16 indicates the occurrence of agglutination, while standard deviation values below 16, mean the non occurrence of agglutination in the analyzed image. Thus, given that agglutination occurred for phenotypes D, c, E and e, and agglutination was not observed for other phenotypes, C and K, the phenotype under analysis is then cEeK-D (confirmed by the analysis performed by the IPST).

B. Results of ABO and Rh tests

The proposed system allows also ABO and RH blood typing [12, 13]. In Figure 7, it is presented the original image of the containers captured after the mixture of blood sample and the specific reagents. Figure 8 presents the final image after the application of the developed image processing algorithm. TABLE II presents the occurrence of agglutination in each container and the correspondent ABO-Rh blood type. The agglutination occurred in Figure 8 with the reagents Anti-B, Anti-AB and Anti-D and not in Figure 8 with the reagent Anti-A, meaning that in this blood sample are present the antigens of type B and D and not the antigens of type A. The blood type is then B positive.

The determination of the occurrence of agglutination in the ABO-Rh blood test is also performed through the value of standard deviation.

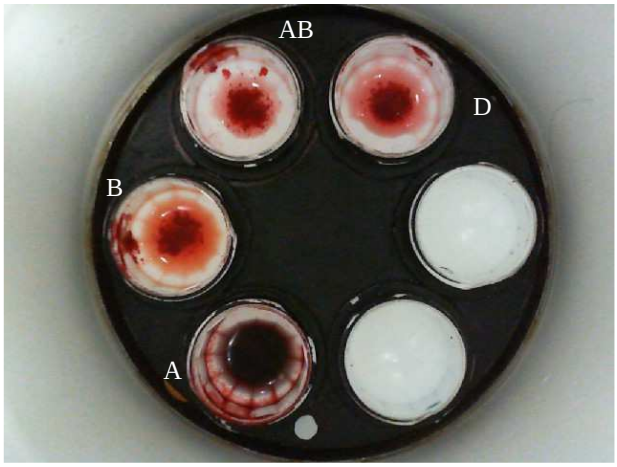

Figure 7. Image captured of blood/reagent mix for determination of ABO and Rh.

 ISBN: 978-1-61208-297-4

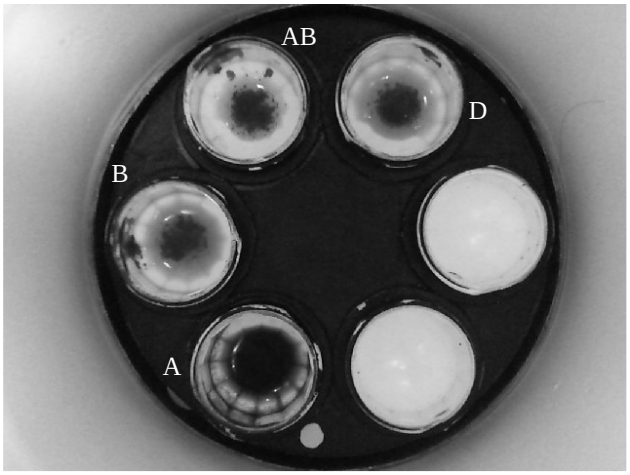

Figure 8. Results of the application of the developed algorithm through the images of Figure 6

TABLE II. RESULTS OF THE DEVELOPED ALGORITHM THROUGH THE IMAGES OF FIGURE 6

Figure 7	Occurrence of Agglutination	Blood Type
A	No	B
B	Yes	
AB	Yes	
D(Rh)	Yes	Positive

By observing TABLE II, it is possible to conclude that the blood type resultant is B Positive, as agglutination occurred with the reagents anti-B, anti-AB and anti-D.

V. CONCLUSION AND FUTURE WORK

This work allows enforcing the validation of the use of the plate test and image processing techniques as a feasible methodology to blood typing. As in [13, 16-18], the plate test has proven to be adequate to detect the occurrence of agglutination, even if it is weak, and the image processing techniques developed allow a correct automatic detection of agglutination, permitting ABO-RH blood typing as well as the phenotypes of the patient.

Once the system obtains results in a short time, about 5 minutes in total, at a low cost and being portable, it is characterized by an innovative solution with commercial added value. The system can be either used for dual operation, mixture (low speed) and centrifuging (high speed), depending of the motor velocity selected. Due to its portability and fast response time it can be used in ambulances or other vehicles for emergency situations.In future, it is intended to include closed loop control to the illumination and the rotational speed of the motor as well as, introduce neural networks to improve the classifications of the developed system. With the neural networks it will be possible to classify blood types as well as pre-transfusion tests more efficiently, quickly and safely.

ACKNOWLEDGMENT

Thanks to the Portuguese Foundation for Science and Technology (FCT) for funding through the PhD scholarship SFRH/BD/81094/2011.

This work is funded also by FEDER funds through the "Programa Operacional Factores de Competitividade - COMPETE" and by national funds by FCT- Fundação para a Ciência e a Tecnologia, project reference FCOMP-01-0124-FEDER-022674.

REFERENCES

[1] R. S. Rod, P. Tate, and D. S. Trent, "Anatomina & Fisionlogia", Lusociencia, 6nd ed., Loures, 2005.

[2] V. A. Hoffbrand, E. J. Pettit, and H. A. P. Moss, “Fundamentos em Hematologia”, Artmed, 4nd Edition., Porto Alegre, 2004.

[3] R. Caquet, "Guia Prático Climpsi de Análises Clínicas", 1st ed., Lisboa, 2004.

[4] S. L. Mitchell, J. B. Brain, and I. Bates, “Dacie and Lewis Practical Haematology”, Elsevier Health Sciences. 9th Edition. ISBN: 0-443-06377-X, 2001.

[5] J. D. Roback, B. J. Grossman, T. Harris, and C. D. Hillyer, “Technical Manual”, AABB, 17th Edition, 2011.

[6] C. D. Hillyer, L. E. Silberstein, P. M. Ness, K. C. Anderson, and J. D. Roback, 2007. Blood Banking and Transfusion Medicine Basic Principles and Practice. Churchill Livingstone Elsevier. 2nd Edition. ISBN-13: 978-0-443-06981-9

[7] D. B. L. McClelland, “Handbook of Transfusion Medicine”, United Kingdom Blood Service, 4th Edition, 2007. ISBN-10 0 11 3226772. Online: http://www.transfusionguidelines.org.uk/docs/pdfs/htm_edition-4_all-pages.pdf; retrieved: June, 2013

[8] M. Cressiers, “Datasheet of Diamed Diaclon Anti-A, Diaclon Anti-B, Diaclon Anti-AB”, 2008.

[9] M. Cressier, “Datasheet of Diamed-ID Micro Typing System, Card-ID”. Diaclon ABO\Rh for patients, 2008.

[10] K. Bezerra, et al. “Advanced Design of a Mechatronic System for Human Blood Typing”, Romanian Review Precision Mechanics, Optics & Mecatronics, 2012. ISSN 1584 - 5982.

[11] V. Moreira, A. Ferraz, V. Carvalho, F. Soares, and J. Machado, 2012. Design of a Mechatronic System for Human Blood Typing in Emergency Situations, ETFA’2012 17th IEEE International Conference on Emerging Technologies & Factory Automation. September 17th to 21th. Kraków, Poland.

[12] A. Ferraz, V. Moreira, D. Silva, V. Carvalho, and F. Soares, “Automatic System for Blood Type Classification Using Image Processing Techniques”, BIODEVICES 2011 International Joint Conference on Biomedical Engineering Systems and Technologies, 26-29 de January, 2011, Rome, Italy.

[13] A. Ferraz, V. Carvalho, F. Soares, and C. P. Leão, “Characterization of Blood Samples Using Image Processing Techniques”, Sensors & Actuators: A. Physical, 2010.

[14] A. B. Myhre, D. McRuer, “Human error – a significant cause of transfusion mortality”, Transfusion. vol. 40, 2000, pp. 879–885.

[15] A. E. Henneman, et al. “Increasing patient safety and efficiency in transfusion therapy using formal process definitions”, Transfus Med Rev, vol. 21, 2007, pp. 49–57.

[16] A. Ferraz, V. Carvalho, and F. Soares, “Development of a Human Blood Type Detection Automatic System”, EUROSENSORS XXIV, 5 - 8 September. Linz, Austria, 2010.

 ISBN: 978-1-61208-297-4

[17] A. Ferraz, V. Carvalho, and P. Brandão, "Automatic Determination of Human Blood Types using Image Processing Techniques", BIODEVICES 2010 International Conference on Biomedical Electronics and Devices 2010. 20 – 23 January. Valence, Spain, 2010.

[18] A. Ferraz, V. Carvalho, and P.Brandão, "Determinação Automática do Tipo Sanguíneo de Humanos Utilizando Técnicas de Processamento de Imagem", CBIS`2008 XI Congresso Brasileiro de Informática em Saúde, 29 November - 3 December , Sao Paulo, Brazil, 2008.

[19] Bio-Rad, "Human Monoclonal IgM Antibodies", 2003. Online: http://www.bio-rad.com/ retrieved: June, 2013 .

[20] Sony Cyber-shot S750 Digital Camera, 2008. Online: http://store.sony.com/p/DSC-S750/en/p/DSCS750 retrieved: June, 2013

[21] IMAQ, "IMAQ Vision Concepts Manual", National Instruments, Austin, 2004.

[22] T. Klinger, T, "Image Processing with LabVIEW and IMAQ Vision", Prentice Hall, New Jersey, 2003.

[23] G. C. Relf, "Image Acquisition and Processing with LabVIEW", CRC Boca Raton, 2003.

 ISBN: 978-1-61208-297-4